2014

Microstructure, crystallography and mechanical properties of low-Si TRIP steels

Fayez Alharbi
University of Wollongong

UNIVERSITY OF WOLLONGONG

School of Mechanical, Materials and Mechatronic Engineering

Microstructure, Crystallography and Mechanical Properties of Low-Si TRIP Steels

Fayez Alharbi

This thesis is presented as part of the requirements for the award of the Degree of the Doctor of Philosophy

University of Wollongong, Australia

August, 2014

ABSTRACT

Transformation-induced plasticity (TRIP) steel has received significant research effort because its high strength to ductility ratios and high energy absorption make it eminently suitable for automotive applications. This work investigates the microstructure, crystallography, and mechanical properties of thermo-mechanically processed (TMP) low-Si high-Al TRIP steels with and without the addition of 0.03Nb and 0.02Ti (wt%) using a combination of optical and electron microscopy, X-ray diffraction, and tensile testing.

The two TRIP steels investigated were subjected to simulated TMP and galvanising and then the results were compared with intercritically annealed–galvanised steels. After undergoing different thermo-mechanical processing schedules it was found that adding Nb and Ti increased the tensile strength (~ 750 MPa) and total elongation (TE) (~ 29 %), as well as improving the strength-ductility balance compared to the base steel (without Nb and Ti) due to a higher volume fraction of RA and a combination of microstructure refinement and precipitation strengthening effects. Despite these gains, both steels suffered a deterioration in the volume fraction of retained austenite and mechanical properties after the additional galvanising simulation, indeed all the TMP and galvanised base steel samples recorded a continuous yielding behaviour during tensile testing. The Nb–Ti steel exhibited discontinuous yielding and extended Lüders banding when TMP was followed by a longer coiling time, while both the base and Nb–Ti steels returned discontinuous yielding with long Lüders elongation after undergoing intercritical annealing–galvanising treatment. This discontinuous yielding behaviour was associated with the much finer ferrite grain size in the intercritically annealed steels and the ageing processes that occur during galvanising. The modified Crussard–Jaoul (C–J) analysis showed three stages of work hardening where the second stage behaviour was ascribed to the different rates of RA transformation.

A new multi-condition phase separation procedure was developed to distinguish polygonal ferrite, martensite, granular bainite, bainitic ferrite, and austenite in both steels using electron back-scattering diffraction (EBSD) data and based on grain orientation spread (GOS) and grain size criterion. The granular bainite consisted of bainitic ferrite plates with a small amount of martensite/retained austenite constituents, whereas the bainitic ferrite consisted of relatively coarse and parallel laths with a signification amount of retained austenite between them. EBSD data from the separated phases was used to investigate how the tensile strain affected the stability of retained austenite (RA), and a

local misorientation analysis was used to assess the stability of RA in different morphologies and at different locations. It was found that the less stable RA in the Nb-Ti steel was related to the dominancy of bainitic ferrite (BF) morphology. For the two investigated TRIP alloys, the stability of RA at the PF/B interfaces was much less than the stability of RA in the bainite, but higher than the stability of RA in the PF. The partial transformation of RA grains at the interphase was related to the carbon enrichment of RA, and therefore that part of RA close to the PF was not as stable as that part of RA close to the bainite.

Using EBSD, the crystallography analysis was conducted on the irregular-shaped ferrite in granular bainite and bainitic ferrite laths that were observed in the current microstructure after thermo-mechanical processing. Granular bainite (GB) was characterised by the realisation of almost all 24 variants of the Kurdjumov-Sachs orientation relationship, which in turn was associated with the self-accommodation of the transformation strain. The absence of a variant selection in the GB was attributed to the dominant role of nucleation during cooling. The recovery of austenite during relatively slow and continuous cooling after deformation precluded the influence of hot deformation of austenite on the variant selection. On the other hand, bainitic ferrite was characterised by a strong variant selection of BF laths that was attributed to a plastic accommodation of the transformation strain in the remaining retained austenite, and less area available for its formation. Variants pairing could not be evaluated in the BF due to the high amount of RA that separated the BF laths. In most cases the GB and BF were formed together in the same prior austenite grain, even though variant selection was still pronounced in the BF, and although the GB displayed some reduction in the number of crystallographic packets (CPs) in the mixed microstructure, most of the variants were formed in each realised CP.

ACKNOWLEDGEMENTS

I would like to thank my supervisors, Prof. Elena Pereloma and Dr. Azdiar Gazder for their support and guidance throughout my PhD studies.

Special thanks to Dr. Ahmed Saleh and Dr. Andrii Kostryzhev for all their support, and also to Drs. Andrew Carman, Ayesha Haq and Sujoy Hazra for supporting me through the first days of my PhD study.

Thanks to laboratory expert Mr Greg Tillman for all the time he spent assisting and teaching me. I am grateful to Mr. Bob deJong and Dr. Liang Chen for their support and training on the Gleeble thermo-mechanical simulator. Thanks also to the technical staff at the Engineering workshop, especially Mr Ron Marshall and Mr. Andrew Scobie.

Prof. Bruno C. De Cooman of Pohang University of Science and Technology, Korea is gratefully acknowledged for providing the TRIP steels and data for the intercritically annealed steels.

I am grateful to the Saudi Basic Industries Corporation (SABIC) for giving me the opportunity and financial support to pursue my higher degree education.

I would like to sincerely thank my family and friends for their constant words of encouragement. My deepest regards to my parents for their love and support. I cannot thank my wife enough for her patience and resilience in all these years, especially my children Fahad, Abdulamalik and Ammar who made me laugh even during the very hard times.

LIST OF PUBLICATIONS

1. “A correlative approach to segmenting phases and ferrite morphologies in transformation-induced plasticity steel using electron back-scattering diffraction and energy dispersive X-ray spectroscopy”, Azdiar A. Gazder, Fayez Alharbi, Hendrik Th. Spanke, David R.G. Mitchell, Elena V. Pereloma. Ultramicroscopy, 2014;147:114-132.

2. “The crystallography of carbide-free bainites in thermomechanically processed low Si transformation induced plasticity steels”, Elena V. Pereloma, Fayez Al-Harbi, Azdiar A. Gazder, Journal of Alloys and Compounds, 2014; 615: 96-110.

3. “The effect of processing parameters on the microstructure and mechanical properties of low-Si transformation-induced plasticity steels”, Alharbi F., Gazder A. A., Kostryzhev A., de Cooman B. C., Pereloma E. V. J., Mater. Sci. 2014; 49:2960-2974.

4. "Effect of thermomechanical processing parameters on the microstructure development in low Si TRIP steel", Fayez Alharbi, Elena V. Pereloma. Materials Science Forum. 2010; 654:254-257

TABLE OF CONTENTS

LIST OF FIGURES

LIST OF TABLES

1 INTRODUCTION

Steels produced for the automotive industry should possess high strength and high formability to satisfy the need for passenger safety and downstream forming processes [1]. To-date, refining the ferrite grain size and precipitation hardening are the only practices used to control the mechanical properties of conventional high strength steels. Since the automotive industry need for high strength and ductility cannot be attained by grain refinement or precipitation hardening alone, this has led to extensive research in improving the properties of automotive steel using different techniques. Controlling the volume fraction of microstructural constituents by varying the composition and thermo-mechanical processing (TMP) schedule has resulted in the development of four different types of multiphase steels such as dual phase steel, bainitic steel, tri-phase steel, and transformation induced plasticity (TRIP) steel, all of which contain different amounts of polygonal ferrite, bainite, retained austenite (RA), and martensite.

Dual phase steel provides a combination of adequate strength and ductility generated mainly by the produced microstructure which satisfies most of the automotive sector's requirements. The microstructure of dual phase steel consists of a large amount of polygonal ferrite and 10-15% martensite, which allows it to achieve the possible highest elongation [2]. The carbon content in dual phase steel is usually less than 0.1wt.% to avoid the formation of twinned martensite that would negatively affect its toughness [2, 3]. The mechanical properties of this type of microstructure takes concurrent advantage of the soft ferritic and hard martensitic phases, and research to further improve its mechanical properties has shown that this can be attained by introducing bainite into dual phase steel. On this basis, tri-phase steels consisting of polygonal ferrite, bainite, and martensite, offer even higher ductility compared to dual phase steels due to the presence of bainite in the microstructure.

Any improvement in the ductility of tri-phase steel is proportionally related to the amount of retained austenite, so the transformation of metastable retained austenite at room temperature to martensite during deformation was responsible for the increase in ductility. This transformation effect was initially discovered by Zackay *et al.* [4] in austenitic stainless steel, and was known as the transformation induced plasticity effect. Despite the importance of the overall chemical composition of TRIP steel, the processing

parameters are equally important (Fig. 1.1) because they form the desired combination of phases.

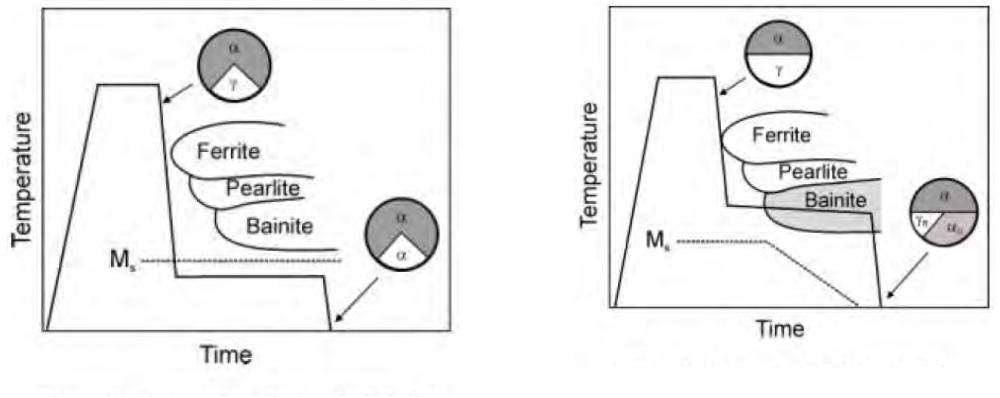

a) b)

Figure 1.1: Schematic diagram of TMP processing cycle of a) dual phase steel and b) TRIP steel [3].

1.1 Transformation Induced Plasticity Steel

TRIP steels provide the unique ability to combine high strength and high elongation (ultimate tensile strength (UTS) >1000 MPa and total elongation, 25-40%), unlike other types of automotive steels, Fig. 1.2. This class of steels are also known as TRIP-assisted steels, especially when austenite is a minor phase in the microstructure and it is low alloyed steel. The transformation of austenite to martensite at room temperature was due to the external load which also increased the strain hardening coefficient and ductility of the steel. It was suggested that the improvement in ductility was due to additional dislocations that formed during tensile testing as a result of the barriers created during deformation. These barriers should be stronger than the dislocations that normally formed during deformation.

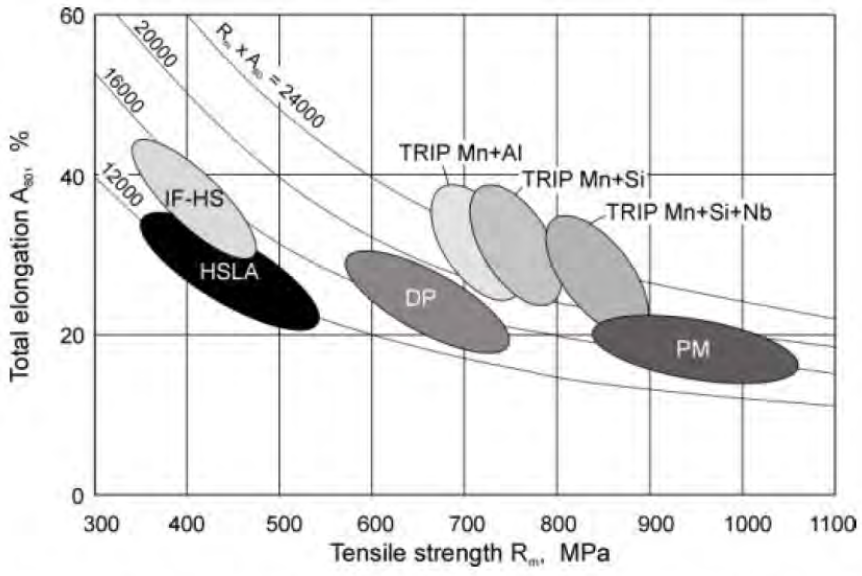

Figure 1.2: The extraordinary properties of TRIP steels compared to other steels [3].

The transformation of austenite at the right time during a uniform elongation regime was essential to promote ductility. This can be attained by controlling the stability of the retained austenite, which could be a combination of chemical and mechanical stability. The former one is related to the martensite start (Ms) temperature. The Ms temperature should be lowered below room temperature in order to ensure that transformation occurs during deformation. This could be achieved via the enrichment of the RA with carbon during ferrite and bainitic transformations, with the latter one being controlled by size, morphology, and distribution of the RA.

A typical microstructure of TRIP steel consists of polygonal ferrite, bainite and retained austenite. As per preliminary understanding, it was first stated that the maximum amount of the RA should exist in the microstructure of TRIP steel in order to increase formability. Later on it was discovered that although the amount of the RA is important, the relative stability of RA with strain was even more important in order to sustain the TRIP effect [5]. More recently, several studies have also suggested that the contribution of RA to an overall improvement in the mechanical properties is minor and that the major contribution is the result of the formation and the interaction between other phases during deformation [6].

As was mentioned earlier, the TRIP phenomena was discovered by Zackay *et al.* [4] in high cost steels containing alloying elements such as Ni and Cr. Thereafter, many researchers began to investigate the same effect using cheaper steel compositions. As a consequence, it was found that the addition of 1.5 - 2 wt.% Si would lead to the retaining of austenite at

room temperature due to suppression of cementite formation during bainite transformation. This fact was proven afterwards by many researchers [1].

The chemical stability of RA is controlled by its carbon content which can be increased by increasing the content of Si. A large amount of Si delays the formation of cementite in bainitic ferrite which in turn enriches the remaining austenite with carbon. However, high Si TRIP steel has a poor surface finish after hot rolling, and low galvanisability [7] and as such needs to undergo special and expensive coating processes such as electro-galvanising. Due to the disadvantages of a high Si content, alternative alloying additions such as Al that have a similar potential to suppress cementite formation have been explored [8].

1.2 Thesis Objectives

TRIP steels can be produced by either intercritical annealing (IA) or thermo-mechanical processing (TMP). The goal of both processes is to increase the volume fraction of stabilised RA and achieve the required combination of mechanical properties. From an industrial perspective, the cost of producing TMP TRIP steels is less than IA-TRIP but designing the microstructure by IA is easier than by TMP. Controlling the microstructural design during TMP is difficult because the processing parameters must be strictly controlled during hot rolling which influences the final TRIP steel microstructure quite significantly.

The industrial difficulty of producing TMP TRIP steels has resulted in an over emphasised research into intercritically annealed TRIP steels which has led to further insights into the effect that the processing parameters have on the microstructure and mechanical properties of TRIP steel. Despite this, a comparison of the effect of different processing routes on (i.e. TMP versus IA) on the mechanical properties of TRIP steel is an important area of study that needs further investigations.

The effect of galvanising heat treatment has been considered for TRIP steels produced by IA after cold rolling [9]. In contrast, the literature lacks an understanding of the influence of galvanising treatments on thermo-mechanically processed (TMP) TRIP steels. Hence, this area also needs further research in order to evaluate the effect of different processing parameters and heat treatments on TMP TRIP steels, particularly low-Si, high-Al TRIP steel. Since previous research has shown how micro-alloying additions influence the TMP high Si TRIP [10] steel and IA TRIP steels [11], their influence on the TMP low Si TRIP steels should also be considered.

The development of high Si TRIP steel has limited TRIP steel to hidden automotive components for applications where their appearance is less important. On the other hand, the improvement of the surface quality and coating ability of TRIP steels by reducing the Si content will increase the number of potential applications for TRIP steels. This also shows the importance and need for more investigations into the surface quality of low-Si TRIP steels, particularly those subjected to TMP.

However, the complex microstructure of TRIP steel due to the formation of multiple phases such as polygonal ferrite (PF), bainite, martensite, and retained austenite (RA), makes it challenging to characterise its microstructure. To this end, many studies have attempted to characterise the microstructure using various microscopy–based techniques.

Among all these techniques, electron back-scattering diffraction (EBSD) has been used with varying degrees of success to distinguish between phases [12, 13]. However, all these approaches were designed for specific microstructures where few phases exist and they are not necessarily applicable to all multi-phase microstructures, particularly thermo-mechanically processed TRIP steels. Therefore, the validity of all the existing methods for phase separation in TMP TRIP steels needs to be evaluated.

Many studies have investigated the crystallography and variant selection in bainite and martensite. Most of these papers have emphasised the effect of external loads on variant selection during phase transformation [14-16] but only a few have focused on the crystallography of phases in hot rolled steels. However, the martensite [17-20] and carbide-containing bainites such as upper bainite and lower bainite [17, 21] have attracted more attention than carbide-free bainites. Although the different morphologies of carbide-free bainite such as granular bainite and bainitic ferrite, have been discussed in other references from different aspects, there is a general lack of crystallographic analysis of these morphologies in the literature. This kind of detailed analysis increases our understanding of the factors influencing the amount and arrangement of each group of bainitic ferrite variants in different austenite grains. Unfortunately, the potential relationship between the fraction of RA and crystallography of bainitic ferrite in each prior austenite grain has currently been ignored, which means the crystallographic relationship between the bainitic ferrite morphology and amount of RA also needs careful analysis.

Based on the above, the objectives of this study are:

- To evaluate the effect of thermo-mechanical processing and subsequent galvanising simulations on the microstructure–property relationships in a low-Si TRIP steel and a Nb -Ti low-Si TRIP steel.
- To develop a phase segmentation methodology that can distinguish between austenite, martensite, polygonal ferrite and bainite in EBSD maps of thermo-mechanically processed TRIP steels.
- Use EBSD to investigate the crystallography of different morphologies of bainitic ferrite by assessing the orientation relationship between austenite and bainitic ferrite, variant selection, variant pairing and the arrangement of Bain groups and crystallographic packets in each austenite grain.

1.3 Thesis Outline

This thesis is divided into seven chapters.

- **Chapter 1** provides a brief introduction to TRIP steels and their processing routes, and states the aims of the thesis. It finishes with a brief description of the thesis content.

- **Chapter 2** is a Literature Review which analyses the effects of the chemical composition and processing parameters that influence the mechanical properties and microstructure of TRIP steels. One of the main experimental techniques, EBSD, is introduced with a particular emphasis on its application to study multi-phase steels and their crystallography.

- **Chapter** 3 describes the material and experimental techniques used. This chapter describes the various simulation schedules used, such as the TMP schedules, galvanising heat treatment, and intercritical annealing cycles. The sample preparation for different characterisation techniques such as scanning electron microscopy (SEM), EBSD, transmission electron microscopy (TEM), optical microscopy (using colour etching) and X-ray diffraction (XRD) are also discussed. Finally, tensile tests conducted on the sub-sized samples are also addressed in this chapter.

- **Chapter 4** compares the effect of coiling time and galvanising simulation on the microstructure and mechanical properties of two low-Si high-Al TRIP steels with and without the addition of Nb-Ti. This chapter focuses on the effect of TMP parameters on the fraction of RA and its carbon content. Attention has been directed towards the work hardening behaviour after both processing routes; TMP and IA. The microstructure-property relationships achieved after different processing simulations are also compared and discussed.

- **Chapter 5** introduces a newly developed method for phase segmentation based on a multi-criteria algorithm, and then compares this method with pre-existing methods for phase separation. Here the bcc phase in the multiphase steel is separated into polygonal ferrite, bainite, and martensite phases. Moreover, the effect of the tensile deformation on each phase is discussed on the basis of the local

misorientation, area fraction and the grain size of each distinct phase. The stability of RA in each steel and the factors influencing it are also discussed.

- **Chapter 6** discusses the crystallography of different bainite morphologies (granular bainite and bainitic ferrite) in detail, including the arrangement and realisation of variants in the crystallographic packets and Bain groups, and variant pairing. Furthermore, the variant selection in different bainite morphologies and the relationship between the fraction of RA and bainite crystallography and morphology was also examined. This chapter provides further understanding of the formation mechanism of the bainitic ferrite morphologies.

- **Chapter 7** consists of general conclusions and future work.

2 LITERATURE REVIEW

TRIP steels have attracted the attention of many researchers because they are a very interesting class of industrial alloys from a physical metallurgical point of view, and have significant prospective downstream applications. Therefore, many studies have focussed on investigating the overarching factors influencing the behaviour of TRIP. The following sections detail previous studies on TRIP steels and include the effect of chemical composition, different processing, and the microstructure and mechanical properties.

2.1 Composition of TRIP Steel

A typical chemical composition of TRIP-assisted steel is 0.15C-1.5Mn-1.5Si (wt.%) such that low alloy TRIP steels usually contain less than 3.5 wt.% of the total alloying elements [1]. Even though they are essential to TRIP steels, carbon, silicon, manganese, aluminium and phosphorous have different levels of ability to retain austenite below room temperature by preventing the formation of carbides, however, each of them has disadvantages which limit their maximum addition to TRIP steel. It has been reported that TRIP steel with 1.5wt.% Si or Al can retain a large volume fraction of RA [22]. As mentioned earlier, the disadvantage of high silicon TRIP steel is poor coatability, so low Si TRIP steel with additions of Al (as a partial replacement for Si) was suggested to overcome this drawback. Other alloying addition effects were also examined as a replacement for Si.

Some elements are austenite stabilisers while others are ferrite stabilisers, but by far, carbon is still the most effective element at stabilising austenite, as shown in Fig. 2.1.

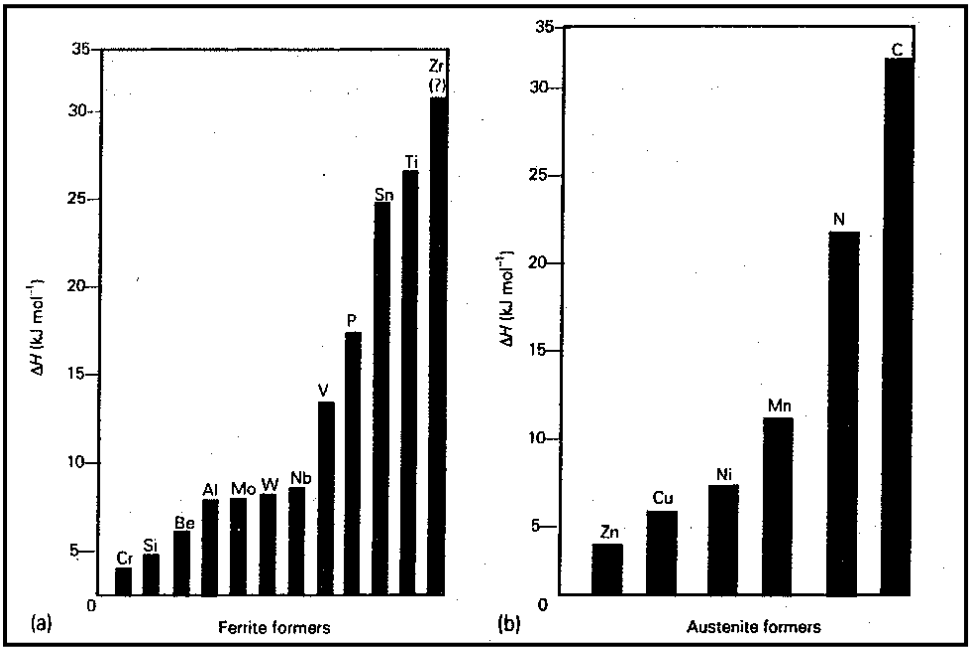

Figure 2.1. Comparison between ferrite stabilising and austenite stabilising elements [23]

As a result the volume fraction of retained austenite in TRIP steel tends to be directly proportional to the overall carbon content [24], but a low carbon content is still recommended to improve weldability. The effect of additions of alloys on the critical transformation temperatures such as the bainite and martensite starting temperatures is also important when designing TRIP steels. The following empirical Eqs. 2.1 and 2.2 from Ref. [23] and [25] show the influence of each element on the transformation temperatures while their effects on the recrystallisation stop temperature (T_{nr}) are expressed by Eq. 2.3 and shown in Fig. 2.2.

$$Bs\ (°C) = 830 - 270\ C - 90\ Mn - 37\ Ni - 70\ Cr - 83\ Mo\ (wt\%) \quad (2.1)$$

$$Ms(°C) = 539 - 423\ C - 30.4\ Mn - 7.5Si + 30Al\ (wt\%) \quad (2.2)$$

$$T_{nr}(°C) = 887 + 464C + (6645Nb - 664\sqrt{Nb}) + (732V - 230\sqrt{V}) + 890Ti + 363Al - 357Si \quad (2.3)$$

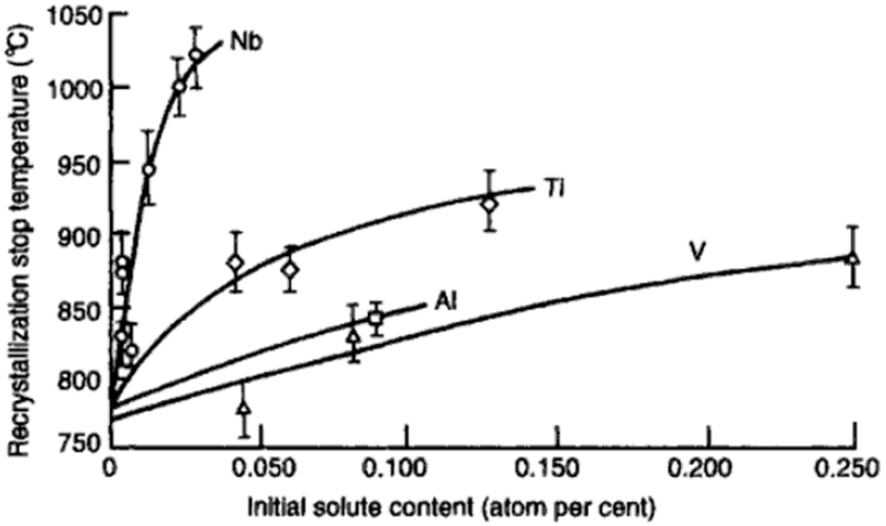

Figure 2.2. Effect of alloying addition on the recrystallisation stop temperature [26]

Other alloying elements such as Ti, V, and Nb have a critical role in improving the strength and hardenability of TRIP steel. In the following sections the effects of every one of the above alloying elements is discussed in more detail.

2.1.1 Silicon

Si is considered to be the most important element in the TRIP steels, which is why many studies have focussed on its role in the TRIP phenomena. Si is a ferrite stabiliser and its addition has been reported to lead to an increase in A_{c1}, A_{c3} temperatures as well as the temperature range between them [27]. The carbon activity in ferrite and austenite is increased by the addition of Si, but because Si has low solubility in cementite, it plays a critical role in preventing cementite forming during the bainite transformation stage [28]. The effect of Si on lowering the pearlite start temperature is shown in the Continues Cooling Transformation (CCT) diagrams (Fig. 2.3) [29]. Overall though, the addition of Si was also found to reduce the volume fraction of bainite [30]. With respect to its mechanical properties, the addition of Si raised the work hardening coefficient and the ultimate tensile strength by solid-solution strengthening [31].

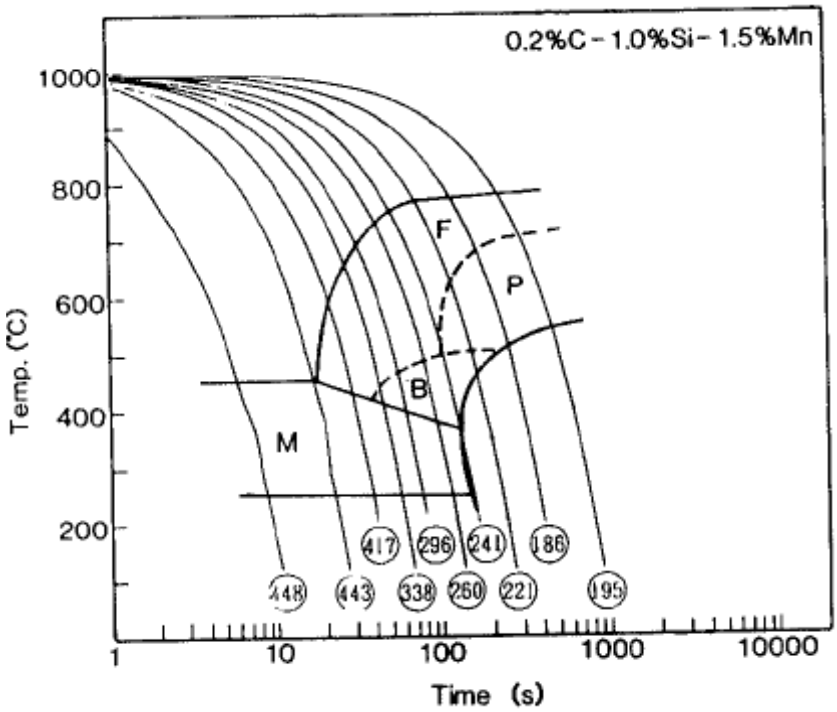

a)

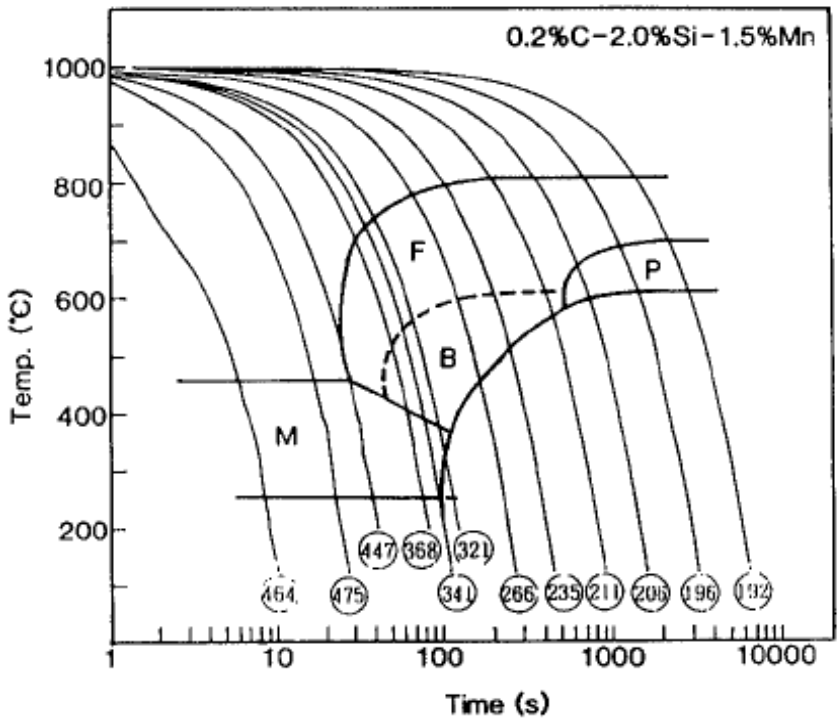

b)

Figure 2.3. CCT diagram for a) 1wt.% Si and b) 2wt.%Si TRIP steel [29].

Because Si helps prevent carbide precipitation, several researchers focussed on investigating the mechanism by which Si accomplishes this [32]. Moreover, increasing the content of Si lowers the martensite start temperature Ms, which improves the stability of austenite [30]. It was reported that the maximum amount of retained austenite can be obtained in hot rolled low carbon steel containing 2 wt.% Si and 1.5 wt.% Mn [29].

Whereas silicon is important to retain austenite, it also slows the kinetics of the bainite transformation which means a longer processing time and faster cooling rates are required [27, 33, 34]. Besides that, a high Si content leads to poor surface quality after hot rolling. The galvanizeability of high Si TRIP steel in a hot dip galvanizing line is a real concern [9, 35], therefore experiments have been carried out to develop low Si or even Si-free TRIP steels [34].

A low Si combined with other alloying elements can provide even better mechanical properties than high Si TRIP steels [7, 36], but as Fig. 2.4 shows, low-Si C-Mn TRIP steels will not improve the overall mechanical properties because very small amounts of austenite are retained [22]. A combination of high ultimate tensile strength (800 MPa) and high elongation (20%) was achieved using low Si CMnAl TRIP steel [37].

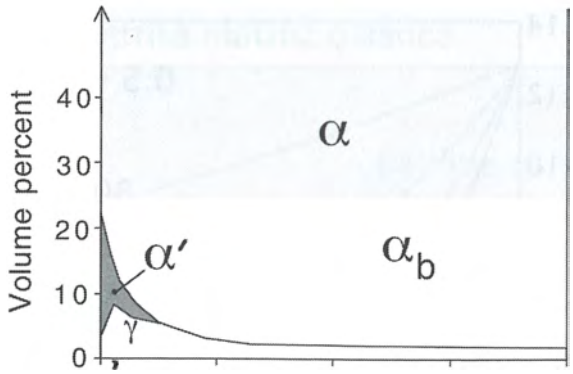

(a)

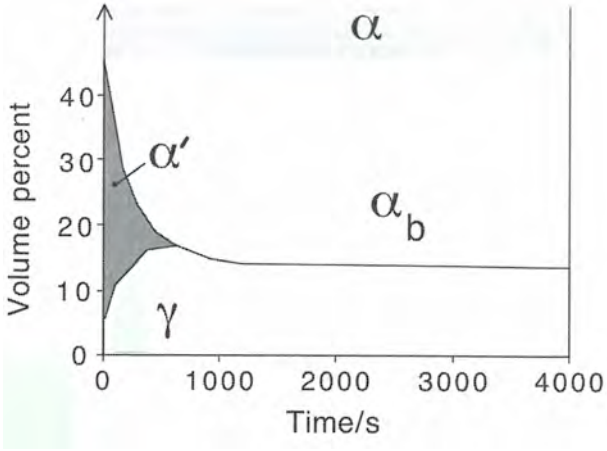

(b)

Figure 2.4 The amount of different phases in (a) low Si and (b) high Si TRIP steel [23].

2.1.2 Manganese

Mn is an austenite stabiliser that has a strong effect on the amount of retained austenite and hence on the ductility. Mn lowers the carbon activity coefficient in ferrite and austenite, and also increases the hardenability of steel, but in practice, its alloying content does not exceed 2.5 wt.% in order to avoid the formation of bands which would also diminish the ductility [38]. Mn reduces the martensite start temperature of Ms. It was observed in Ref. [29] that increasing Mn from 1 to 1.5 wt.% in hot rolled steel increases the volume fraction of martensite. Most TRIP steels contain about 1.5% Mn to improve its properties and obtain the maximum amount of retained austenite [29]. Mn helps to enrich austenite by carbon as it increases the solubility of carbon in austenite, but too much Mn leads to the formation of highly stabilised retained austenite which does not improve the mechanical properties [28]. Mn does not have any effect on the galvanisability of TRIP steel because it is reduced by Al during the zinc coating process [7].

Baik *et al.* [30] studied the influence of Mn, Si, and Nb on the bainite and austenite volume fractions in TRIP steel, and found that an increase of Mn leads to increase in Ms, which was explained by the retarding effect of Mn on the transformation of ferrite. It was also reported that the increase in tensile strength associated with Mn resulted from the solid solution strengthening and an increase in the volume fraction of bainite, although it was believed that the volume fraction of bainite had more influence on the tensile strength.

Tsukatani *et al.* [29] stated that the amount of retained austenite can be increased in 0.2C-2Si (wt.%) even more by increasing the Mn from 1 to 1.5wt.%, which shows how important Mn is in enriching austenite by carbon. Figure 2.5 [29] shows the significant effect that Si and Mn has on the mechanical properties of hot rolled TRIP steel. The tensile strength and elongation were increased by increasing the amount of Si and/ or Mn, indeed they achieved a tensile strength of 780 MPa and a 37% elongation in 0.2 wt.%C TRIP steel containing 2 wt.%Si and 1.5 wt.% Mn.

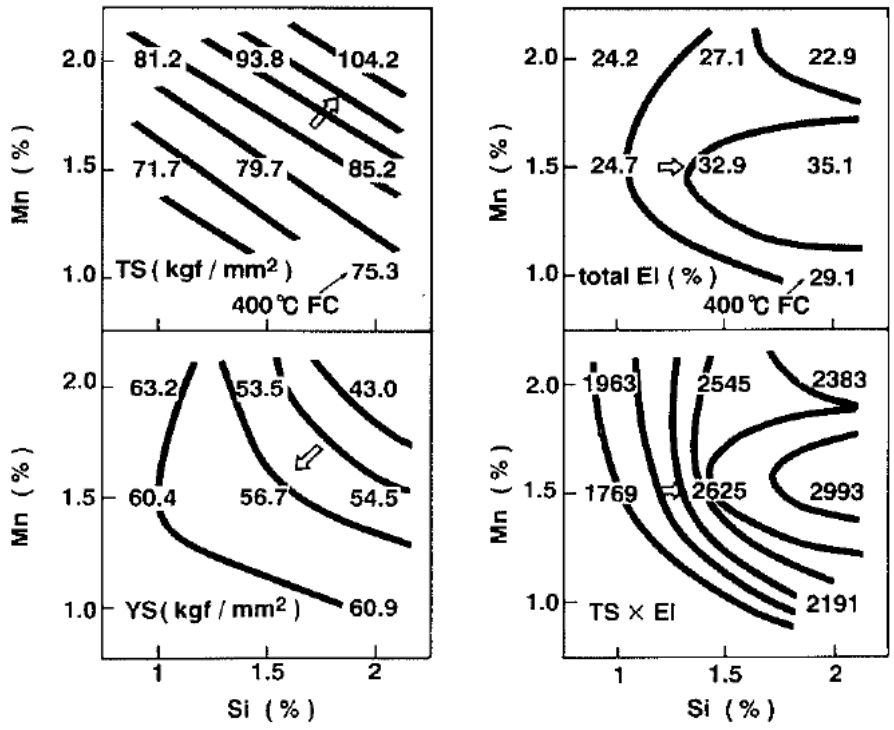

Figure 2.5 The effect of Si and Mn on the mechanical properties of hot rolled TRIP steel [29].

2.1.3 Aluminium

Al acts like Si in preventing the formation of carbide due to the insolubility of Al in cementite, but it does have a low solid solution strengthening effect, and therefore it has negligible effect on the tensile strength. To overcome surface finish issue associated with Si in TRIP steel, Si can be replaced by Al which can retard the formation of cementite while having excellent galvanisability during hot dip galvanising [28]. Thus the galvanisability of TRIP steel can be improved dramatically by partially or totally replacing the Si with Al [7, 9]. Moreover, Al-contained TRIP helped the steel perform better than high Si TRIP steel in terms of its mechanical properties and uniform elongation due to the high volume fraction of retained austenite [39, 40]. Whereas replacing all the Si with Al resulted in a reasonable amount of retained austenite and improved the properties, however, a combination of Si and Al produces better mechanical properties [41]. The addition of Al increases A_{r3} temperature which means more ferrite forms and less holding time is needed during the transformation of bainite compared to TRIP steel containing Si [33, 34]. The stability of the retained austenite, which is important for the TRIP effect, was found to be higher with CMnAl TRIP steel than the Si- TRIP steel [42]. This was attributed to the high enrichment of carbon in austenite[43]. Al has a significant effect on the transformation temperature, indeed the addition of Al can increase the A_{c1} and A_{c2} and the temperature range between them [27]. The bainite reaction rate of TRIP steel containing Al is high, therefore a short holding time is enough to improve its mechanical properties [27, 43]. Godet *el al.* [22] investigated the differences in transformation between high Si, low Si, and Al TRIP steel. The volume fraction of ferrite increased in Al TRIP steel because the Al is considered to be a strong ferrite stabiliser. They showed that to produce 10% RA with a low amount of martensite needs 7 minutes for Si TRIP steel and 2 minutes for Al TRIP steel [22]. As expected, a long bainitic holding time in low Si TRIP steel did not result in any retained austenite. In contrast, Traint *et al.* [43] stated that completely replacing Si with Al can produce a TRIP steel with high volume fraction of stable RA. Meyer *et al.* [39] studied the mechanical properties of high-Si low-Al TRIP steel and low-Si high-Al cold rolled TRIP steel and showed that replacing the Si with Al drastically improved the formability and galvanizability of TRIP steel. Moreover the strain hardening coefficient in C-Mn-Si-Al TRIP steel did not change with strain, which is an important feature in the stretch forming operation, but the strain hardening coefficient can be as high as 0.25 by increasing the Al up to 1.7 in CMnAl TRIP steel[34].

2.1.4 Molybdenum

Improving the strength of TRIP steel can be attained by the addition of Mo due to its solid solution strengthening. The addition of Mo lowers the ferrite and pearlite transformation temperature, so it is very effective at retarding the formation of cementite. Different researchers attempted to partially replace the Si with Mo; for instance, Bout *et al.* [44] achieved a combination of high strength and high elongation by replacing 0.5 Si by Mo in a high Si TRIP steel.

The addition of Mo also delays recrystallisation and precipitation due to its strong solute drag effect which improves the Nb efficiency in retaining austenite [45]. Like Si, Mo increases the solubility of carbon in austenite which reduces the carbide formation. Therefore, Si addition can be reduced by the addition of Mo.

Bout *et al.* [44] studied the effect of Mo on the retained austenite and mechanical properties of TMP C-Mn-Nb TRIP steel with different levels of Si. A partial replacement of Si by Mo increased the time required to form ferrite from 4 minutes to 50 minutes, thus a limited amount of ferrite was formed after the addition of Mo to 1.5%Si TRIP steel. Moreover, the elongation and volume fraction of retained austenite was increased by the addition of Mo only with a low isothermal bainite transformation temperature of 300 °C.

A group of researchers found that the mechanical properties can be further improved by a combined addition of Nb and Mo [46]. The addition of Nb to hot rolled TRIP steel increased the retained austenite (RA) fraction at 400°C coiling temperature, so an increase in RA due to 0.03wt% addition of Nb was about 4% higher than in other investigated steels. However, at higher coiling temperatures above 500°C, the content of retained austenite fell to zero in all the samples except those steels containing Mo. At a high coiling temperature (CT), the retained austenite was higher in the 0.1wt%Mo compared to the 0.2wt%Mo steel, with the highest elongation and strength being attained with Nb and Nb-Mo TRIP steel at 400°C CT.

2.1.5 Titanium and Niobium

The effect of the micro-alloying elements such as Ti and Nb is significant in increasing the tensile strength by precipitation strengthening. This increase in strength was not associated with a deficiency in weldability, unlike in steel with a high carbon content. The micro-alloying addition (Ti and V) increases the transformation start temperature of ferrite and pearlite while simultaneously lowering the bainite and martensite

transformation temperatures, as shown in CCT diagrams in Fig. 2.6 [37]. Obviously, the increase in UTS that can be gained from the addition of Ti will reduce elongation [37].

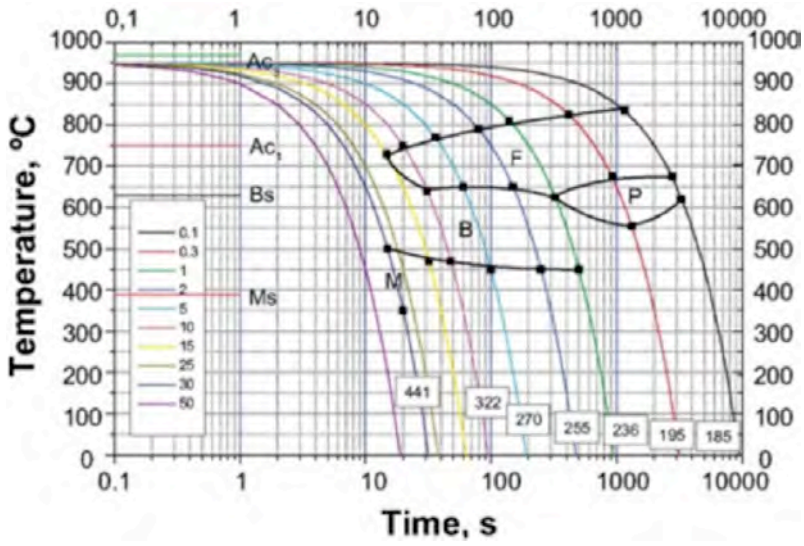

a)

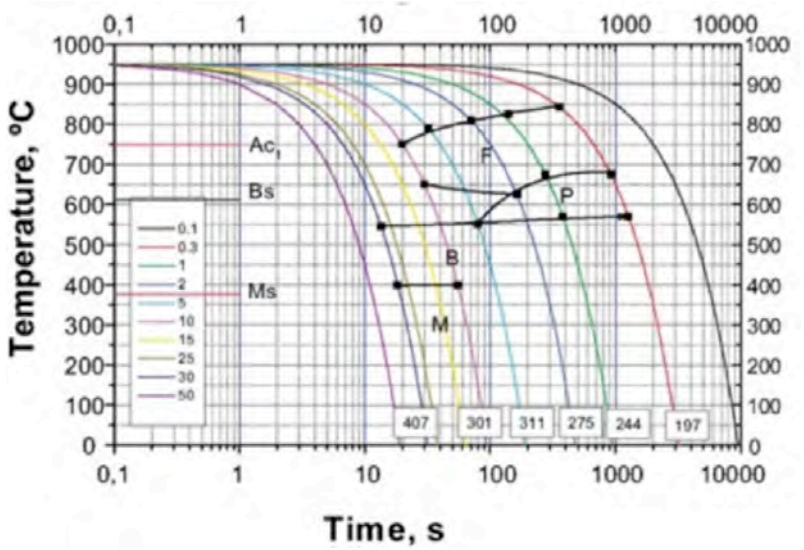

b)

Figure 2.6 CCT diagram of TRIP steels: a) 0.24C-1.51Mn-1.12Al-0.27Si-0.082P and b) 0.26C-1.64Mn-1.35Al-0.39Si-0.049P-0.099Ti-0.053V [37].

The presence of microalloy carbides and nitrides controls the austenite grain growth. Therefore, as the dissolution temperature of the microalloy carbides or nitrides increases, the grain coarsening temperature increases. Grajcar [47] studied the influence of austenitisation temperature on the grain growth of austenite for a low carbon Mn-Si-Al

TRIP steel. Their experiments were carried out in a range of 850°C to 1200°C. Because the austenite grain growth is suppressed by microalloy carbides or nitrides, it has been found that fine microstructure can be achieved at a low temperature (below 1050°C). However, above 1100°C the austenite grain size shows a slight increase. As TiN has a very high dissolution temperature (>1600°C), only 0.0032wt.% Ti went in solid solution out of nominal 0.023wt.%Ti after solution treatment at ~1200°C with the rest of Ti remain in TiN. On the other hand, the NbCN precipitates retard the austenite grain growth in the range of 900°C to 1180°C [47]. Cuddy *et al.* [48] showed that the complete dissolution temperatures for TiC, TiN, NbCN are 1090°C -1225°C, 1645°C -1710°C and 995°C -1285°C, respectively. Thus, Ti is the most effective element to inhibit the austenite grain growth.

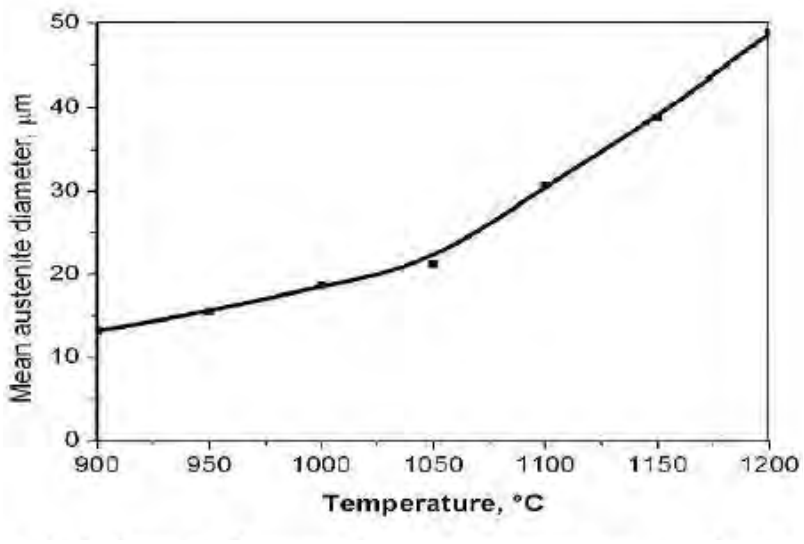

Figure 2.7. Effect of temperature on the austenite grain size [47].

The influence of niobium on the transformation of bainite is very limited and results in only slightly increases in its volume fraction [30]. It was stated that Nb had a slight or negligible effect on the transformation temperatures of bainite and martensite [30], while the addition of niobium refines the austenite grain size and the bainitic laths [10]. The effect of Nb was clear on the grain refinement and austenite pancaking which affected the behaviour of TRIP [43]. There was a slight reduction in the retained austenite volume fraction associated with increasing the concentration of Nb, as shown in Fig. 2.8 [43, 49]. The suggested optimum amount of additional Nb to low Si TRIP steel to produce a high ultimate strength (739 MPa) and high elongation (38%) was 0.014 wt% [49], and it was seen that an additional 0.0045wt%Nb to TRIP steel increased its strength by 30 MPa [43].

Bai *et al.* [50] achieved 10% of RA via hot rolling using 0.035wt.% Nb in 0.2C-1.5Mn-1.5Si (wt.%) TRIP steel, but the influence of Nb on the stability of RA was not confirmed [43]. However, some reports indicated that the stability of RA had deteriorated slightly when the content of Nb was increased [49].

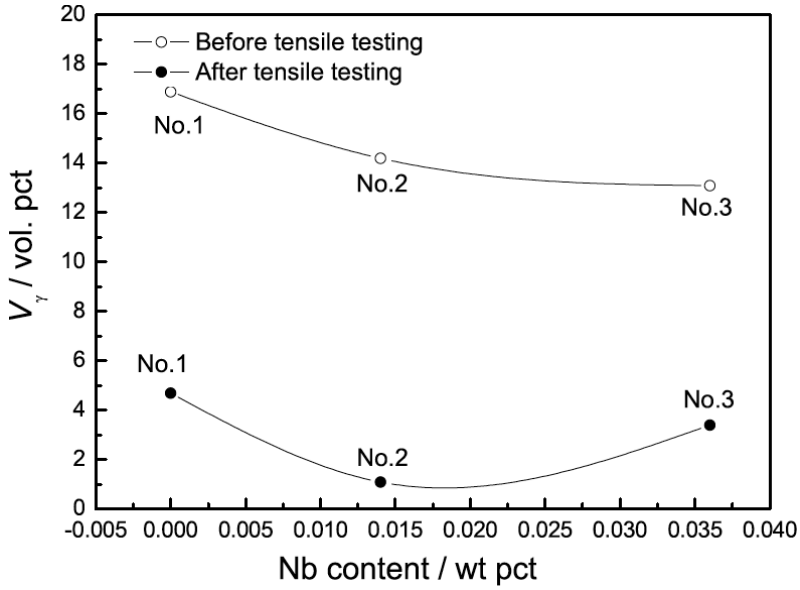

Figure 2.8. Effect of Nb on the austenite volume fraction before and after tensile test[49].

Timokhina *et al.* [10]claimed that non-Nb steel had better mechanical properties (Fig. 2.9), in terms of elongation, compared with Nb TRIP steel, even though the amount of RA formed in both steels was similar (RA= 14%). These findings were attributed to lower carbon content in the retained austenite of Nb-containing TRIP steel compared to non-Nb steel, which was associated with the consumption of carbon by NbC precipitates in ferrite, and bainite making less carbon available for enriching the RA. By way of contrast, Hashimoto *et al.* [46] found that adding 0.05Nb to C-Mn-Si TRIP steel improved its mechanical properties, a contradictory result caused by the different processing parameters applied. Moreover, the yield strength was higher in Nb steel than non-Nb steel because the Nb alloy influenced the distribution of RA. Indeed the carbon contents in the RA located between the polygonal ferrite grains or lath were lower than in the RA located between bainitic ferrite grains [10]; thus affecting the stability of RA. Nb had a direct effect on the response of different phases to the strain applied [10].

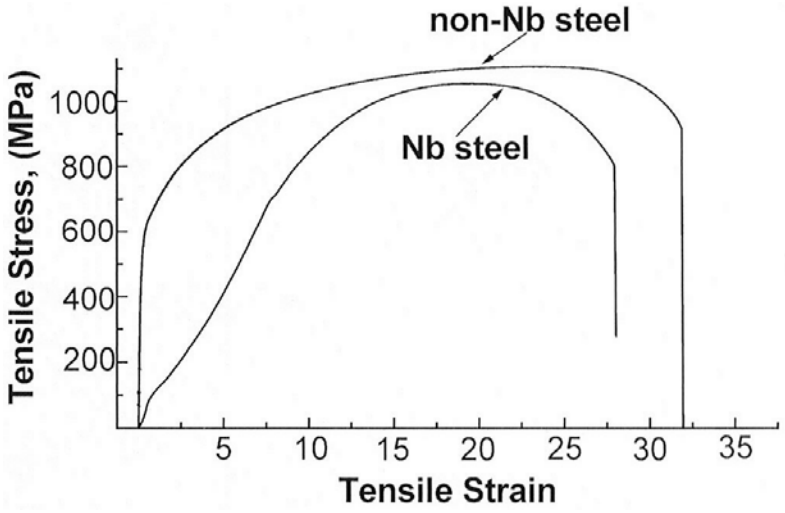

Figure 2.9. Effect of Nb addition on the mechanical properties of TRIP steel [10].

2.1.6 Phosphorus

Phosphorus**,** P, has a high solid solution strengthening effect [51, 52]. The solid solution strengthening effect of P is doubled when it is combined with Si in TRIP steel [52-54]. P has a major influence on retarding the formation of cementite so it can be used as a partial replacement for Si and/or Al. However, Al and Si should be used in conjunction with P due to limitations on the amount of P arising from its segregation. On the other hand, the kinetic of galvannealing was reduced as a result of adding P [55].

The addition of phosphorus was very effective at increasing the amount of retained austenite, as well as the strength, and it also increases the stability of RA during a long austempering process [52]. However the strain rate sensitivity of CMnP TRIP steel was low compared to Al and Si TRIP steel [56], and the replacement of Si by Al or P in TRIP steel reduced the rate of transformation [28].

2.2 Processing

The following section discusses the thermo-mechanical processing (TMP) approach to producing TRIP steel because it is the main focus of this study. It also briefly describes other processing methods such as intercritical annealing which used to produce TRIP steels, and which could be used to improve the stability of RA. On the other hand, the effect of downstream processing such as galvanising and galvannealing on the final properties

and microstructure is critical and might be harmful. Therefore, the following section will also discuss these routes and their effects.

2.2.1 Thermo-mechanical processing

TRIP steel is often produced by intercritical annealing (IA) because the processing parameters can be controlled precisely. Intercritical annealing is used on a cold rolled product that was heated up to the austenite-ferrite region to form austenite, and then cooled down into the bainite transformation region. During bainitic transformation the carbon migrates from bainite to austenite to enrich RA with carbon. However, controlling the previous hot rolling and cold rolling parameters to produce cold rolled TRIP sheet is important to achieve the required properties during IA process [45].

The second method of producing TRIP steel is thermo-mechanical processing, during which the processing parameters are carefully controlled to produce the required microstructure. Unlike in IA, the steel starts from fully austenitic microstructure then cooled down to room temperature to produce the bainite and retained austenite at low temperature, followed by quenching. This process is cheaper than IA since no further processing (such as annealing) is required [23]. Nevertheless, controlling the microstructure during the hot rolling is more complicated in industry due to difficulty in controlling the processing parameters. The hot rolling process for TRIP steel production consists of roughing rolling and finishing rolling, during which, the steel is deformed in recrystallised austenite and the non-recrystallised austenite region, respectively [57]. The main goal of these processes is to refine the microstructure, which in turn improves the mechanical properties such as the tensile strength and toughness. During deformation in the recrystallisation region, the microstructure of steel is refined by a repetitive process of recrystallisation. During rolling in the non-recrystallisation region, the microstructure is pancaked, more grain boundary areas are formed and in-grain defects, such as a shear bands and deformation twins, which serve as additional nucleation sites for ferrite formation leading to ferrite grain refinement and corresponding improvement in the mechanical properties. Moreover, rolling in non-recrystallisation region also leads to the refinement of the bainite constituent in multiphase steel. It has been stated that the refinement of ferrite and bainite by deformation at these two stages are beneficial for TRIP steel in terms of increasing the amount and stability of retained austenite [57]. However, other works stated that pancaking reduces the amount of RA while the deformation in the intercritical region has a remarkable effect on refining the

microstructure and on the amount of RA[58]. An extensive study conducted by Timokhina *et al*.[57] on the effect of various amounts of deformation on TRIP steel concluded that the refining the microstructure will not always enhance the properties[58]. It was suggested that the optimum engineering strain (ε) that increased the amount and stability of RA was 0.25 in the recrystallisation region and 0.47 in the non-recrystallisation region.

On the other hand, selecting the correct cooling rate, coiling temperature, and time at the end of the TMP are essential in order to produce the required amount of ferrite and to avoid carbide formation. Also, the bainite morphology and the stability of retained austenite are controlled at this important stage. Due to the importance of the coiling temperature for the TRIP steel properties, several works were conducted to study this behaviour. It was found that for the thermomechanically processed 0.18C-1.66Si-1.4Mn-0.025Nb (wt.%) steel that the ultimate tensile strength increased when the bainite transformation temperature was reduced due to bainite refinement, while the elongation was maximum after holding for 300s at 400°C [44]. However, the chemical composition of the TRIP steel dictates the design of the TMP schedule, because it strongly influences the critical transformation temperatures and the final microstructure [29].

2.2.2 Intercritical Annealing

Intercritical annealing (IA) is used to produce retained austenite at the final microstructure by controlling the critical temperature and holding time of the cold rolled steel. The steel is heated up to the intercritical region between A_{c1} and A_{c3} to form a certain amount of austenite, while the residual ferrite recrystallises. At a specified cooling rate, some austenite could also transform into polygonal ferrite at high temperature, and then at low temperature the bainite transformation takes place. During this isothermal bainitic transformation, the remaining austenite is enriched with carbon, so it can be retained during quenching [23]. This produced microstructure was influenced mainly by the isothermal bainitic transformation temperature and time.

Numerous research has been carried out to understand how the processing parameters affect TRIP steel [38, 41, 59, 60]. For instance, Li *et al*. [41] studied the effect of different bainitic transformation temperatures (400 °C and 460 °C) and various holding times (120 s and 300 s) after intercritical annealing at 780°C for 5 minutes. They found that the resulting mechanical properties for tensile strength ranged from 600 MPa to 800MPa and from 28 to 35% for elongation. However, these results were also affected by the amounts of Si and Al addition.

2.2.3 Galvanising

The hot dip galvanizing is the process of covering the base metal by zinc (99% Zn) to protect the steel from corrosion and improve its appearance. Cold rolled and annealed steel is a common substrate material for hot dip galvanising. Hot rolled steel is also used as a substrate material to reduce the cost but its coatability is poor compared to cold rolled steel.

The process of hot dip galvanising begins by immersing the steel at about 460 °C into liquid zinc. During this 5 second immersion the zinc reacts with iron to form a layer of an iron/zinc compound which then is covered by a layer of pure zinc. This process is completed by cooling the final product down to room temperature [2, 61].

Although the objective of hot dip galvanising is to cover the surface with zinc, the heat treatment applied during this process might affect the final mechanical properties, particularly in multi-phase TRIP steel. The following schematic diagram (Fig. 2.10) shows the typical galvanising process for a hot rolled steel [62].

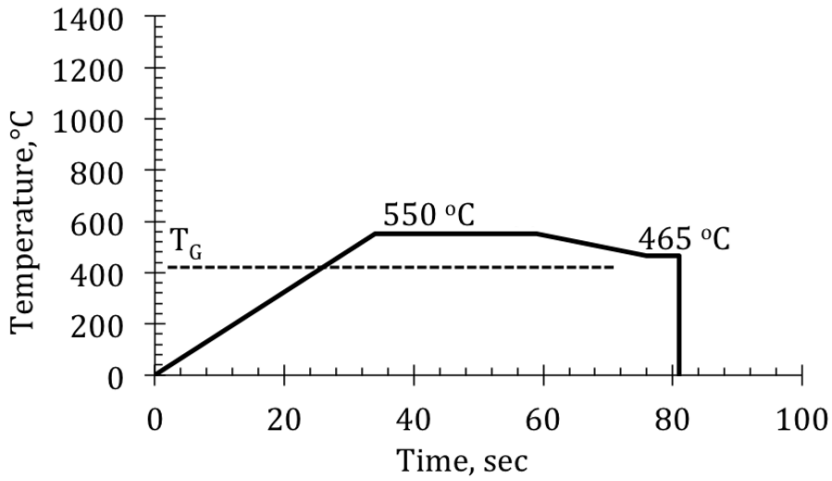

Figure 2.10 Schematic diagram of hot-dip galvanising cycle [62].

The preheating temperature prior to galvanising is important because it improves the quality of the coating; indeed the main objective of this process is to eliminate the segregation of carbon on the surface which leads to uncoated spots. Chattopadhyay *et al*. [62] examined different preheating temperatures (550, 650 and 750 °C) and concluded

that high temperatures (650 and 750 °C) are the best ones to produce a high quality galvanised hot rolled steel.

2.2.4 Galvannealing

Galvannealing is produced by heat treating the galvanised coating after hot dipping in the zinc pot, Fig. 2.11. This process aims to improve the coating properties by raising the temperature of galvanised steel up to 500 °C for about 8 seconds, followed by cooling [63]. The heating rate after dipping is as high as 15 Ks^{-1} to avoid the formation of undesirable coating phases. The cooling rate after galvannealing is also 15 Ks^{-1}. Control of the processing parameters and bath chemistry is essential for galvannealing.

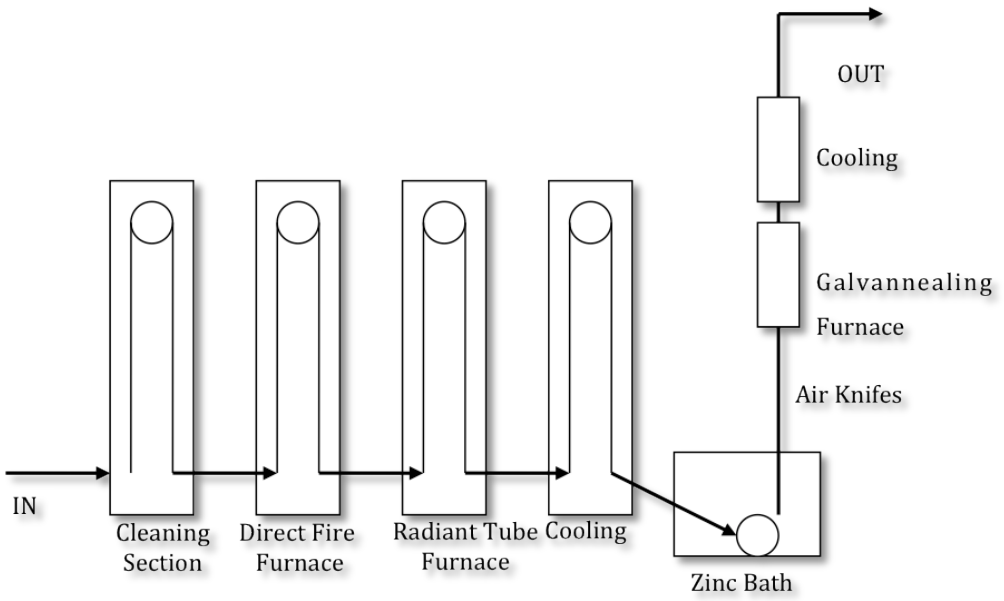

Figure 2.11 Schematic diagram of galvanising and galvannealing line [63].

The coating properties are enhanced in galvannealed steel, and while the corrosion resistance of galvanising might be reduced by the heat treatment used for galvannealing, the formability of galvannealed steel is much improved. Moreover, the weldability and paintability is enhanced in galvannealed steel compared to galvanised steel [2, 63].

Although the above mentioned processing parameters are important for coating features, they might affect the mechanical properties of substrate steel, so this study will consider the possible effect of heat treatment (galvanising or galvannealing) on TRIP steel after hot rolling.

2.3 Microstructure

The typical microstructure of TRIP steel consists mainly of polygonal ferrite (PF), carbide-free bainite, retained austenite, and martensite. Figures 2.12 and 2.13 show the typical microstructure of low alloy TRIP steel. Although the retained austenite phase is an important element in designing TRIP steel, its morphology and amount of other phases are also a vital factor that influencing the mechanical properties and behaviour of retained austenite. The amount of RA can be increased by increasing the amount of polygonal ferrite fraction. It has been found that ~8.5%RA can be increased to ~12%RA in NbMoAl TRIP steel by increasing the amount of PF from 30 to 50%. Formation of 40 to 50% PF has been found to be the optimum amount to achieve the best combination of strength and ductility in TRIP steel [64]. The following sections will focus on the effect of deformation and critical processing temperatures on the microstructure. The stability of retained austenite will be also discussed.

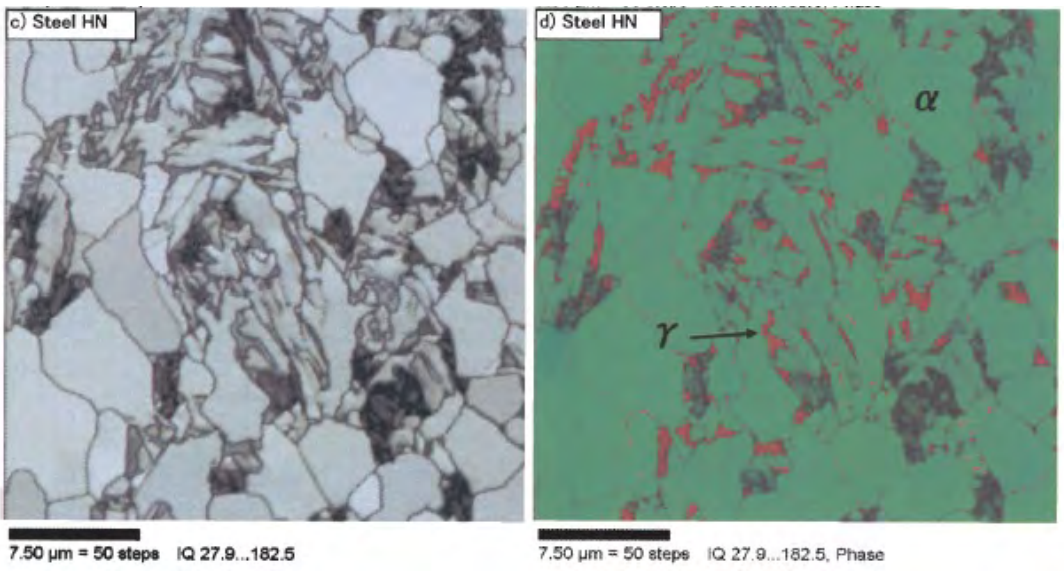

Figure 2.12 Typical microstructure of 0.2C–1.5Si–1.5Mn (wt.%) TRIP steel after hot rolling. EBSP analysis shows the face centred cubic (fcc) in red colour and body centred cubic (BCC) in green colour [46].

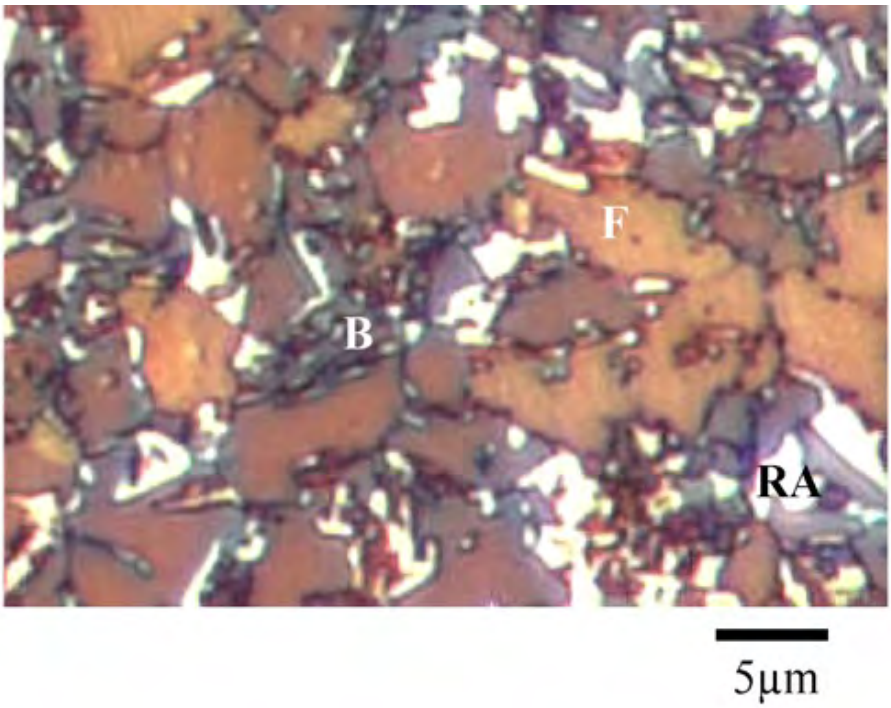

Figure 2.13. Typical microstructure of TRIP steel revealed by colour etching technique [65]. Ferrite is brown, bainite is black, and RA is white.

2.3.1 Effect of deformation

The purpose of the deformation in the recrystallised austenite region and non-recrystallised region is mainly to refine the final microstructure [66]. Refining austenite microstructure results in refining the final microstructure at room temperature. However, this process will definitely leads to an increase in the tensile strength. Moreover, it was stated that refining the microstructure improves the mechanical properties in TRIP steel and increases the amount of RA. It was also suggested that this enhancement in RA was due refinement in the bainite structure and an increase in the interface area per unit volume [5]. However, it should be noted that increasing the amount of retained austenite via grain refinement does not always improve the mechanical properties. According to Yue *et al*. [5], the amount of RA tends to increase with the reduction in the prior austenite grain size, whereas TRIP steel with Nb behaved differently after the precipitation of Nb increased.

Deformation in the non-recrystallisation region (below T_{nr}) produce pancaked microstructure which would further promote grain refinement [67] and enhance the

stability of the RA. This enhancement is explained by the effect of fine bainite produced due to grain refinement. Nevertheless, it was found that the amount of RA reduced after reaching a specific strain [5].

Timokhina *et al*. [57] studied the influence of different amounts of deformation in the non-recrystallised and recrystallised regions (Fig. 2.14). The effect of the volume fraction of polygonal ferrite (PF) on retained austenite was excluded by making the PF 50% in all the tests. Figure 2.14 shows six different combinations of strain 1 (recrystallised austenite region) and 2 (non-recrystallised austenite region) and their effect on the amount of retained austenite and elongation. Carbide-free granular bainite was only observed in cases one and five where strains 1 and 2 were 0.25 and 0.47, and 0.75 and 1.2, respectively. Consequently, the amount of retained austenite was higher compared to the microstructures obtained using other schedules. This showed that the morphology of bainite had a more significant effect on the volume fraction of RA than the ferrite grain size. High deformation in the recrystallised and non-recrystallised austenite region, as in case number six, produced less stable retained austenite, which did not improve the mechanical properties. This promoted the formation of martensite in the microstructure because less stable retained austenite formed, which then transformed to martensite during quenching.

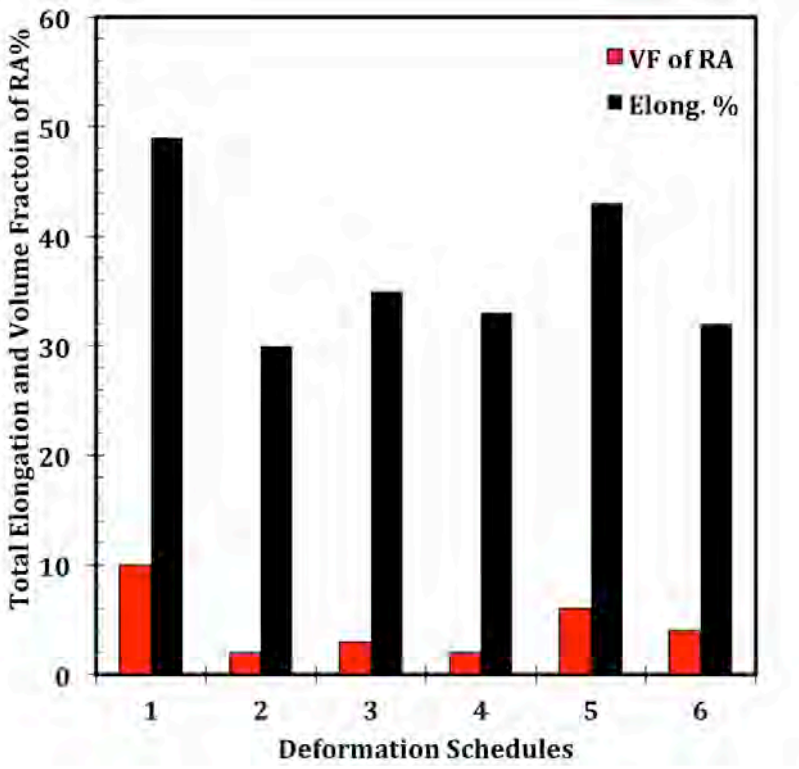

Figure 2.14. The effect of different amounts of deformation on the amount of retained austenite and elongation [57].

2.3.2 Effect of temperature

The two critical temperatures in processing TRIP steel are the accelerated cooling start temperature and the coiling temperature. The accelerated cooling start temperature (or finishing rolling temperature) controls the amount of polygonal ferrite that will be formed. After this temperature the cooling rate was increased to avoid the formation of pearlite because it consumes the carbon needed to stabilise the retained austenite.

The coiling temperature is the most important and critical temperature in designing the TMP schedule because it controls the morphology of bainite and the amount of RA. However, the formation of bainite begins with the formation of bainitic ferrite, and based on the coiling temperature and other factors (such as composition) the formation of cementite can be initiated to form different bainite morphologies such as upper bainite (at high temperature) and lower bainite (at low temperature), Fig. 2.15. These two phases are undesirable because they reduce the amount of RA [57].

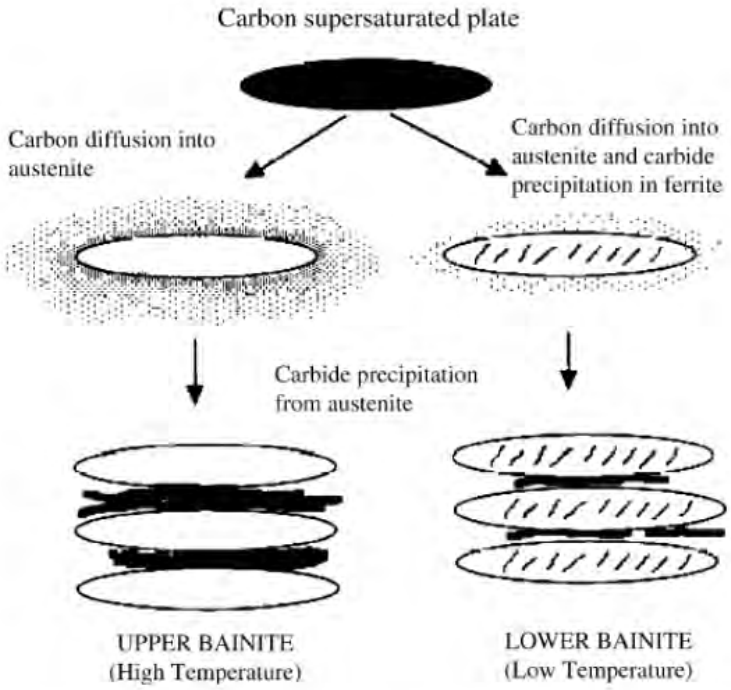

Figure 2.15 An illustration of the formation of upper and lower bainite [23].

Controlling the composition of steel and the TMP parameters leads to the formation of two types of carbide-free bainite such as granular bainite and bainitic ferrite or acicular ferrite, with granular bainite and acicular ferrite having different microstructural appearances. The microstructure of bainite has distinct sheaves of parallel platelets whereas acicular ferrite looks like adjacent platelets pointed in different directions [23].

Hanzaki *et al*. [68] investigated the influence of the coiling temperature and time on C-Mn-Si TRIP steel after hot rolling, and found that these parameters had a remarkable on the amount of retained austenite and morphology, as well as on the morphology of bainite. Increasing the coiling time improved elongation by increasing the amount of retained austenite while the 400 °C was found to be the optimum coiling temperature in terms of increasing elongation [46]. Although the minimum retained austenite was formed at 300 °C, the mechanical properties after coiling at this temperature were found to be better than after coiling at 500 °C, which was related to high carbon content in the retained austenite.

Furthermore, increasing the coiling temperature is also associated with an increase in the platelet size and thickness of the RA interlayers, and it was observed that the morphology of retained austenite varied according to the coiling temperature. The RA can exist in the following five different morphologies which are related to the neighbouring phases:

1. Blocky grains enclosed by polygonal ferrite
2. Islands within the granular bainite or at the interfaces between the polygonal ferrite and bainite
3. Films between the BF laths/plates
4. Blocky crystals enclosed by bainite ferrite sheaves and
5. Austenite/martensite constituent in granular bainite.

Based on the bainitic ferrite morphology and the type and distribution of the second phases, the bainite has been classified into [69] granular bainite, upper bainite with lath-like morphology with the second phases on the lath boundary and lastly lower bainite with lath-like or plate like morphology with cementite within the laths. This classification is summarised in Fig. 2.16. Following the classification of Zajac *et al.* [69] only granular bainite and degenerated upper bainite morphologies can be considered as a carbide-free bainites. In this study these morphologies will be referred to as granular bainite and bainitic ferrite.

Granular bainite is seen in continuously cooled steels and has an arrangement of bainitic ferrite plates with a martensite/austenite constituent [70]. Whereas some researchers reported the presence of low angle boundaries in granular bainite, more recently, others have also observed a high angle and twin boundaries. Bainitic ferrite is formed on cooling and during isothermal holding, and consists of interlayers of retained austenite and/or martensite embedded between the bainitic ferrite laths [71].

Bainite	Morphology	Bainite description
Granular bainite	Irregular ferrite with M/A	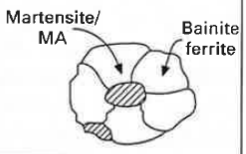
Lath-like upper bainite	Lath-like ferrite with cementite on lath boundaries	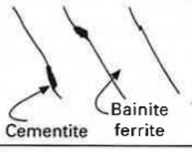
Cementite-free lath-like bainite	Lath-like ferrite with M/A on lath boundaries	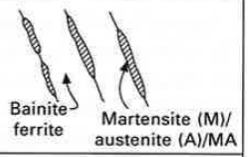
Lath-like lower bainite	Lath-like ferrite with cementite inside the ferrite laths	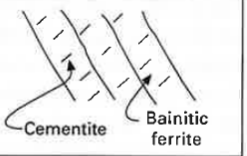
Plate-like lower bainite	Plate-like ferrite with cementite inside the ferrite plates	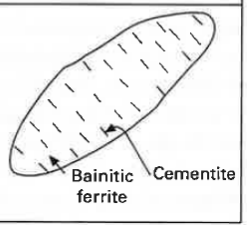

Figure 2.16: Classification of bainite [72]

2.3.3 Orientation relationships

Four orientation relationships (ORs) have been widely used to define the orientation relationships in steel between austenite (parent phase) and bainite or martensite (product phase). These four relationships were proposed by Bain [73], Kurdjumov and Sachs [74], Nishiyama and Wassermann [75, 76], and Greninger and Troiano [77]. In general, the orientation relationships between the parent and product phase can be defined by the crystallographic plane {hkl} and direction <uvw> in two phases and can be expressed in the following form: $\{hkl\}_{parent}$ || $\{hkl\}_{product}$, $<uvw>_{parent}$ || $<uvw>_{product}$. Kurdjumov-Sachs (K-S, {111}γ || {110}α, <110>γ || <111>α) and Nishiyama-Wassermann (N-W, {111}γ || {110}α, <001>α) are rational relationships which differ only by a relative rotation of 5.26° while the Greninger-Troiano (G-T, {111}γ ~ 1° || {110}α, <12 17 5>γ || <17 17 7>α) is an intermediate OR between the Kurdjumov-Sachs and Nishiyama-Wassermann relationships. Although phenomenological theory and experimental data suggest that the ORs for martensite and bainite are irrational (such as Greninger-Troiano (GT)), a majority of researchers utilise the rational ORs for ease of analysis and explanation. The orientations of the Bain (B, {010}γ || {010}α, <001>γ || <101>α) OR differ by 11.06° from the K-S and 9.74° from N-W [78, 79] ORs. These orientation relationships are shown schematically in Fig. 2.17.

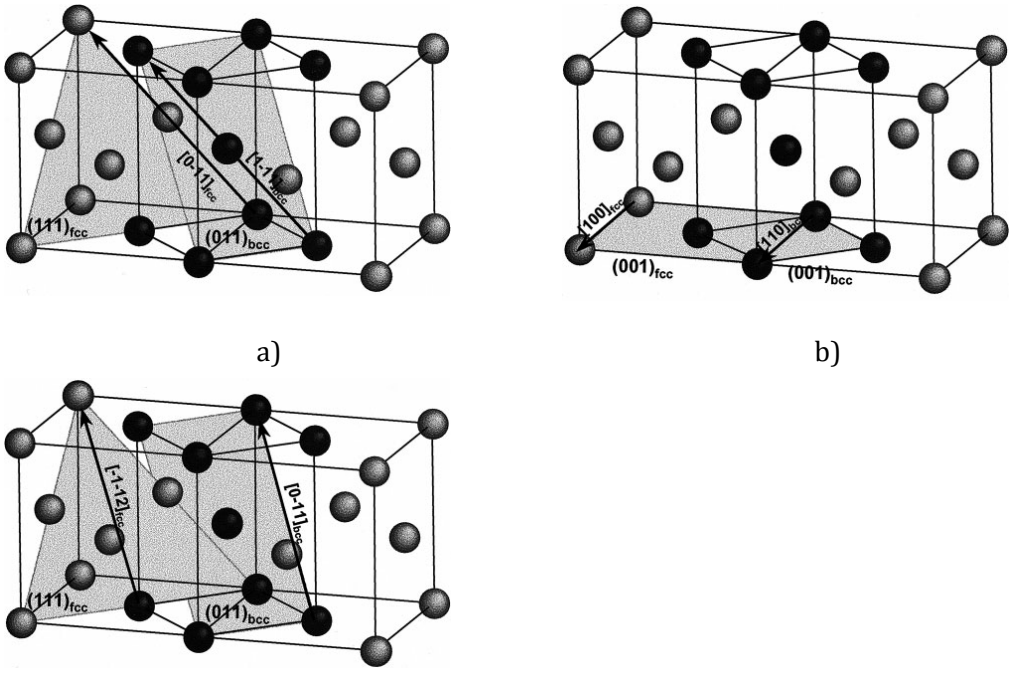

Figure 2.17 Schematic illustration of orientation relationships between fcc and bcc a) KS OR, b) Bain OR and c) NW OR [80].

In most research devoted to steels, the Kurdjumov–Sachs and the Nishiyama–Wassermann relationships were used to study the orientation relationships between the FCC and BCC phases. Although the Bain OR has also been used in literature as a reference or approximation in austenite transformation studies, it is never observed in steels [78]. Due to the symmetry in cubic systems, there are 24 equivalent crystallographic variants in the case of KS OR divided into four crystallographic packets (CPs) and three Bain groups (BGs) [81] (Table 2.1 and Fig. 2.18) that can evolve from a single parent grain (austenite) whereas NW OR has only 12 variants divided into four CPs and three BGs [82] (Table 2.2). In each CP, six KS variants share the same parallel relationship of close-packed planes (CPPs) whereas 8 KS variants in each BG have a common α plane [88]. Furthermore, the blocks are defined as the regions containing variants that belong to the same CP and Bain group [17] whereas a sub-block is defined as block comprising variants with a low angle boundary misorientation between them [19]. The characteristics of the packet and block in the bainite and martensite are crucial and they are strongly related to the strength and toughness of the steel [19].

Theoretically, all these variants possess the same probability of growth, but in reality some variants are restricted due to an external influence. The latter observation is considered as variant selection which is discussed in the following section.

Table 2.1 The 24 variants of KS OR [16, 19, 20, 83, 84]

	Parallel plane			Parallel direction				
Variant number	FCC		BCC	FCC		BCC	CPs	BGs
V1	(111)	//	(011)	$[\bar{1}01]$	//	$[\bar{1}\bar{1}1]$	CP1	B1
V2				$[\bar{1}01]$	//	$[\bar{1}1\bar{1}]$		B2
V3				$[01\bar{1}]$	//	$[\bar{1}\bar{1}1]$		B3
V4				$[01\bar{1}]$	//	$[\bar{1}1\bar{1}]$		B1
V5				$[1\bar{1}0]$	//	$[\bar{1}\bar{1}1]$		B2
V6				$[1\bar{1}0]$	//	$[\bar{1}1\bar{1}]$		B3
V7	$(1\bar{1}1)$	//	(011)	$[10\bar{1}]$	//	$[\bar{1}\bar{1}1]$	CP2	B2
V8				$[10\bar{1}]$	//	$[\bar{1}1\bar{1}]$		B1
V9				$[\bar{1}\bar{1}0]$	//	$[\bar{1}\bar{1}1]$		B3
V10				$[\bar{1}\bar{1}0]$	//	$[\bar{1}1\bar{1}]$		B2
V11				$[011]$	//	$[\bar{1}\bar{1}1]$		B1
V12				$[011]$	//	$[\bar{1}1\bar{1}]$		B3
V13	$(\bar{1}11)$	//	(011)	$[0\bar{1}1]$	//	$[\bar{1}\bar{1}1]$	CP3	B1
V14				$[0\bar{1}1]$	//	$[\bar{1}1\bar{1}]$		B3
V15				$[\bar{1}0\bar{1}]$	//	$[\bar{1}\bar{1}1]$		B2
V16				$[\bar{1}0\bar{1}]$	//	$[\bar{1}1\bar{1}]$		B1
V17				$[110]$	//	$[\bar{1}\bar{1}1]$		B3
V18				$[110]$	//	$[\bar{1}1\bar{1}]$		B2
V19	$(11\bar{1})$	//	(011)	$[\bar{1}10]$	//	$[\bar{1}\bar{1}1]$	CP4	B3
V20				$[\bar{1}10]$	//	$[\bar{1}1\bar{1}]$		B2
V21				$[0\bar{1}\bar{1}]$	//	$[\bar{1}\bar{1}1]$		B1
V22				$[0\bar{1}\bar{1}]$	//	$[\bar{1}1\bar{1}]$		B3
V23				$[101]$	//	$[\bar{1}\bar{1}1]$		B2
V24				$[101]$	//	$[\bar{1}1\bar{1}]$		B1

Table 2.2 The 12 variants of NW OR [82]

	Parallel plane			Parallel direction				
Variant number	FCC		BCC	FCC		BCC	CPs	BGs
V1	(111)	//	(011)	$[2\bar{1}\bar{1}]$	//	$[0\bar{1}1]$	CP1	B2
V2				$[\bar{1}2\bar{1}]$	//	$[0\bar{1}1]$		B3
V3				$[\bar{1}\bar{1}2]$	//	$[0\bar{1}1]$		B1
V4	$(\bar{1}11)$	//	(011)	$[\bar{2}\bar{1}\bar{1}]$	//	$[0\bar{1}1]$	CP2	B2
V5				$[12\bar{1}]$	//	$[0\bar{1}1]$		B3
V6				$[1\bar{1}2]$	//	$[0\bar{1}1]$		B1
V7	$(1\bar{1}1)$	//	(011)	$[21\bar{1}]$	//	$[0\bar{1}1]$	CP3	B2
V8				$[\bar{1}\bar{2}\bar{1}]$	//	$[0\bar{1}1]$		B3
V9				$[\bar{1}12]$	//	$[0\bar{1}1]$		B1
V10	$(\bar{1}\bar{1}1)$	//	(011)	$[\bar{1}21]$	//	$[0\bar{1}1]$	CP4	B2
V11				$[\bar{1}21]$	//	$[0\bar{1}1]$		B3
V12				$[\bar{1}\bar{1}\bar{2}]$	//	$[0\bar{1}1]$		B1

The orientation relationship of bainitic ferrite or martensite laths have been thought to vary from the exact Kurdjumov–Sachs (KS) OR to the Nishiyama–Wasserman (NW) OR. However, KS OR can describe the transformation in low carbon steels more accurately [85]. Some studies used KS OR due to the higher number of variants than NW OR [86], indeed, it is even stated that with bainitic ferrite, there must be 24 possible variants in each prior austenite grain due to the irrational relationship between austenite and bainitic ferrite [87].

The orientation relationship between lath martensite and austenite in a low carbon 0.18 C - 0.006 Si – 0.02 Mn steel (wt.%) was investigated by Kitahara *et al.* [81] who found that KS OR was the closest OR that describes the orientation relationship of the lath martensite. Morito *et al.* [19] studied the crystallography of lath martensite in Fe-C alloys containing 0.0026, 0.18, 0.38 and 0.61 mass% of carbon by TEM and SEM and found that the orientation relationship between austenite and martensite was close to the KS relationship, even though some laths were reported to be closer to the NW relationship. In contrast, an investigation of the crystallography of an Fe–28.5 at.% Ni alloy [82] showed that the Nishiyama–Wassermann orientation relationship best describes the OR between plate martensite and austenite. Zhang *et al.* [20] studied the crystallography of lath martensite in low-carbon-13Cr-9Ni (wt.%) steel via high temperature laser scanning confocal microscopy (LSCM) where a high amount of RA was retained at room temperature, and found that the lath martensite has a KS orientation relationship with the retained austenite with a deviation of less than 3°.

Takayama *et al.* [17] investigated the orientation relationship of martensite and bainite in 0.15C–1.5Mn–0.2Si mass%. They found that the both bainitic ferrite (BF) and martensite hold orientation relationships close to KS OR with respect to the austenite matrix. Verbeken *et al.* [78] investigated the crystallographic orientation relationships of bainite microstructure in two TRIP steels and found that the orientation relationship between bainite and austenite was closer to the KS OR than the NW OR. Godet *et al.* [85] found that the orientation relationship between bainite and austenite in 0.4C -1.5Si -1.5Mn(wt%) TRIP steel differed from an exact KS OR by 6° to 7°.

However, Gong *et al.* [16] investigated the crystallography of ausformed bainite and martensite in 0.79C–1.98Mn–1.51Si–0.98Cr–0.24Mo–1.06Al– 1.58Co (wt.%) steel and found that the orientation relationship between austenite and bainitic ferrite was closer to the NW relationship than to the KS one. This discrepancy between the above mentioned results might be related to the accuracy of the experiment and the small angular deviation between the KS and NW OR which was estimated to be only 5.26°.

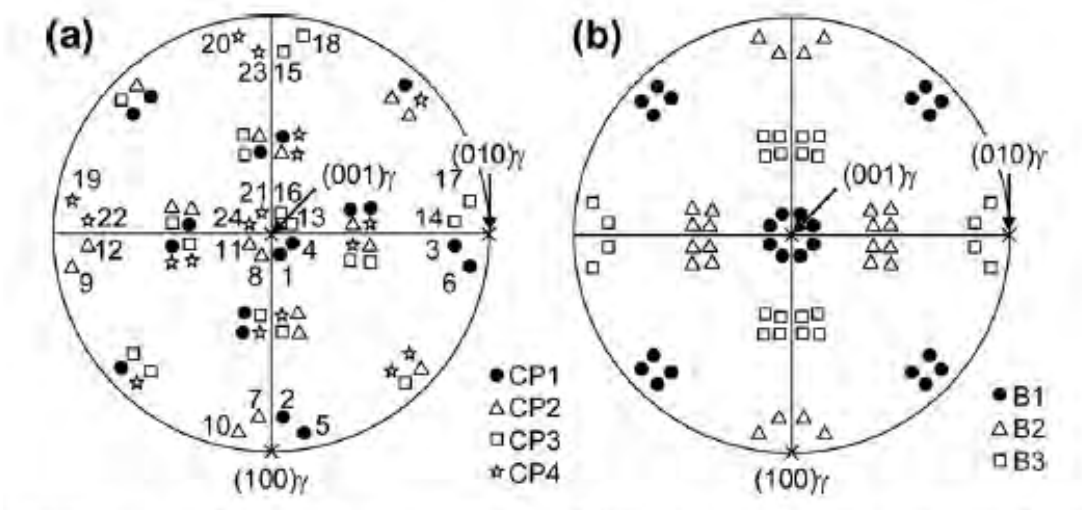

Figure 2.18: <001>α directions of KS variants belonging to the same (a) CP group and (b) Bain group are represented by the same symbol in the (001)γ pole figure [17].

2.3.3.1 Variant selection

During phase transformation, the realisation of all 24 KS variants or 12 NW variants is necessary to accommodate plastic deformation as a result of the volume change during phase transformation. However, the absence of some variants due to external stress or strain is known as variant selection and leads to a considerable sharpening of the transformation texture. Moreover, when transformation strain is accommodated by austenite and is accompanied by variant selection [89] at high temperature, it is known as plastic accommodation (PA), whereas the formation of all variants in a single austenite grain is known as self accommodation (SA) [20].

In the literature the factors influencing the realisation of a few variants (variant selection) is sometimes contradictory [90] and requires further investigation. Gong *et al.* [16] investigated the influence of austenite deformation in nanobainitic steel and found that ausforming led to a strong variant selection and that increasing the ausforming temperature reduced variant selection. He *et al.* [91] investigated variant selection in 0.22C-1.56Si- 1.50Mn-0.031Al-0.045Nb-0.017Ti (mass %) TRIP steel, and showed that variant selection is not linked to the prior deformation of austenite because deformed and non-deformed austenite grains exhibited variant selection. Malet *et al.* [92] showed that variant selection in hot-rolled bainitic TRIP-aided steels increased by increasing the deformation of austenite, while Godet *et al.* [85] showed that the deformation of austenite must reach a critical strain to induce variant selection.

Because variant selection is important, many studies have investigated the factors influencing variant selection and on that basis, have tried to predict the preferred variants during transformation. Furthermore, several models [79, 85, 93] have attempted to explain variant selection based on specific criteria such as the influence of the geometrical shape of the deformed austenite, the interaction between the strain accompanying the transformation and the applied or residual stresses, the role of active slip systems in the austenite, and the interaction between dislocations. Here, some of the proposed models include more than one of the aforementioned criteria [89].

Malet *et al.* [92] linked variant selection during the formation of martensite and bainite to slip activity in austenite during deformation where only those CPs were formed whose {111}γ planes had an almost 45° relationship with the rolling or normal directions. It was found that variant selection was also influenced by the orientation of the parent austenite grains and the type of substructure developed within them during deformation. Miyamoto

et al. [84] showed that martensite variants were realised whose (011)α planes were parallel to the primary and secondary slip (111)γ planes such that they only formed from those austenite grains that contained microbands and not from the other austenite grains that contained tangled dislocation substructures. Gong *et al.* [16] investigated variant selection in nanobainitic steel ausformed at 300 °C and linked it to the parallel relationships between the Burgers vector of partial dislocations operating on a slip plane in austenite, and the shear direction of a selected variant .

In contrast, Kundu *et al.* [14] linked variant selection without deformation to the space limitation which hindered the formation of all variants. Consequently, they introduced the term "naturally absent variants" to describe variant selection without deformation. Takayama *et al.* [17] investigated the influence of the transformation temperature and carbon content on variant selection in 0.15 C–1.5Mn–0.2Si (mass%) steel, and found that variant selection is induced by increasing the transformation temperature or carbon content. The realisation of all variants at lower temperatures was explained by the need for self-accommodation of the transformation strain. It was also observed that the formation of specific variant pairs can accommodate the transformation strain more efficiently than others. For instance, KS variant pairs V1/V2 can accommodate the transformation strain more efficiently than V1/V4 [94]. On this basis, Takayama *et al.* [17] categorised the observed variant pairing in bainitic ferrite and martensite into three types, as shown in Fig. 2.19.

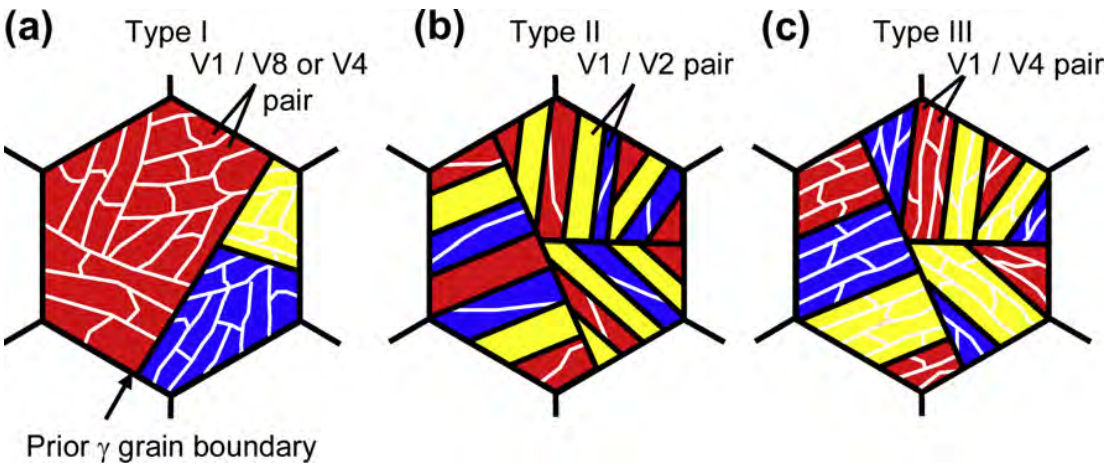

Figure 2.19. Three types of variant paring in bainite (a and b) and lath martensite (c). a) formed at 580 °C and (b) formed at 450 °C. Low-angle boundaries = white and high-angle boundaries =black lines [17].

Furuhara *et al.* [21] found the same influence of the transformation temperature in Fe–9Ni–0.15-0.5C (mass%) steel on the dominancy of specific variant pairs at different temperatures. Moreover, it was shown that the influence of the carbon content in the variant pairing was reduced at high transformation temperatures. It was suggested that variant selection at high temperatures is responsible for the coarsening of the block size in bainite; an observation that was not observed in martensite.

2.3.4 Stability of retained austenite

The high elongation and strength associated with TRIP steel is linked in many studies with the high initial amount of retained austenite (RA). However, the transformation of RA to martensite during straining at room temperature is responsible for the improvement in the mechanical properties. Therefore, if the transformation of the RA occurs early or never happened, it will not contribute to the TRIP effect. This leads to the importance of the stability of RA because it controls the kinetics of RA transformation during deformation. The stability of RA can be measured simply by deforming a sample with different amounts of strain and then determine the amount of RA left afterwards, and the rate at which the RA transforms will indicate its level of stability. The following equation was used to evaluate the stability of RA [50]:

$$\text{Log } f_{\gamma 0} = \log f_{\gamma} - K \cdot \varepsilon \qquad (2.4)$$

where $f_{\gamma 0}$ and f_{γ} are the retained austenite volume fraction at zero strain and final strain.

Bai *et al*. [50] used the above equation to measure the stability of the RA and found that the k values were 0.45 and 0.73 for samples held for 120 s and 300 s at 400°C, respectively. These values indicate that the stability of e RA in the sample after 120 s hold was higher, although the chemical stability of RA in 300 s sample was higher due to the high level of carbon in the austenite.

The stability of RA is commonly described by the low M_S temperature, indeed it has been suggested that the M_d temperature is the best measurement of the stability of RA [1], because this temperature is related to the automotive application. The M_d temperature is defined as the temperature above which no martensite transformation happens during deformation. Because M_d is difficult to measure, it is appropriate to measure the M_d^{30} temperature where it is defined as the temperature at which 50% of the RA transformed to martensite at 30% strain. However, it was suggested that for automotive steels the

optimum stability of RA corresponds to the composition at which M_d is higher than the ambient temperature and less than 100°C [1].

Because this subject is important, many studies were performed to evaluate the factors that influence the stability of RA, and it has been stated that RA should be chemically and mechanically stabilised to improve its mechanical properties.

2.3.4.1 Chemical stability

The only way to retain austenite at room temperature is by enriching it with carbon during the formation of polygonal ferrite and bainite, but if there is not enough carbon in austenite it will transform to martensite during cooling. Moreover, when the carbon level in retained austenite is low, the chance of transforming the retained austenite at low strains is very high. The RA with a carbon content of less than 0.5 wt% or higher than 1.8 wt% does not contribute to the TRIP effect, so on that basis, the carbon content in retained austenite or the chemical stability of retained austenite is critical to the behaviour of TRIP steel. The gradual transformation of RA to martensite during deformation is essential to attain high elongation in TRIP steel. This gradual transformation is controlled mainly by the amount of carbon in RA.

Since this subject is important, several studies focussed on measuring the carbon content in retained austenite, with X-ray diffraction (XRD), convergent beam Kikuchi line diffraction patterns (CBKLDPs) [95] and Atom Probe Tomography (APT) being among the methods used to estimate the quantity of carbon in retained austenite. A recent study found that the distribution of carbon in RA was not homogeneous [96], which means the behaviour of retained austenite is more complicated and depends on the local carbon content rather than the average concentration of carbon in RA [97].

2.3.4.2 Mechanical stability

The second important factor that influences the stability of retained austenite is mechanical stability, which is defined by the size, location, and morphology of the retained austenite and bainite.

The grain size of the RA plays an important role in its stability. A small RA grain size is more stable because the number of martensite nucleation sites decreased which delays the start of transformation [98-100] and also because smaller retained austenite grains typically have a higher carbon content, which reduces the martensite start transformation temperature [101].The grain size of the RA should be selected carefully as the coarse grain

has very low stability thus transform in an early stage of straining whereas the very small grain provide very high stability and resist the transformation and do not contribute to the improvement in the mechanical properties [98]. Bai *et al.* [50] investigated the influence of the RA grain size on the thermo-mechanically processed Nb microalloyed Mn-Si TRIP steel and found that RA with ~1μm grain size contribute well to the TRIP effect which helps enhance its mechanical properties [50].

According to its location, the RA formed between bainitic ferrite laths is more stable than the RA formed between the polygonal ferrite grains. Timokhina *et al.* [10] found that the RA grains located between the PF grains has low stability thus it transformed at low strain. On the other hand, the RA grains located at the interface between PF and bainite has higher stability than the RA grains between PF grains but less stability than the RA films formed between the bainite laths [10]. However, the size and morphology of the RA grains are another factor influencing the stability such that the RA formed in film shape is more stable than the one with blocky shape [102]. In addition, the refinement of bainitic ferrite increases the stability of RA. In contrast, other study showed that, the RA formed between the parallel bainitic ferrite laths was less stable in Nb-containing TRIP steel [10] and it was suggested that the granular bainite is the best microstructure because it increases the stability of RA [10].

The number and type of phases surrounding the RA grain can also influence the stability of RA. For instance, Lomholt *et al.* investigated the transformation of RA on TRIP steel using EBSD and observed the full transformation of RA bounded by more than two ferrite grains. In contrast, it has been seen that the RA grains bounded by only two ferrite grain were only partially transformed [101]. However, Zhang and Findley [103] have stated that the chemical stability of RA due to high carbon content is the main reason for the higher stability of RA inside BF, compared to PF. Their analysis showed that the differences in the stress partitioning from the BF or PF to adjacent RA do not affect RA stability.

2.4 Mechanical Properties

The key objective of investigating the effect of processing parameters and the microstructure of TRIP steel is to obtain the mechanical properties which satisfy the target application; a combination of the high tensile strength and adequate elongation needed for automotive steels; achieving this goal is therefore the focus of many research groups.

The transformation of austenite to martensite during a tensile test delayed the necking process, so as a result uniform elongation increased, as Fig. 2.20 shows. Therefore, the

TRIP effect enhancing elongation only occurs when the gradual transformation of retained austenite during deformation takes place [23].

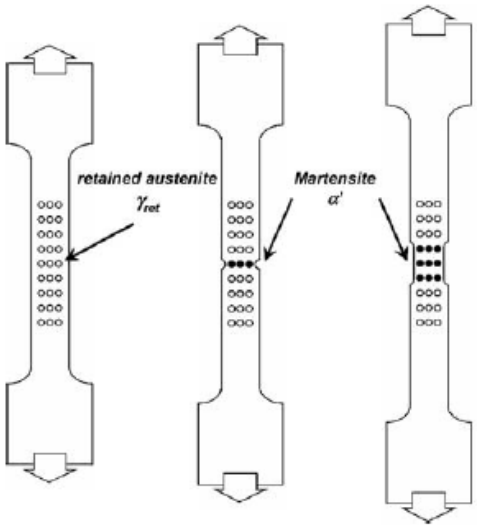

Figure 2.20 The transformation of retained austenite during tensile test and its effect on delaying the necking process [1].

Moreover, the stress-strain behaviour of the ferrite phase differs from bainite phase in that the ferrite phase has low strain hardening and low strength while the carbide-free bainite is characterised by high work hardening and high strength, as shown in Fig. 2.21 [1]. Therefore the amount of each phase present in the microstructure of TRIP steel will have its effect on the overall mechanical properties.

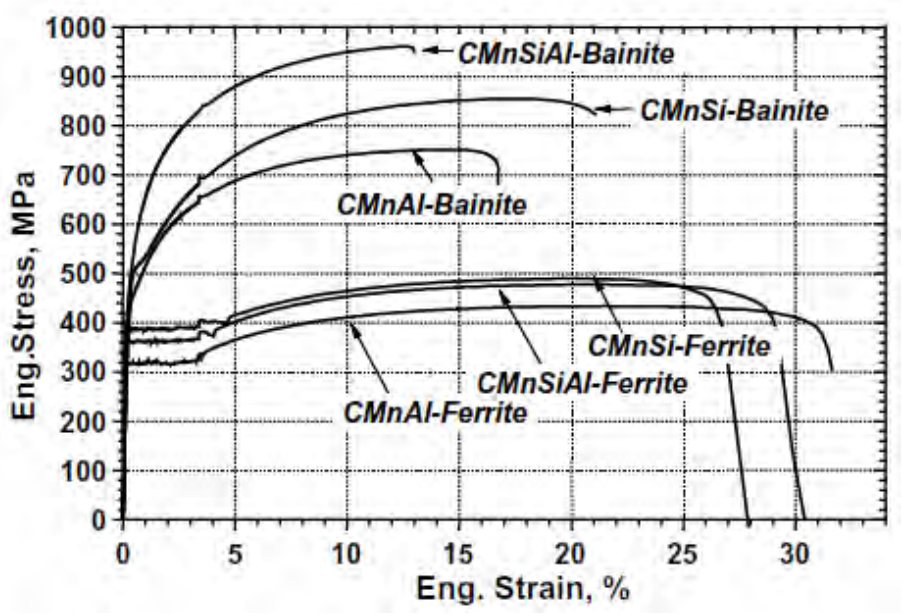

Figure 2.21 The stress-strain curves of different phases existing in TRIP steel [1].

The researchers investigating various processing parameters aimed at altering the microstructure to gain the best properties. Bouet *et al*. [44] investigated the effect of different isothermal bainite temperatures (300°C, 400°C and 500°C) at different holding times (120, 300 and 600 s), and achieved the ultimate tensile strength (UTS) of 1270 MPa and an elongation of 36%.

The chemical composition also has a significant effect on the mechanical properties of TRIP steel. It has been found that due to the effect of Nb addition the total elongation reduced by 50% [10]. Also, it was reported that, partial replacement of Si by Al in TRIP steel leads to reduction in strength [52]. Table 2.3 summarises the mechanical properties achieved by different groups of researchers using different processing techniques and steel compositions.

Table 2.3. Summary of the mechanical properties of TRIP steels based on the data available in the literature

Process	UTS (MPa)	Y.S (MPa)	Elong. (%)	Ref.
TMP	924	537	49	[57]
TMP	940	658	23.7	[104]
TMP	790	-	36	[36]
TMP	822	-	32	[46]
TMP	1330	-	46	[68]
TMP	791	-	36	[105]
IA	1100	710	23.4	[45]
IA	790	412	27	[106]
IA	980	-	33	[24]
IA	750	-	26	[39]
IA	739	-	38	[49]
IA	635	460	27	[34]
IA	680	404	32	[107]
IA	780	-	24	[108]
IA	994	714	27.5	[40]

- IA refers to Intercritical Annealing
- TMP refers to Thermo-mechanical processing

2.5 Application of Electron Back-scattering Diffraction to Study Multi-phase Microstructures

2.5.1 Electron back-scattering diffraction

Electron back-scattering diffraction (EBSD) is based on the acquisition of diffraction patterns from the surface of a sample tilted between 60° to 70° from the horizontal stage or 20° to 30° to the incident electron beam. The observation of an electron back-scattered diffraction pattern (EBSP) was first reported by Nishikawa and Kikuchi in 1928 [109, 110].

The EBSPs are captured on a phosphor screen by backscatter diffraction of a stationary beam from a volume of crystal material which consists of pairs of parallel lines, where each pair is known as a Kikuchi band. A typical EBSD system compromises acquisition hardware which consists of a phosphor screen on which the EBSPs are captured (Fig. 2.22) and software which solves individual EBSPs and stores the orientation data in a rectangular grid for later analysis by offline processing software. Since EBSD is relatively fast and automated, it is useful to obtain statistically representative data sets on microstructural characteristics such as grain orientation, grain sizes, texture analysis and phase identification.

The diffraction pattern quality is an important parameter that is affected by surface defects and the grain boundary. The points that have very low pattern quality will be non-indexed and result in map areas without orientation information. In this case, the orientation from their neighbours can be used to fill these areas in and thus fix the non-index points. However, in the case of highly deformed materials, the non-indexed points will be more due to the strain imparted to the bulk sample and thus, the filling-in of non-indexed points can only be undertaken in a limited manner.

As stated earlier, EBSD provides a powerful tool to study the microstructural features such as the morphology and size of grain and constituents. The grain size and subgrain size is measured using conventional approaches that originated from optical microscopy and consist of an equivalent circle diameter or the linear intercept method with each subgrain or grain identified on the basis of a critical boundary misorientation angle. Usually critical boundary misorientation angles of 2° and 15° are used to distinguish between the subgrain and grain boundaries. Here the scanning step size is also an important mapping

parameter because a minimum of 5 pixels should exist within the boundaries for the structure to qualify as “real”.

EBSD can distinguish between phases or constituents based on the diffraction pattern of each crystal structure such as the face centred cubic (fcc) and body centred cubic (bcc). Where phases share the same crystal structure, space group and approximately the similar lattice parameter (such as ferrite and bainite), a distinction is made on the basis of morphology and/or internal misorientation criteria. Due to the relative importance of phase separation in this study, the next section will discuss the various methods that can be used to separate the phases in EBSD [109].

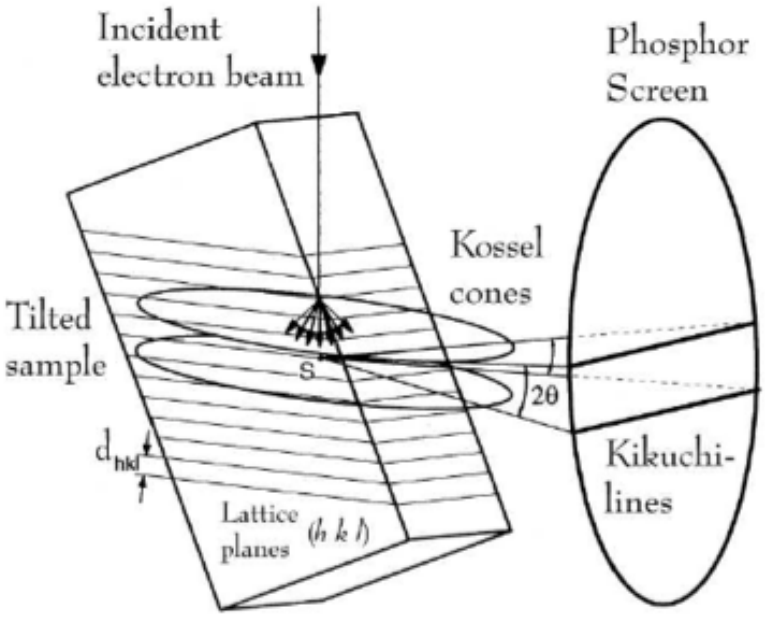

Figure 2.22 Generation of Kikuchi lines on the phosphor screen [109].

2.5.2 Phase separation

EBSD can easily distinguish between fcc and bcc due to the different crystallographic structure between them and when there is a difference of at least 10% in the values of their lattice parameter. Therefore, other constituents with the same crystal structure and approximately the same lattice parameter, such as bainite, martensite, and polygonal ferrite, cannot be separated on this basis. In the literature, different methods have been used to separate these phases, including the use different criteria such as local misorientation (kernel average misorientation, KAM) [12], band contrast (BC) [13, 65, 111], band slope (BS) [112], grain size (GS) [112] and grain-averaged functions based on the band contrast and internal misorientation [13].

The local misorientation in EBSD can be evaluated using various mathematical methods [113] and include the kernel average misorientation (KAM), the grain orientation spread (GOS) and the grain average misorientation (GAM). Figure 2.23 below shows a schematic diagram of the different mathematical methods by which the criteria can be calculated. In the KAM, the average misorientation between the pixel at the center of the kernel and the individual pixels at the perimeter of the kernel are assigned to the central pixel. Here the kernel size is defined by the user. In GOS, the average misorientation of all pixels within a subgrain or grain is assigned to all the pixels belonging to that subgrain or grain (i.e. every pixel has the same average value). The non-orientation scalar maps in EBSD such as the image quality (IQ), confidence index (CI), band contrast (BC) or band slope (BS) can also be used to make distinctions between phases.

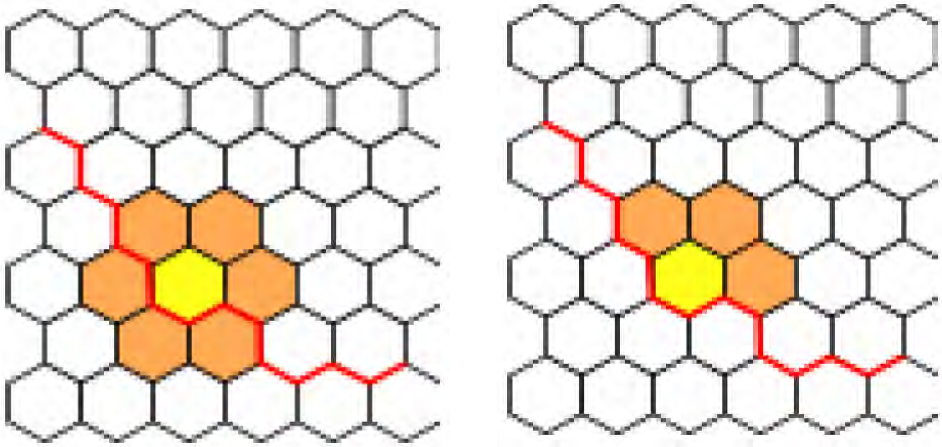

a) b)

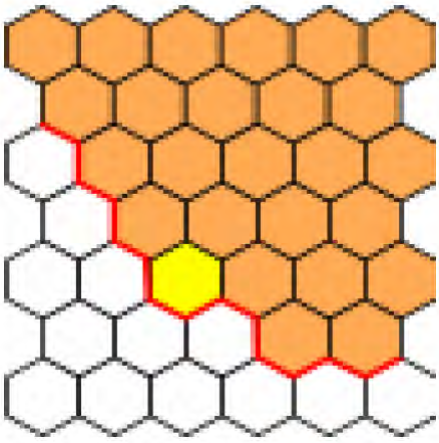

c)

Figure 2.23. The different method of evaluating the misorientation in the EBSD. a) KAM, b) GAM and c) GOS. The red line represents the critical misorientation (grain or sub-grain boundary) which is not considered in the calculation.

The BC (also known as the image quality (IQ) or pattern quality (PQ)) and BS were the early methods used for phase separation. BC defines the average intensity of the Hough peaks. Hough peaks represent the intensity maximum of the Kikuchi band after applying an image processing procedure for locating the bands of EBSD pattern which is called "Hough transform". The BS denotes the average slope of the intensity change between the Hough peaks and their surrounding background [112]. The BC can evaluate the sharpness of the EBSPs. A high value of diffraction pattern sharpness is expected in the case a perfect crystal lattices which in turn, returns high BC value. Therefore, the variation in the BC and BS is based on the amount of lattice defects in each grain, e.g. the higher the lattice defect, the lower the BC value. This relationship between image quality and lattice defects is used to characterise the microstructures. For example, bainite and martensite is characterised by higher amounts of lattice defects compared to ferrite and thus the value of BC tends to be low in bainite and even lower in the martensite.

Based on the BC criteria, ferrite was separated from martensite in dual phase steel [114] and in Fe–0.12C–3.28Ni steel [115, 116]. Polygonal ferrite was also separated from bainite in TRIP steel [65, 80] and bainite was separated from martensite in SAE 9254 steel [117] using the BC method. On the other hand, BS criteria was used in Ref. [118] to separate bainite from ferrite in TRIP steel.

A certain threshold value is used in these techniques to divide the distribution of BC into two regions where a high and low contrast represents two phases. To use this technique the BC distribution should essentially consist of two clear peaks that can easily be separated by selecting (or thresholding) the lowest value between them, as shown in Fig. 2.24.

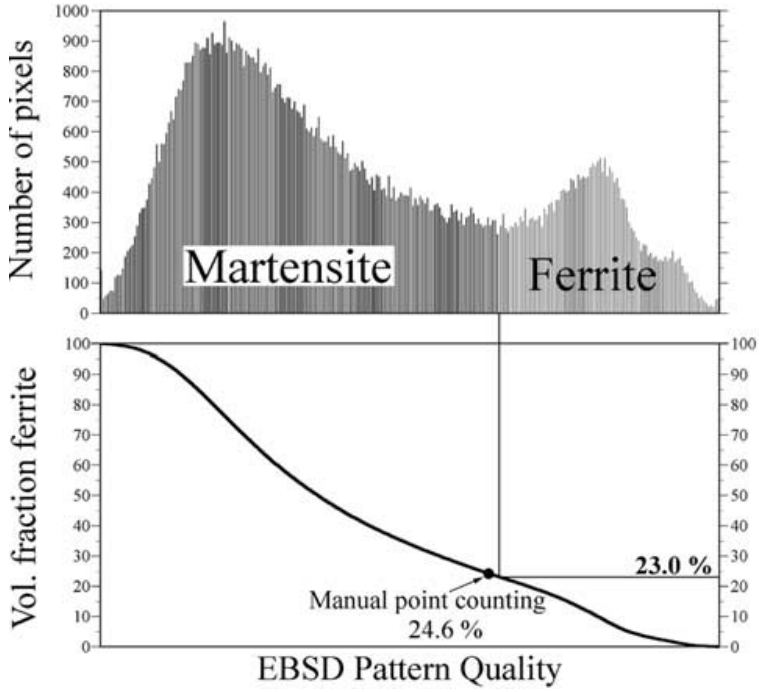

Figure 2.24 Pattern quality histogram separated into two regions representing martensite and ferrite, based on a selected threshold value [73].

However, this thresholding method will not be successful if the distribution of BC only shows one peak or if a significant peak overlap occurs as is the case in multi-phase steel. Therefore it has been suggested that the BC method alone is not enough to separate all phases in complex microstructures such as the one in TRIP steel [13]. Moreover, pattern quality cannot be applied to deformed materials because the pattern quality of ferrite could be as low as the bainite [65], which is why a combination of two criteria was used to separate between [112] martensite and ferrite in a dual phase steel; in this method, BC or BS as well as grain size criteria were used together.

To improve the BC criteria with a single peak distribution, a mathematical Multi-peak model was developed by Wu *et al*. [111] on the assumption that an asymmetric BC

distribution of all pixels can be divided into several normal distributions equal to the number of the phases present in the microstructure. The volume fraction of each phase was estimated from the area under each peak. Moreover, this model also considered the influence of the grain boundary region in the separation process. The multi-peak model has been applied successfully in IF, dual phase, high-strength-low-alloy (HSLA) steels [111] and TRIP steel [65] to separate between different constituents such as ferrite, bainite and martensite phases.

The stored energy (or dislocations content) due to the transformation of bainite [119] affects the orientation gradient of these structures and can be used as an effective separation criterion. Depending on the microstructure, the KAM scheme can be applied with care because this criteria is very susceptible to orientation noise [109]. After examining different misorientation gradient methods, Zaefferer *et al.* [12] chose the third nearest neighbour kernel average misorientation (KAM) as a criterion to distinguish between ferrite and bainite in an inter-critically annealed TRIP steel. Ferrite was characterised by low KAM values whereas those areas with high KAM values were assigned to the bainitic ferrite phase. The same procedure has been successfully applied in TRIP steel and confirmed via the orientation relationship between bainite and austenite [120]. However, the KAM method cannot be used to separate the phases on highly deformed microstructure because the bimodal distribution of KAM changes to a single peak distribution after 2.35 % deformation [120]. It has been suggested that other parameters such as grain size can be added to this procedure when non-granular bainite exists in the microstructure [12].

The internal average misorientation (also termed grain average misorientation, GAM) can be used as an effective separation criteria as it has an underlying metallurgical/ microstructural basis. Kang *et al*. [13] used grain averaging as an alternative criterion for phase separation. This is different from other methods as it makes the separation based on grains and not on pixels and provides a clear discrimination between various substructures. They successfully implemented this method in conjunction with the band contrast (BC) parameter in dual phase steel and separated ferrite and martensite. It was stated that the definition of the grain boundary angle is important in this procedure as it directly affects the martensite area fraction. However, in the case of TRIP steel, it was found that the BC needs to be supplemented with average misorientation data in order to undertake phase separation [13]. Different bainite morphologies make the separation more complex and led to the need for multi-condition schemes to be applied. Zhu *et al*. [121] utilised a combination of several functions such as BC, BS, grain internal mean

misorientation (GIMM or grain orientation spread, GOS), grain size and grain shape to characterise the phases in complex microstructures.

From the above, it appears that different microstructures respond differently to the selected separation criteria [112, 121], and due to the complexity of the microstructure in this study, the procedures developed in the literature were not entirely applicable. The microstructure in this study contains a mixture of different bainite morphologies such as granular bainite and bainitic ferrite (lath-like shape) formed as several bands along the rolling direction interleaved between the ferrite phase, so this complex microstructure made it difficult to apply any of the literature based separation procedures.

3 EXPERIMENTAL AND ANALYTICAL PROCEDURES

This chapter reviews the materials investigated and the experimental procedures used in this study. A Gleeble 3500 (physical simulator) was utilised in this study to simulate the TMP schedule followed by microstructure characterisation via optical microscopy (OM), X-ray diffraction (XRD), scanning electron microscope (SEM), electron backscattering diffraction (EBSD) and transmission electron microscopy (TEM). These techniques are addressed briefly in this chapter, while the mechanical properties were evaluated by tensile testing on sub-sized samples.

3.1 Materials

A base low Si TRIP steel and the one with Ti and Nb additions (Table 3.1) were received as 6 mm thick hot rolled plate from GIFT-POSTECH. Three processing schedules were carried out on 8 (RD) × 20 (TD) × 6 (ND) mm^3 samples (Figure 3.1 a and b) using a Gleeble 3500 thermo-mechanical simulator.

Table 3.1 The nominal chemical composition of two low Si TRIP steels in wt.%.

Steel	C	Mn	Si	Al	P	Nb	Ti
Base	0.15	2.00	0.30	1.00	0.05	-	-
Nb-Ti	0.15	2.00	0.30	1.00	0.01	0.03	0.02

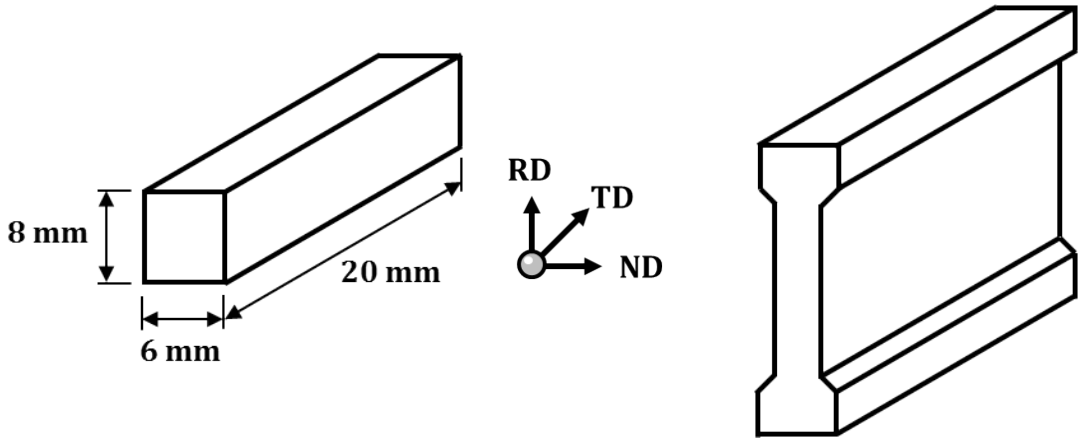

(a) (b)

Figure 3.1 Schematic of the sample geometry and dimensions (a) before and (b) after thermo-mechanical processing.

3.2 Physical Simulations using Gleeble 3500

The Gleeble 3500 thermo-mechanical simulator is a very powerful tool that can simulate most TMP schedules that involve high deformation and complicated heat treatment. Another feature is that only a small sample is required to conduct a very precise experiment. Therefore, the Gleeble 3500, operating in hydra-wedge mode, was used to simulate the designed TMP schedules. The sample temperature was controlled based on

thermocouples that were spot-welded to the samples to measure the instantaneous temperature.

Although different TMP schedules were examined, a similar amount of deformation was applied in all cases. The strain applied in the recrystallisation region was 0.25 and the strain below the non-recrystallisation temperature (T_{nr}) was 0.47. These selected strain values were expected to give an optimum microstructure [57]. In industry, there are many different ways to produce TRIP steel and this depends mainly on the mill configuration and targeted final thickness. Therefore, the accumulated finishing strain in industry can vary from 1 to more than 2.5 [57]. All the critical temperatures were obtained from the literature, as well as from a rough calculation based on the empirical equations available in the literature.

Three different TMP schedules, described in the following sections, were based on a variation of the coiling time and the subsequent heat treatment. In addition, the intercritical heat treatment (IA) schedule, which was conducted at GIFT-POSTECH on the same materials, is also described in the following sections.

3.2.1 Thermo-mechanical processing

In the case of the first two schedules (Fig. 3.2), the samples were heated at 2 Ks^{-1} to 1250 °C, held for 120 s followed by cooling to 1100 °C where a 25% roughing reduction was applied. The samples were then held for 120 s in order to condition the recrystallised austenite and then cooled down to the 47% finish rolling temperature (T_{FR}) below the non-recrystallised austenite region (T_{FR} = 850 °C for the base steel and 875 °C for the Nb-Ti steel). This difference in the T_{FR} between the two steels was due to the increase of T_{NR} resulted from the addition of Ti and Nb (see Eq. 2.3).

Following the second 47% finishing reduction, the samples were slow cooled at 1 Ks^{-1} to the accelerated cooling start temperature (T_{AC} = 680 °C for the base steel and 690 °C for the Nb-Ti steel) to form ~50% polygonal ferrite. At the T_{AC} temperature, the cooling rate was increased further to 20 Ks^{-1} to avoid pearlite formation. Finally, the sample was held at 470 °C coiling temperature (T_C) for different coiling times (t_c) to form bainite, and then quenched in water. When a short coiling time of t_c = 125 s was used, the samples were denoted as TMP-S but when the coiling time was long (t_c = 1200 s), the samples were referred to as TMP-L.

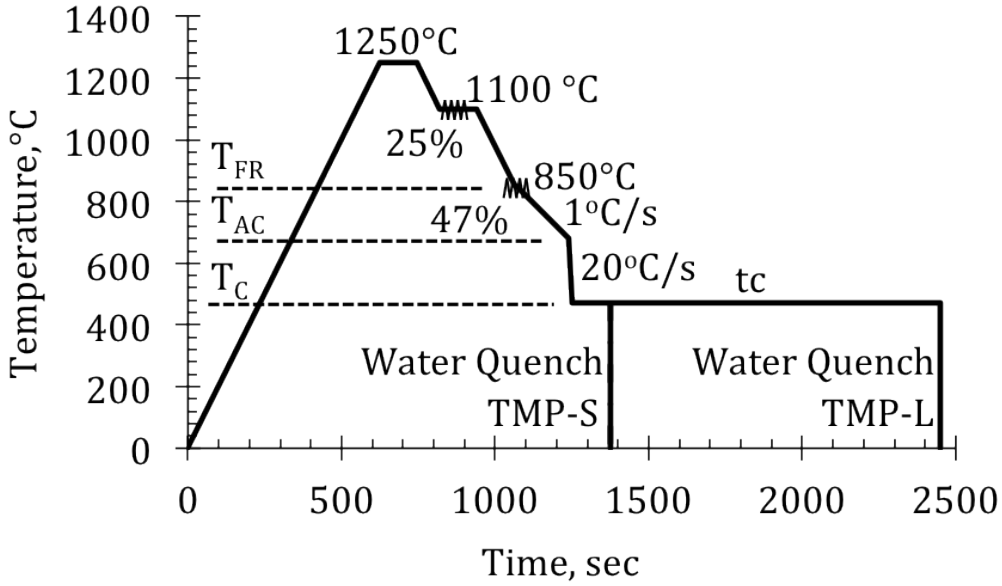

Figure 3.2 Schematics of the thermo-mechanical processing schedules for short (TMP-S) and long (TMP-L) coiling times (t_c = 125 and 1200 s), respectively. T_{FR} = finish rolling temperature; T_{AC} = start of accelerated cooling temperature, T_C = coiling temperature.

3.2.2 Galvanising heat treatment

The third schedule was to simulate the galvanising process (Fig. 3.3), here the TMP-L samples were reheated at 25 Ks^{-1} to 550 °C and held for 25 s. This step is undertaken in industry to allow the carbon to segregate at the surface of hot rolled steel and avoid a silicon oxide layer forming [62, 122]. The samples were then cooled at 5 Ks^{-1} to TC = 465 °C (above the zinc melting point), held for 5 s and air cooled to room temperature. Although galvanising heat treatment is designed to improve the zinc coating reaction, here it was simulated to investigate its influence on the microstructure and mechanical properties of TRIP steels [2, 63].

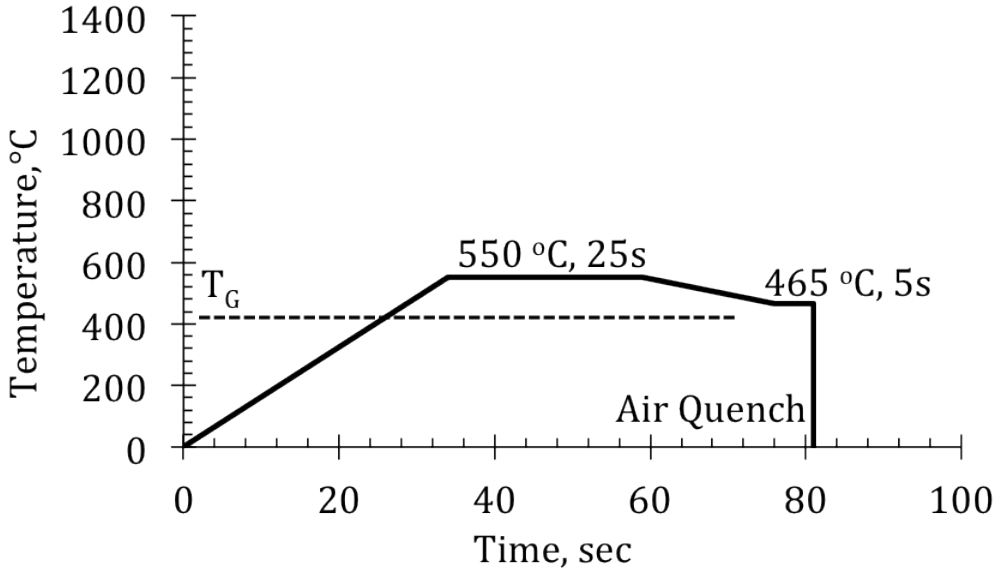

Figure 3.3 Schematics of the galvanising treatment schedules denoted as TMP-LG which is undertaken after TMP-L schedules. T_G = galvanising temperature.

3.3 Intercritical Annealing Heat Treatment

To compare the efficacy of TMP-S treatment, an inter-critically annealed-galvanising (IA-G) schedule was undertaken on the two steels at GIFT-POSTECH. As Fig. 3.4 shows, cold rolled samples of both steels were reheated to a temperature within the inter-critical (ferrite-austenite) region (T_{IA} = 863 °C for base steel and 871 °C for Nb-Ti steel) and held for 120 s to form ~50% polygonal ferrite followed by rapid cooling at 30 Ks^{-1} to the isothermal bainite formation temperature (T_C = 465 °C). The sample was held at this temperature for 125 s to account for the formation of bainite during the first 120 s, after which it was galvanised in a zinc pot for 5 s, followed by air cooling at 30 Ks^{-1} to room temperature.

It was understood from the above that the isothermal bainite formation stages for the TMP-S and IA-G schedules were similar to the holding that was undertaken for 125 s at T_C = 470 °C and 465 °C, respectively.

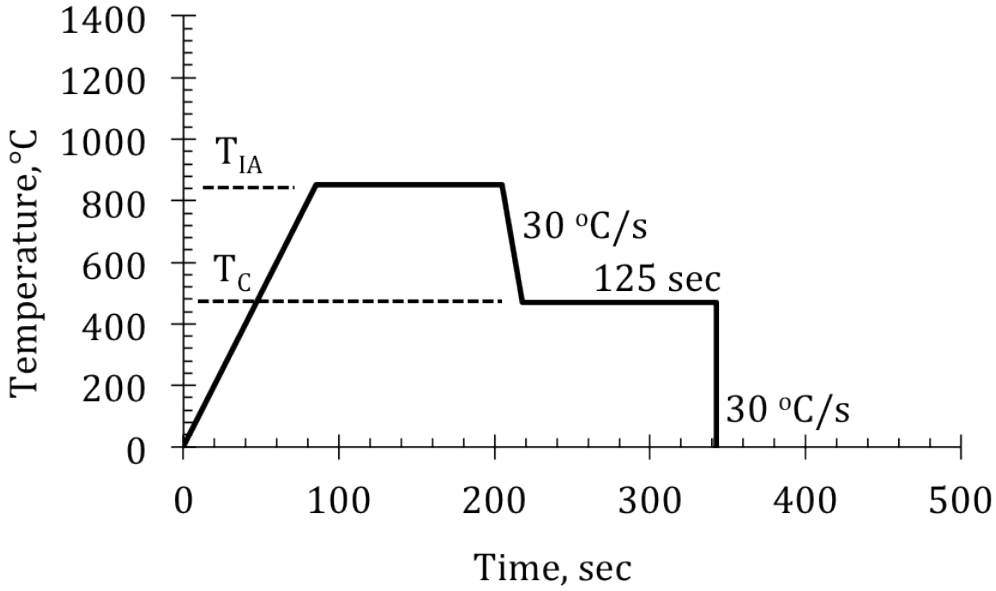

Figure 3.4 Schematic diagram of the intercritical annealing – galvanising treatment schedule denoted as IA-G. T_C = coiling and galvanizing temperature; T_{IA} = intercritical annealing temperature.

3.4 Samples Preparation and Microscopy

All Gleeble samples were wire-cut to the dog-bone shape for the tensile test (the dimensions are shown in Section 3.6). The surfaces of the samples along the gauge length (RD/TD plane), were prepared for XRD analysis prior to tensile testing. After XRD analysis, the samples were prepared for tensile testing by thinning the thickness of the sample from both sides and in equal amount. This step is necessary to reduce the load required during tensile test due to the force limitation on the tensile stage. Therefore, the sample thickness was reduced to 0.9 mm by removing ~0.75mm from each side of the sample surface. The sample thinning has been performed by polishing the sample on 9 µm pads until reaching the target thickness followed by polishing to a scratch-free condition with 1µm diamond pads.

After the tensile test, the samples were cut into three parts; the non-tensile deformed part which is from grip of the sample, the middle part of the sample which has undergone uniform elongation with strain corresponding to the ultimate tensile strength (UTS) and the fracture part. Based on this cutting, the samples were then examined after three strain states; TMP (initial), at UTS, and at fracture.

The microstructure was characterised by a combination of optical microscopy and secondary and transmission electron imaging. However, the optical microscopy (OM) and SEM analyses were only applied on the grip part of the sample (Initial), while an EBSD analysis was applied on all three parts of the samples. All these analyses were conducted on the RD/ND plane except XRD and TEM, which were conducted on RD/TD plane due to size limitation, as shown in Figure 3.5.

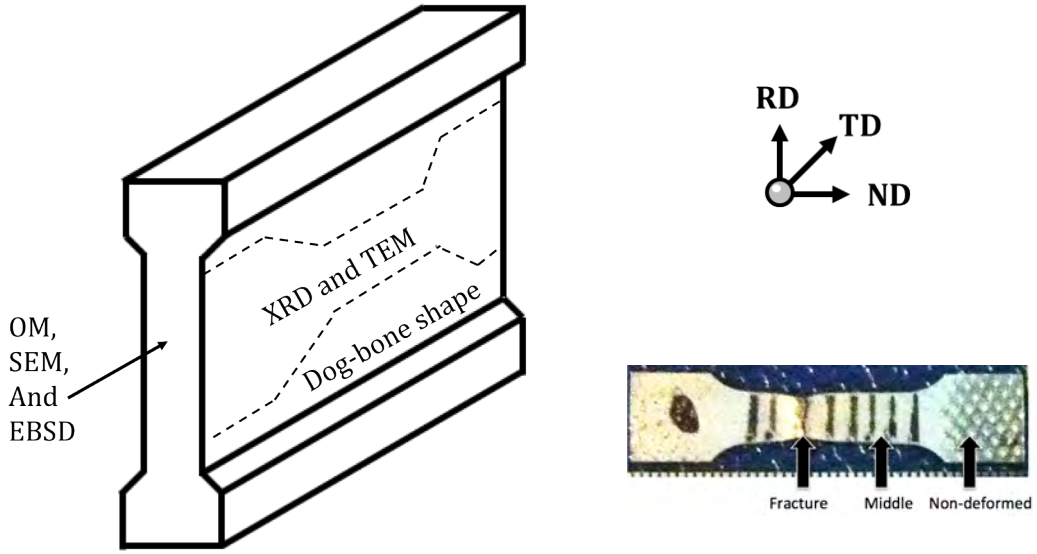

a)

Figure 3.5 Schematic of the sample geometry after thermo-mechanical processing indicating the cross section plane for each analysis technique used in this study. (OM: Optical Microscopy, SEM: Scanning Electron Microscopy, EBSD: Electron Back-Scatter Diffraction, TEM: Transmission Electron Microscopy and XRD: X-ray Diffraction)

3.4.1 Optical microscopy

After cutting, samples were cold mounted instead of hot mounting to avoid any transformation of the RA. They were then mechanically ground with silicon carbide (SiC) paper grade 320 using water as a lubricant, followed by polishing on 9 µm and 3 µm pads. Finally, the samples were polished to a scratch-free condition with 1µm diamond pads and then cleaned with soap, water, and alcohol and then dried with hot air.

To reveal the microstructure, two types of etchants were applied on the as-polished samples surfaces: (1) 2% Nital solution and (2) Klemm's colour etchant [123, 124]. The Nital etchant technique was enough to reveal the polygonal ferrite and bainite

microstructure while the second etchant was needed to reveal other constituents such as retained austenite and martensite.

Several previous works successfully revealed the RA and martensite in TRIP steel using the heat tinting technique [10, 123], a technique that consists of etching the sample with 2% Nital and then heating it in an open atmosphere furnace at 200°C for 30 - 80 minutes. This technique is sensitive to temperature and time so several attempts should be made to find the optimum result. However, this technique could not distinguish between all the constituents in the current microstructure. Another etching techniques (such as LePera etchant) [39, 123] have also failed to distinguish clearly between RA and other phases.

The austenite and martensite phases were distinguished optically in the current microstructure using Klemm's [123, 124] colour etchant. Klemm's etchant is a mixture of (1) 50 mL water saturated with sodium thiosulfate, ($Na_2S_2O_5$) and (2) 1g potassium metabisulfite, $K_2S_2O_5$. The RA appears as white after applying this etchant while other phases appear dark. However, the weak nature of the etched film [124] resulted in inconsistent colour schemes in some samples. The grain size was measured by the mean linear intercept method.

3.4.2 Scanning electron microscopy

Secondary electron imaging was undertaken on a JEOL JSM-7001F field emission gun - scanning electron microscope at 3-15 kV accelerating voltage. A determination of the chemical composition of 20-25 precipitates after the TMP-L (base and Nb-Ti steels) and the TMP-LG (Nb-Ti steel) schedules was performed using an Oxford Instruments 80 mm^2 X-Max energy dispersive X-ray spectroscopy (EDS) detector and the AZtec software suite.

3.4.3 Electron back-scattering diffraction

The sample for EBSD was prepared using 1200 silicon carbide paper followed by electro-polishing with Struers Lectropol-5. The electrolyte consisted of 330 ml methanol, 330 ml butoxyethanol, and 40 ml perchloric acid. The electro-polishing was carried out in 90 s with 50V and 1.2mA. The mechanical preparation was found to be not appropriate for the current microstructure because a lot of the RA can be transformed during preparation. However, the slight polishing before the electropolishing cannot be avoided but its effect on the amount of RA in studied area was minimised by subsequent electropolishing. For

example, ~0.1mm thickness of mechanically polished foil was reduced to 600-500 nm in the observation area of electropoloshed thin TEM foil. Several microns layer was also removed during electropolishing of the samples for XRD and EBSD.

EBSD was conducted at the centre of the ND/RD cross-section with a JEOL JSM-7001F field emission gun – scanning electron microscope operating at 15 kV and ~5 nA and fitted with a Nordlys- II detector interfacing with the AZtec software suite. A step size of 50 nm and a map size 105x79 μm^2 was maintained constant for all conditions.

3.4.4 Transmission electron microscopy

The grip of each tensile sample was punched out to produce a 3 mm diameter disk, which was then ground to ~100 μm thickness using 1200 SiC paper. All the TEM disks were electropolished using a twin-jet Struers Tenupol-5 electropolisher in a solution of 95% methanol and 5% perchloric acid at 30V, 150mA and -25 °C. Bright-field imaging and selected area diffraction were undertaken on thin foils using a JEOL 2011 transmission electron microscope operating at 200 kV.

3.5 X-ray Diffraction

The simplicity and accuracy of X-ray diffraction (XRD) analysis makes it one of the most common techniques used to determine the RA [96], so the volume fraction (VF) of the RA was estimated by XRD using the direct comparison method [125]. XRD is one of the best technique to determine the amount of retained austenite and it can detect RA down to 0.5% [126]. The XRD analysis was conducted on the TD/RD plane for 2θ = 60-100° [125] where most of the austenite and ferrite peaks could be obtained, as shown in Fig. 3.6.

The carbon content (wt.%) in the RA was calculated as follows [127]:

$$a_\gamma = \left[0.363067 + \frac{0.0783}{1+0.2151\left(\frac{100}{C}-1\right)}\right] + \left[25.92 - \frac{51}{1+0.2151\left(\frac{100}{C}-1\right)}\right] 10^{-6}(T-727) \quad (3.1)$$

where a_γ is the RA lattice parameter and T is temperature (°C).

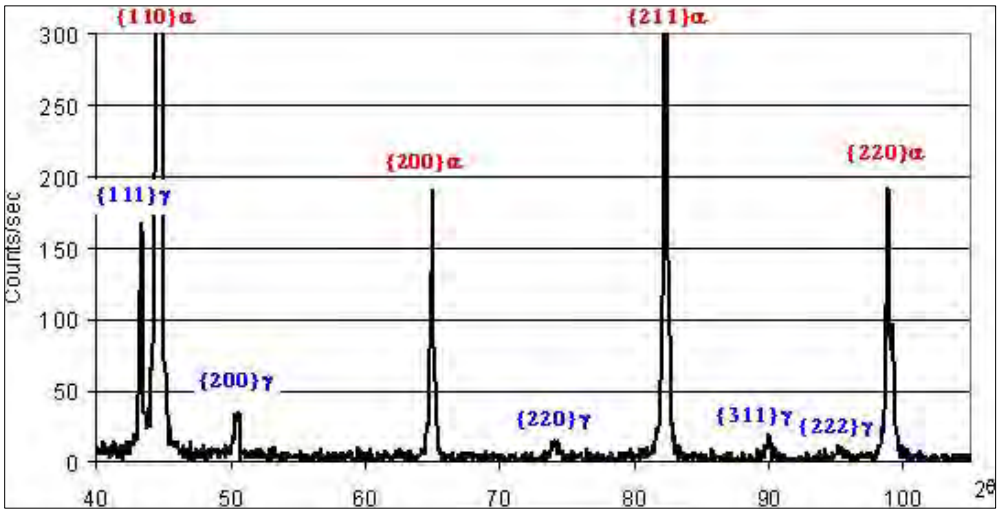

Figure 3.6 X-ray diffraction pattern of austenite and ferrite peaks [128]

The step size of the XRD was 0.02° and the scan speed was 1°/min. The resulting data was analysed using Traces software and the volume fraction of the RA was measured by applying the direct comparison method onto the integrated intensity of the $(220)_{\gamma}$, $(311)_{\gamma}$, $(200)_{\alpha}$ and $(220)_{\alpha}$ peaks, as shown in the following equation;

$$\frac{I^{\gamma}}{I^{\alpha}} = \frac{R^{\gamma} f_{\gamma}}{R^{\alpha} f_{\alpha}} \tag{3.2}$$

where I^{γ}, I^{α}, f_{γ} and f_{α} are the integrated intensity of austenite, the integrated intensity of ferrite, and the volume fraction of austenite and volume fraction of ferrite, respectively. The total amount of the volume fraction of austenite and ferrite should equal one to solve this equation, so R^{γ} and R^{α} can be calculated by the following equation:

$$R = \left(\frac{1}{v^2}\right)\left[FF * P\left(\frac{1+cos^2 2\theta}{sin^2\theta cos\theta}\right)\right] exp(-2M) \tag{3.3}$$

Where v, FF, P and exp(-2M) are the volume of the unit cell (m3), structural factor, multiplicity factor and temperature factor, respectively.

3.6 Mechanical Testing

Tensile dog-bone samples were wire-cut according to: (i) the sub-size ASTM-E8M standard [129] for the TMP-S, TMP-L and TMP-LG samples (Fig. 3.7a) and, (ii) the EN 10002 (Type 2) standard [88] for the IA-G samples (Fig. 3.7b). The use of a sub-size sample geometry was necessary for all TMP conditions due to the initial sample size limitations for thermo-mechanical processing on the Gleeble TMP simulator. Uniaxial tensile testing was conducted on a minimum of two dog-bone samples per condition at a constant strain rate of 4.5×10^{-4} using: (i) an in-house modified 5kN Kammrath and Weiss GmbH tensile stage for all TMP samples at UOW and, (ii) a 50 kN Instron 5569 screw-driven tensile machine for the IA-G samples at GIFT-POSTECH.

The yield strength (YS) was defined as the 0.2% offset proof stress or the point after Lüders banding has been completed in the case of continuous and discontinuous yielding, respectively. Thereafter, the work hardening rate $\Theta = d\sigma / d\varepsilon$ and the strain hardening exponent (n-value) were calculated from the true stress and true strain curves [130]. The strain hardening exponent indicated the uniformity of strain distribution during the forming operation such that the n value increased with greater resistance to thinning during forming operations. The instantaneous strain hardening exponent was independent of the any power law and can be defined as $n = \left[\left(\varepsilon / \sigma\right) \cdot \Theta\right]$ [131]

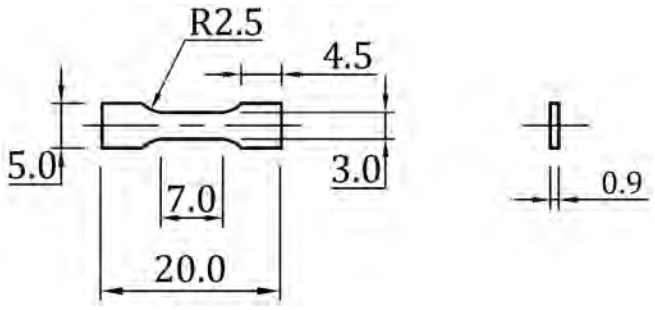

(a)

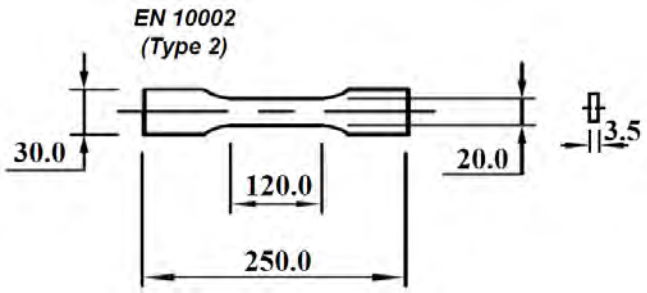

(b)

Figure 3.7 Schematics of the dimensions of the tensile dog-bones (a) wire-cut from the RD/TD plane along the TD direction of the TMP-S, TMP-L, and TMP-LG samples, and (b) the IA-G samples. All the dimensions are in mm.

3.6.1 Empirical models to describe the work hardening rate

Different empirical models have been proposed to describe the rate of work hardening during uniform straining to characterise the behaviour of TRIP steel during forming operations. While the Hollomon model [132] is limited to interpreting the work hardening behaviour of single phase steels, other empirical equations such as the Ludwik [133], Voce [134], Swift [135] and Ludwigson [136] relationships have only been partially satisfactory in interpreting complex phase steels. Studies on dual-phase steels have shown that the modified Crussard–Jaoul (C–J) model (based on the Swift relationship) successfully describes their two-stage work hardening behaviour. In multiphase TRIP steels, the work hardening rate is controlled by the dislocation accumulation mechanism as well as by the strain-induced transformation of austenite [137]. Thus, any further modifications to the model must account for the evolving volume fraction and strength of the various phases at different strains [138]. Since the work hardening rate of TRIP steels is typically characterised by three stages [139], the dynamic composite model [138] is more appropriate. Since information on the evolving volume fraction of each phase at different strains was not available during tensile testing, the present study applied the modified C–J equations to characterise the work hardening behaviour.

4 THE EFFECT OF PROCESSING PARAMETERS ON THE MICROSTRUCTURE AND MECHANICAL PROPERTIES OF LOW-SI TRIP STEELS

A base low Si, high Al Transformation Induced Plasticity steel, and one with 0.03Nb and 0.02Ti (wt.%) additions were subjected to thermo-mechanical processing and galvanizing simulations. The microstructure and mechanical properties were analysed using a combination of optical and electron microscopy, and X-ray diffraction and tensile testing, and then the results were compared with those from intercritically annealed – galvanised steels. Since information on the evolving volume fraction of each phase at different strains was not available during tensile tesing, the present study applied the modified C-J equations to characterise the work hardening behaviour.

This chapter is divided into 3 sections; (1) the effect of composition on the microstructure and mechanical properties after short and long coiling times, and (2) the effect of galvanising after a long coiling time (TMP-L) on the microstructure and mechanical properties. The last section discusses the difference between the effect of intercritical annealing and TMP on the microstructure and mechanical properties.

4.1 The Effect of Composition on the Microstructure and Mechanical Properties after Short and Long Coiling Times

4.1.1 Microstructure

The microstructures of the base and Nb-Ti steels after a short coiling time TMP-S schedule are shown in Figs. 4.1a, 4.1b, and 4.2a and 4.2b.The microstructure in both steels consists predominantly of ~45-48% polygonal ferrite (PF) and ~35-40% bainite (B), while the remainder comprises the austenite and martensite phases. The PF and bainite phases appear as light and dark grey after Nital etching (Figs. 4.1a and 4.2a), whereas the PF, bainite, austenite, and martensite phases appear as light blue/brown, dark brown, and white and black after colour etching, respectively (Figs. 4.1b and 4.2b).

PF tends to be of approximately equiaxed shape with 12±8 μm and 10±6 μm grain size (Table 4.1) for the base and Nb-Ti steels, respectively. The bainite lath thickness ranges between 0.5 to 1 μm such that they are slightly coarser in the base steel compared to the Nb-Ti steel. The ~7% volume fraction of the RA phase was similar to both the base and Nb-Ti steels. The RA appeared as blocky grains between the PF grains or at the interface between the PF and bainite, or as fine layers between the BF laths. Based on the measurements taken using a combination of secondary electron and bright field imaging via scanning and transmission microscopy, the RA grains in both steels were ~0.1 to 0.3 μm thick such that they are slightly coarser in the base steel than the Nb-Ti steel. The majority of the martensite phase was found between PF grains and at the interface of the PF and bainite.

The microstructures of the base and Nb-Ti steels after a long coiling time TMP-L schedule (Figs. 4.1c, 4.1d, 4.2c and 4.2d) were similar to those after TMP-S. The values of the volume fractions and the grain size of the ferrite phase after TMP-L remained similar to those obtained after the TMP-S treatment. As the TEM micrographs (Fig. 4.3) show, there were two bainite morphologies after TMP-L consisting of fine laths of bainitic ferrite (BF) and plates of granular bainite (GB).

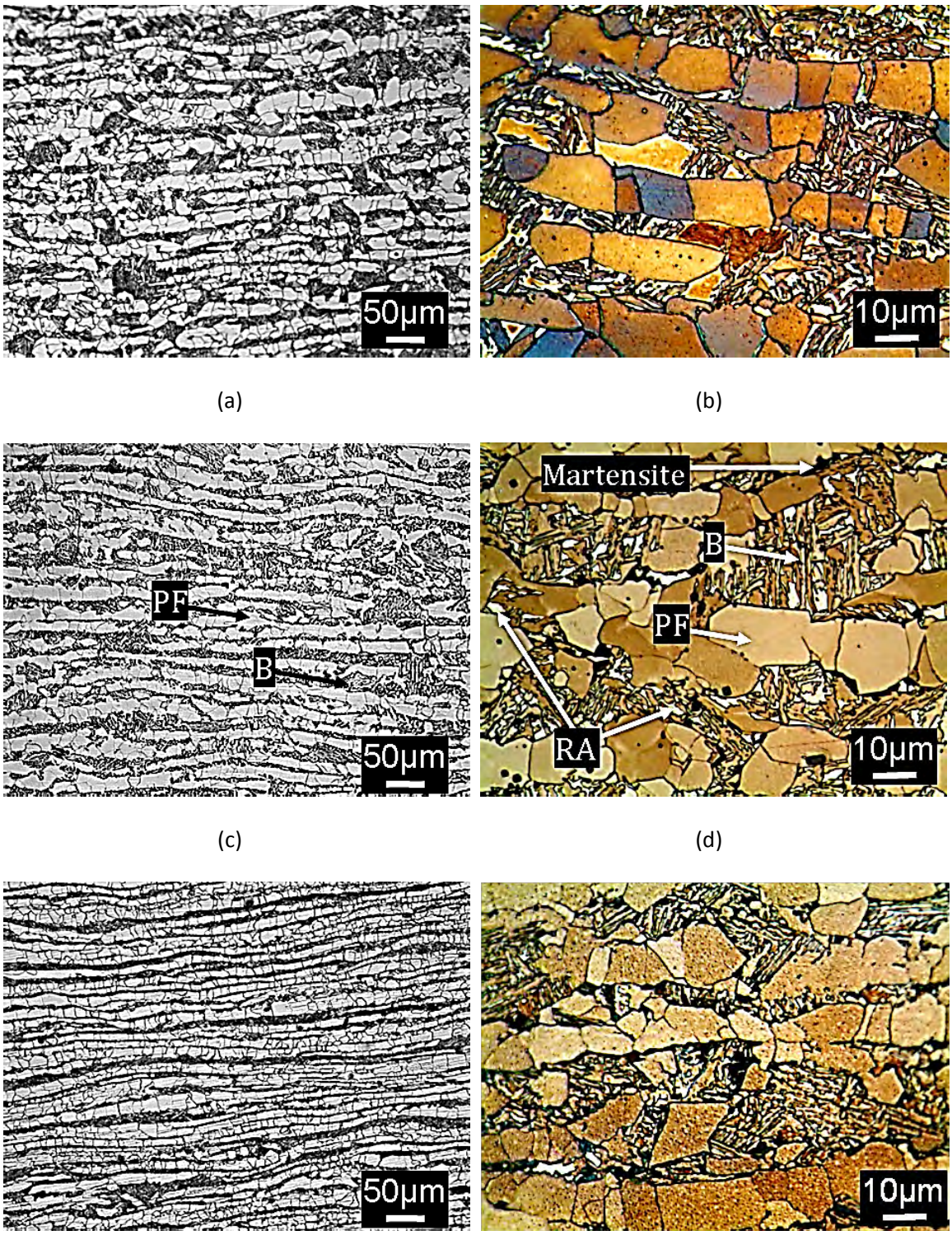

Figure 4.1: (a, c, e) Nital and (b, d, f) colour etched microstructures of the base steel after (a, b) TMP-S, (c, d) TMP-L and (e, f) and TMP-LG schedules. PF = polygonal ferrite; BF = bainitic ferrite; M = martensite and RA = retained austenite.

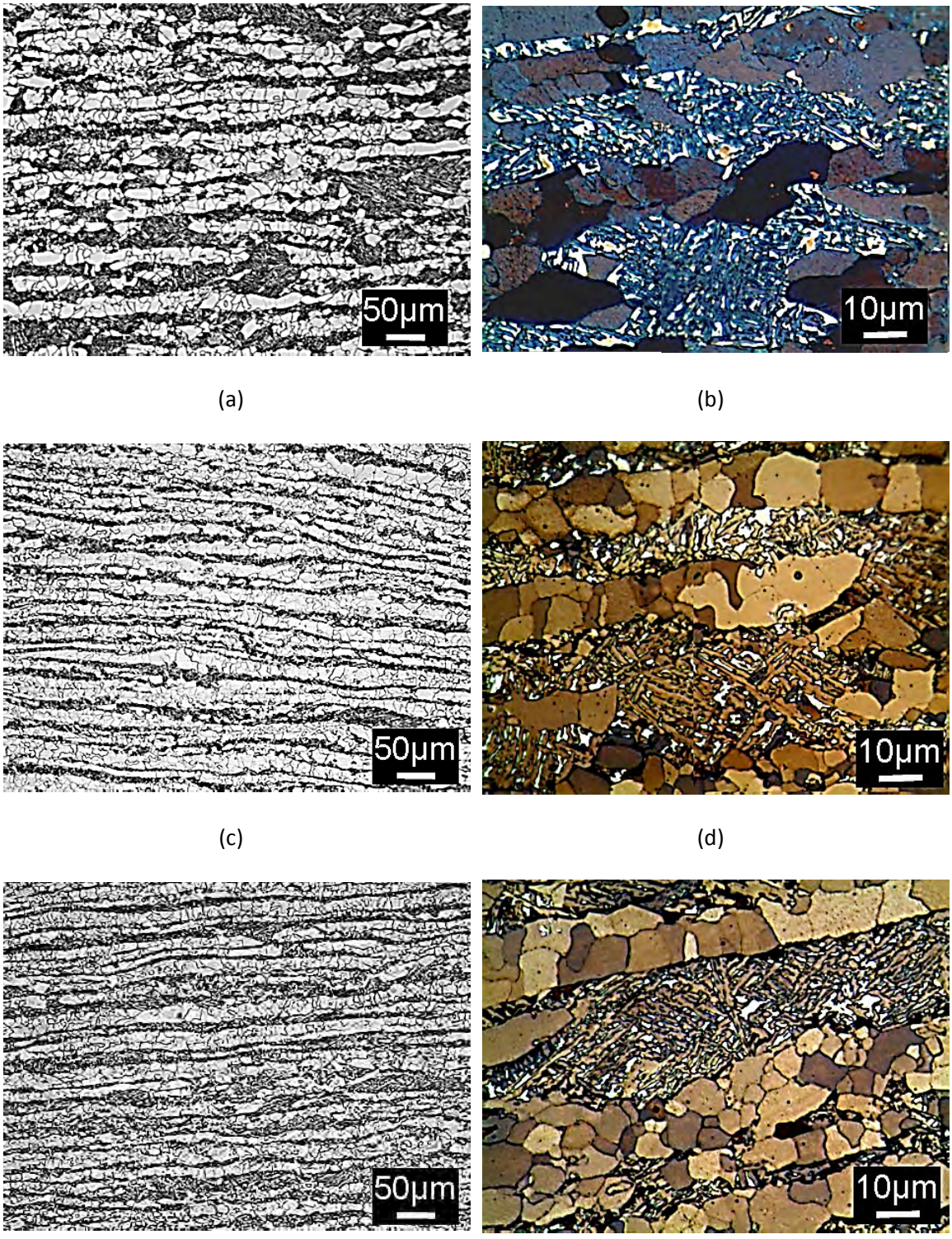

Figure 4.2: (a, c, e) Nital and (b, d, f) colour etched microstructures of the Nb-Ti steel after (a, b) TMP-S, (c, d) TMP-L and (e, f) and TMP-LG schedules.

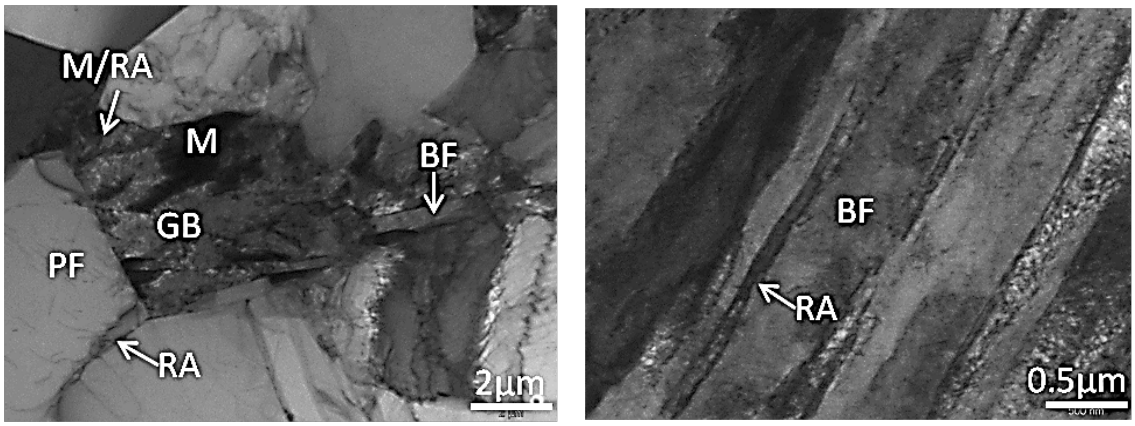

(a) (b)

Figure 4.3: Representative bright field micrographs of the various bainitic morphologies seen in the base steel after the TMP-L schedule. PF = polygonal ferrite; BF = bainitic ferrite; M = martensite and RA = retained austenite.

In stark comparison to the TMP-S schedule, the TMP-L treatment showed that the volume fraction of the RA phase had decreased to ~4±1% in the base steel and increased to ~13% in the Nb-Ti steel as a direct result of microalloying (Table 4.1). Based on the micrographs after colour etching, the fraction of martensite was also slightly higher in the base steel compared to the Nb-Ti steel (Figs. 4.1d and 4.2d).

The EDS analysis of the precipitates in the TMP-L base steel revealed the presence of 100-200 nm (Al,Si)(N,O) and (Mn,Cu)S particles that were randomly scattered throughout the sample volume (Fig. 4.4a). In the TMP-L Nb-Ti steel (Fig. 4.4b), three major types of precipitates were observed: (i) 60–150 nm sized (Ti,Nb)(C,N), (ii) <100 nm Nb(C,N) and, (iii) >40 nm NbC (Figs. 4.4e-g).

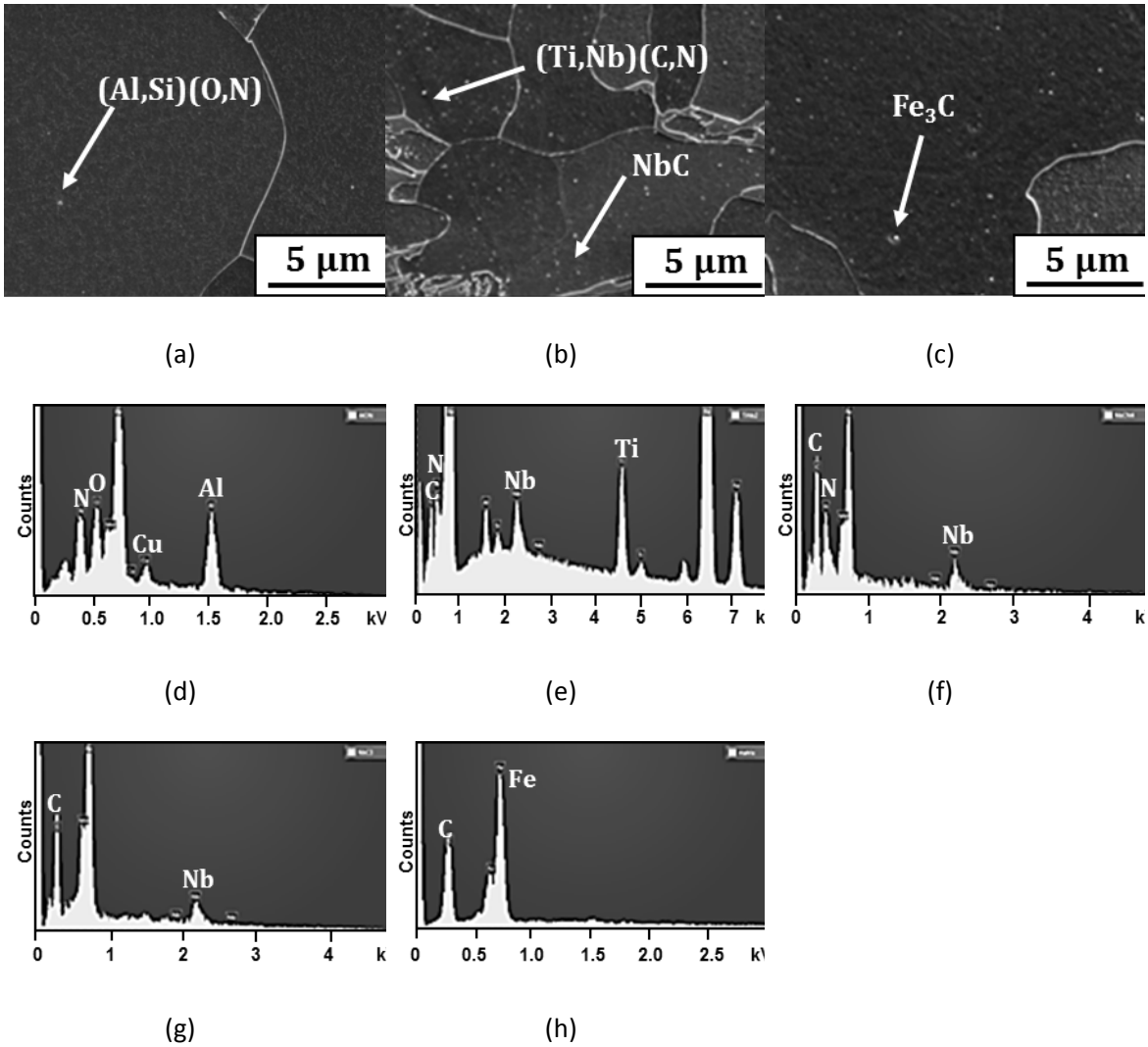

Figure 4.4: Representative secondary electron micrographs of the (a) TMP-L base, (b) TMP-L Nb-Ti and, (c) TMP-LG Nb-Ti steels. (d-h) Example of EDS spectra of (d) an Al(O,N)+Cu particle from the TMP-L base steel, (e) (Ti,Nb)(C,N), (f) Nb(C,N) and (g) NbC particles from the TMP-L Nb-Ti steel, (h) Fe_3C particles in the matrix of the TMP-LG Nb-Ti steel.

Table 4.1: A summary of the simulation processing parameters and the phase statistics of the base and Nb-Ti steels.

Steel	Schedule	Processing parameters				Phase statistics			
						Polygonal ferrite		Retained austenite	
		T_{AC}	T_C	t_c	T_G	VF	GS	VF	C
		°C	°C	s	°C	%	µm	%	wt.%
Base	TMP-S	680	465	125	--	48±1	12±8	7±1	1.3±0
	TMP-L	680	470	1200	--	47±1	12±6	4±1	1.2±0
	TMP-LG	665	470	1200	465	46±3	12±8	2±1	1.1±0.1
	IA-G	--	465	125	--	50	5	10	1.1
Nb-Ti	TMP-S	690	465	125	--	45±1	10±6	7	1.2±0
	TMP-L	690	470	1200	--	49±3	8±4	13±0	1.1±0
	TMP-LG	690	470	1200	465	47±1	11±7	6±4	1±0.1
	IA-G	--	465	125	--	50	5	8	1.1

Legend: T_{AC} = accelerated cooling start temperature; T_C = coiling temperature; t_c = coiling time; T_G = galvanising temperature; VF = volume fraction; GS = grain size; C = carbon content; YS = 0.2% proof stress; UTS = ultimate tensile strength; UE = uniform elongation; TE = total elongation. The volume fraction and grain size of PF was measured using optical microscopy while the volume fraction of RA and carbon content in RA was measured using XRD as described in section 3.4.1 and 3.5.

4.1.2 Mechanical properties

After the TMP-S treatment both steels exhibited continuous yielding and smooth work hardening curves (Figs. 4.5a-d), the base steel recorded yield and ultimate tensile (UTS) strengths of 491±35 MPa and 745±6 MPa, respectively, while the Nb-Ti steel returned a YS = 474 MPa and a UTS =782 MPa. The uniform (UE) and total (TE) elongations in both steels were similar at ~20% and 29%, respectively. As Fig. 4.5e shows, the TMP-S base steel reached a maximum n-value of 0.19 at a higher strain of ~0.06, fluctuated around this value until ~0.14 strain and then decreased slightly to n ~ 0.18 at 0.17 strain. In the TMP-S Ni-Ti steel (Fig. 4.5f), a maximum n-value of ~0.24 was reached at a higher strain of ~0.1 and remained steady until it decreased slightly to n ~ 0.22 at 0.15 strain, followed by a further decrease to n ~0.18 at 0.18 strain.

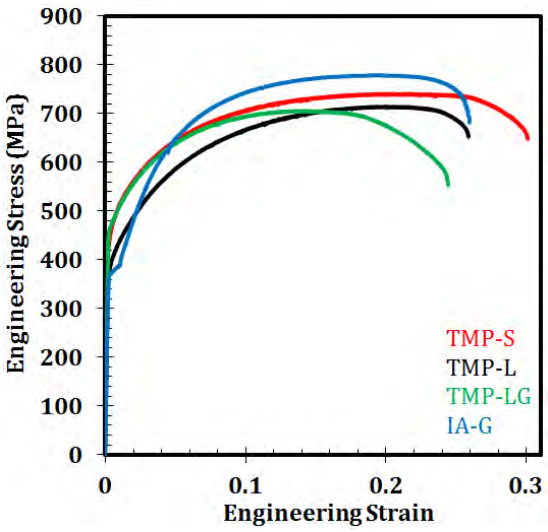

(a)

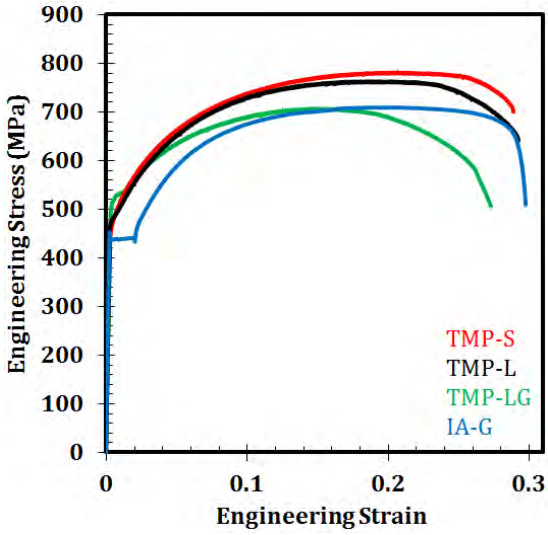

(b)

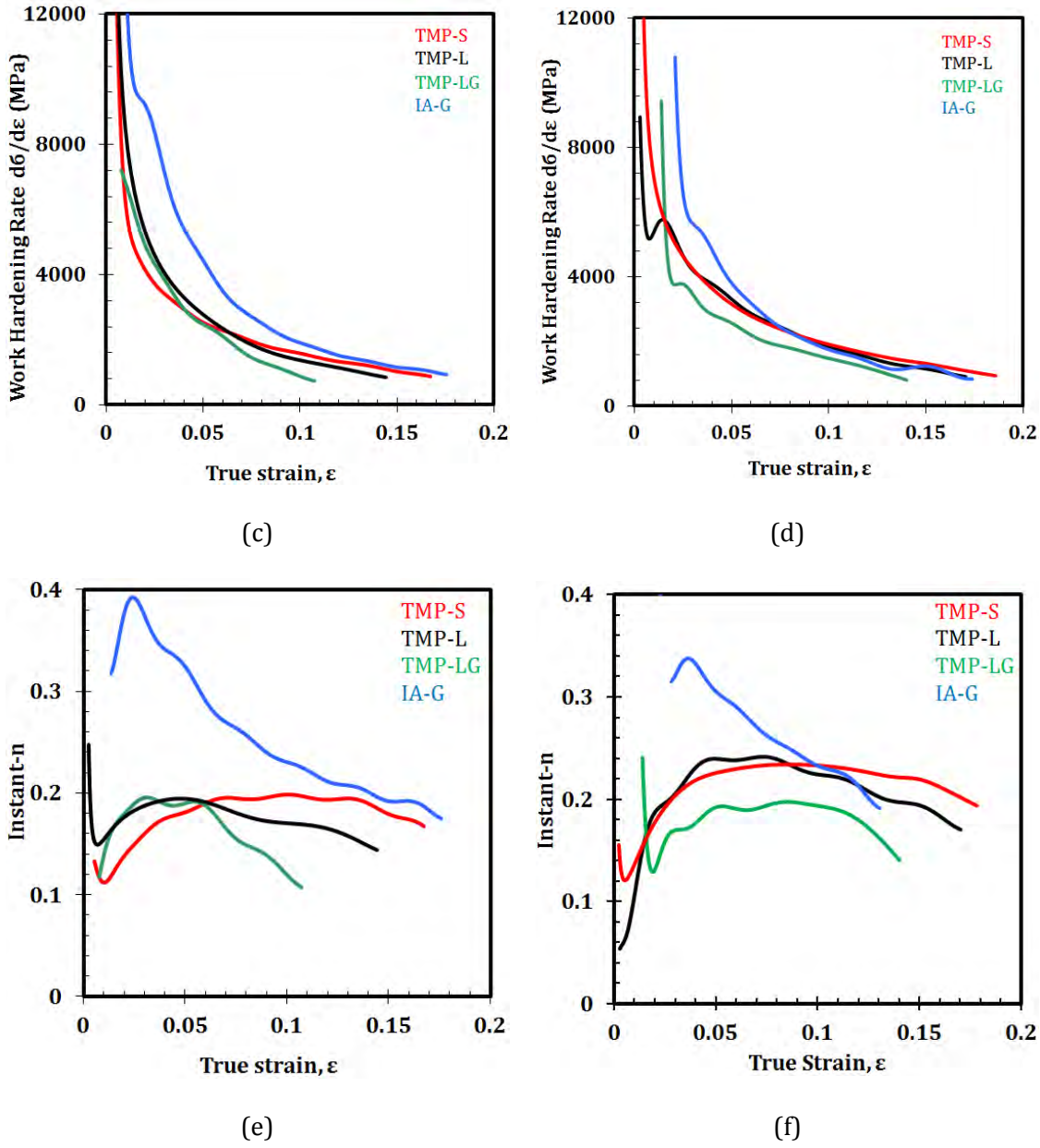

Figure 4.5: The variation in (a, b) the engineering stress versus strain, (c, d) the work hardening rate versus true strain and, (e, f) the instantaneous n-value versus true strain in the (a, c, e) base and (b, d, f) Nb-Ti steels.

The representative stress-strain, work hardening, and instant-n curves are shown in Fig. 4.5 while the average data is given in Table 4.2. After the TMP-L treatment, the average yield (YS) and ultimate tensile (UTS) strengths were 445±44 MPa and 722±34 MPa for the base steel and 476±7 MPa and 749±20 MPa for the Nb-Ti steel, respectively. The uniform and total elongations were 15% and 25% for the base steel and 18% and 29% for the Nb-Ti steel, respectively. The base steel exhibited continuous yielding behavior which

returned a smooth work hardening curve and instantaneous n-values with a maximum of 0.2 at 0.05 strain followed by a gradual decrease to 0.15 at ~0.15 strain. On the other hand, the TMP-L Nb-Ti steel showed slight discontinuous yielding such that the work hardening curve declined steeply up to 0.01 strains with a local maxima at 0.02 strain. The n-value reached a maximum of 0.24 between strains of 0.05-0.08 followed by a gradual decrease to n ~ 0.18 at 0.17 strains.

Table 4.2: A summary of the mechanical properties of the base and Nb-Ti steel.

Steel	**Schedule**	**Mechanical properties**			
		YS MPa	UTS MPa	UE %	TE %
Base	TMP-S	491±35	745±6	20±3	29±2
	TMP-L	445±44	722±34	15±0	25±4
	TMP-LG	476±6	699±9	12±2	24±1
	IA-G	360	787	19	26
Nb-Ti	TMP-S	474±23	782±38	20±2	29±3
	TMP-L	476±7	749±20	18±0	29±0
	TMP-LG	499±6	685±32	13±2	26±2
	IA-G	438	710	20	30

Legend: YS = 0.2% proof stress; UTS = ultimate tensile strength; UE = uniform elongation; TE = total elongation.

In the short (TMP-S) and long (TMP-L) coiling time schedules, the parameters for austenisation and the formation of PF were kept constant, which resulted in the formation of approximately similar (50%) volume fractions of PF. The isothermal bainite transformation temperature (= the coiling temperature, T_C) during simulated coiling was

also kept similar (465-470 °C) such that only the coiling time (t_c) was varied between 125 s and 1200 s in the case of TMP-S and TMP-L, respectively.

These variations in the coiling time had a pronounced effect on the microstructure and mechanical properties of the two steels (Tables 4.1 and 4.2); for instance the YS of the base steel decreased with longer coiling time while the UTS values decreased with an increasing coiling time in both steels. With respect to ductility, both steels recorded a decrease in their UE and TE values with higher coiling times. In this case, the base steel was affected more severely by longer coiling times which resulted in even smaller ductility values. It is clear from this that longer coiling times led to an overall deterioration of the strength-ductility balance in both steels.

Although the PF grain size in the base steel after TMP-S could be regarded as only slightly coarser (12 ± 8 μm) than the Nb-Ti steel (10 ± 6μm), the YS of the base steel after TMP-S was higher compared to the Nb-Ti steel. This disparity could be related to the complexity of the microstructure in our multiphase steel and the dominant effect of other microstructural parameters such as the morphology of the bainite. The base steel consisted predominantly of fine 0.35 μm sized plates of granular bainite (GB), whereas the Nb-Ti steel mostly consisted of coarse 0.81 μm sized bainitic ferrite (BF) laths. It is therefore entirely plausible that this variation in the dislocation mean free path between GB and BF was primarily responsible for the differences in the macroscopic mechanical properties of the two steels after TMP-S treatment. Generally speaking, the combination of strength and elongation after the TMP-S and TMP-L schedules was slightly better in the Nb-Ti steel than the base steel. This was ascribed to the finer microstructure of the Nb-Ti steel and the additional solid solution and/or precipitation strengthening via alloying with Nb and Ti. While the above is in agreement with previous reports for high Si, Nb-containing steels [140], other variations between the two steels are detailed below.

During the longer coiling times, the formation of bainite was accompanied by a carbon enrichment of the RA located in-between the bainitic ferrite laths or plates. If the transformation of bainite is completed with the steel remaining at a high temperature, the next stage of phase transformation can be initiated wherein: (i) the carbon-enriched austenite begins to decompose with the formation of the ferrite phase and carbides, and, (ii) in the remaining BF which is supersaturated with carbon, the segregation of carbon to dislocations and/or the formation of fine carbides takes place. These latter observations were noted previously during the bake hardening of high-Si TRIP steels [141].

It is clear that the transformation of bainite was completed sometime between 125 s and 1200 s in the base steel, whereas this amount of transformation time was insufficient for

the Nb-Ti steel. This was ascertained by the fact that the volume fraction of the RA decreased between the TMP-S and TMP-L treatments in the base steel whereas it continued to increase in the Nb-Ti steel (Table 4.1). Specifically to Nb-Ti steel, the significance of the interaction between the other phases in dictating the overall mechanical response is also highlighted here. The increase in the volume fraction of RA helped the Nb-Ti steel to maintain its YS and TE levels while reducing the rate of decrease in the UTS and UE values after the TMP-S and TMP-L schedules.

However, the effect of a nearly doubled volume fraction of the RA phase content after the TMP-L schedules in the Nb-Ti steel underlines the more crucial effect of the alloying elements on the kinetics of the bainitic transformation. In the presence of Nb, the bainitic transformation was more sluggish as the prior austenite grain size was reduced [142] which resulted in a low volume fraction of stable austenite; *i.e.*- a higher volume fraction of untransformed austenite with lower chemical stability such that it readily transforms to martensite upon tensile deformation.

4.2 The Effect of Galvanising after the Long Coiling Time on the Microstructure and Mechanical Properties

4.2.1 Microstructure

Figures 4.1e, 4.1f, 4.2e and 4.2f show the microstructure of the samples after the galvanising TMP-LG schedule. In the base and Nb-Ti steels, colour etching returned more martensite (black areas) and a small number of white grains of the RA phase. These results were confirmed via XRD which also showed that the volume fraction of RA had decreased from 4±1% and 13±0% after TMP-L to 2±1% and 6±4% after TMP-LG in the base and Nb-Ti steels, respectively (Table 4.1). In addition to (Ti,Nb)(C,N) and Nb(C,N) particles observed in the TMP-L Nb-Ti steel, the formation of Fe_3C particles (Figs. 4.4h, 4.4i) was detected in this steel after galvanising (TMP-LG).

4.2.2 Mechanical properties

The tensile test results (Figs. 4.5a and b) showed that the base steel underwent continuous yielding whereas the Nb-Ti steel depicted Lüders banding. Compared to the TMP-L samples, the TMP-LG samples recorded an increase in the YS of both steels (from 445±44 to 476±6 MPa for the base steel and from 476±7 to 499±6 MPa for Nb-Ti steel) while the UTS had reduced from 722±34 to 699±9 MPa in the base steel and from 749±20 to 685±32

MPa in the Nb-Ti steel. Correspondingly, the uniform and total elongations in both steels had also reduced from 15-18% and 25-29% after TMP-L to 12-13% and 24-26% after TMP-G treatment, respectively.

The work hardening and instantaneous n-value curves (Figs. 4.5c-4.5f) show marked differences between the TMP-L and the TMP-LG schedules. In the TMP-LG base steel, the n-value declined from a strain of ~0.06 at a faster rate and reached its lowest value of 0.11 at ~0.11 strain. In the TMP-LG Nb-Ti steel, the n-value fluctuated around the maximum n-value of ~0.195 between strains of 0.05-0.12. Overall, the n-curve for the Nb-Ti steel after TMP-LG recorded its lowest values compared to all the other schedules.

During the TMP-LG industrial galvanising schedule, a further decomposition of the RA takes place; as evidenced by the low volume fractions of RA in both steels (Table 4.1). While both steels recorded increases in their yield strength between the TMP-L and TMP-LG conditions, the UTS, UE, and TE values were reduced. Since a larger volume fraction of RA pre-existed in the TMP-L Nb-Ti steel, the degradation in its mechanical properties after the TMP-LG schedule was more severe than in the base steel. In addition, while carbon segregates to dislocations and grain boundaries, it also formed carbides in the PF and BF phases after TMP-L and TMP-LG treatment (Figs. 4.4b-4.4h). In particular, carbon segregation could take place in the areas of high dislocation density surrounding the martensite crystals that are newly formed upon quenching from the coiling temperature [141]. The small amount of martensite formed on cooling will also undergo a typical tempering process; with the formation of intermediate carbides or cementite during the TMP-LG schedule [143, 144]. Thus, all these changes will contribute to the interaction of dislocations with carbon atoms and with precipitates during tensile testing such that they will result in an increase in YS and a reduction in ductility values.

An important difference in the stress-strain curves between the base and Nb-Ti steels is that the former showed continuous yielding up to the TMP-LG schedule (Fig. 4.5a) whereas the latter experienced discontinuous yielding after the TMP-L and TMP-LG treatments (Fig. 4.5b). Similar strain hardening behaviour occurred for dual-phase and IA TRIP steels after pre-straining and bake hardening [140, 145]. Discontinuous yielding via Lüders banding is typical evidence of dislocations locking either by Cottrell atmospheres and/or by fine precipitates and their subsequent unlocking, or the formation of new mobile dislocations [130]. However, after TMP-LG treatment the yield point phenomena became more pronounced because carbon atoms had more time to segregate to dislocations and form Cottrell atmospheres.

As reported previously, new dislocations were generated in the ferrite phase either: (i) upon cooling after isothermal holding at 470 °C due to the volume change associated with the phase transformation of the unstable austenite to martensite or, (ii) during tensile testing when there were soft ferrite regions adjacent to hard martensite or austenite crystals [141, 145]. Since the Nb-Ti steel consistently returned higher volume fractions of RA than the base steel for corresponding conditions (Table 4.1), it could be expected that a higher number of mobile dislocations was generated in this steel as a result of the transformation from austenite to martensite during straining. This could be one of the contributing factors to the pronounced yield point phenomena observed in the Nb-Ti steel after TMP-L and TMP-LG processing.

In addition, the difference in the yielding behaviors between the base and Nb-Ti steel can be further explained by considering the interaction of carbon with dislocations and the ability of the Nb, Ti and Fe atoms to form carbides. In the base steel, the interaction of carbon atoms with dislocations would be preferred mechanism as the binding energy between dislocations and carbon was 0.75 eV; which in turn was higher than the 0.5 eV binding energy between the Fe and C atoms to form Fe_3C [146]. On the other hand, and to serve as an example, the binding energy between the Nb and C atoms to form NbC was 2.3 eV [140], so it could be speculated that the amount of C available in the base steel was enough to form saturated Cottrell atmospheres at dislocations. Contrarily, some of the carbon in the Nb-Ti steel would be used up to form Nb-Ti carbides which would lead to much weaker Cottrell atmospheres forming that are more easily unlocked on loading.

The appearance of Lüders strain in IA TRIP steels was previously attributed to the localisation of deformation and the static strain ageing in the ferrite phase [11, 147]. Thus, in the case of Nb-Ti steel, it can also be said that the discontinuous yielding behavior is the combined effect of the finer ferrite grain size (leading to a localisation of the deformation within this phase) [148] and the ageing that occurs during the TMP-LG schedule.

To this end the work hardening behavior of the steels was analysed using the modified C-J analysis [149, 150]. The representative $\ln(d\sigma/d\varepsilon)$ versus $\ln(\sigma)$ plots are shown in Fig. 4.6 with the results from fitting presented in Table 4.3. Since the modified C-J analysis was unable to fit the flow curve over the entire uniform strain range region, the work hardening curves were divided into a maximum of three stages and different m-values were determined for each work hardening stage (Fig. 4.6).

If Figure 4.6 is used as a representative example, the behaviour of the Nb-Ti steel during each of the three stages is seen to vary rather significantly after the TMP-S (Fig. 4.6a) and TMP-L (Fig. 4.6b) schedules. This can be ascribed to the amount and the morphology of

phase constituents; which in turn, control the behaviour during the various stages of work hardening. During Stage 1, the deformation of the soft ferrite phase leads to an accumulation of mobile dislocations in the regions near the interface between the ferrite and the harder phases such as RA and martensite. In Stage 2, the RA transforms to martensite due to the accumulation of strain energy in the RA phase. During Stage 3, the deformation of ferrite and martensite continues while the work hardening rate continuously decreases.

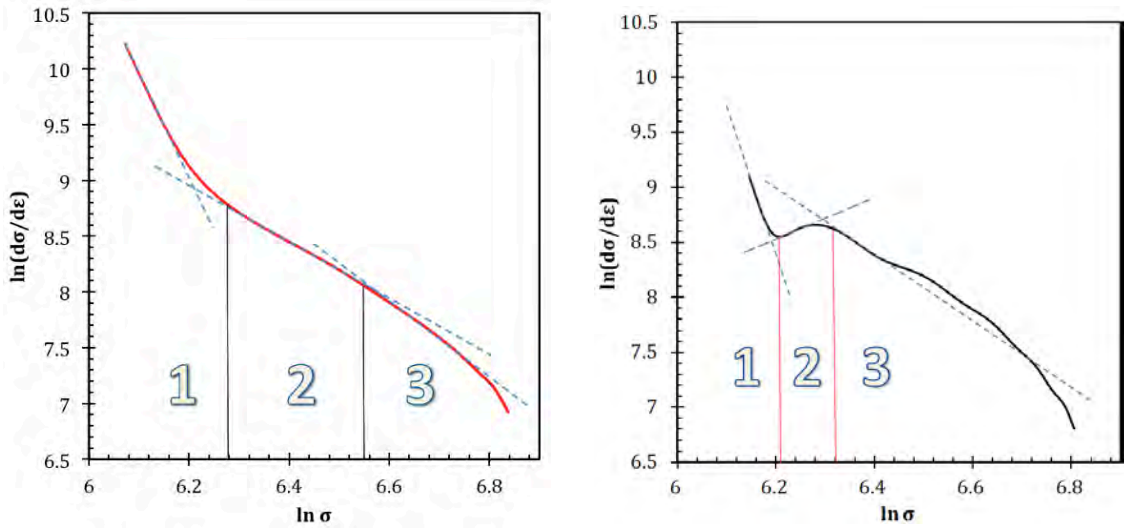

(a) (b)

Figure 4.6: Representative work hardening behaviours shown using examples of Nb-Ti steel after (a) TMP-S and (b) TMP-L schedules. Based on the modified C-J analysis, three distinct stages of work hardening can be seen.

Table 4.3: Comparison of the modified Crussard–Jaoul (C-J) analysis with the experimental results at the different stages of work hardening in the base and Nb-Ti steels.

Steel	**Schedule**	**Modified C-J**			**Experimental**
		Stage 1	Stage 2	Stage 3	
		m_1*	m_2	m_3	m†
Base	TMP-S	7.66	4.05	4.91	6.18
	TMP-L	12.96	2.87	4.18	7.05
	TMP-LG	7.25	3.89	6.47	10.03
	IA-G	1.99	1.41	5.02	6.06
Nb-Ti	TMP-S	10.20	3.53	4.11	5.46
	TMP-L	13.69	-0.98	4.03	5.97
	TMP-LG	21.25	0.66	4.95	7.91
	IA-G	8.48	2.05	5.42	6.09

*1-$m_{1\text{-}3}$ = slopes at Stages 1 to 3

†$m = 1/(\varepsilon_u\text{-}\varepsilon_y)$; where ε_u = maximum uniform true strain, ε_y = strain at 0.2% offset proof stress or the strain where Lüders banding is completed.

In Stage 1 the rate of dislocation accumulation was strongly linked to the ferrite grain size where the influence of the finer ferrite grain size led to the smallest m_1 –values being recorded after the IA-G schedule in both steels. Previous reports have also claimed that high m_1 -values were related to the larger volume fraction of martensite present in the initial microstructure [150]. However, the influence of this factor is not clear from the present study because the highest m_1 -values were returned after the TMP-L and TMP-LG schedules for the base and Nb-Ti steels, respectively (Table 4.3).

The behaviour in Stage 2 was similar to dual phase steels [137] that were returned after the TMP-S, TMP-L and TMP-LG schedules in the base steel and after the TMP-S schedule in the Nb-Ti steel (Fig. 4.6a). Alternatively, and as depicted in Fig. 4.6b, the behaviour in Stage 2 that was typically associated with the TRIP effect was noted after the TMP-L and TMP-LG treatments in the Nb-Ti steel. During Stage 2 an accumulation of strain energy in the RA phase occurred several times over and resulted in a gradual transformation of the RA to martensite, and in turn, the phase transformation increased the work hardening rate (leading to a slope change) by inhibiting the dislocation glide process. Consequently, the differences in the behaviour and slope of Stage 2 hardening in the studied steels could be explained by the rate the RA transformed during uniform straining. This above phenomenon has previously been proven by observing areas of high dislocation density surrounding the newly formed martensite crystals [141].

The differences in the shape of the strain hardening exponent curves over the period of uniform elongation allude to variations in the rate of strain-induced austenite transformation (Figs. 4.5e, 4.5f). In general, more gradual increases and sustained n-values are correlated with a slower transformation of RA to martensite over longer strain ranges such that the TRIP effect then tends to contribute more significantly towards extending the overall ductility of the steel. The stability of RA during uniaxial tensile testing of the base and Nb-Ti steels after TMP-L processing was investigated in detail in the Chapter 5, and some results were published in the Ref. [64]. In that study, Electron Back-Scattering Diffraction was used to track the changes in the area fraction of the RA up to the UTS value, and while the base steel recorded a more gradual change in the area fraction of RA from 5% (initial, $\varepsilon = 0\%$) to 1.2% (at UTS, $\varepsilon = 15\%$), the Nb-Ti steel exhibited a more rapid transformation of the RA fraction from 9.4% (initial, $\varepsilon = 0\%$) to 1.4% (at UTS, $\varepsilon = 18\%$).

To this end the following examples highlight the importance of the volume fraction and the carbon content of the RA phase in dictating the overall shape of the strain hardening exponent curves of both steels. In the base steel, the gradual transformation of the highest

amount of RA with the highest carbon content after the TMP-S schedule was responsible for the behaviour of the n-value and a good combination of strength and ductility. With the Nb-Ti steel, the most gradual transformation of RA during tensile straining was obtained after the TMP-S schedule. This could be due to the carbon content of the RA after TMP-S being slightly higher than that obtained after the TMP-L schedule when the highest volume fraction of the RA was returned. Since the volume fraction and carbon content (chemical stability) of the RA were the lowest after the TMP-LG treatment, both steels presented sharp rises in the strain hardening exponent which in turn was correlated to the rapid transformation of RA to martensite during the early stages of straining. It should be noted that while the chemical stability was used to explain the overall stability of RA, the difference in the carbon content after TMP-S and TMP-L was insignificant. Thus, the overall stability of RA could also be affected by other parameters such as the mechanical stability of RA.

4.3 The Effect of Intercritical Annealing on the Microstructure and Mechanical Properties

4.3.1 Microstructure

The secondary electron images of the microstructures after TMP-S and IA-G are shown in Figs. 4.7a and 4.7c for the base steels and in Figs. 4.7b and 4.7d for the Nb-Ti steels, respectively. It is obvious that the two processing techniques resulted in completely different microstructures. While the images recorded similar volume fractions of PF for both steels, the PF grain size after TMP-S was approximately twice that after the IA-G schedule (Table 4.1). After TMP-S, austenite, bainite, and martensite phases existed within banded areas, whereas after the IA-G treatment the same phases were equiaxed and interspersed between the PF grains. Compared to the TMP-S condition, both steels after IA-G possessed slightly larger volume fractions of RA with a lower carbon content.

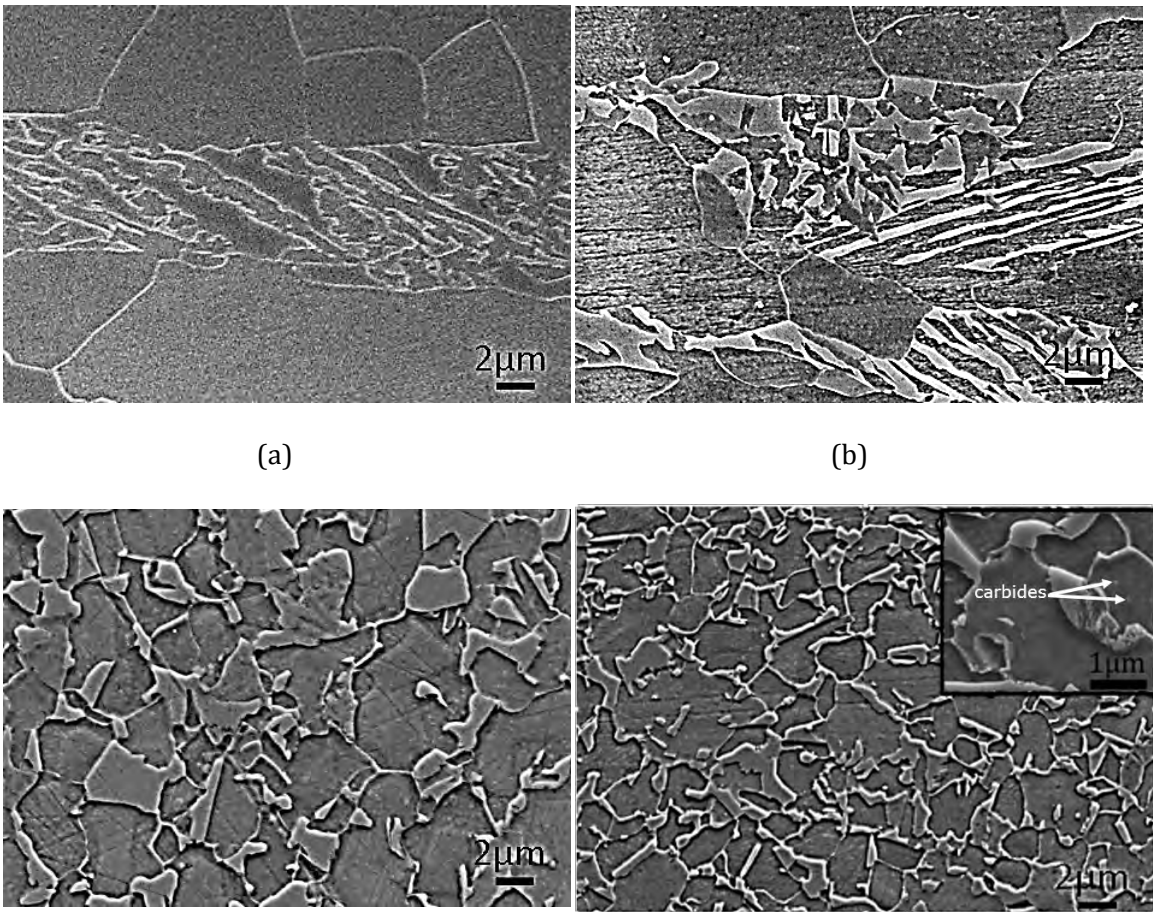

Figure 4.7: Representative secondary electron micrographs after (a, b) TMP-S and (c, d) IA-G processing of the (a, c) base and (b, d) Nb-Ti steels. In (d), the inset shows the initial decomposition of the RA phase. Figures c and d are courtesy of Prof. B.C. de Cooman, POSTECH.

Although both steels in the TMP-S and IA-G conditions contained ~50% PF in the microstructure, the morphology and distribution of the phases varied significantly. For instance, during TMP-S treatment the formation of the PF grains takes place predominantly at the boundaries of the elongated prior austenite grains upon cooling at 1 Ks^{-1} such that the process was interrupted when cooling was further accelerated to 20 Ks^{-1}. As a direct result of the accelerated cooling, the bainite transformation then occurs in-between the rows of the PF grains during the isothermal holding step (T_C = 465 °C for t_c = 125 s and/or 1200 s). Consequently, the majority of the RA and martensite crystals are located within the bainite regions. Due to such clearly developed directionality in the

microstructure, significant anisotropy in the mechanical properties could be expected between the longitudinal and transverse directions of the TMP samples.

Alternatively, the microstructure in the IA-G steels first developed as a reverse transformation of the cold rolled microstructure into a mixture of austenite and ferrite, such that the subsequent formation of bainite occurred during isothermal holding. This resulted in a more homogeneous distribution of equiaxed PF grains and bainitic areas.

4.3.2 Mechanical properties

Due to the rather significant variation in the tensile sample geometries of the TMP and IA-G samples, a comparison of their mechanical properties is limited to only discussing their overall trends in terms of yielding (continuous versus discontinuous) and work hardening behaviour.

The tensile curves after the IA-G schedules recorded discontinuous yielding in both steels (Figs. 4.5a and 4.5b), whereas compared to the TMP-S condition, the YS after IA-G was ~131 and ~36 MPa lower in the base and Nb-Ti steels, respectively (Table 4.1). In contrast, if the UTS values after the two schedules are compared, the values are ~42 MPa higher in the base steel and ~72 MPa lower in the Nb-Ti steel. In the IA-G samples, a visible change in the gradient of the work hardening curves occurred at ~0.016 strain for the base steel and ~0.03 strain for the Nb-Ti steel (Figs. 4.5c, 4.5d). Unlike all the other conditions, a further change in the work hardening rate occurred at strains of ~0.14 and ~0.153 in the Nb-Ti IA-G steel. In both steels, the shape of the instantaneous n-value curve was very different after the IA-G schedules (Figs. 4.5e, 4.5f). A rather narrow peak with maximum n-values of ~0.39 and ~0.34 at 0.03 and 0.035 strains was followed by sharp declines to ~0.175 and ~0.19 at 0.175 and 0.13 strains for the base and Nb-Ti steels, respectively.

The main distinctive feature of the IA-G stress-strain curves of both steels is the rather pronounced yield point elongation and a continuous reduction in the n-value with greater tensile strain. These results are similar to the behaviour of tempered dual-phase steels [106] and of C-Mn-Si steels subjected to quenching and partitioning treatment [151]. The yield point phenomenon indicated that during IA-G treatment, some dislocation pinning by carbon atoms occurred in the ferrite phase and based on SEM observations, small carbide particles were also present in the areas of decomposed austenite (Fig. 4.7d inset). As discussed previously, the finer ferrite grain size combined with the ageing processes that occurred during the IA-G schedule [11, 148] could have caused the pronounced Lüders strain and increase in Lüders elongation.

In both IA-G steels, the work hardening behaviour during Stage 2 was similar to the TRIP steels (Fig. 4.6b), whereas in the TMP-S steels it was similar to one of the dual-phase steels (Fig. 4.6a), On the other hand, the presence of a single maximum n-value early in the tensile test in both IA-G steels indicated that a large amount of the RA transformed to martensite upon initial straining. This can be correlated to the fact that the RA was less stable in the IA-G steels compared to the TMP-S steels. This lower stability could be due to several factors among which a slightly lower carbon content of RA in IA-G steels and also the presence of refined and rigid bainite plates which could assist in an earlier load transfer and the transformation to martensite of adjacent RA layers [152].

4.4 Conclusions

The microstructure-property relationships in a base low Si, high Al TRIP steel and one with 0.03Nb and 0.02Ti (wt.%) additions were analysed after different thermo-mechanical processing schedules such that:

1. Thermo-mechanical processing of the base steel with a short coiling time of 125 s at 470°C resulted in the highest amount of the retained austenite phase and the best combination of mechanical strength and elongation. All thermo-mechanically processed base steel samples recorded continuous yielding behaviour.
2. The addition of Nb and Ti slightly refined the final microstructure of the steel after thermo-mechanical processing but led to an increase in the time required for the development of a high volume fraction of the stable retained austenite phase. Compared to the base steel, the strength-ductility balance in the Nb-Ti steel improved slightly due to a combination of microstructure refinement and a higher volume fraction of RA and precipitation strengthening. The Nb-Ti steel exhibited discontinuous yielding behaviour after thermo-mechanical processing when a long coiling time of 1200 s was undertaken.
3. The intercritically annealed samples of the base and Nb-Ti steels showed discontinuous yielding with long Lüders elongation. A steep reduction in the instantaneous n-value from its maximum at a small value of tensile strain was noted. This was explained by the refinement of the polygonal ferrite grains and the ageing processes that occurred during galvanising.
4. The modified C-J analysis showed three stages of work hardening in the studied steels. However, the Stage 2 behaviour was found to differ with the adopted processing schedule and was associated with the different rates of RA transformation.

5 EBSD CHARACTERISATION OF MICROSTRUCTURE IN TRIP STEELS

In this chapter a microanalysis was applied to the same samples that were investigated in Chapter 4, utilising the power of electron back-scattering diffraction (EBSD). This analysis provides more important information about the investigated materials. The EBSD can easily detect the retained austenite (RA) phase in the microstructure using its unique crystallographic structure information and can therefore distinguish between the retained austenite grains and the other phases. However, other phases such as ferrite, bainite, and martensite were indexed with the same crystal structure and were not automatically separated out during the EBSD map acquisition, therefore further analysis of such multiphase microstructures containing various ferrite morphologies must begin with a method that accurately distinguishes between all the constituent phases. The techniques available in the literature were unable to separate between the phases in the samples of the current study, therefore a new method was developed and successfully applied in both thermo-mechanically processed TRIP steels (base and Nb-Ti steels). This newly developed technique consistently distinguished between polygonal ferrite (PF), bainitic ferrite (BF), granular bainite (GB), and martensite (M) based on multi-condition criteria, and only using EBSD data.

In the second section of this chapter, the orientation data of separated phases was used to investigate the effect of the tensile strain on each of them after tensile deformation. It is well known that the transformation of retained austenite to martensite during loading leads to better combinations of strength and ductility. In this regard, moderately stable retained austenite is desirable for an effective TRIP effect whereas highly stable or unstable retained austenite does not contribute to an improvement in the mechanical properties. Therefore, it is important to understand all the factors influencing the stability of retained austenite, such as its grain size, morphology, and area fraction. Moreover, other phases adjacent to the retained austenite are also important in terms of defining the overall stability of retained austenite.

In this study the effect of strain on the stability of retained austenite was investigated using EBSD and uniaxial tensile testing. The EBSD analysis followed the changes in the

microstructure (with attention to the transformation of retained austenite in particular), as a function of applied strain and linked this behaviour with the mechanical properties presented in the previous sections of Chapter 4. This chapter is divided into two main sections: (i) phase/ferrite morphology segmentation, and (ii) the effect of strain on the stability of retained austenite. The analysis of EBSD data was based on the phase/ferrite morphology segmentation methodology developed in Section 5.1. The effect of the area fraction, grain size and morphology of each phase/ferrite morphology on the retained austenite stability is discussed thereafter in Section 5.2.

5.1 Phase/Ferrite Morphology Segmentation

As with Chapter 4, the base and Nb-Ti steels (after TMP-L) were used to obtain EBSD data. These steels were examined after three strain states, after TMP (zero tensile strain), at UTS, and at fracture. The raw EBSD data recorded only two phases in the microstructure, fcc austenite and bcc ferrite, and some non-indexed areas. In this study, four phases were distinguished via the developed procedure, which is mainly based on the internal average misorientation (GOS) and the grain size criterion. The threshold value used in this study was based on evaluating the slope of the normalised cumulative distribution with respect to the origin [153], so the threshold value was selected when the change in the slope with respect to the origin tended to 1. This thresholding technique was applied on both the internal average misorientation (GOS) and grain size criteria.

Figs. 5.1a and b show the map of the two chemistries before segmentation while Figs. 5.1c and d show all four phases for the base and Nb-Ti steels after segmentation in their TMP state. Although the segmentation procedure was applied successfully in the analysis of six EBSD maps at TMP (zero tensile strain), UTS and fracture for the base and Nb-Ti steels, the following section only details the segmentation procedure on the Nb-Ti steel in its TMP state before tensile testing (zero tensile strain) as a representative example.

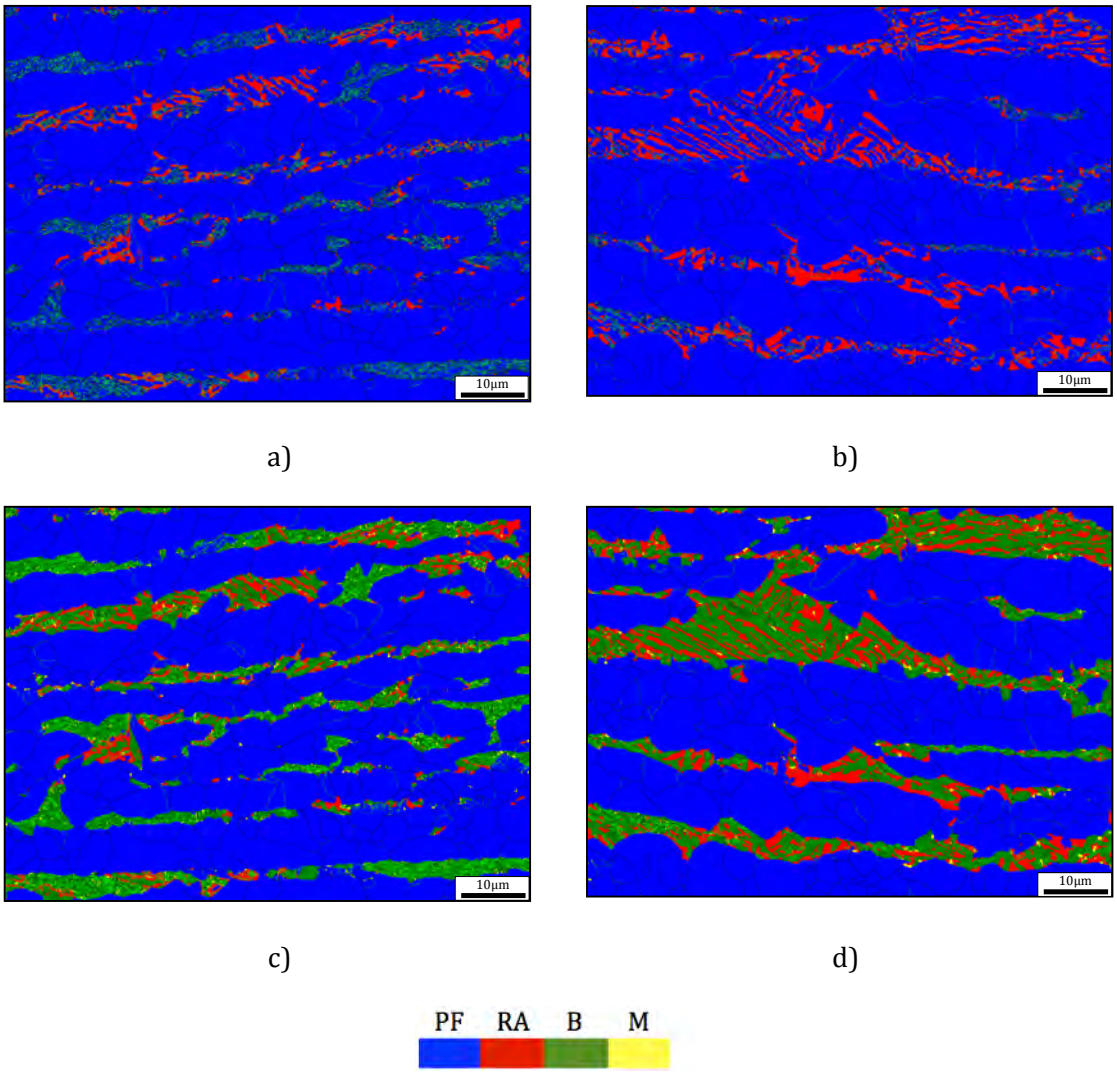

Figure 5.1: EBSD maps before and after segmentation. a) base TRIP steel before segmentation, b) Nb-Ti TRIP steel before segmentation, c) base TRIP steel after segmentation, d) Nb-Ti TRIP steel after segmentation.

Preliminary processing of the map involved cleaning the map by removing wild orientation spikes followed by extrapolating up to 6 neighbours to fill-in non-indexed areas that tended to concentrate at the grain boundaries. Based on the grain shape criterion, the negative slopes of the major axis of the fitted equivalent circle ellipsoid were removed. Throughout this cleaning procedure, the minimum misorientation for grain reconstruction was 2° and the grain boundary completion angle was 2°.

The original map acquired from EBSD only consisted of the fcc and bcc phases (Fig. 5.2 a), so the procedure developed for segmenting the map began by creating a subset for the bcc ferrite phase (Fig. 5.2 b). In the following paragraphs, only pixels belonging to this bcc ferrite subset were used for phase/morphology segmentation.

The procedure consists of two main steps; step one is to separate the martensite from other phases by applying the internal average misorientation criterion (GOS criterion) to the bcc subset. Based on the threshold value on the normalised cumulative distribution of the internal average misorientation, which was estimated to be 1.00° (Fig. 5.2c), the main bcc subset was divided into two subsets:

- The first subset consisted of a combination of martensite and polygonal ferrite (Fig. 5.2d) and
- The second subset consisted of ferrite in bainite (hereafter referred to as bainite) and polygonal ferrite (Fig. 5.2e).

At this stage, both subsets contained pixels belonging to polygonal ferrite (Figs. 5.2d and e), so the following steps were undertaken to subtract the polygonal ferrite from both subsets.

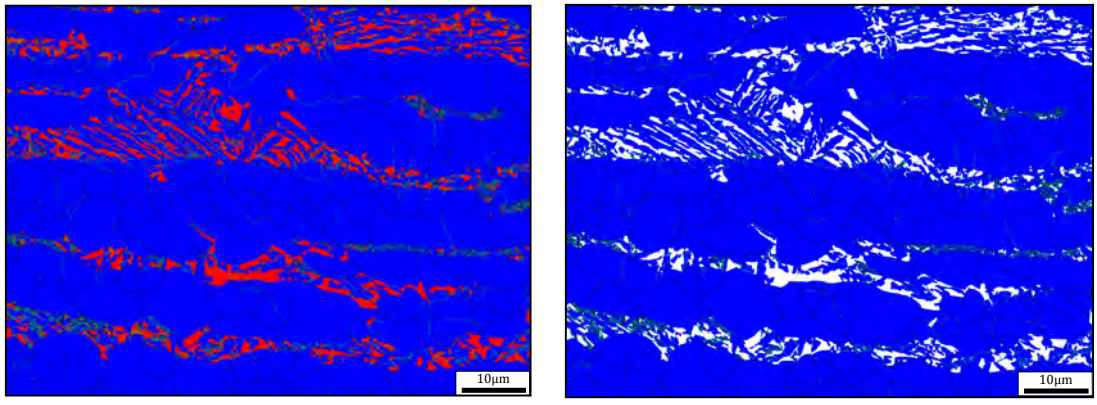

a) b)

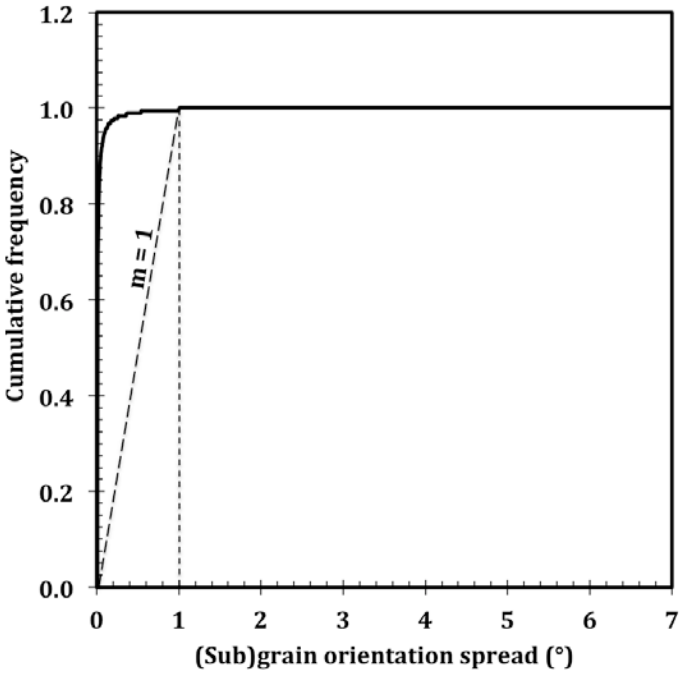

c)

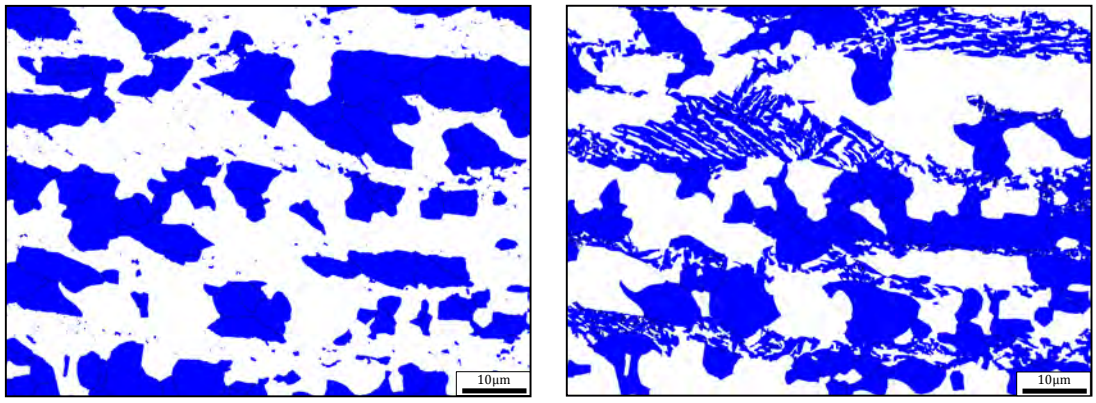

d) e)

Figure 5.2: EBSD map of Nb-Ti steel a) fcc and bcc phases, b) only bcc phase, c) the normalised cumulative distribution of the internal average misorientation indicating the threshold value used for segmentation, d) a map comprising only martensite and polygonal ferrite and e) a map comprising only ferrite in bainite and polygonal ferrite as a result of the first segmentation stage.

In stage two of the segmentation procedure, a grain size criterion was applied on the first subset (Fig. 5.2d) to separate the polygonal ferrite from martensite. Figure 5.3a shows that the normalised cumulative distribution of the grain size of the subset only contained martensite and polygonal ferrite where a thresholding value of 0.8 µm was used (based on evaluating the slope of the normalised cumulative distribution of the grain size) to

distinguish between martensite and polygonal ferrite. Accordingly, the martensite was identified with a grain size of less than 0.8 μm, while the polygonal ferrite was identified based on a grain size of more than 0.8 μm. This step resulted in two subsets:

- The first subset only contained martensite (Fig. 5.3b)
- The second subset contained the first fraction of polygonal ferrite (Fig. 5.3c).

Following this, the second fraction of polygonal ferrite was separated from ferrite in bainite (Fig. 5.2e).

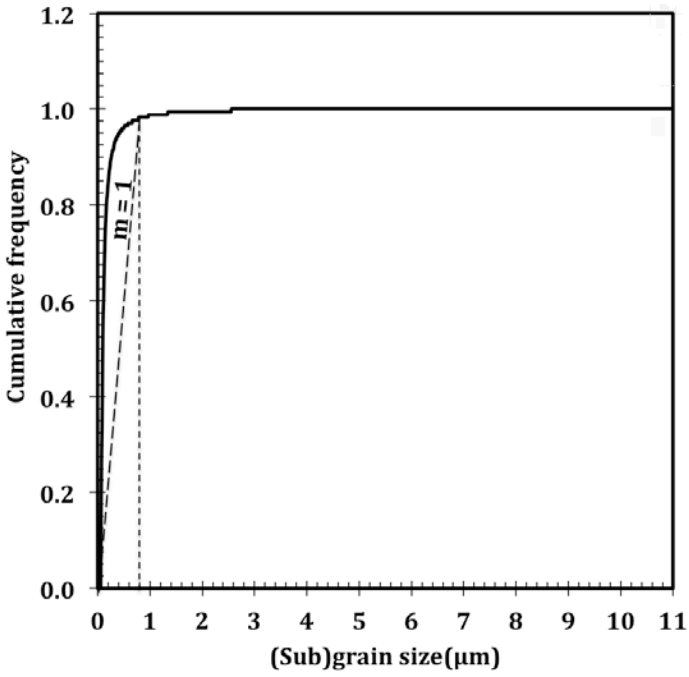

a)

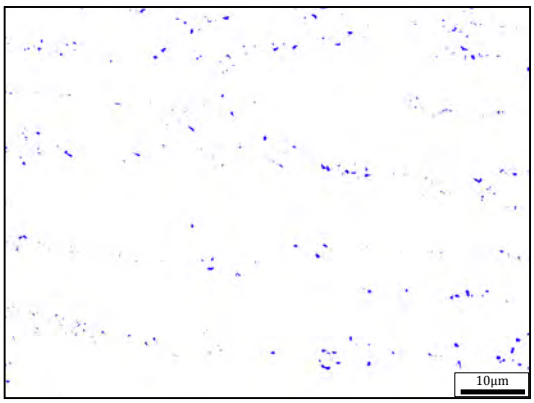

b)

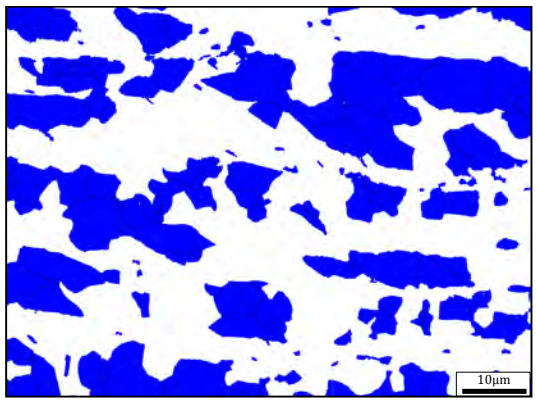

c)

Figure 5.3: a) Grain size frequency curve, b) martensite results from grain size less than 0.8 μm and c) polygonal ferrite results from grain size above 0.8 microns.

The subset containing a combination of polygonal ferrite and ferrite in bainite (Fig. 5.2e) was separated based on the fact that the fraction of the low angle boundaries in the bainite were higher than polygonal ferrite with most of these boundaries comprising misorientation angles of less than 2°. Therefore, the grain size criterion with a 2° critical boundary misorientation was unable to distinguish between the two phases, as shown in Figs. 5.4a. For the purpose of separating bainite from polygonal ferrite, the critical misorientation angle of the subgrain boundaries were reduced to 0.5° and the critical subgrain boundary completion angles were reduced to 0.1°. Figure 5.4b shows how ferrite in bainite becomes automatically distinguishable (blue colour) after reducing the critical misorientation to identify subgrain boundaries to 0.5°.

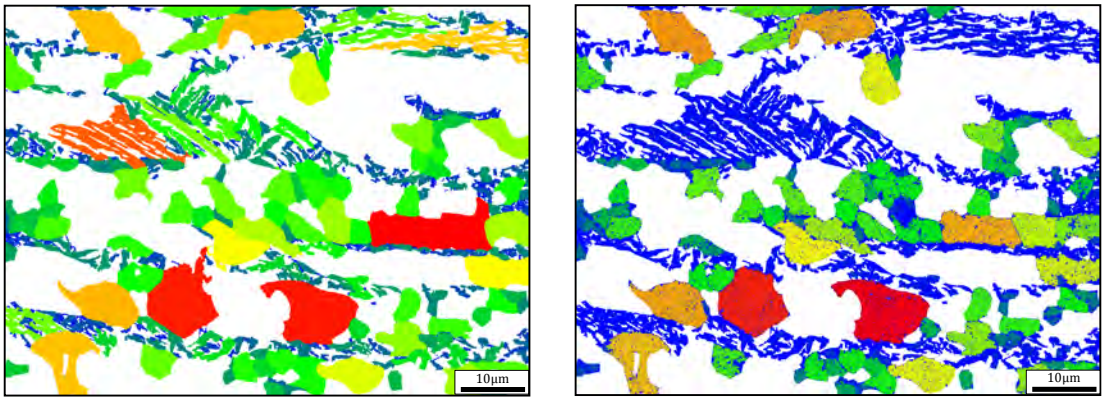

a) b)

Figure 5.4: a) Grain size map with 2° critical misorientation, b) Grain size map with 0.5° critical misorientation. In both maps the rainbow colour indicates the grain size from small grain (blue) to large grain (red).

The subgrain size threshold value was estimated to be 1.07 µm from the normalised cumulative distribution of the grain size shown in Fig. 5.5a. Based on that, a subset of ferrite in bainite and polygonal ferrite was separated into two subsets, one for bainite (Figs. 5.5b) and one for polygonal ferrite (Fig. 5.5c). Although the grain size criterion successfully separated ferrite in bainite from polygonal ferrite, many pixels from polygonal ferrite still remain in the bainite subset, as shown in Fig. 5.5b.

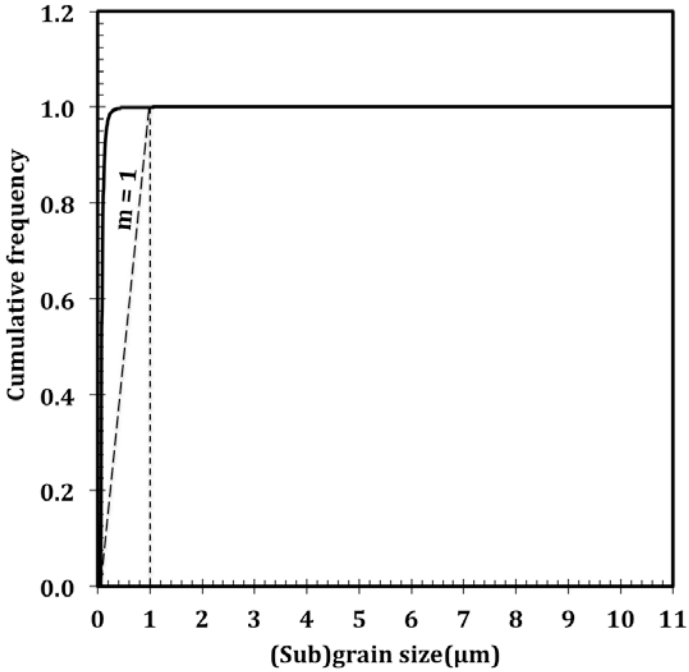

a)

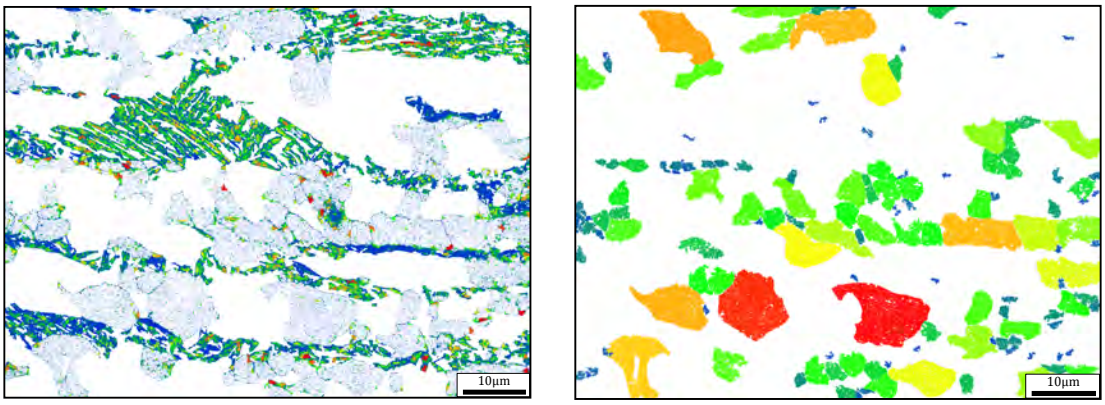

b) c)

Figure 5.5: a) Grain size frequency curve to separate ferrite in bainite b) Grain size below threshold value, 1.07 µm (rainbow colour), c) Grain size above threshold value, 1.07 µm (rainbow colour, the grain size from small grain (blue) to large grain (red).).

In the following procedure these pixelations in the bainite subset (Fig. 5.5b) were removed by dilating the ferrite subset (Fig. 5.5c) by one pixel (Fig. 5.6a) to capture the pixelations in the bainite subset. This was followed by subtracting the dilated subset (Fig. 5.6a) from the original subset (Fig. 5.5c). This step led to the creation of a subset that only contained polygonal ferrite pixels (Fig. 5.6b).

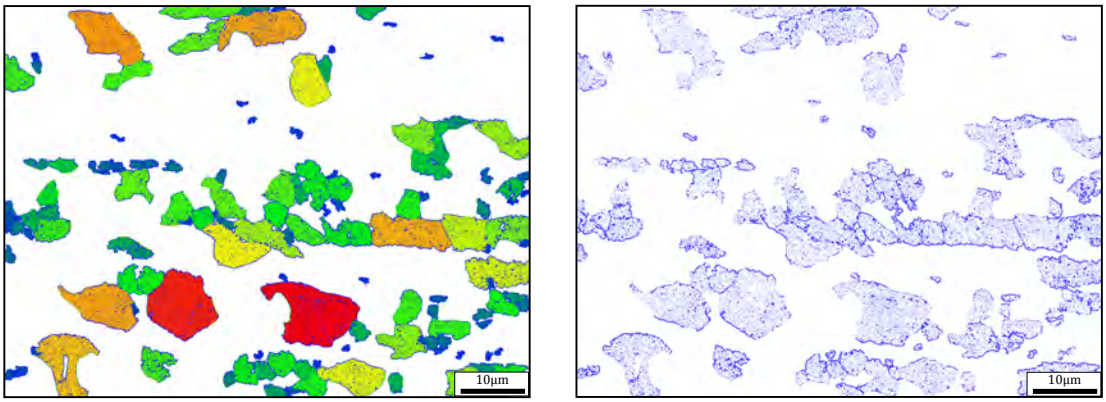

a) b)

Figure 5.6: Polygonal ferrite subset a) after dilation by one pixel (rainbow colour), b) pixelations belonging to polygonal ferrite.

The pixelations subset (Fig. 5.6b) was subtracted from the bainite subset (Fig. 5.5b). The result of this step is the final ferrite in bainite subset (Fig. 5.7a). This final bainite subset (Fig. 5.7a) was subtracted from the subset that contained bainite and polygonal ferrite (Fig. 5.2e) in order to obtain the second fraction of polygonal ferrite (Fig. 5.7b). Following this, the first (Fig. 5.3c) and second (Fig. 5.7b) polygonal ferrite fractions were combined together to form the final polygonal ferrite subset (Fig. 5.8a).

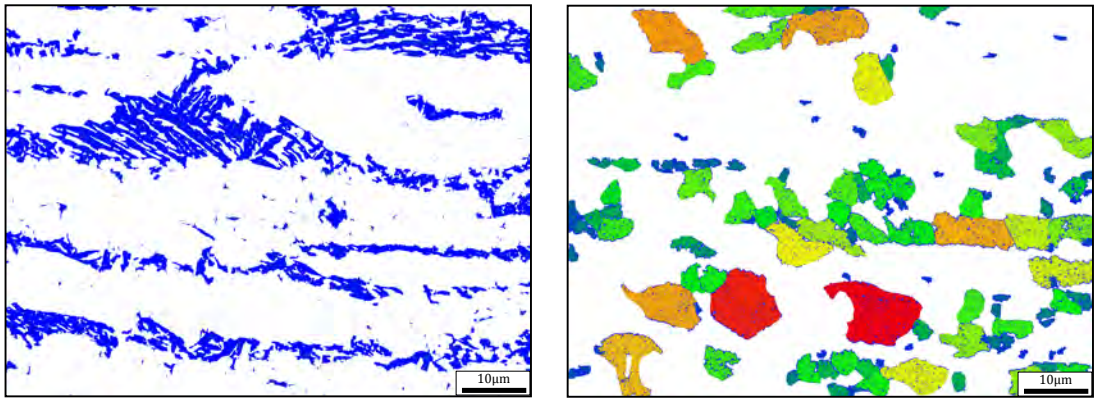

a) b)

Figure 5.7: a) Bainite after correcting to remove the pixelations, b) the second polygonal ferrite subset (rainbow colour of grain sizes from small (blue) to large grain (red)).

At this point, individual phases were assigned to each of the three bcc subsets with different colours; polygonal ferrite in blue, retained austenite in red, ferrite in bainite in green and martensite in yellow (Fig. 5.8b).

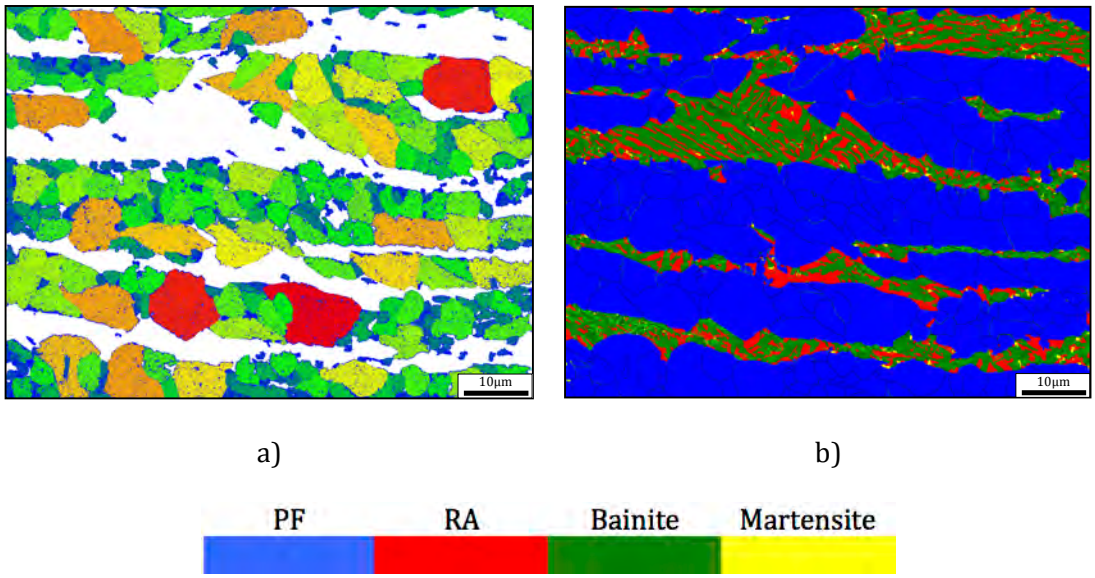

Figure 5.8: a) Polygonal ferrite after combining two maps (rainbow colour) and b) final segmentation map.

5.1.1 Further segmentation of the bainite morphologies

As it is clear from Fig. 5.8b that the bainite consists of two distinct morphologies; namely granular bainite and bainitic ferrite. Granular bainite is characterised by a higher density of low-angle boundaries and a relatively small area fraction of blocky retained austenite. On the other hand, bainitic ferrite is characterised by high aspect ratio arrangements of bainitic ferrite laths with a relatively larger area fraction of interlath retained austenite. The method of segmentation of ferrite in these two morphologies of carbide-free bainite (granular bainite and bainitic ferrite) is illustrated in the following section while the crystallography of these two morphologies is discussed in Chapter 6.

Although, these two morphologies are visually distinguishable, the above segmentation procedure does not individually separate them. This raises the need for another segmentation procedure that is able to separate the different bainite morphologies. To this end, while it was not possible to segment granular bainite and bainitic ferrite in the Nb-Ti steel, it was possible to segment them in the base steel because both morphologies were present in almost equal amounts in the microstructure of the latter steel. In general, the segmentation between the two morphologies was based on their grain sizes and was similar to the method used earlier to separate between bainite and polygonal ferrite, as shown in Fig. 5.4.

The first attempt to separate between the two morphologies in the base steel using a grain size criterion with boundary angles of 2° was unsuccessful until the boundary identification angle was reduced to 0.5° and the completion angle was reduced to 0.1°. The influence of these two definitions of the grain boundary on the grain size is shown in Fig. 5.9a and b. Based on the value of the subgrain size threshold (in this case, 1μm) from the normalised cumulative distribution of the grain size, the bainite subset in the base steel was separated into two subsets; bainitic ferrite laths (Fig. 5.9 c) and ferrite in granular bainite (Fig. 5.9 d). Although the grain size criterion was separated the two morphologies successfully, there were still a lot of tiny pixels from bainitic ferrite laths within the granular bainite subset, as shown in Fig. 5.9d.

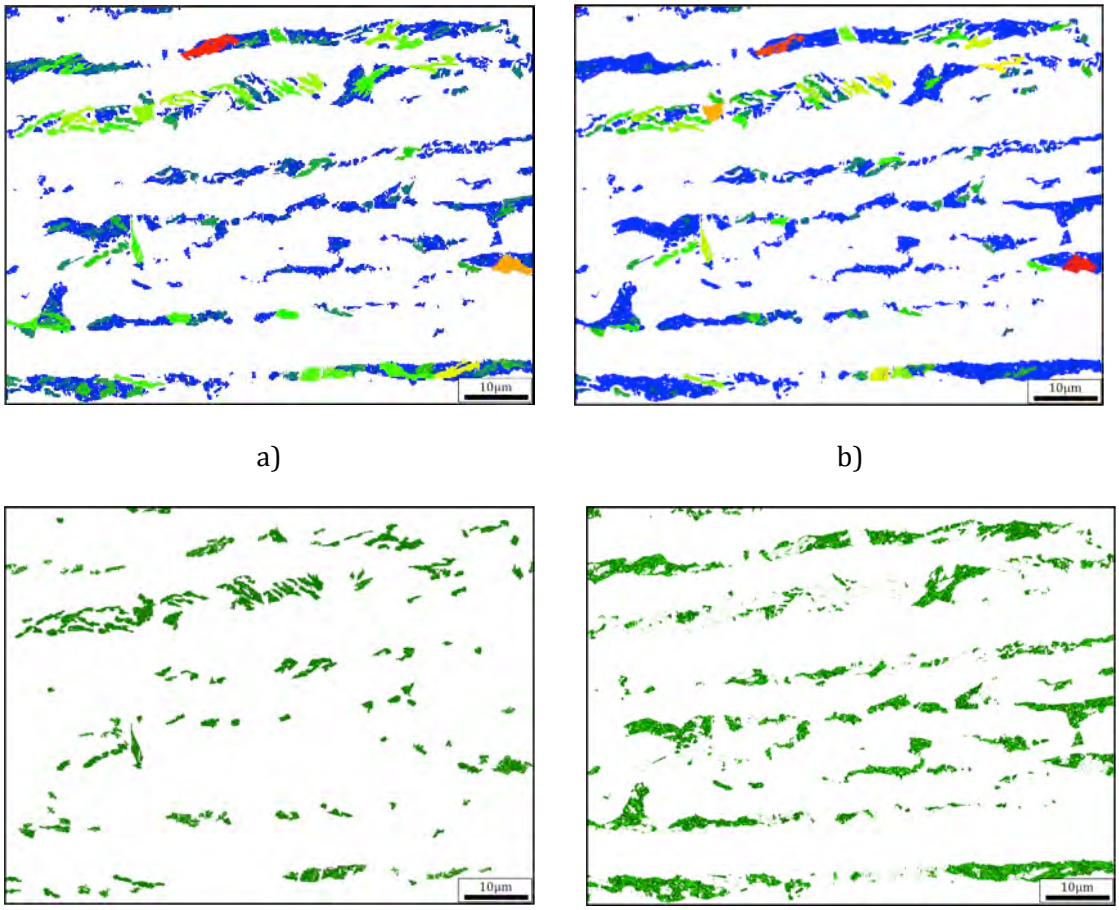

a) b)

c) d)

Figure 5.9: Grain size map of ferrite in bainite in base steel a) with 2° critical misorientation and b) with 0.5° critical misorientation (rainbow colour). c) bainitic ferrite laths subset and d) ferrite in granular bainite subset after thresholding the normalised cumulative distribution of the grain size.

These pixelations in the ferrite in granular bainite subset (Fig. 5.9d) were removed by expanding the bainitic ferrite laths subset (Fig. 5.9c) by one pixel, as shown in Fig. 5.10a, to cover the missing pixels, followed by subtracting the dilated subset (Fig. 5.10a) from the original subset (Fig. 5.9c). This step resulted in the creation of a subset that only contained pixelations (Fig. 5.10b), which was then subtracted from the granular bainite subset (Fig. 5.9d), resulting in the final ferrite in granular bainite subset (Fig. 5.10d). This final subset (Fig. 5.10d) was then subtracted from the original subset that contained both bainites (Fig. 5.9b) to obtain the final bainitic ferrite laths subset shown in Fig. 5.10c. The outcome of this procedure is presented in Fig. 5.10e where the polygonal ferrite is blue, the retained austenite is red, the martensite is yellow, the ferrite in granular bainite is dark green and bainitic ferrite laths are light green. It must be re-emphasised that while this procedure to

segment the ferrite in bainitic morphologies was generally successful in the base steel, care should be exercised during this procedure because there is potential for error when some of the ferrite in granular bainite areas are separated as bainitic ferrite due to the relatively lower fraction of low-angle boundary in the former areas.

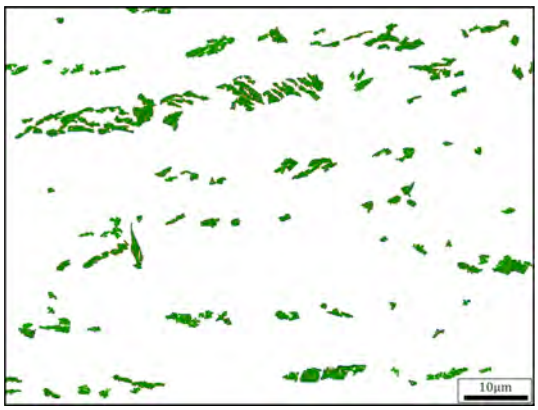

a)

b)

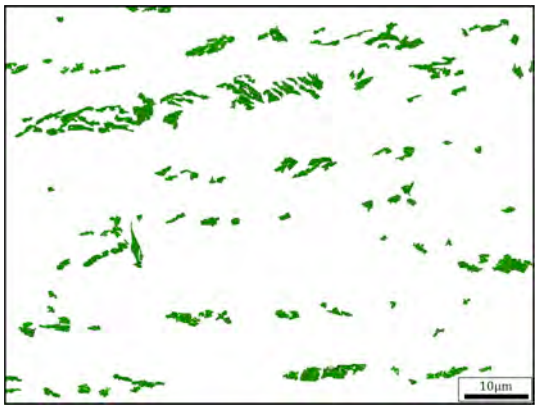

c)

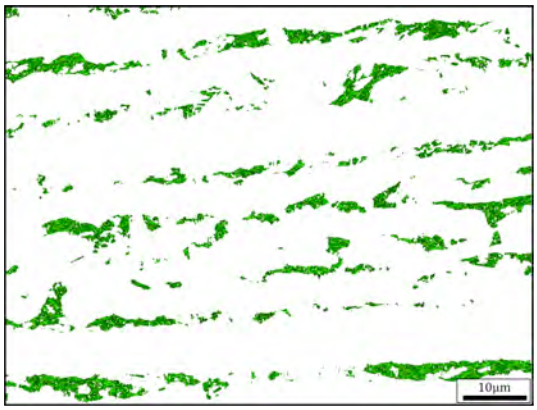

d)

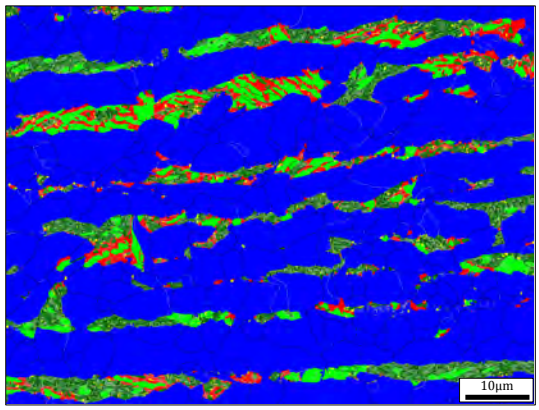

e)

Figure 5.10: The bainitic ferrite laths subset a) after dilation by one pixel and b) pixelation belonging to bainitic ferrite laths. c) Final bainitic ferrite laths subset (BF) and d) final ferrite in granular bainite subset (GB). e) The outcome of segmentation of the ferrite in bainite in base steel into two morphologies (ferrite in granular bainite and bainitic ferrite laths).

5.1.2 Analysis of the phase/ferrite morphology segmentation procedure

The developed procedure was applied on the base and Nb-Ti TRIP steels. The resultant area fractions of the phases at different strains are summarised in Table 5.1. Some areas at fracture condition remain non-indexed due to the high strain and high amount of martensite. The area fraction of martensite was less than 1% in both steels in their TMP state, which increased during uniaxial tensile strain due to the transformation of retained austenite.

Table 5.1: A summary of the area fraction of phases in the base steel and Nb-Ti steel at different strains.

		Polygonal Ferrite	**Retained Austenite**	**Bainite**	**Martensite**	**Non-indexed**
Base	Zero (ε = 0)	77.6	5.00	16.5	0.9	0.0
	UTS (ε = 15%)	74.3	1.20	17.7	6.8	0.0
	Fracture (ε = 25%)	65.0	0.27	26.0	4.6	4.3
Nb-Ti	Zero (ε = 0)	71.3	9.40	18.8	0.5	0.0
	UTS (ε = 18%)	64.3	1.40	25.5	8.8	0.0
	Fracture (ε = 29%)	60.0	0.06	28.0	6.0	6.0

The amount of polygonal ferrite and bainite varied at each strain because different strain conditions were represented by different samples. Therefore, the area fraction of retained austenite, martensite, and non-indexed areas were normalised with respect to the sum of polygonal ferrite and bainite fractions (non-transforming phases) at different tensile strains, as shown in Table 5.2. The influence of the tensile strain on the fraction and microstructural characteristics of each constituent phase/ferrite morphology will be discussed in detail in Section 5.2.

Table 5.2: A summary of the area fraction of phases in the base steel and Nb-Ti steel normalised to the polygonal ferrite and bainite fractions at different tensile strains.

		Polygonal Ferrite	**Retained Austenite**	**Bainite**	**Martensite**	**Non-indexed**
Base	Zero (ε = 0)	--	0.053	--	0.010	0.000
	UTS (ε = 15%)	--	0.013	--	0.074	0.000
	Fracture (ε = 25%)	--	0.003	--	0.051	0.047
Nb-Ti	Zero (ε = 0)	--	0.104	--	0.006	0.000
	UTS (ε = 18%)	--	0.016	--	0.098	0.000
	Fracture (ε = 29%)	--	0.001	--	0.068	0.068

Since the microstructure of TRIP steel is complex, identifying the phase/ferrite morphology was more challenging than with other microstructures. Several studies have suggested different segmentation methods; but each of them suffers from limitations. These methods are based on different criteria such as local misorientation [12], band contrast (BC) [13, 65, 111], band slope (BS) [112], grain size (GS) [112], and grain-averaged function based on the band contrast and internal misorientation [13]. In this study every attempt to perform phase/ferrite morphology segmentation utilising the techniques described in literature failed because TMP multi-phase microstructures responded differently to the single step segmentation criteria [112, 121].

The band contrast (BC), which is similar to the image quality (IQ) or pattern quality (PQ) criteria, was one of the earliest methods used for phase/ferrite morphology segmentation. The variation in BC was related to the amount of lattice defects in each grain, and it is known that the higher the lattice defect, the lower the BC value. Therefore, bainite and martensite are characterised by low BC values as the amount of the lattice defects are larger compared to polygonal ferrite. However, one of the main disadvantages of using the BC method for segmentation is that the band contrast ranges vary from sample to sample because the band contrast of an EBSD map is influenced by the focusing conditions of the microscope and EBSD hardware settings that are optimised for each sample [120].

A successful segmentation procedure was developed by Wilson and his co-workers [115] to distinguish ferrite from martensite in Fe-0.12C-3.28Ni (wt.%) based on the pattern quality (or IQ). The BC histogram of their study clearly showed two distinct peaks for each phase. This method used the bimodal band contrast profile to separate the phases with minimum overlap but it was not successful in the present study because the BC distribution of the current TRIP steel (Fig. 5.11) only showed a single peak. This same limitation was also observed by Wilson *et al.* [115] in HSLA-100 steel. Although the dilatometric analysis showed that there was 30% of ferrite and 70% of martensite in the HSLA steel, the PQ distribution only showed a single peak without a bimodal distribution.

Kang *et al.* [13] averaged the band contrast to overcome the issue of overlapping in the distribution between martensite and ferrite. This method makes the segmentation based on grains not pixels to provide a smooth and clear discrimination. They successfully implemented this method based on band contrast (BC) on dual phase steel (ferrite and martensite). It was stated that the definition of the grain boundary angle was important because it affects the martensite fraction. However, it was found that the BC needs to be supplemented with average misorientation in order to do phase/ferrite morphology segmentation in TRIP steel [13], but once again, this procedure is only successful if the band contrast of the bcc phase returns a bimodal distribution.

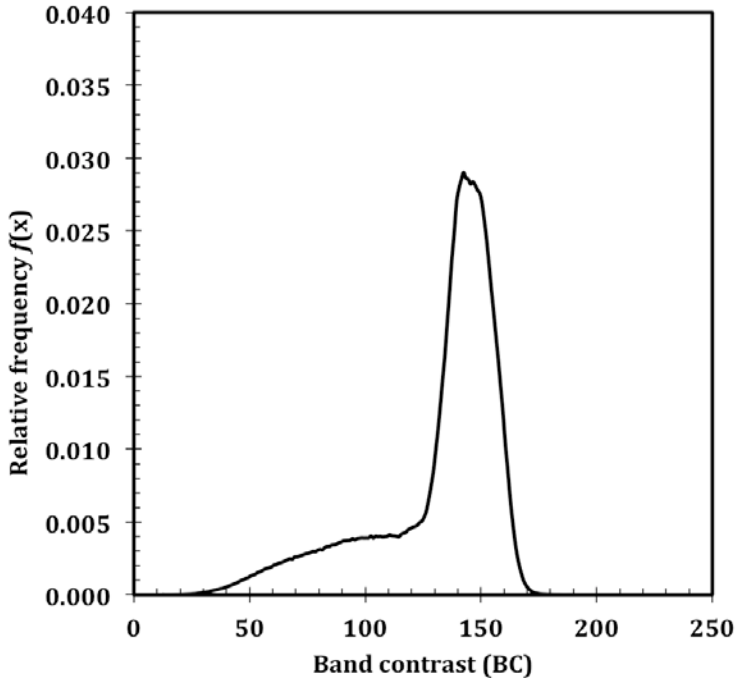

a)

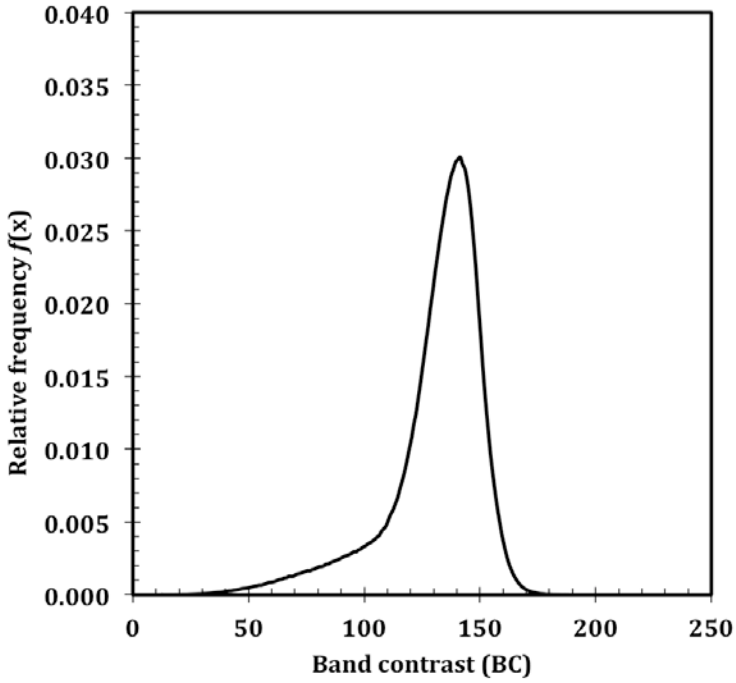

b)

Figure 5.11: Band contrast histogram of the bcc phase for a) base and b) Nb-Ti steel.

When the BC method was used in this study, only the grain boundary regions were selected as part of a "second phase" because the band contrast usually shows low values near any type of grain boundary that are within the same range as the bainite and martensite. Thus the mix between the grain boundary and other phases using BC criterion was difficult to avoid and led to an incorrect result. However, identifying the (sub)grain boundary regions by means of a critical grain boundary misorientation angle can be one of the methods used to resolve the effect of the grain boundary [111]. However, other studies have shown that the BC method alone is not enough to separate complex microstructure such as TRIP steel [13] and it cannot be applied on deformed materials because the quality of ferrite becomes very low after deformation [65].

Wu *et al.* [111] introduced an improvement to the image quality method by eliminating the influence of the grain boundary region on the IQ value and normalising the IQ curve, followed by applying a multi-peak model. In their study it was assumed that a single-phase microstructure should return a single symmetric peak of the IQ distribution. Therefore, IQ distribution of the multiphase microstructure should be in an asymmetric shape and the segmentation should yield symmetric peaks whose numbers are equal to the number of phases or constituents in the microstructure. The area fraction of each phase/ferrite

morphology was estimated from the area under each peak. This method was applied on a TRIP steel [65] to separate ferrite and bainite.

On the other hand, the results of the band contrast distribution on the current microstructure clearly showed an overlap between martensite and bainite peaks in the base steel (Fig. 5.12a) while the overlap with polygonal ferrite was less. Moreover, the results of the band contrast distribution in the Nb-Ti steel (Fig. 5.12b) showed a greater degree of overlap between peaks. The difference in the band contrast distribution between the base steel and Nb-Ti steel could be attributed to the difference in the amount of granular bainite and bainitic ferrite. Thus after segmenting the bainite of the base steel into granular bainite and bainitic ferrite, as shown in Fig.5.12c, the bainitic ferrite distribution showed more overlap with polygonal ferrite than granular bainite. On the other hand, the absence (or small fraction) of granular bainite in the Nb-Ti steel, as shown in Fig. 5.12b, led to a large overlap between bainite and polygonal ferrite in the Nb-Ti steel. Therefore, it can be concluded that the image quality criteria could not separate between phases, particularly the bainitic ferrite and polygonal ferrite, because the variation in band contrast between them is very small, as shown in Fig. 5.12b and c.

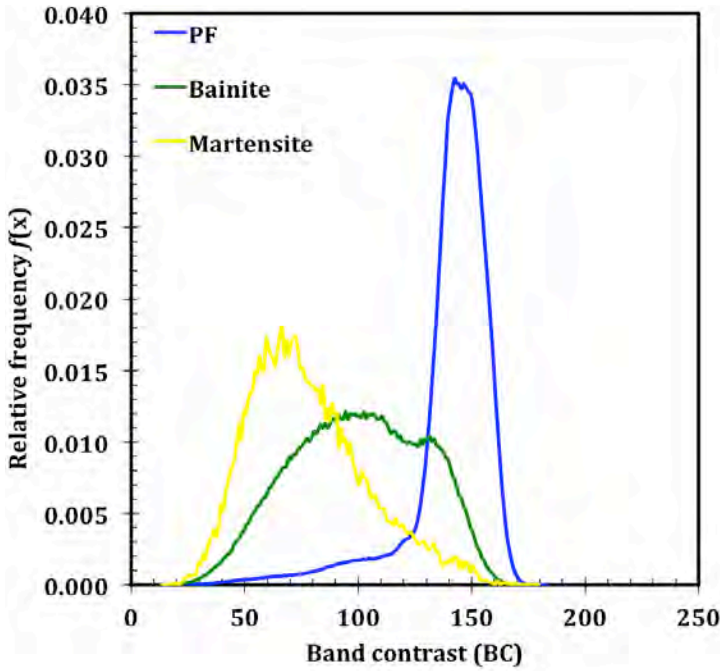

a)

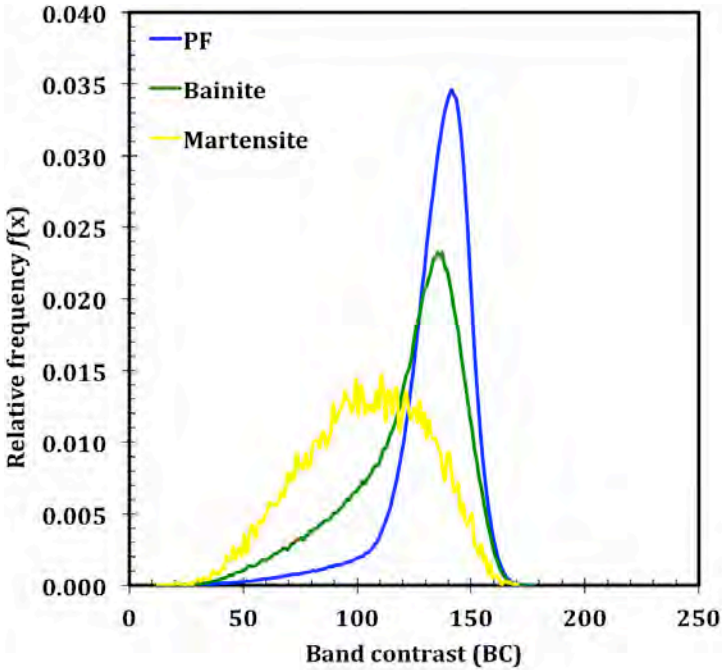

b)

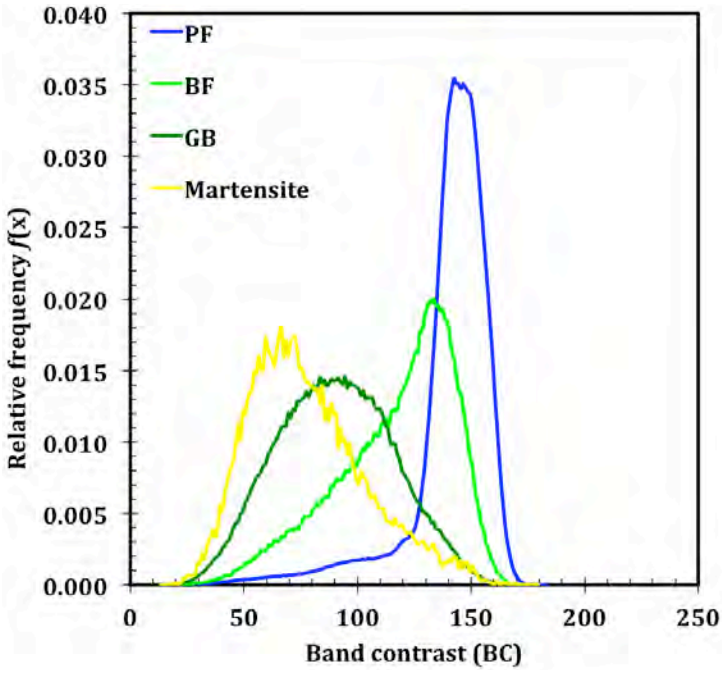

c)

Figure 5.12: Band contrast histogram of each phase/ferrite morphology in (a and c) base steel and b) Nb-Ti steel. c) band contrast histogram of each phase/ferrite morphology after separating between ferrite in granular bainite and bainitic ferrite laths.

The stored energy (geometrical necessary dislocation, GND) formed due to the transformation of bainite affected the orientation gradient such that the latter fact can only be used as criteria for segmentation. The kernel average misorientation (KAM) where the misorientation between pixels was calculated and mapped is one way of evaluating the orientation gradient in EBSD map, but this method is characterised by orientation noise [109]. In the KAM criterion, the misorientation variation was evaluated at a pixel level, unlike the grain orientation spread criterion (GOS criterion) where the variation in misorientation was evaluated at a substructure level. Zaefferer *et al.* [12] chose the kernel average misorientation, KAM as a method to separate ferrite and bainite in Al-containing TRIP steel. Based on an analysis of the boundaries between the phases, the cumulative KAM curve was thresholded into two areas representing the two phases. The procedure was successfully applied in another TRIP steel and confirmed via the orientation relationship between bainite and austenite [120]. However, it was suggested that other parameters need to be added to this procedure when different types of bainite are formed in the microstructure [12]. However, the current results showed a clear overlap between the KAM values of each phase with overlap between the bainitic ferrite laths and polygonal ferrite was higher than between the ferrite in granular bainite and polygonal ferrite in the base steel (Fig 5.13c). The absence of a significant fraction of granular bainite in the Nb-Ti steel would not allow for segmentation between the ferrite morphologies based on the KAM criterion.

Accordingly, the procedures developed in the literature were not applicable to this study, which is mainly due to the complexity of the microstructure and the presence of many phases in the microstructure. The microstructure in this study contained mixtures of different bainite morphologies such as granular bainite and bainitic ferrite formed as several bands along the rolling direction, as seen in the optical micrographs (Chapter 5) and EBSD maps. This complexity in the microstructure made it difficult to apply any of the segmentation procedures used previously in the literature, and also led to the need for more than one-step segmentation criteria to be applied on the same microstructure. Zhu *et al.* [121] utilised a combination of several functions such as BC, BS, average granular misorientation, grain size, and grain shape to characterise their complex microstructure. In this study, the developed procedure was based on two components; the grain orientation spread (GOS) and subgrain size.

The long range grain orientation spread criterion (GOS) was used successfully in this study to do the first stage of phase/ferrite morphology segmentation which resulted in the segmentation between martensite and the first portion of polygonal ferrite (Fig. 5.2d), and

ferrite in bainite and the second part of polygonal ferrite (Fig. 5.2e). In this study the grain size was found the best criteria for separating ferrite in bainite from polygonal ferrite (Fig. 5.3) and separating martensite from the second part of polygonal ferrite (Fig. 5.5). In this method the grain size is defined by a specified critical misorientation, which is usually 2°. However, the critical misorientation used to define the grain boundary must be selected carefully because it has a profound influence on the result of the segmentation. The difference in grain size between the bainite and ferrite was found very useful if the critical misorientation reduced to a relatively low value (i.e. 0.5°). The critical misorientation effect in the segmentation procedure has also been reported by other researchers while they used different criteria for segmentation [13]. It has been reported that a grain boundary definition angle of less than 0.5° led to better results, but a reduction of the critical misorientation from 2° to 0.5°, leads to scattered pixels from ferrite around bainite, and from bainitic ferrite around granular bainite, after segmentation. This issue was also been raised when different criteria were used [12]. In this study this issue was resolved by applying the steps described in Section 5.1.

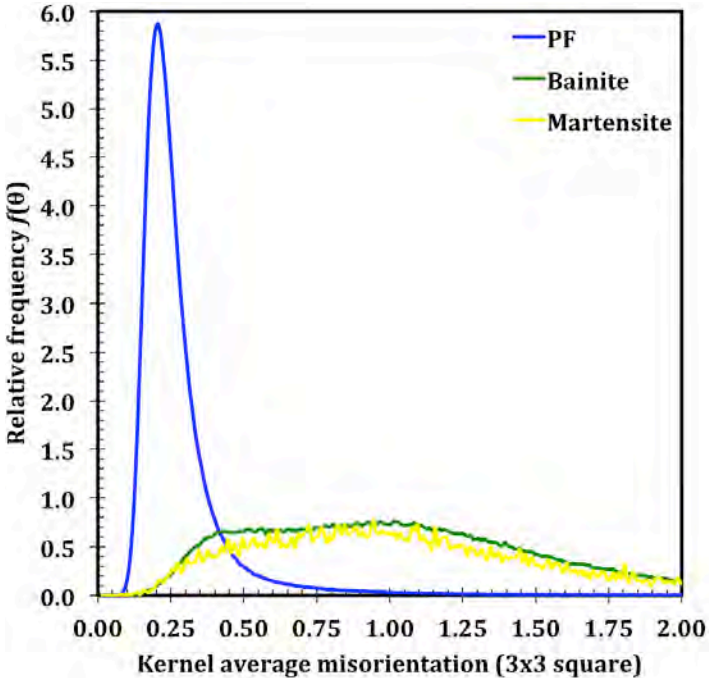
PF
Bainite
Martensite
Relative frequency f(θ)
Kernel average misorientation (3x3 square)
0.0
0.5
1.0
1.5
2.0
2.5
3.0
3.5
4.0
4.5
5.0
5.5
6.0
0.00
0.25
0.50
0.75
1.00
1.25
1.50
1.75
2.00

a)

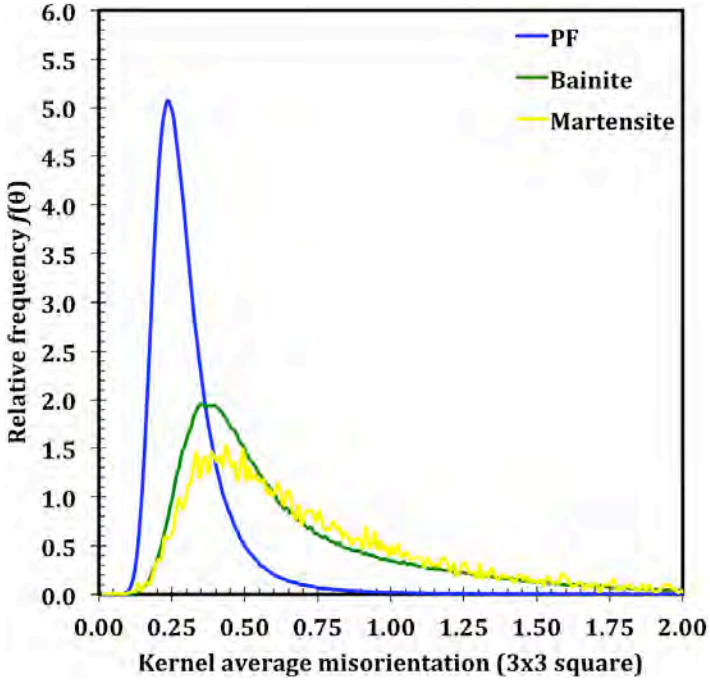
PF
Bainite
Martensite
Relative frequency f(θ)
Kernel average misorientation (3x3 square)
0.0
0.5
1.0
1.5
2.0
2.5
3.0
3.5
4.0
4.5
5.0
5.5
6.0
0.00
0.25
0.50
0.75
1.00
1.25
1.50
1.75
2.00

b)

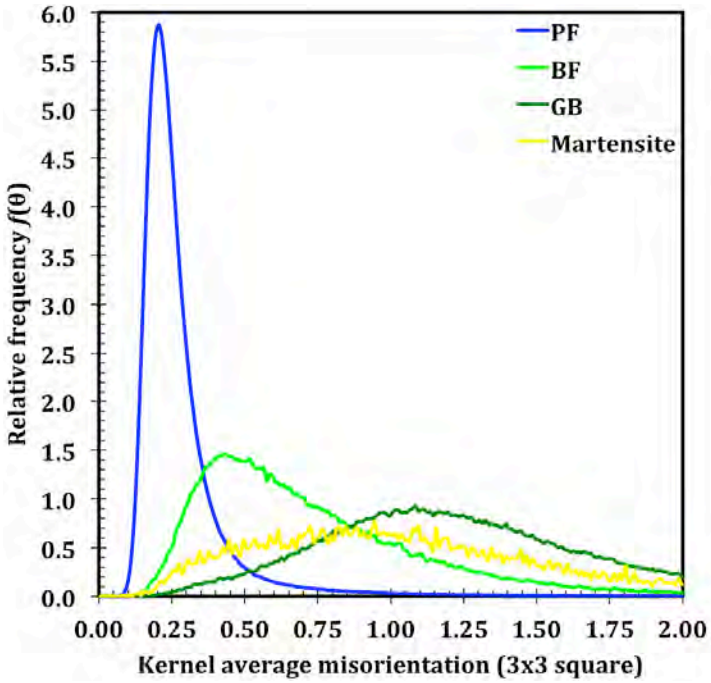

c)

Figure 5.13 KAM histogram of each phase in the base steel (a and c) and Nb-Ti steel (b). Note that only ferrite is considered in bainites. In c) the KAM histogram is shown for ferrite in granular bainite and bainitic ferrite laths in the base steel.

5.2 The Effect of Strain on the Stability of Retained Austenite

Based on the segmentation methodology developed in Section 5.1, the effects of the area fraction, grain size and morphology of each phase on the retained austenite stability are analysed in this section.

5.2.1 The Change of the Retained Austenite Amount with Tensile Deformation

The newly developed segmentation procedure was used to analyse the base and Nb-Ti steel at different strains during uniaxial tensile testing: after TMP (Figs. 5.14 a and b, zero tensile strain), UTS (Figs. 5.14 c and d) and at fracture (Figs. 5.14 e and f). The high amount of martensite and high strain at UTS and fracture led to an increase in the non-indexed area (especially in regions near grain boundaries and at interfaces between phases/ferrite morphologies) such that phase identification was not possible in these areas (white colour in Fig. 5.14 e and f).

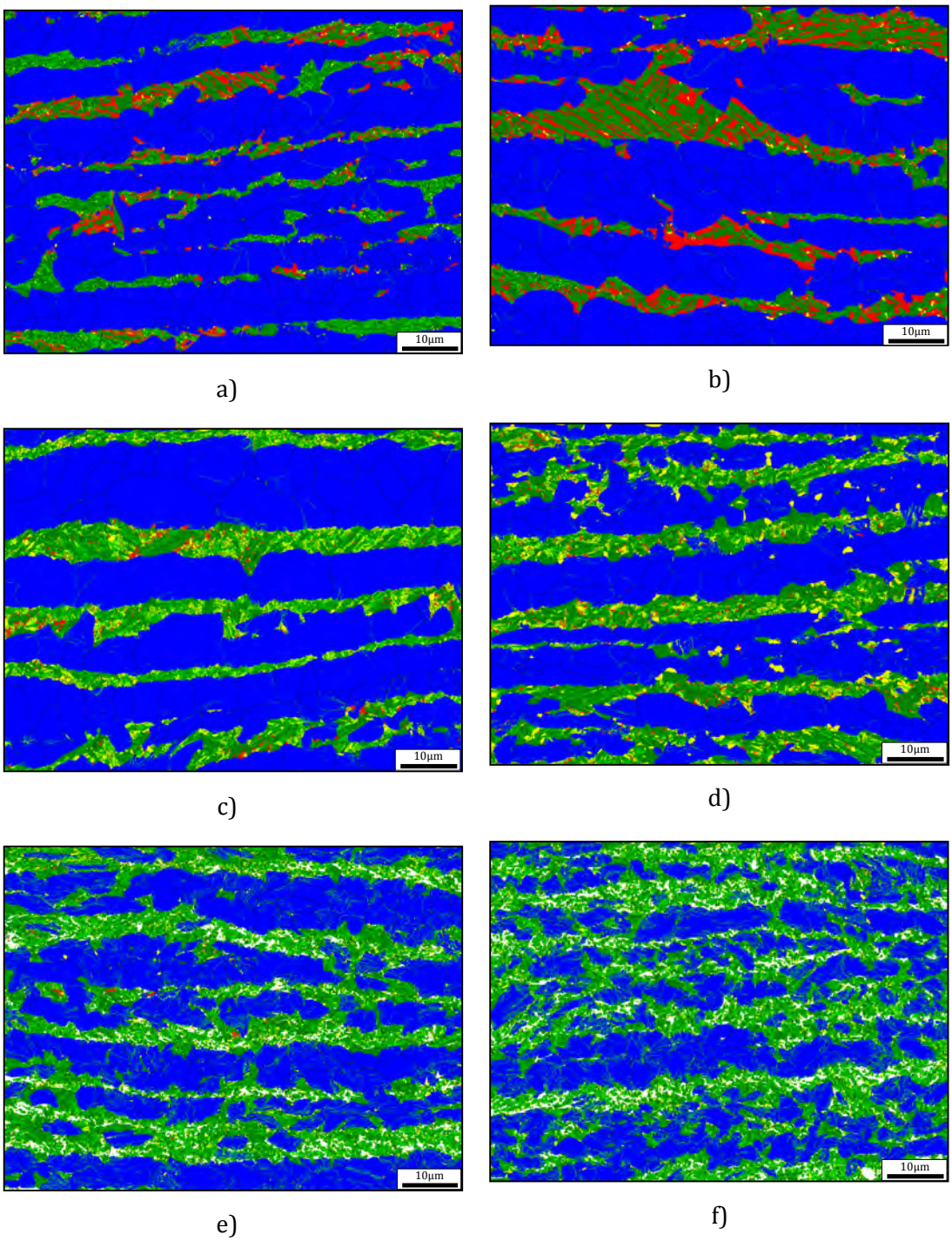

Figure 5.14: EBSD phase maps for the base steel (a, c and e) and Nb-Ti steel (b, d and f) at three different tensile deformation conditions; after TMP (zero tensile strain, a and b), at UTS (c and d) and at fracture (e and f). HAGBs= black colour, LAGBs= light green colour. The polygonal ferrite (PF) = blue, retained austenite (RA) = red, ferrite in bainite = green and martensite = yellow; white are non-indexed areas.

Prior to the tensile test (after TMP, zero tensile strain), the EBSD maps indicated the presence of ~70% polygonal ferrite and ~20% of bainite in the microstructures of the steels (Table 5.1). The area fraction of retained austenite and martensite were normalised with respect to the sum of polygonal ferrite and bainite fractions in Table 5.2. The normalised area fraction of retained austenite in the base and Nb-Ti steel was determined as 0.05 and 0.104, respectively. A small normalised area fraction of martensite was also identified: 0.01 and 0.006 in the base and Nb-Ti steel, respectively. It was assumed that this martensite formed on quenching from the isothermal hold temperature from unstable retained austenite. It was necessary to highlight that two morphologies of bainite were clearly seen in EBSD maps: granular bainite with high internal misorientation and very small fractions of retained austenite or retained austenite/martensite constituent and bainitic ferrite containing a majority of the retained austenite in the form of relatively coarse interlayers (~0.2-1 μm thick). Since the base steel contained a higher fraction of granular bainite and the Nb-Ti steel contained a higher fraction of bainitic ferrite (Chapter 4), these differences could also be correlated to the lower and higher amounts of retained austenite in these steels, respectively. At UTS, the normalised retained austenite fraction decreased drastically to 0.013 in the base steel after straining to ε = 15% and to 0.016 in the Nb-Ti steel after straining to ε = 18%. Upon fracture, the retained austenite fraction decreased even further, reaching 0.003 (ε =25%) and 0.001 (ε =29%) in the base and in Nb-Ti steel, respectively. This reduction in the amount of retained austenite after straining was associated with an increase in the amount of martensite due to strain-induced transformation. Figure 5.15 shows the area fraction of martensite and retained austenite at different strain levels for both steels. The normalised martensite fraction at UTS was 0.074 and 0.098 in the base and Nb-Ti steel, respectively. At fracture the normalised area fraction of martensite fraction reduced to 0.051 in the base steel and to 0.068 in the Nb-Ti steel. Here, it should be noted that the area fraction of martensite at fracture should be approximately equal to the sum of the area fraction of retained austenite and martensite at zero strain. Therefore, the area fraction of martensite at the fracture condition is shown higher in Fig. 5.15 because the non-indexed areas were included in the calculation of the martensite fraction. However, the calculation of martensite area fraction at fracture might involve some errors because the non-indexed area can be part of other phases such as retained austenite or regions of high stress concentration, such as near the interfaces.

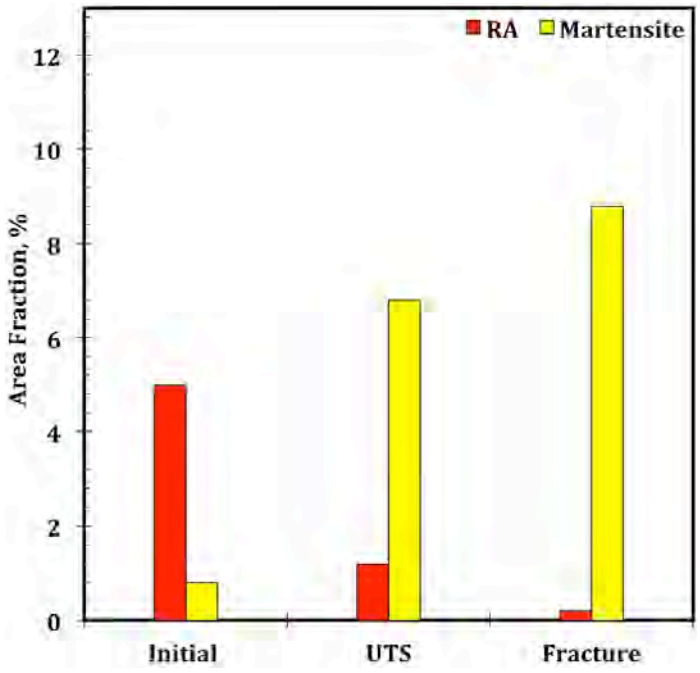

a)

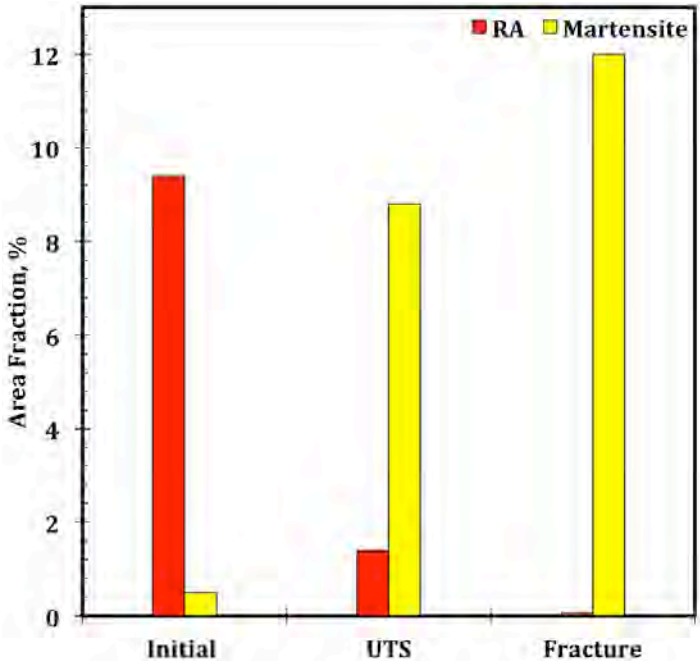

b)

Figure 5.15: The variation in the retained austenite and martensite amounts during uniaxial tensile testing for a) base steel and b) Nb-Ti steel.

The EBSD analyses a small area compared with other techniques such as x-ray diffraction. In the current study, the EBSD map size was ~105 × 79 μm^2 while the analysed area by XRD was ~3x15mm^2, but it still returned comparable results. A comparison of the results for the retained austenite detected by EBSD with XRD (Table 5.3) showed that the EBSD gave smaller absolute values of the retained austenite area fraction for Nb-Ti steel but still correctly identified the trend of a larger area fraction of retained austenite in the Nb-Ti steel compared to the base steel. That trend was similar to the one reported in the literature [65, 112]. The difference between these two techniques could be attributed to:

- The local area analysis via EBSD compared to the bulk (volume –based) analysis via XRD and
- Large analysis depth of XRD compared to EBSD (11μm vs. 50nm)

The higher difference between two techniques for the Nb-Ti steel could be attributed to the finer microstructure of Nb-Ti steel compared to the coarser microstructure in the base steel.

Table 5.3: The amount of retained austenite, % before the uniaxial tensile test calculated from EBSD and XRD data.

	EBSD	**XRD**
Base	5	4±1
Nb-Ti	9.4	13±0

The small initial area fraction of martensite was due to the transformation of a small fraction of unstable or low stability retained austenite (most probably due to its relatively very low carbon content) during quenching from isothermal holding.

The high amount of retained austenite in the Nb-Ti steel might be responsible for the higher elongation compared to the base steel (Fig. 4.5). However, the TRIP effect which contributed to the ductility was controlled more by the characteristics of retained austenite than the area fraction. It has been stated here before that the resistance of retained austenite to transformation during deformation could be affected by many factors, such as its grain size and morphology [10, 57], but it should be noted that the morphology and properties of other phases/ferrite morphologies close to the retained austenite also have a substantial influence on the overall stability of retained austenite.

The rate at which the retained fraction of austenite was transforming during the tensile test (i.e. change of RA amount with strain) was a good indication of its overall stability. For instance, the transformation rate of retained austenite in the Nb-Ti steel from 9.4 to ~1.4% was faster than in the base steel (from 5% to ~1.2%) which suggests that the stability of retained austenite was higher in the base steel than in the Nb-Ti steel. This high transformation rate of the RA in the Nb-added high Si TRIP steel has been reported previously in the literature [10]. On the other hand, the high stability of retained austenite in the base steel can be attributed to its mechanical or chemical stability. An XRD analysis (as mentioned in the previous chapter) showed that the average carbon content in the retained austenite in the base steel (1.2 wt.%) was only slightly higher than (1.1 wt.%) in the Nb-Ti steel, and since the variation in carbon content was very small and within the error of measurement, it cannot explain why the retained austenite was stable in the base steel. Thus, the mechanical stability of the retained austenite will be discussed in the following sections.

5.2.2 Internal Misorientation Analysis via the Kernel Average Misorientation (KAM)

One of the advantages of EBSD analysis is the ability to study the effect of the deformation on each phase by evaluating the kernel average misorientation (KAM) [65, 109, 113, 118]. It is believed that an increase in KAM is always associated with an increase in the dislocation density of geometrically necessary dislocations (GNDs) [119]. The relative frequency of KAM at different stages of tensile test (zero tensile strain, at UTS and at fracture) for all bcc phases/morphologies (polygonal ferrite, bainite and martensite) and for the fcc phase (retained austenite) are shown in Figs. 5.16 a and b. As the tensile strain increases the peaks shift to the right towards higher average KAM angles along with an overall broadening of the distribution. This indicates an increase in the accumulated strain in these phases.

Consequently, for each phase in both steels, the variation of mean local misorientation with strain is presented in Figs. 5.16 c and d. The standard deviation of the average KAM values in each phase were large, which makes reaching definitive conclusions about each phase/ferrite morphology difficult. Nevertheless, KAM analysis gives some general idea about the strain distribution, especially between the bcc and fcc phases. The standard deviation of KAM in polygonal ferrite was small due to the low orientation gradient within the polygonal ferrite grains.

As expected, the results showed that polygonal ferrite had low average KAM values compared to the harder phases (bainite, martensite). Accordingly, the plastic strain during deformation will not be uniformly distributed in the multiphase steel, where the polygonal ferrite yields first, and then after a certain amount of work hardening the stress is transferred to harder phases such as bainite, austenite, and martensite [147, 154]. However, it has been reported that strain partitioning varies according to the microstructure and chemical composition [155].

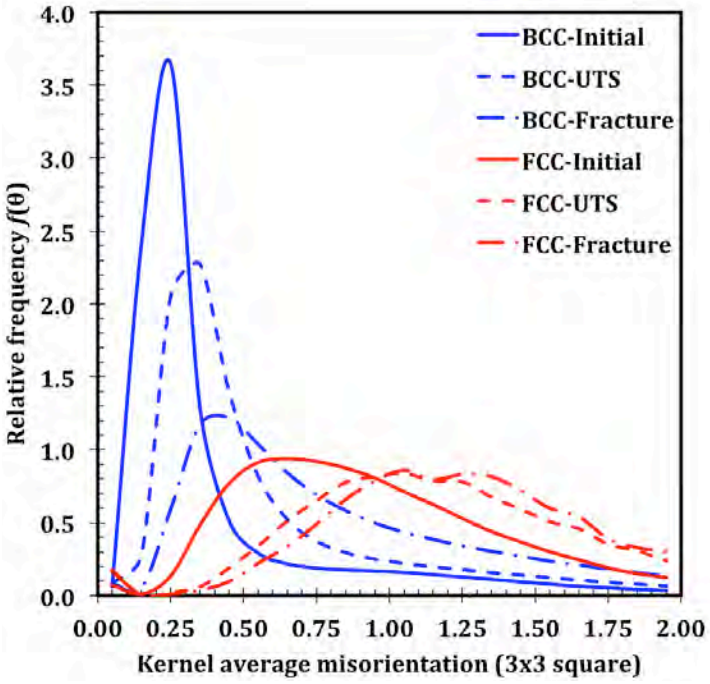
BCC-Initial
BCC-UTS
BCC-Fracture
FCC-Initial
FCC-UTS
FCC-Fracture
Relative frequency f(θ)
Kernel average misorientation (3x3 square)
0.0
0.5
1.0
1.5
2.0
2.5
3.0
3.5
4.0
0.00
0.25
0.50
0.75
1.00
1.25
1.50
1.75
2.00

a)

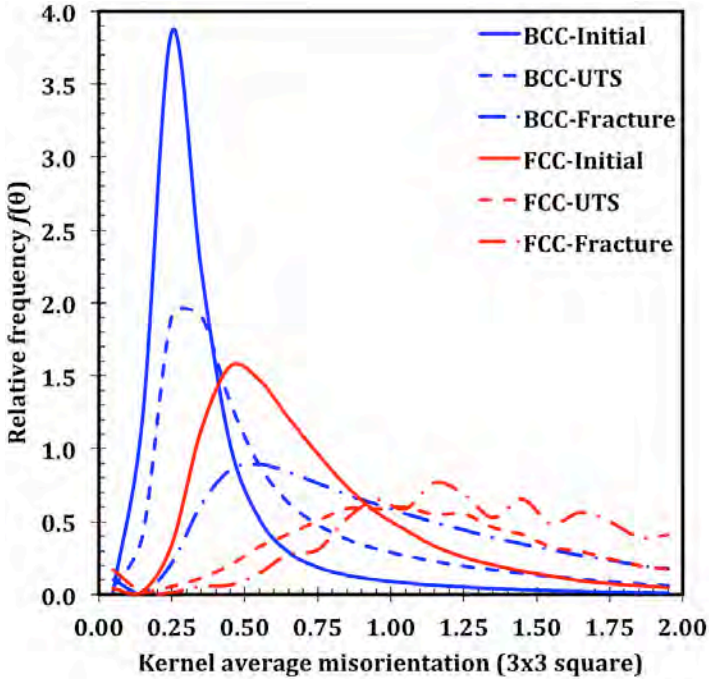
BCC-Initial
BCC-UTS
BCC-Fracture
FCC-Initial
FCC-UTS
FCC-Fracture
Relative frequency f(θ)
Kernel average misorientation (3x3 square)
0.0
0.5
1.0
1.5
2.0
2.5
3.0
3.5
4.0
0.00
0.25
0.50
0.75
1.00
1.25
1.50
1.75
2.00

b)

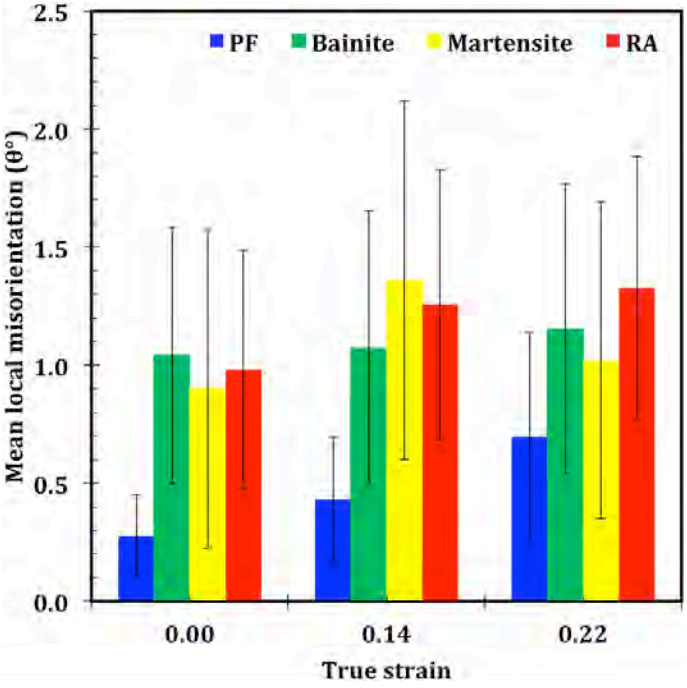

c)

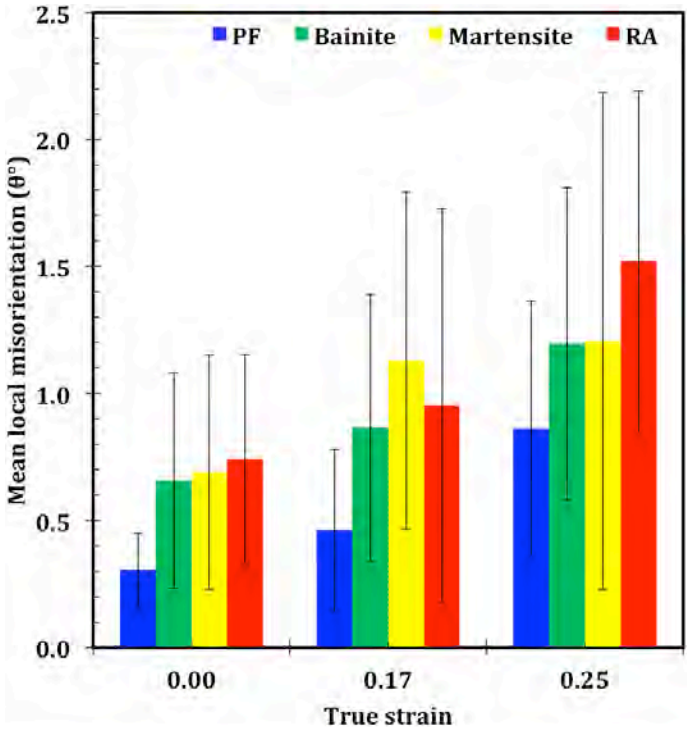

d)

Figure 5.16: Kernel average misorientation distribution of the bcc (bainite, polygonal ferrite (PF) and martensite) and retained austenite (RA) phases at different tensile strains (a and b) and the mean and standard deviation of the KAM value for each phase/morphology (c and d) for base (a and c) and Nb-Ti (b and d) steels.

The KAM (Figs. 5.16c and d) of the retained austenite before deformation was higher than the polygonal ferrite and bainite due to the deformation applied in the non-recrystallisation region during TMP. However, the retained austenite shows faster rates of increase in the average KAM value compared to the bainite and martensite, while the rate of increase in the KAM value of the soft polygonal ferrite was the highest among all phases/ferrite morphologies [156]. This was associated with the rapid work hardening of polygonal ferrite.

The higher rate of increase in the average KAM value of retained austenite during deformation in the Nb-Ti steel than in the base steel was also associated with a higher rate of increase in the KAM of bainite. This finding was predicted because most of the retained austenite is present within the bainite in both steels. Other studies [65] conducted on TRIP steel showed that an increase in KAM with deformation was significant in the bcc phase where the KAM of the retained austenite increased by 10% while the KAM in the ferrite increased by almost 100%; the latter can be explained by high strain accommodated by bcc compared to the fcc phase. However, that study did not distinguish between the hard and soft phases within the bcc phase.

In contrast, the bainite phase had a higher KAM in the base steel than the Nb-Ti steel, whereas the increasing rate of KAM with deformation was higher in the Nb-Ti steel. The dominant granular bainite in the base steel as opposed to the bainitic ferrite in the Nb-Ti steel is suggested as the reason for these differences in the KAM, because the ferrite in granular bainite initially showed a higher KAM than the bainitic ferrite.

It should be noted here that as the tensile strain increases, the non-indexed areas of the map also increase, and therefore the KAM calculations for all phases/morphologies suffered from errors related to the non-inclusion of the absent KAM values in non-indexed regions.

The maximum KAM values were predominantly returned at/near the grain boundaries due to the accumulation of dislocation tangles at the grain boundary [157]. The effect of volume expansion while the austenite was transforming to martensite on the local misorientation gradient in ferrite was also observed in DP steels containing 24% - 38% martensite [119].

5.2.3 The Relationship between Retained Austenite Subgrain Size and its Stability

It was important to track the change in the grain size of the retained austenite during deformation in order to understand the relationship between its stability and its size. Figure 5.17 shows the equivalent grain diameter distribution for both chemistries at different strain conditions: at zero tensile strain, at UTS, and at fracture. The minimum grain size considered in the grain size evaluation was 0.15 μm, which was three times the step size of the EBSD map scanning.

The average grain size of retained austenite before tensile deformation in the base steel was slightly coarser than the Nb-Ti steel. At UTS, the grain size of the retained austenite was less than 1 μm in the base steel and less than 0.8 μm in the Nb-Ti steel, whereas at the fracture, the remaining retained austenite had a grain size of less than 0.7 μm in both chemistries.

The retained austenite grain size in the Nb-Ti steel was relatively finer than in the base steel because the addition of Nb and Ti affected the prior austenite grain size and consequently the coarseness of the final microstructure. In general, a small retained austenite grain size is more stable because a decrease in the number of martensite nucleation sites delays the start of transformation [98-100]. It is also commonly stated that smaller retained austenite grains typically have a higher carbon content, which reduces the martensite start transformation temperature [101]. The low stability of retained austenite in the Nb-Ti steel, despite the fine retained austenite size, could indicate that for deformation levels up to UTS the size effect of the retained austenite in the Nb-Ti steel was less dominant than the chemical stability.

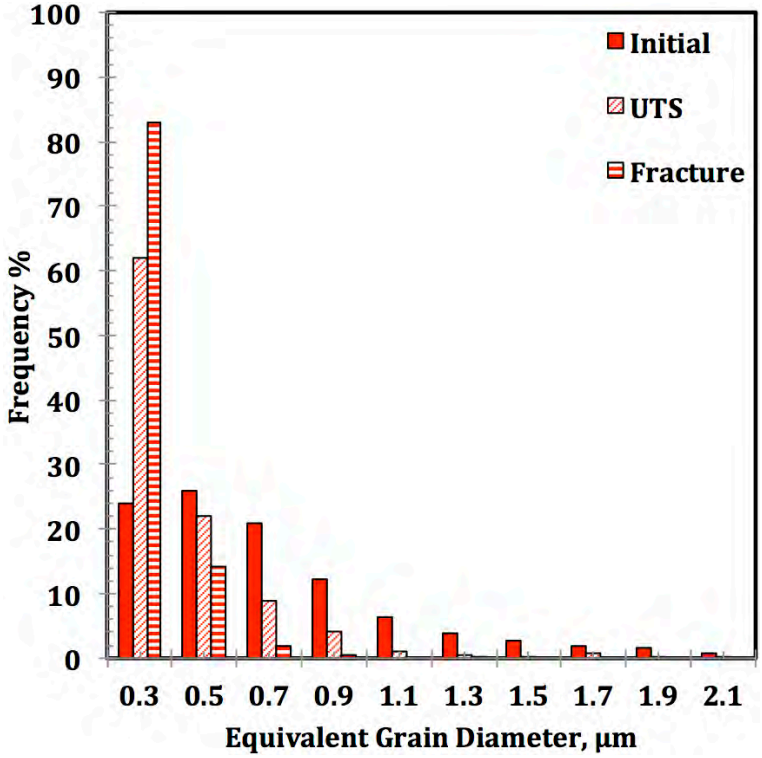

a)

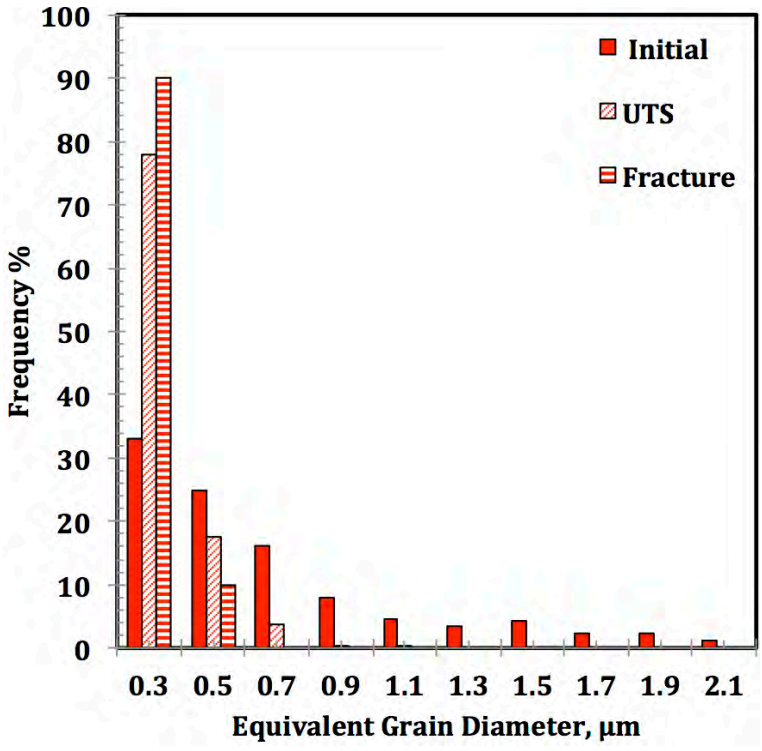

b)

Figure 5.17: The variation in the distribution of equivalent subgrain diameter of RA during tensile test for a) base steel and b) Nb-Ti steel.

5.2.4 The Effect of Retained Austenite Morphology on its Stability

The retained austenite was located at different locations and formed in various morphologies due to the TMP processing used in this study. Based on the grain aspect ratio, the retained austenite was categorised into two morphologies, film and blocky shape, and an aspect ratio of 1.5 was used to make this differentiation. The results showed that ~65% - 73% of the retained austenite had a film-like morphology and ~ 27%-35% had a blocky shape in both steels. This was strongly related to the presence of two bainite morphologies: granular bainite and bainitic ferrite. The blocky retained austenite was predominantly located in the granular bainite whereas lath-like retained austenite was in the bainitic ferrite. In addition, the amount of retained austenite was much higher in the bainitic ferrite than in the granular bainite (Fig. 5.14). Table 5.3 shows the exact amount of retained austenite in each phase and retained austenite morphology in bainite. For this analysis, any retained austenite located at the polygonal ferrite/bainite interface in an un-deformed condition was allocated to bainite.

Table 5.4: The effect of straining on the retained austenite morphology.

Steels		**Retained austenite (%)**		**Retained austenite aspect ratio in bainite (AR≤ 1.5 = blocky and > 1.5 = Films)**	
		In PF %	In Bainite %	Blocky %	Film %
Base	Initial	1.3	98.7	27	73
	UTS	~0	100	33.2	66.8
	Fracture	0	100	33.8	66.2
Nb-Ti	Initial	0.5	99.5	34.5	65.5
	UTS	~0	100	34.7	65.3
	Fracture	0	100	34.4	65.6

The shape of retained austenite (blocky or film) is another important factor for mechanical stability as well as the size of retained austenite [152]. In this study, both steels have almost the same ratio of these morphologies (~35% blocky/65% film). Although the low stability of the blocky retained austenite was reported in the literature [102], we observed that the blocky shape had a similar stability to the film morphology during the tensile test. However, most of the retained austenite with film-like morphology existed in a parallel orientation, which is another factor that reduces the stability of retained austenite compared to randomly oriented retained austenite [158].

To confirm the effect of the shape of retained austenite, a morphology analysis was also applied a second time, but only on large grain size retained austenite to avoid the effect of the subgrain size on the stability. Nevertheless, the ratio of the blocky type to the film shape remained the same as in Table 5.4. This suggested that the shape of retained austenite had a minor effect on the stability of retained austenite in this study because both transformed at approximately the same rate.

The presence of blocky retained austenite after tensile deformation could also be attributed to the subdivision of the retained austenite films into small blocky grains of retained austenite, as shown in Fig. 5.18. A misleading conclusion on the stability of blocky retained austenite due to partial transformation was also reported by Lomholt *et al.* [101]. Moreover, the size of the retained austenite can play a major role in the stability of the blocky retained austenite because these very small grains are very stable and thus may never transform to martensite.

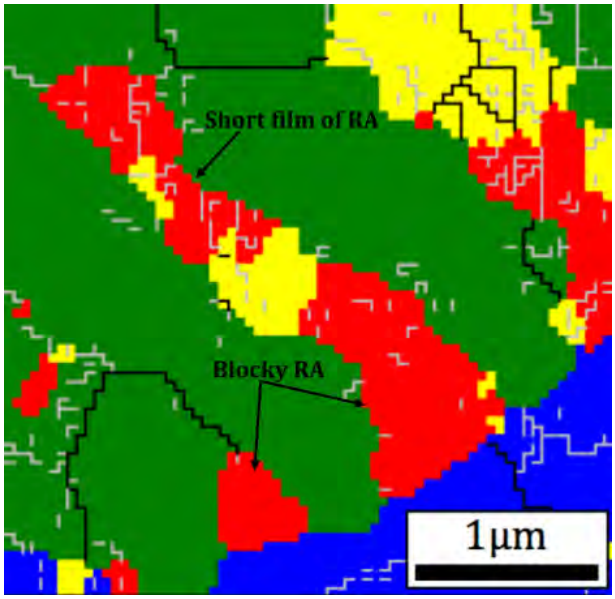

Figure 5.18: The partial transformation of the retained austenite in the Nb-Ti steel at UTS, which divided the retained austenite films into blocky retained austenite or short films.

5.2.5 The Stability of Retained Austenite in Polygonal Ferrite

The retained austenite was formed at three main locations: between the polygonal ferrite grains, at the polygonal ferrite/bainite interface and within the bainite grains. However, most of retained austenite was found within the bainitic ferrite laths with some minor fraction at the polygonal ferrite/bainite interface. The amount of retained austenite between the polygonal ferrite grains was very small which is 1.3% and 0.5% of the total amount of retained austenite in the base and Nb-Ti steel, respectively (Table 5.4). Following tensile deformation, almost no retained austenite was observed in the polygonal ferrite grains in both steels.

The low stability of retained austenite in the polygonal ferrite occurred because the polygonal ferrite is the softest phase among all phases present and work hardens first at the beginning of deformation. Then the load transfers to the retained austenite grains within the polygonal ferrite grains as the yield strength of the retained austenite is higher than the polygonal ferrite [152] due to the high carbon content in the retained austenite. Therefore, the mechanical stability of retained austenite in the polygonal ferrite was lower compared to the retained austenite formed within other harder phases, such as bainite. Similar results were reported in Ref. [10] where only 2% and 5% of retained austenite out of a total of 13% and 11% were detected between polygonal ferrite grains in the base and Nb high Si TRIP steels, respectively. However, all the retained austenite located between polygonal ferrite grains transformed to martensite after 0.1 strain.

The stability of the retained austenite in the polygonal ferrite was also influenced by the number of neighbouring polygonal ferrite grains. The influence of the number of polygonal ferrite grains neighbouring retained austenite on the stability of retained austenite was investigated by Lomholt *et al.* [101]. An in situ EBSD analysis on 0.24C-2Mn-1.6Al-0.6Cr+Mo-0.2Nb+Ti (wt%) TRIP steel tracked the transformation of retained austenite with tensile deformation up to 7.9% elongation. It has been found that most of the retained austenite grains bounded by more than two ferrite grains were fully transformed to martensite. Moreover, most of the retained austenite grains bounded by two ferrite grains were partially transformed [101] whereas the retained austenite embedded in the polygonal ferrite grain had a higher stability [159]. Moreover, the retained austenite grains were influenced by the ferrite grain boundary. That part of the retained austenite close to the grain boundary transformed whereas the part that was far from the grain boundary was more stable. It was stated that the partial transformation that started at the grain boundary of ferrite was due to the local strain gradient in the vicinity of the grain

boundary [101]. The shear stress was highest at the grain boundary, which in turn encouraged the transformation of retained austenite to martensite.

In the current study, Fig. 5.19a shows the full transformation of a small retained austenite grain and Fig. 5.19b shows the partial transformation of a large retained austenite grain after tensile testing. It was speculated that the martensite grains shown in Fig. 5.19 were formed during tensile testing because only very small fractions of martensite were observed before deformation. The location of tiny retained austenite grains between polygonal ferrite grains and at the grain boundary, Fig. 5.19a, forced the retained austenite grains to transform. On the other hand, although the retained austenite grain shown in Fig. 5.19b was large, it was very stable and only partially transformed because it had not been affected by the grain boundary and was located inside the polygonal ferrite grain. Similarly, small retained austenite grains in the polygonal ferrite showed higher stability because they were located far from the grain boundary of polygonal ferrite (Fig. 5.19 c). This behaviour agrees with Ref. [26] where the ferrite grain boundary and the number of surrounding polygonal ferrite grains influenced the stability of the retained austenite within the polygonal ferrite microstructure.

The amount of low angle boundaries around the transformed and untransformed retained austenite grains increased, as shown in Fig. 5.19, due to an increase in the density of GNDs and their rearrangement into low energy configurations; this was also evidence of the strain fields in these areas. This increase of GNDs was required to accommodate: (i) the inhomogeneity of plastic deformation around hard austenite/martensite crystals in polygonal ferrite and, (ii) the volume expansion accompanying the martensite transformation.

The presence of a deformation zone around the martensite or austenite grains (Fig. 5.19) can also affect the stress partitioning between the phases and also increase the strength of the polygonal ferrite [10, 160]. Moreover, other factors such as size, blocky shape, and carbon content could explain the low stability of the retained austenite in polygonal ferrite. Of these, probably chemical stability will be a dominant factor because the retained austenite in polygonal ferrite is expected to have a lower carbon content (due to the intake of carbon only from austenite to polygonal ferrite transformation) than the retained austenite in bainite. On another hand, the retained austenite in bainite has the benefit of additional carbon enrichment which diffuses out of bainitic ferrite during its growth [161, 162].

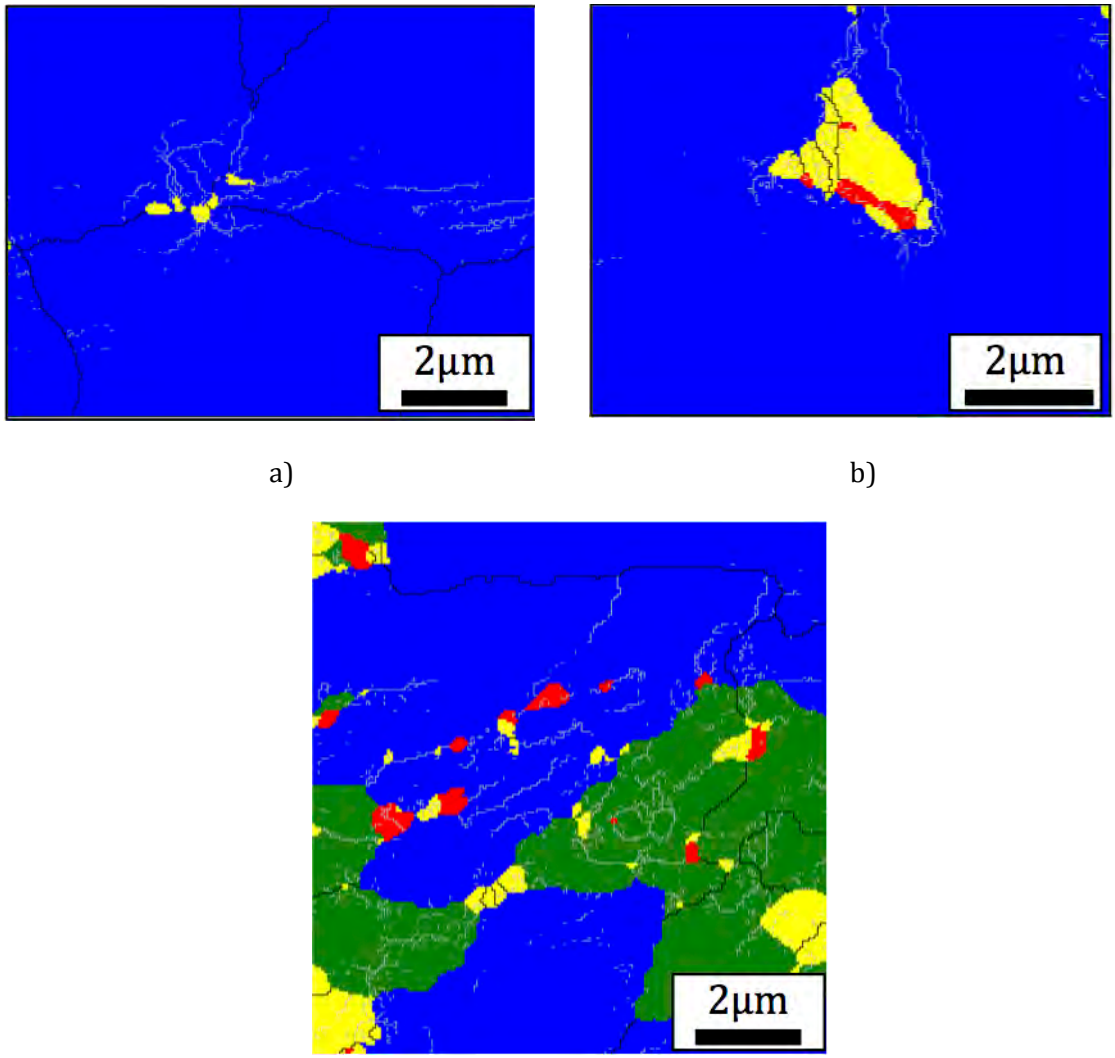

a) b)

c)

Figure 5.19: Examples of the transformation behaviour of the retained austenite grains located in polygonal ferrite: a) large martensite/retained austenite grain within one polygonal ferrite grain, b) small martensite/retained austenite grains at the boundary of polygonal ferrite grains and c) non-transformed small retained austenite grains within the polygonal ferrite grain.

5.2.6 The Stability of the Retained Austenite at the Polygonal Ferrite/ Bainite Interface

Prior to tensile deformation, there was a considerable amount of retained austenite at the interface of bainite and polygonal ferrite, but a larger fraction of these grains had transformed to martensite than those located within the bainite after tension; which is clear from the increased number of martensite grains at the interphase boundary at UTS (Fig. 5.20). Both steels showed a similar low stability of retained austenite at the polygonal ferrite/bainite interface. In this study it was difficult to estimate the amount of retained austenite at the interface before deformation because most of the retained austenite films grew from the interphase boundary into the interior of the bainite. This made it difficult to distinguish between the retained austenite grains at the interface and retained austenite grains within the bainite. In contrast, after tension, the retained austenite grains at the interphase boundary were more distinguishable. Accordingly, in both steels the amount of retained austenite grains at the interface after deformation was estimated to be ~30% of the total retained austenite whereas ~70% remained within the bainite.

Prior to tensile deformation, the amount of retained austenite formed at the interface of polygonal ferrite and bainite in the high Si TRIP steel investigated by Timokhina *et al.* [10] was ~18-25% of the total amount of retained austenite present. It was stated that after deformation, the retained austenite formed at the interface of polygonal ferrite and bainite had a higher stability than the retained austenite formed within polygonal ferrite grains but a lower stability than the retained austenite formed within bainite grains. Moreover, the amount of retained austenite at the polygonal ferrite/bainite interface had reduced to ~5% of the total retained austenite fraction present at UTS. The low carbon content in the retained austenite grains was suggested as the reason for the low stability of retained austenite at the polygonal ferrite/bainite interface. Surprisingly, the amount of retained austenite at the interphase boundary at UTS in this and a previous study [10] was ~0.4%, but this fraction is equivalent to 30% and 5% of the total amount of retained austenite remaining in low Si and high Si TRIP steels, respectively. Although both steels (high and low Si TRIP steels) had different carbon contents in the retained austenite (~1.2 vs. ~1.6-1.8 wt.%), the transformation of retained austenite at the interface was similar. It can therefore be speculated that the stability of retained austenite at the polygonal ferrite/bainite interphase boundary is always low and was not influenced by the average carbon content in the retained austenite.

However, it was reported previously [10, 98, 102, 152] that the non-uniform distribution of carbon between and within different retained austenite grains, and the formation of martensite in some parts of the retained austenite grains could be responsible for an

overall reduction in the stability of retained austenite. Consequently, the partial transformation that was mostly observed in that part of the retained austenite close to the polygonal ferrite in this study (Fig. 5.20) could be explained by the influence of the low chemical stability of the retained austenite as well as the higher stresses near the interface regions.

The variation in carbon in the retained austenite grains at the polygonal ferrite/bainite interface was influenced by the diffusion distance during the formation of bainite. So when the diffusion distance is very small, the variation of carbon in the retained austenite grain was expected to be high, particularly in the large retained austenite grains. Therefore, it is important to estimate the diffusion distance during bainite transformation to understand the chemical stability of the retained austenite.

The carbon diffusion distance in the retained austenite grains depends mainly on temperature and time, and therefore it was expected that the variation in carbon in a large retained austenite grain would be more than in a small grain. Additionally, the centre of a large retained austenite grain will have less carbon if there was not enough time for the carbon to reach the centre during the bainitic transformation. The diffusion distance of the carbon in austenite can be calculated based on the diffusivity equation [163, 164]:

$$D = D_0 \exp\left[\frac{-Q}{RT}\right] \tag{5.2}$$

Where D is diffusivity in m^2/s, D_0 is the proportionality constant $=1.9\times10^{-5}$ m^2/s, Q is the activation energy of the diffusion= 157000 J/mol, R is the molar gas constant= 8.3 J/mol.K and T is the temperature in K. Based on the diffusivity equation, the diffusion distance of carbon in the retained austenite during the bainitic transformation can be calculated as follows:

$$x = \sqrt{Dt} \tag{5.3}$$

Where x is the diffusion distance, D is the diffusivity, and t is the time in seconds. According to above equations the diffusivity of carbon in the retained austenite during the bainitic transformation at 470°C for 1200 s was estimated as 1.71×10^{-16} m^2/s and the diffusion distance as 0.5 μm. From this it can be concluded that the time and temperature applied in this study during bainitic transformation was enough for carbon to reach the centre of the 1μm retained austenite grains. However, other factors may influence the diffusion distance, such as effect of other alloying elements on the diffusivity of carbon, but they were not considered in the above equations. Thus, this distance may be even less than the estimated value.

The small diffusion distance can also explain the partial transformation of retained austenite at the polygonal ferrite/bainite interface. Figure 5.21 shows that the part of the retained austenite far from the bainite interphase (>0.5 μm) was fully transformed while that part of the retained austenite grain close to the bainite was untransformed. This result indicated how important chemical stability is on the transformation of retained austenite at the polygonal ferrite/bainite interface.

Furthermore, the strain heterogeneity in TRIP steel can also influence the stability of retained austenite [152, 155]. Polygonal ferrite work hardens faster in the regions close to polygonal ferrite/bainite interface because bainite is harder than polygonal ferrite, thus more strain accumulates at the polygonal ferrite/bainite interface. To accommodate the inhomogeneity of plastic deformation more dislocations are formed which then rearrange themselves to lower energy configurations. This was clear from the increase in the fraction of low angle boundaries at the polygonal ferrite/bainite interface (Fig. 5.20). Therefore, not only does the stress concentration increase near polygonal ferrite/bainite interface but a load transfer from polygonal ferrite to bainite also takes place at the interphase boundary. Both these factors increase the transformation of retained austenite at the interface, which in turn can explain the high amount of martensite at the interphase.

The influence of the partial transformation of retained austenite on the rate of transformation is debatable because on one hand, the mechanical stability of retained austenite is reduced as the external stress is propagated directly to the retained austenite through the hard martensite phase; which then conversely increases the total driving force for the retained austenite to transform to martensite [29]. But on the other hand, it has been suggested that the newly formed martensite delays the transformation of remaining retained austenite by shielding the retained austenite from plastic deformation [101].

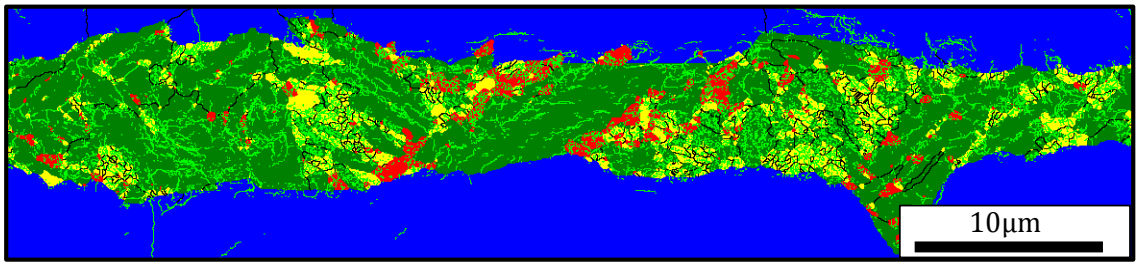

a)

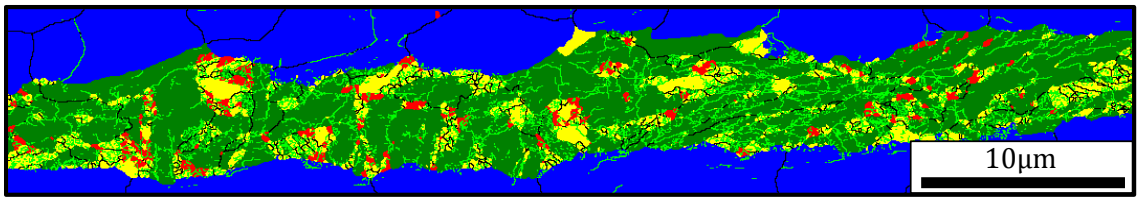

b)

Figure 5.20: EBSD phase maps showing the partial transformation of retained austenite at UTS: a) base steel and b) Nb-Ti steel. HAGBs= black lines, LAGBs= light green lines. The polygonal ferrite (PF) = blue, retained austenite (RA) = red, bainite = green and martensite = yellow.

It should be pointed out that the orientation and shape of the retained austenite grains with respect to the polygonal ferrite/bainite interface also affects their stability. The retained austenite grains located at the interface of polygonal ferrite/bainite after tensile deformation are either parallel to the interface boundary (Fig. 5.21) or protruding in the polygonal ferrite grains (Fig. 5.22). It has been observed that the stability of the protruding retained austenite grains is higher than the retained austenite grains that are oriented parallel to the polygonal ferrite/bainite interface. At UTS most of the retained austenite grains oriented parallel to the polygonal ferrite/bainite interface were transformed to martensite. In most cases, that part of the retained austenite which was in contact with polygonal ferrite was fully transformed, whereas the part of the retained austenite in contact with bainite remained untransformed. However, the grain size of the untransformed retained austenite at the interface was very small which may be why these grains have a high mechanical stability, as shown in Fig. 5.21.

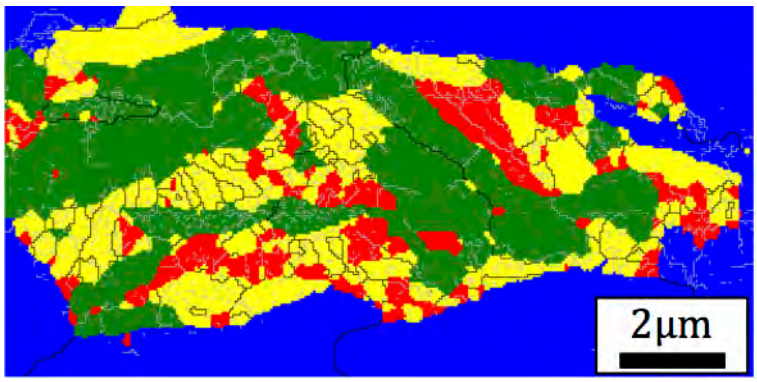

Figure 5.21: Partial transformation behaviour of retained austenite at the polygonal ferrite/bainite interface in the Nb-Ti steel at UTS. Minor amount of small retained austenite grains are observed at the interphase boundary. HAGBs= Black colour, LAGBs=

Light green colour. The polygonal ferrite (PF) = blue, retained austenite (RA) = red, ferrite in bainite = green and martensite = yellow.

In contrast, the retained austenite grains protruding into the polygonal ferrite could be large or small, as shown in Figs. 5.22 and 5.23, and while these large retained austenite grains were unstable [50], they did not transform. However, more than one side of these retained austenite grains were in contact with polygonal ferrite which should enhance their transformation and reduce their overall stability. It has been found in the literature [101], that most retained austenite grains bounded by more than two ferrite grains were fully transformed to martensite whereas most of the retained austenite grains bounded by two ferrite grains were partially transformed. The protruding retained austenite grains were also in contact with bainite as well as polygonal ferrite from more than one side. Moreover, these retained austenite grains show a higher density of low angle boundaries, as shown in Fig. 5.22a. The sub-division of the large retained austenite grains into subgrains can also be suggested as a factor that enhances the stability of retained austenite because it reduced the effective volume for martensite nucleation. In the current study, the number of retained austenite grains that experience enhanced stability by sub-division were not statistically enough to draw a definitive conclusion, but it is a factor that may need further investigation.

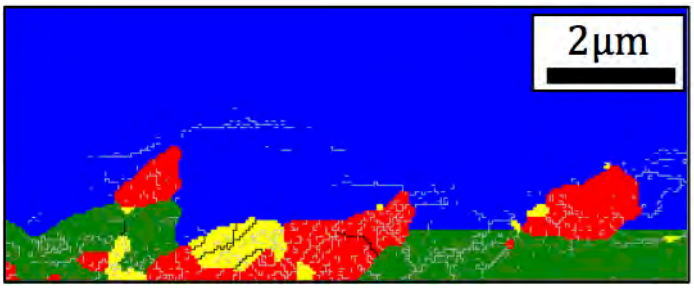

a)

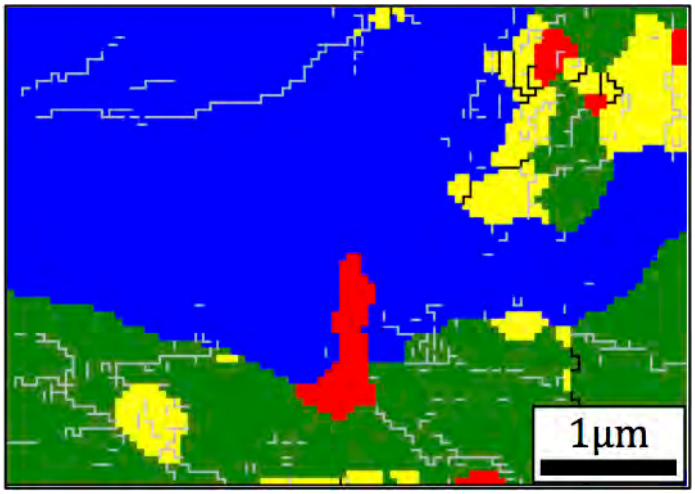

b)

Figure 5.22: An example of protruding retained austenite grains in the polygonal ferrite grains at the interface of polygonal ferrite/bainite in base steel. HAGBs= Black colour, LAGBs= Light green colour. The polygonal ferrite (PF) = blue, retained austenite (RA) = red, ferrite in bainite = green and martensite = yellow.

On the other hand, some larger retained austenite grains protruding inside the polygonal ferrite grains transformed differently (Fig. 5.23), in that the large retained austenite grains transformed fully whereas the smaller grains only partially transformed. Such behaviour can be attributed to the low mechanical stability of the large retained austenite grains, especially if they were not subdivided into sub-grains. However, it was very surprising that the foremost tip of the retained austenite grain that protruded into polygonal ferrite remained untransformed. This means that other factors that can influence the stability of retained austenite could be of important; such as the Mn variation in the retained austenite grains. Tirumalasetty *et al.* [165] investigated the influence of the chemical composition on the transformation of retained austenite grains in Si-added TRIP steel and Al-added TRIP steel by means of EBSD and electron probe microanalysis (EPMA). They found that the stability of the retained austenite reduced with an increasing content of Mn in the austenite grains. This behaviour was attributed to the internal stresses formed in the retained austenite lattice due to the variation in concentration of Mn, such that those areas with a higher stability in the large retained austenite grains might have lower contents of Mn. The effect of Mn on the stability of retained austenite was not conducted in this study and is therefore outside the scope of this work.

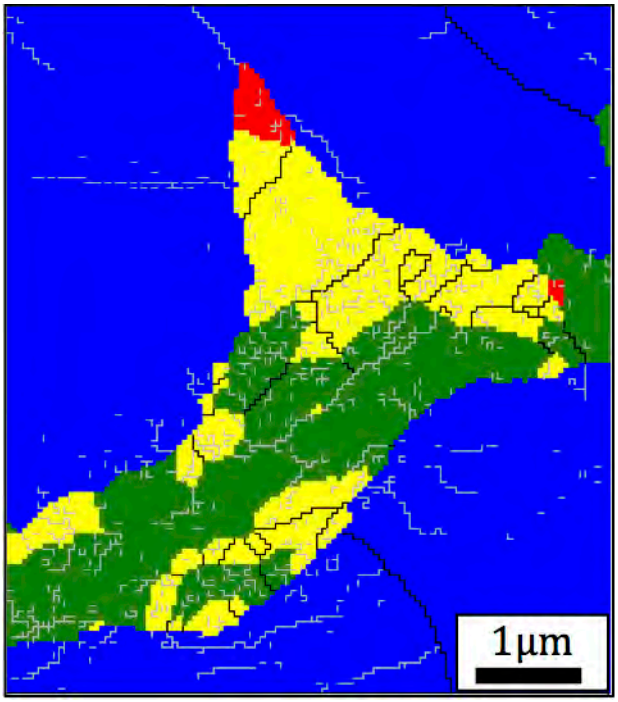

Figure 5.23: An example of protruding retained austenite grains into polygonal ferrite grain at the interface of polygonal ferrite/bainite in base steel. HAGBs= black colour, LAGBs= silver colour. The polygonal ferrite (PF) = blue, retained austenite (RA) = red, ferrite in bainite = green and martensite = yellow.

5.2.7 The Effect of Bainite Morphology on the Retained Austenite Stability

Most of the retained austenite that remained in the microstructure was found within the bainitic ferrite (Fig. 5.19) because bainitic ferrite laths act like a shield that protects the retained austenite from external loads and adds more stability to the retained austenite [137]. As discussed in Section 5.1.4, bainite was present in the bainitic ferrite (lath shape) and granular bainite morphologies, and most of the bainite laths had a parallel orientation in both chemistries. Here ferrite in granular bainite was characterised by a high amount of substructure compared to bainitic ferrite. It is also observed that the lath-shaped bainitic ferrite was the dominant phase in the Nb-Ti steel while the granular bainite was the dominant phase in the base steel. Similar observations regarding the effect that the addition of alloying elements has on the type of bainite were also found in high Si TRIP steel [10].

The difference in the dominant bainite phase morphology explains the high average KAM of the bainite phase in the base steel compared to the Nb-Ti steel, as shown in the Fig. 5.16. The average KAM of the bainite was 1.04° and 0.66° in the base steel and Nb-Ti steel, respectively. The average KAM increased by ~3% after deformation in the base steel whereas the increase in the KAM in the Nb-Ti steel was ~30%. The exact effect of the bainite morphology on the stability of retained austenite was not clear, however the high transformation rate in Nb-Ti steel where bainitic ferrite was the dominant phase could indicate that the stability of retained austenite was lower in the bainitic ferrite compared to granular bainite, which contradicts previous studies [10]. A similar low stability of film-like retained austenite compared to the blocky retained austenite was reported in Ref. [152] and it was linked to the load transfer when bainitic ferrite has a parallel lath-like structure. Based on the rate of increase in KAM values during tension, it could be suggested that bainitic ferrite accommodated higher strains than granular bainite, thus, more strain transferred to the retained austenite formed within the bainitic ferrite.

Another factor that can influence the stability of the retained austenite located between the bainitic ferrite laths is the carbon distribution. As Fig. 5.24 shows, the area that transformed to martensite was more likely to have less carbon and was therefore less stable than those more stable areas with high carbon content. The transformation of retained austenite mainly occurred at the centre of the retained austenite grains and far from the bainite boundary (Fig. 5.24). This partial transformation behaviour can be linked to the diffusion distance of carbon, which was estimated to be 0.5 μm or even less (in section 5.1.6), and the distance from the interface to the centre of this retained austenite well that exceeds it. This leads to less carbon content at the centre of the retained

austenite grain, so the centre of the retained austenite grain was fully transformed. However, some part of the outer surface of the retained austenite grain was also transformed, possibly due to the inhomogeneous strain distribution evident from the high density of low angle boundaries in some areas around the retained austenite grain, as shown in Fig. 5.24.

It is clear that both chemical and mechanical stability play a role in the deformation-induced transformation of retained austenite to martensite. However, it should be noted that all of the above discussions regarding mechanical stability (size and shape) are based on two-dimensional analysis and do not take into account other factors such as grain rotation and orientation with respect to the deformation axis. These will require further investigation in future.

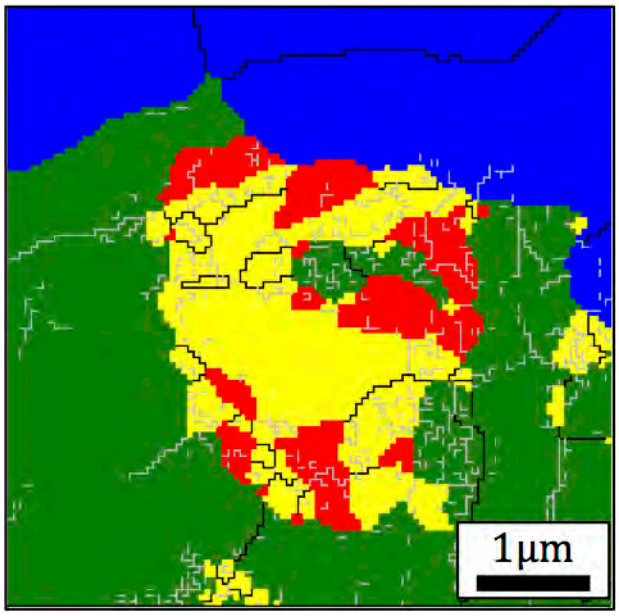

Figure 5.24: The partial transformation of the retained austenite grain in bainite in the Nb-Ti steel at UTS. HAGBs= black colour, LAGBs= Light green colour. The polygonal ferrite (PF) = blue, retained austenite (RA) = red, ferrite in bainite = green and martensite = yellow.

5.3 Conclusions:

1. A newly developed procedure for phase segmentation was successfully applied on two thermo-mechanically processed TRIP steels using EBSD data. Based on grain orientation spread (GOS) and subgrain size criterion, this method was able to distinguish between three phases; polygonal ferrite, bainite and martensite.
2. The variations in the amount of retained austenite at different tensile strains were measured by EBSD. The transformation rate of retained austenite in the Nb-Ti steel was higher than in the base steel, which is an indication of the higher stability of retained austenite in the base steel.
3. The higher stability of retained austenite in the base steel was related to the dominancy of granular bainite in the base steel compared to the dominancy of bainitic ferrite in the Nb-Ti steel. However, a higher initial amount of retained austenite was found in the bainitic ferrite morphology.
4. A local misorientation analysis was conducted on each phase in both steels. The rate of increase in the average KAM values of the bainite phase with tension in the Nb-Ti steel was higher than in the base steel. This behaviour was related to the dominancy of bainitic ferrite morphology in the Nb-Ti steel and deemed to be responsible for the lower stability of retained austenite in bainitic ferrite compared to granular bainite.
5. The stability of large and small retained austenite grains was investigated in this study. It was found that a partial transformation of retained austenite grains could lead to a misleading conclusion regarding the high stability of small retained austenite grains because the partial transformation of large retained austenite grains in turn introduced small retained austenite grains.
6. The stability of the retained austenite at different locations was discussed in this study. Most of the retained austenite was between the bainitic ferrite laths and a small amount of retained austenite was at the polygonal ferrite/bainite interface. The stability of retained austenite at the interface was much less than the stability of retained austenite in the bainite, but higher than the stability of retained austenite in the polygonal ferrite.
7. The partial transformation of retained austenite grains at the interphase was related to the carbon enrichment of retained austenite. Therefore, the part of the retained austenite close to the polygonal ferrite was less stable than the part of the retained austenite close to the bainite. However, it is believed that the

transformation of retained austenite is more complex and is influenced by many factors such as the Mn segregation and the grain orientation which led to non-anticipated transformation behaviour in some of the retained austenite grains.

6 ANALYSIS OF THE CRYSTALLOGRAPHY OF BAINITE

In the previous chapter (Chapter 5), it was shown that the amount of RA in the bainitic ferrite was higher than the RA in the granular bainite. It was also suggested that the dominancy of the granular bainite in the base steel was the main source of the high stability of RA in the base steel. Therefore, the crystallography analysis of the ferrite in different bainite morphologies observed in the current microstructure should increase our understanding of the transformation mechanism of these morphologies. Such analysis was conducted for the first time using EBSD.

This analysis began by finding the closest orientation relationship between the parent austenite and ferrite in bainite that formed during cooling and isothermal holding, and then examined the variants realisation and their arrangement. Furthermore, a special Matlab code was written to calculate the ORs between the parent and product phases and to assign a specific variant to each grain based on the minimum misorientation criteria.

This chapter will cover in the first three sections the methodology of selecting the prior austenite grain, the orientation relationship, and the Matlab code. The output of Matlab code was divided into four sections: the CP arrangement, the Bain arrangement, variant pairs, and variants selection, and in each section the crystallography of ferrite in GB and ferrite laths in BF was differentiated and discussed.

6.1 Selection of a Single Prior Austenite Grain

Reconstructing a prior austenite grain was a necessary step to study the orientation relationship (OR) between austenite and bainite, if no retained austenite is present in the final microstructure. This reconstruction will give the orientation of the parent austenite that can be used for a crystallographic analysis of the product phase such as bainitic ferrite in each individual grain of austenite. An accurate determination of the prior austenite orientation is critical for studying crystallography. Therefore, several models have been developed to reconstruct the prior austenite microstructure [83, 84, 166, 167] that would give an approximate orientation of the parent phase. However, the accuracy of these models are affected by several parameters such as possible variant selection and/or deformation of the product phase [168], as well as by the type of orientation relationships (KS, NW, Bain or GT) selected and used in the model.

Fortunately, in this study the amount of RA was high enough for crystallography analysis without reconstructing the grains [20, 169]. Figure 6.1a shows an example of a cut from an EBSD map that represents a single prior-austenite grain and contains high amount of RA. This area was considered to be a single prior-austenite grain based on the inverse-pole figure (IPF) (Fig. 6.1b) and the pole figure (PF) (Fig. 6.1c) [92]. The IPF shows that the RA had almost the same orientation (approximately one colour) used to indicate a single prior austenite grain; this was also confirmed by the concentration of {001} poles in the pole figure (Fig. 6.1c). All the areas for analysis were selected based on this approach for identifying a single prior austenite grain. A typical spread in prior austenite grain orientation was ~7°±3° and it was associated with austenite being subjected to hot rolling.

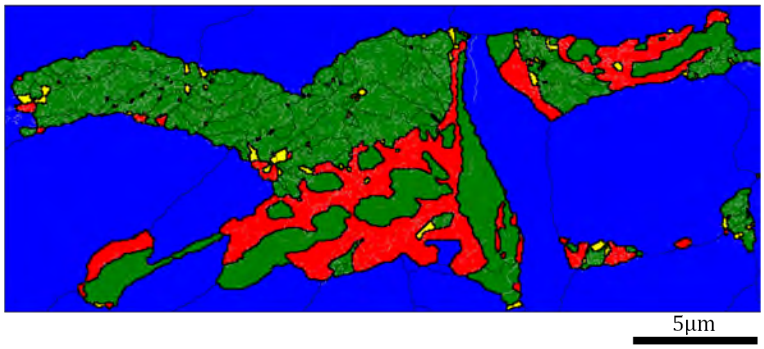

a)

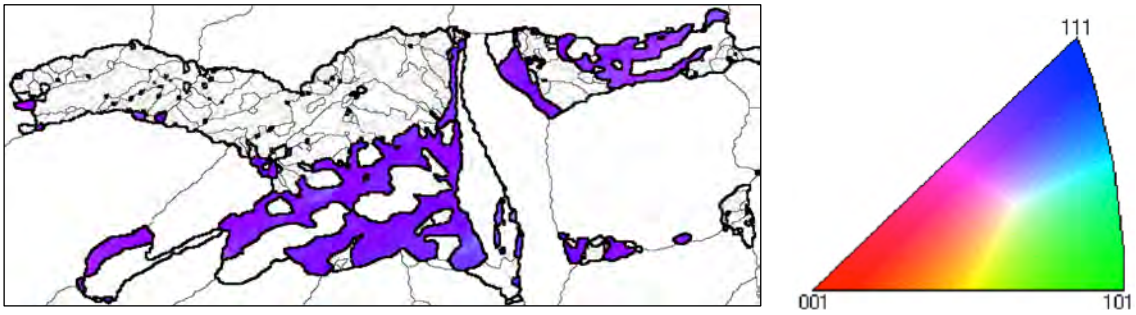

b)

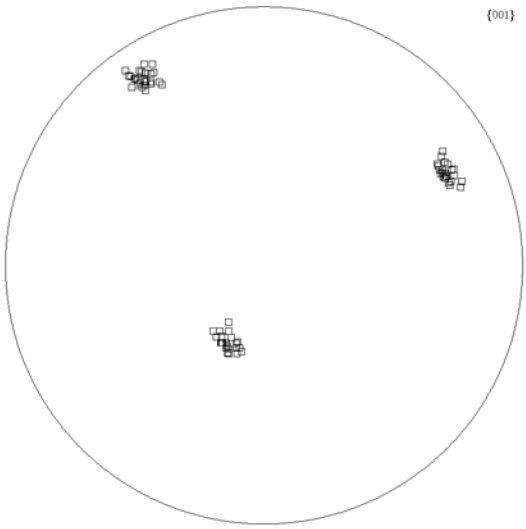

c)

Figure 6.1: An example of a single prior-austenite grain in base steel; a) phase map, b) inverse-pole figure map of the RA and c) {001} pole figure (PF) of the RA. RA = red, PF = blue, ferrite in bainite = green, and martensite = yellow). In (a) thick black line represents phase boundaries, thin black line = HAGBs and sliver lines = LAGBs.

6.2 The Orientation Relationships

There are several theoretical orientation relationships that define the crystallographic relationship between the parent face-centred cubic (fcc) lattice (austenite) and the product body-centred cubic (bcc) lattice or body-centred tetragonal (bct) (martensite or bainitic ferrite), which are widely accepted and used. These relationships are summarised in Table 6.1 and were discussed in the Literature Review in Chapter 2. The most common ORs are Kurdjumov-Sachs (KS) ORs, which were originally determined based on the investigations done on low carbon martensitic steel [74] and Nishiyama-Wasserman (NW) ORs, which were experimentally determined based on Fe-Ni alloys [75, 76]. These ORs are empirical relationships which for simplicity is expressed rationally [168].

Table 6.1: The most common fcc-bcc orientation relationships

	Plane	Direction
Kurdjumov-Sachs (KS) [74]	{111}γ//{110}α	<110>γ//<111>α
Nishiyama-Wassermann (NW) [75, 76]	{111}γ//{110}α	<112>γ//<110>α or <011>γ//<001>α
Greninger-Troiano (GT) [77]	{111}γ~1°//{110}α	<12,17,5>γ//<17,17,7>α
Bain [73]	{010}γ//{010}α	<001>γ//<101>α

An analysis of the data indicated that although the deviation from the exact theoretical KS and NW ORs were very close, the KS ORs had a smaller deviation angle. The average deviation angle of Nb-Ti steel from KS OR was 4.8° while the average deviation angle in the base steel from KS OR was 4.6°. Moreover, the comparison between the theoretical and experimental pole figures (PF) for KS ORs showed a very close resemblance (Fig. 6.2). It was also reported in the literature that the KS OR was the closest OR in TRIP steels [17, 20, 21, 92] and other types of steels [78, 84, 170-173]. Abbasi *et al.* [86] found it difficult to distinguish between a KS OR and other orientation relationships, so the use of KS OR was

expedient based on the highest number of possible variants compared to other ORs. It was also stated by Bhadeshia [87] that there must be 24 possible variants in each prior austenite grain due to the irrational relationship between austenite and bainitic ferrite laths, and although Beladi *et al.* [174] used NW OR, it was stated that the laths had ORs close to the KS ones.

Based on all the above, it was decided to apply the KS ORs in this study to define the orientation relationship between the retained austenite as parent phase and ferrite in GB and BF as a product phase. Although the martensite phase is another product phase present in the current microstructure (Fig. 6.1a), it was not considered in the analysis because it was present in very small amounts and was outside the scope of this study.

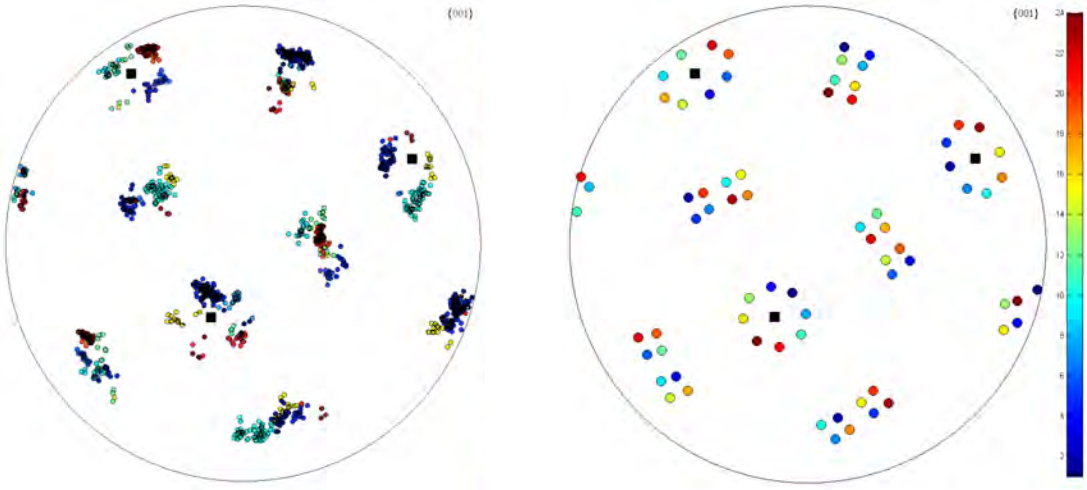

a) b)

Figure 6.2: An example of the {001} pole figure for the orientation relationships between the ferrite in bainite and the RA in base steel, which corresponds to Figure 6.1: a) experimental PF, b) theoretical PF. The average orientation of the RA grain is represented by black squares in a) and b).

In the preliminary analysis in this study, 24 KS variants were assigned based on the minimum misorientation, without setting a constraint on the misorientation angle; this step was used to investigate how large the deviation was from the KS ORs, and in most maps the deviation from KS ORs in was between 0-10°. This observation was also similar to the deviation from the KS orientation at the interface of the RA and ferrite in bainite

(via built-in OR model in HKL software), which showed that the deviation was in the same interval of (0-10°) in all the maps. Verbeken *et al.* [78] used 5° as the maximum deviation in their analysis. Their choice was related to the misorientation between KS and NW ORs, which is 5.26°. However, in their study the percentage of the grains with a misorientation of less than 5° was 47% in one steel and 61% on the other steel, whereas in this current study more than 89% of the map had a misorientation of less than 5°, and therefore the average deviation from the KS OR in all maps was less than 5° even with the 0-10° interval used in this study.

6.3 The Procedure for Crystallographic Analysis

An in-house Matlab code was written for the variant determination and then the results of this program were used as input for the Oxford Channel 5 HKL software to give a visual representation.

The initial step in the program was to convert the 24 KS variants and the experimental data to matrix algebra. However, the 24 KS variants are presented as planes and directions while the experimental data were presented as three Euler angles, so different equations were used for the conversion to matrices followed by calculating the orientation transformation matrices of all KS variants and experimental data, as discussed in the following sections. Finally, a specific KS variant was assigned to each data point in the EBSD map.

6.3.1 Calculation of the theoretical transformation matrices

In a single austenite grain, 24 KS variants (bainite or martensite) can be formed due to the symmetry in the cubic system. These variants were categorised into four packets (CPs, CP1-CP4) based on four different austenite planes, as shown in Table 6.2. Each variant was designated as "V" followed by a variant number from 1 to 24, as shown in the Table 6.2. In each CP there are three Bain groups (BGs, B1-B3) as depicted in Fig. 2.18.

Table 6.2: The 24 variants of KS OR [16, 19, 20, 83, 84]

	Parallel plane			Parallel direction				
Variant number	FCC		BCC	FCC		BCC	CPs	BGs
V1	(111)	//	(011)	$[\bar{1}01]$	//	$[\bar{1}\bar{1}1]$	CP1	B1
V2				$[\bar{1}01]$	//	$[\bar{1}1\bar{1}]$		B2
V3				$[01\bar{1}]$	//	$[\bar{1}\bar{1}1]$		B3
V4				$[01\bar{1}]$	//	$[\bar{1}1\bar{1}]$		B1
V5				$[1\bar{1}0]$	//	$[\bar{1}\bar{1}1]$		B2
V6				$[1\bar{1}0]$	//	$[\bar{1}1\bar{1}]$		B3
V7	$(1\bar{1}1)$	//	(011)	$[10\bar{1}]$	//	$[\bar{1}\bar{1}1]$	CP2	B2
V8				$[10\bar{1}]$	//	$[\bar{1}1\bar{1}]$		B1
V9				$[\bar{1}\bar{1}0]$	//	$[\bar{1}\bar{1}1]$		B3
V10				$[\bar{1}\bar{1}0]$	//	$[\bar{1}1\bar{1}]$		B2
V11				[011]	//	$[\bar{1}\bar{1}1]$		B1
V12				[011]	//	$[\bar{1}1\bar{1}]$		B3
V13	$(\bar{1}11)$	//	(011)	$[0\bar{1}1]$	//	$[\bar{1}\bar{1}1]$	CP3	B1
V14				$[0\bar{1}1]$	//	$[\bar{1}1\bar{1}]$		B3
V15				$[\bar{1}0\bar{1}]$	//	$[\bar{1}\bar{1}1]$		B2
V16				$[\bar{1}0\bar{1}]$	//	$[\bar{1}1\bar{1}]$		B1
V17				[110]	//	$[\bar{1}\bar{1}1]$		B3
V18				[110]	//	$[\bar{1}1\bar{1}]$		B2
V19	$(11\bar{1})$	//	(011)	$[\bar{1}10]$	//	$[\bar{1}\bar{1}1]$	CP4	B3
V20				$[\bar{1}10]$	//	$[\bar{1}1\bar{1}]$		B2
V21				$[0\bar{1}\bar{1}]$	//	$[\bar{1}\bar{1}1]$		B1
V22				$[0\bar{1}\bar{1}]$	//	$[\bar{1}1\bar{1}]$		B3
V23				[101]	//	$[\bar{1}\bar{1}1]$		B2
V24				[101]	//	$[\bar{1}1\bar{1}]$		B1

Each KS variant was expressed as a parallel relationship between the plane and direction of the fcc and bcc. These relationships can be expressed as an orientation transformation matrix (T_{KS}) by multiplying the orientation matrix of bcc (g_{bcc}) by the inverse orientation matrix of fcc (g_{fcc}), as shown in the following equation Eq. (6.1):

$$T_{KS} = g_{bcc} g_{fcc}^{-1} \tag{6.1}$$

Since the variants are presented in Miller indices for bcc and fcc (Table 6.2), the orientation matrix (g) can be calculated by Eq. (6.2).

$$g = \begin{pmatrix} \frac{u}{n} & \frac{kw - lv}{mn} & \frac{h}{m} \\ \frac{v}{n} & \frac{lu - hw}{mn} & \frac{k}{m} \\ \frac{w}{n} & \frac{hv - ku}{mn} & \frac{l}{m} \end{pmatrix} \quad (6.2)$$

Where $m = \sqrt{h^2 + k^2 + l^2}$, $n = \sqrt{u^2 + v^2 + w^2}$ and (hkl) and [uvw] are the plane and direction, respectively.

For example, the plane and direction of the bcc and fcc for V1 in Table 6.2 can be converted to a rotation matrices (g) to calculate the transformation matrix (T_{KS}), as follows:

$$T_{KS} = g_{bcc} g_{fcc}^{-1} \Rightarrow \begin{pmatrix} 0.742 & -0.667 & -0.075 \\ 0.650 & 0.742 & -0.167 \\ 0.167 & 0.075 & 0.983 \end{pmatrix} = \begin{pmatrix} -0.577 & 0.816 & 0.000 \\ -0.577 & -0.408 & 0.707 \\ 0.577 & 0.402 & 0.707 \end{pmatrix} \begin{pmatrix} -0.707 & 0.408 & 0.577 \\ 0.000 & -0.816 & 0.577 \\ 0.707 & 0.408 & 0.577 \end{pmatrix}^{-1} \quad (6.3)$$

These calculations lead 24 orientation matrices for fcc and bcc corresponding to 24 variants in addition to 24 transformation matrices (T_{KS}) for each variant, as shown in Table 6.3. Moreover, multiplying the 24 T_{KS} by the orientation of any prior austenite grain led to 24 variants of bcc being transformed from that austenite grain. For example, the orientations of the 24 variants that were transformed from a single austenite grain (001) are plotted in different colours in the PF, as shown in Fig. 6.3.

Table 6.3: The orientation matrices and transformation matrices for the KS OR. [81, 168]

Variant #	Transformation Matrix (T_{KS})	Variant #	Transformation Matrix (T_{KS})
V1	$\begin{pmatrix} 0.742 & -0.667 & -0.075 \\ 0.650 & 0.742 & -0.167 \\ 0.167 & 0.075 & 0.983 \end{pmatrix}$	V13	$\begin{pmatrix} 0.667 & 0.742 & -0.075 \\ -0.742 & 0.650 & -0.167 \\ -0.075 & 0.167 & 0.983 \end{pmatrix}$
V2	$\begin{pmatrix} 0.075 & 0.667 & -0.742 \\ -0.167 & 0.742 & 0.650 \\ 0.983 & 0.075 & 0.167 \end{pmatrix}$	V14	$\begin{pmatrix} -0.667 & 0.075 & -0.075 \\ -0.742 & -0.167 & 0.650 \\ -0.075 & 0.983 & 0.167 \end{pmatrix}$
V3	$\begin{pmatrix} -0.667 & -0.075 & 0.742 \\ 0.742 & -0.167 & 0.650 \\ 0.075 & 0.983 & 0.167 \end{pmatrix}$	V15	$\begin{pmatrix} 0.075 & -0.667 & 0.742 \\ 0.167 & 0.742 & 0.650 \\ -0.983 & 0.075 & 0.167 \end{pmatrix}$
V4	$\begin{pmatrix} 0.667 & -0.742 & 0.075 \\ 0.742 & 0.650 & -0.167 \\ 0.075 & 0.167 & 0.983 \end{pmatrix}$	V16	$\begin{pmatrix} 0.742 & 0.667 & 0.075 \\ -0.650 & 0.742 & -0.167 \\ -0.167 & 0.075 & 0.983 \end{pmatrix}$
V5	$\begin{pmatrix} -0.075 & 0.742 & -0.667 \\ -0.167 & 0.650 & 0.742 \\ 0.983 & 0.167 & 0.075 \end{pmatrix}$	V17	$\begin{pmatrix} -0.742 & -0.075 & -0.667 \\ -0.650 & -0.167 & 0.742 \\ -0.167 & 0.983 & 0.075 \end{pmatrix}$
V6	$\begin{pmatrix} -0.742 & 0.075 & 0.667 \\ 0.650 & -0.167 & 0.742 \\ 0.167 & 0.983 & 0.075 \end{pmatrix}$	V18	$\begin{pmatrix} -0.075 & -0.742 & 0.667 \\ 0.167 & 0.650 & 0.742 \\ -0.983 & 0.167 & 0.075 \end{pmatrix}$
V7	$\begin{pmatrix} -0.075 & 0.667 & 0.742 \\ -0.167 & -0.742 & 0.650 \\ 0.983 & -0.075 & 0.167 \end{pmatrix}$	V19	$\begin{pmatrix} 0.742 & -0.075 & 0.667 \\ 0.650 & -0.167 & -0.742 \\ 0.167 & 0.983 & -0.075 \end{pmatrix}$
V8	$\begin{pmatrix} -0.742 & -0.667 & 0.075 \\ 0.650 & -0.742 & -0.167 \\ 0.167 & -0.075 & 0.983 \end{pmatrix}$	V20	$\begin{pmatrix} 0.075 & -0.742 & -0.667 \\ -0.167 & 0.650 & -0.742 \\ 0.983 & 0.167 & -0.075 \end{pmatrix}$
V9	$\begin{pmatrix} 0.742 & 0.075 & -0.667 \\ 0.650 & 0.167 & 0.742 \\ 0.167 & -0.983 & 0.075 \end{pmatrix}$	V21	$\begin{pmatrix} -0.667 & 0.742 & 0.075 \\ 0.742 & 0.650 & 0.167 \\ 0.075 & 0.167 & -0.983 \end{pmatrix}$
V10	$\begin{pmatrix} 0.075 & 0.742 & 0.667 \\ -0.167 & -0.650 & 0.742 \\ 0.983 & -0.167 & 0.075 \end{pmatrix}$	V22	$\begin{pmatrix} 0.667 & 0.075 & 0.742 \\ 0.742 & -0.167 & -0.650 \\ 0.075 & 0.983 & -0.167 \end{pmatrix}$
V11	$\begin{pmatrix} -0.667 & -0.742 & -0.075 \\ 0.742 & -0.650 & -0.167 \\ 0.075 & -0.167 & 0.983 \end{pmatrix}$	V23	$\begin{pmatrix} -0.075 & -0.667 & -0.742 \\ -0.167 & 0.742 & -0.650 \\ 0.983 & 0.075 & -0.167 \end{pmatrix}$
V12	$\begin{pmatrix} 0.667 & -0.075 & -0.742 \\ 0.742 & 0.167 & 0.650 \\ 0.075 & -0.983 & 0.167 \end{pmatrix}$	V24	$\begin{pmatrix} -0.742 & 0.667 & -0.075 \\ 0.650 & 0.742 & 0.167 \\ 0.167 & 0.075 & -0.983 \end{pmatrix}$

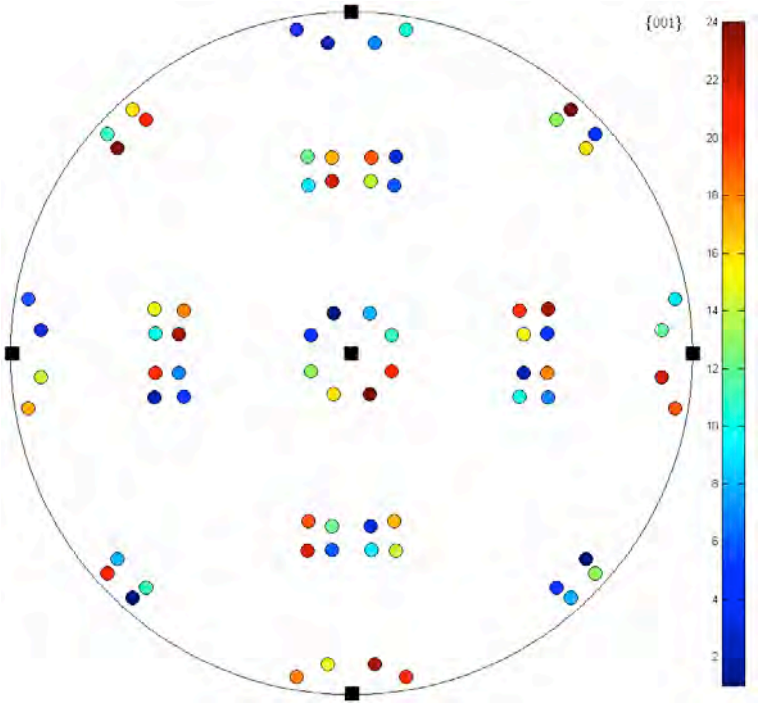

Figure 6.3: The {001} pole figure where circles represent the 24 KS variants transformed from (001) austenite, which is shown as black squares.

The misorientation angle and the axis between the KS variants can be obtained by multiplying the (T_{KS}) of each variant (V1 – V24) by the inverse of the reference variant $(T_{KS})^{-1}$ such as V1, by using Eq. 6.4. . However, the symmetry in the cubic system means that each operation in Eq. 6.4 leads to 24 matrices when it is multiplied by the symmetrical matrices shown in Table 6.4. The minimum misorientation angle and the orientation axis between the two KS variants can be obtained by applying Eqs. 6.5 and 6.6 onto the Δg matrix.

$$\Delta g = T_{2-24} T_1^{-1} \tag{6.4}$$

$$\theta = \cos^{-1} \frac{g_{11} + g_{22} + g_{33} - 1}{2} \tag{6.5}$$

$$\mathbf{r} = [(g_{23} - g_{32})/2\sin(\theta) \quad (g_{31} - g_{13})/2\sin(\theta) \quad (g_{12} - g_{21})/2\sin(\theta)] \tag{6.6}$$

Based on Eq. 6.4, for example, the relationship of all the variants relative to V1 can be obtained by calculating the minimum angle and axis, as shown in Table 6.5, which

compares well with the literature [81], and by following a similar procedure, the misorientation angles between all the variants relative to each other can be calculated as shown in Table 6.6.

Table 6.4: The 24 symmetric matrices for cubic system.

$\begin{pmatrix} 1 & 0 & 0 \\ 0 & 1 & 0 \\ 0 & 0 & 1 \end{pmatrix}$	$\begin{pmatrix} 0 & 0 & \bar{1} \\ 0 & \bar{1} & 0 \\ \bar{1} & 0 & 0 \end{pmatrix}$	$\begin{pmatrix} 0 & 0 & \bar{1} \\ 0 & 1 & 0 \\ 1 & 0 & 0 \end{pmatrix}$	$\begin{pmatrix} \bar{1} & 0 & 0 \\ 0 & 1 & 0 \\ 0 & 0 & \bar{1} \end{pmatrix}$	$\begin{pmatrix} 0 & 0 & 1 \\ 0 & 1 & 0 \\ \bar{1} & 0 & 0 \end{pmatrix}$	$\begin{pmatrix} 1 & 0 & 0 \\ 0 & 0 & \bar{1} \\ 0 & 1 & 0 \end{pmatrix}$
$\begin{pmatrix} 1 & 0 & 0 \\ 0 & \bar{1} & 0 \\ 0 & 0 & \bar{1} \end{pmatrix}$	$\begin{pmatrix} 1 & 0 & 0 \\ 0 & 0 & 1 \\ 0 & \bar{1} & 0 \end{pmatrix}$	$\begin{pmatrix} 0 & \bar{1} & 0 \\ 1 & 0 & 0 \\ 0 & 0 & 1 \end{pmatrix}$	$\begin{pmatrix} \bar{1} & 0 & 0 \\ 0 & \bar{1} & 0 \\ 0 & 0 & 1 \end{pmatrix}$	$\begin{pmatrix} 0 & 1 & 0 \\ \bar{1} & 0 & 0 \\ 0 & 0 & 1 \end{pmatrix}$	$\begin{pmatrix} 0 & 0 & 1 \\ 1 & 0 & 0 \\ 0 & 1 & 0 \end{pmatrix}$
$\begin{pmatrix} 0 & 1 & 0 \\ 0 & 0 & 1 \\ 1 & 0 & 0 \end{pmatrix}$	$\begin{pmatrix} 0 & 0 & \bar{1} \\ \bar{1} & 0 & 0 \\ 0 & 1 & 0 \end{pmatrix}$	$\begin{pmatrix} 0 & \bar{1} & 0 \\ 0 & 0 & 1 \\ \bar{1} & 0 & 0 \end{pmatrix}$	$\begin{pmatrix} 0 & 1 & 0 \\ 0 & 0 & \bar{1} \\ \bar{1} & 0 & 0 \end{pmatrix}$	$\begin{pmatrix} 0 & 0 & \bar{1} \\ 1 & 0 & 0 \\ 0 & \bar{1} & 0 \end{pmatrix}$	$\begin{pmatrix} 0 & 0 & 1 \\ \bar{1} & 0 & 0 \\ 0 & \bar{1} & 0 \end{pmatrix}$
$\begin{pmatrix} 0 & \bar{1} & 0 \\ 0 & 0 & \bar{1} \\ 1 & 0 & 0 \end{pmatrix}$	$\begin{pmatrix} 0 & 1 & 0 \\ 1 & 0 & 0 \\ 0 & 0 & \bar{1} \end{pmatrix}$	$\begin{pmatrix} \bar{1} & 0 & 0 \\ 0 & 0 & 1 \\ 0 & 1 & 0 \end{pmatrix}$	$\begin{pmatrix} 0 & 0 & 1 \\ 0 & \bar{1} & 0 \\ 1 & 0 & 0 \end{pmatrix}$	$\begin{pmatrix} 0 & \bar{1} & 0 \\ \bar{1} & 0 & 0 \\ 0 & 0 & \bar{1} \end{pmatrix}$	$\begin{pmatrix} \bar{1} & 0 & 0 \\ 0 & 0 & \bar{1} \\ 0 & \bar{1} & 0 \end{pmatrix}$

Table 6.5: Misorientation axis and angles of all KS OR variants relative to V1. Variants belong to each CP (CP1, CP2, CP3 and CP4) are grouped [17].

Variant number	Rotation axis (r)	Misorientation From V1 (θ)	CP
V1--			CP1
V2	[-0.58, -0.58, 0.58]	60°	
V3	[0, 0.71, 0.71]	60°	
V4	[0, -0.71, -0.71]	10.5°	
V5	[0, -0.71, -0.71]	60°	
V6	[0, 0.71, 0.71]	49.5°	
V7	[-0.58, -0.58, 0.58]	49.5°	CP2
V8	[0.58, 0.58, -0.58]	10.5°	
V9	[-0.61, 0.19, -0.77]	50.5°	
V10	[-0.74, -0.46, 0.49]	50.5°	
V11	[0.93, 0.35, 0.07]	14.9°	
V12	[-0.36, 0.6, 0.71]	57.2°	
V13	[0.35, -0.93, -0.07]	14.9°	CP3
V14	[-0.49, 0.46, -0.74]	50.5°	
V15	[-0.74, -0.25, 0.63]	57.2°	
V16	[0.66, -0.66, -0.36]	20.6°	
V17	[-0.66, 0.36, -0.66]	51.7°	
V18	[-0.72, -0.3, 0.63]	47.1°	
V19	[-0.19, 0.77, 0.61]	50.5°	CP4
V20	[0.36, 0.71, -0.6]	57.2°	
V21	[0.96, 0, -0.3]	20.6°	
V22	[-0.3, 0.63, 0.72]	47.1°	
V23	[-0.25, -0.63, -0.74]	57.2°	
V24	[0.91, -0.41, 0]	21.1°	

Table 6.6: The misorientation angles between all KS OR variants

	V1	V2	V3	V4	V5	V6	V7	V8	V9	V10	V11	V12	V13	V14	V15	V16	V17	V18	V19	V20	V21	V22	V23	V24
V1	0.00	60.00	60.00	10.53	60.00	49.47	49.47	10.53	50.51	50.51	14.88	57.21	14.88	50.51	57.21	20.61	51.73	47.11	50.51	57.21	20.61	47.11	57.21	21.06
V2	60.00	0.00	49.47	60.00	10.53	60.00	10.53	49.47	57.21	14.88	50.51	50.51	57.21	50.51	21.06	57.21	47.11	20.61	50.51	14.88	47.11	51.73	20.61	57.21
V3	60.00	49.47	0.00	60.00	60.00	10.53	50.51	57.21	20.61	47.11	57.21	21.06	49.47	10.53	50.51	50.51	14.88	57.21	14.88	50.51	57.21	20.61	51.73	47.11
V4	10.53	60.00	60.00	0.00	49.47	60.00	50.51	14.88	47.11	51.73	20.61	57.21	10.53	49.47	57.21	14.88	50.51	50.51	57.21	50.51	21.06	57.21	47.11	20.61
V5	60.00	10.53	60.00	49.47	0.00	60.00	14.88	50.51	57.21	20.61	51.73	47.11	50.51	57.21	20.61	47.11	57.21	21.06	49.47	10.53	50.51	50.51	14.88	57.21
V6	49.47	60.00	10.53	60.00	60.00	0.00	57.21	50.51	21.06	57.21	47.11	20.61	50.51	14.88	47.11	51.73	20.61	57.21	10.53	49.47	57.21	14.88	50.51	50.51
V7	49.47	10.53	50.51	50.51	14.88	57.21	0.00	60.00	60.00	10.53	60.00	49.47	47.11	51.73	20.61	57.21	50.51	14.88	47.11	20.61	57.21	50.51	21.06	57.21
V8	10.53	49.47	57.21	14.88	50.51	50.51	60.00	0.00	49.47	60.00	10.53	60.00	20.61	47.11	57.21	21.06	50.51	57.21	51.73	47.11	14.88	50.51	57.21	20.61
V9	50.51	57.21	20.61	47.11	57.21	21.06	60.00	49.47	0.00	60.00	60.00	10.53	57.21	14.88	50.51	50.51	10.53	49.47	20.61	57.21	50.51	14.88	47.11	51.73
V10	50.51	14.88	47.11	51.73	20.61	57.21	10.53	60.00	60.00	0.00	49.47	60.00	50.51	50.51	14.88	57.21	49.47	10.53	57.21	21.06	50.51	57.21	20.61	47.11
V11	14.88	50.51	57.21	20.61	51.73	47.11	60.00	10.53	60.00	49.47	0.00	60.00	21.06	57.21	47.11	20.61	57.21	50.51	50.51	50.51	10.53	49.47	57.21	14.88
V12	57.21	50.51	21.06	57.21	47.11	20.61	49.47	60.00	10.53	60.00	60.00	0.00	57.21	20.61	51.73	47.11	14.88	50.51	14.88	57.21	49.47	10.53	50.51	50.51
V13	14.88	57.21	49.47	10.53	50.51	50.51	47.11	20.61	57.21	50.51	21.06	57.21	0.00	60.00	60.00	10.53	60.00	49.47	47.11	51.73	20.61	57.21	50.51	14.88
V14	50.51	50.51	10.53	49.47	57.21	14.88	51.73	47.11	14.88	50.51	57.21	20.61	60.00	0.00	49.47	60.00	10.53	60.00	20.61	47.11	57.21	21.06	50.51	57.21
V15	57.21	21.06	50.51	57.21	20.61	47.11	20.61	57.21	50.51	14.88	47.11	51.73	60.00	49.47	0.00	60.00	60.00	10.53	57.21	14.88	50.51	50.51	10.53	49.47
V16	20.61	57.21	50.51	14.88	47.11	51.73	57.21	21.06	50.51	57.21	20.61	47.11	10.53	60.00	60.00	0.00	49.47	60.00	50.51	50.51	14.88	57.21	49.47	10.53
V17	51.73	47.11	14.88	50.51	57.21	20.61	50.51	50.51	10.53	49.47	57.21	14.88	60.00	10.53	60.00	49.47	0.00	60.00	21.06	57.21	47.11	20.61	57.21	50.51
V18	47.11	20.61	57.21	50.51	21.06	57.21	14.88	57.21	49.47	10.53	50.51	50.51	49.47	60.00	10.53	60.00	60.00	0.00	57.21	20.61	51.73	47.11	14.88	50.51
V19	50.51	50.51	14.88	57.21	49.47	10.53	47.11	51.73	20.61	57.21	50.51	14.88	47.11	20.61	57.21	50.51	21.06	57.21	0.00	60.00	60.00	10.53	60.00	49.47
V20	57.21	14.88	50.51	50.51	10.53	49.47	20.61	47.11	57.21	21.06	50.51	57.21	51.73	47.11	14.88	50.51	57.21	20.61	60.00	0.00	49.47	60.00	10.53	60.00
V21	20.61	47.11	57.21	21.06	50.51	57.21	57.21	14.88	50.51	50.51	10.53	49.47	20.61	57.21	50.51	14.88	47.11	51.73	60.00	49.47	0.00	60.00	60.00	10.53
V22	47.11	51.73	20.61	57.21	50.51	14.88	50.51	50.51	14.88	57.21	49.47	10.53	57.21	21.06	50.51	57.21	20.61	47.11	10.53	60.00	60.00	0.00	49.47	60.00
V23	57.21	20.61	51.73	47.11	14.88	50.51	21.06	57.21	47.11	20.61	57.21	50.51	50.51	50.51	10.53	49.47	57.21	14.88	60.00	10.53	60.00	49.47	0.00	60.00
V24	21.06	57.21	47.11	20.61	57.21	50.51	57.21	20.61	51.73	47.11	14.88	50.51	14.88	57.21	49.47	10.53	50.51	50.51	49.47	60.00	10.53	60.00	60.00	0.00

6.3.2 Calculation of the experimental transformation matrices

The three Euler angles of the average orientation of the RA grain and each pixel of the product bcc phase (bainite or martensite) were converted into an orientation matrix using Eq. 6.7 [175]:

$$g = \begin{pmatrix} g_{11} & g_{12} & g_{13} \\ g_{21} & g_{22} & g_{23} \\ g_{31} & g_{32} & g_{11} \end{pmatrix} \quad (6.7)$$

Where;

g_{11}=cosϕ1cosϕ2-sinϕ1sinϕ2cosΦ, g_{12}=sinϕ1cosϕ2+cosϕ1sinϕ2cosΦ, g_{13}=sinϕ2sinΦ

g_{21}=-cosϕ1sinϕ2-sinϕ1cosϕ2cosΦ, g_{22}=-sinϕ1sinϕ2+cosϕ1cosϕ2cosΦ, g_{23}=cosϕ2sinΦ

g_{31}=sinϕ1sinΦ, g_{32}=-cosϕ1sinΦ, g_{33}=cosΦ

As with the matrices operation performed on the KS variant, the rotation matrices of the product bcc phase were multiplied by the inverse of the rotation matrices of the RA grain, which yields the experimental transformation matrices (T_{Exp}), as shown in Eq. 6.8. Due to the cubic crystal symmetry, a single orientation can be described using 24 equivalent notations, as shown in Table 6.4, and therefore each experimental transformation matrix was multiplied by the 24 symmetric matrices, which yielded to 24 (T_{Exp}) for each data point.

$$T_{Exp} = g_{bcc} g_{fcc}^{-1} \quad (6.8)$$

6.3.3 Calculation of the misorientation angle between theoretical and experimental data

The 24 theoretical transformation matrices (T_{KS}) were multiplied by the inverse of each experimental transformation matrix (T_{Exp}). The output matrix (T) is used to calculate the misorientation angle (θ) and the rotation axis (**r**) between each variant and the product phase using Eqs. 6.5 and 6.6 [82]. The output 24 angles that corresponded to 24 KS variants were compared and a specific variant was assigned to each pixel based on the minimum misorientation angle.

Based on this procedure, the variant number of each pixel was distinguished for each prior austenite, as shown in Fig. 6.4b, while crystallographic packets and Bain groups were obtained for each cut, as shown in Figs. 6.4c and d, respectively. For each cut, the experimental and theoretical {001} pole figures of the realised variants and retained austenite were plotted (Figs. 6.4e and f), and then the normalised frequency was calculated and presented for all variants realised in each prior austenite grain, as shown in Fig. 6.4g. The black lines represent the HAGBs (>15°) and silver colour lines represent LAGBs (2-15°), while the interphase boundaries were drawn on all maps as a thick black line.

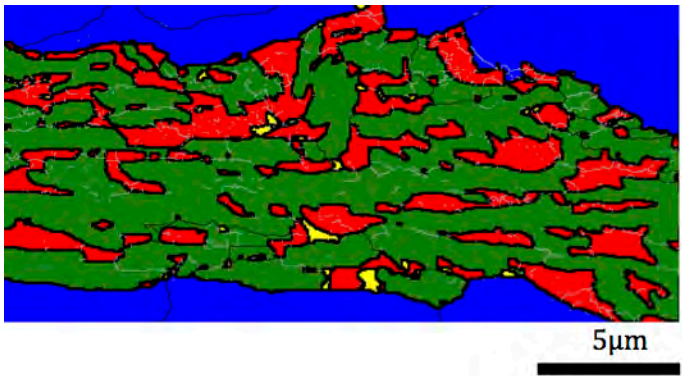

a)

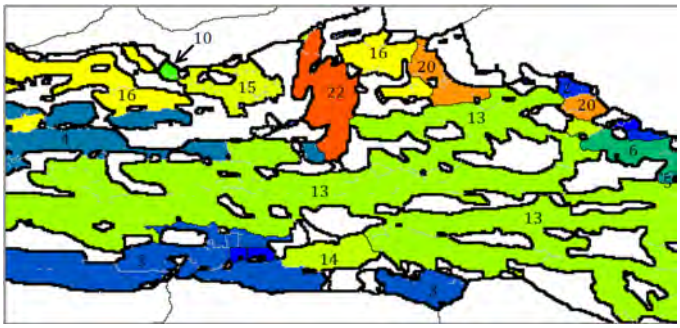

b)

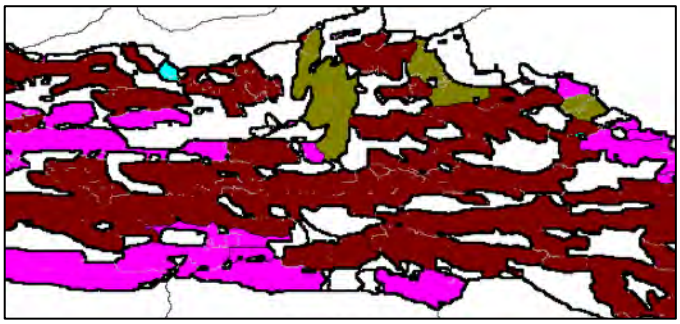

c)

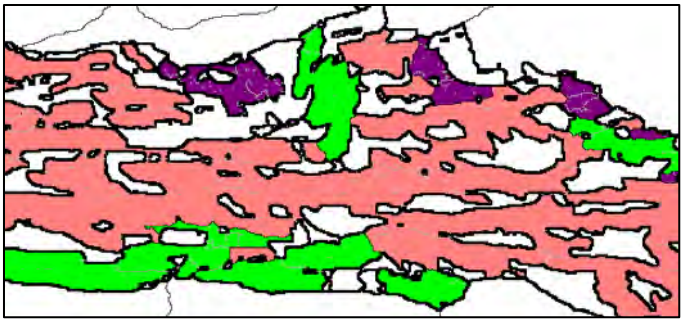

d)

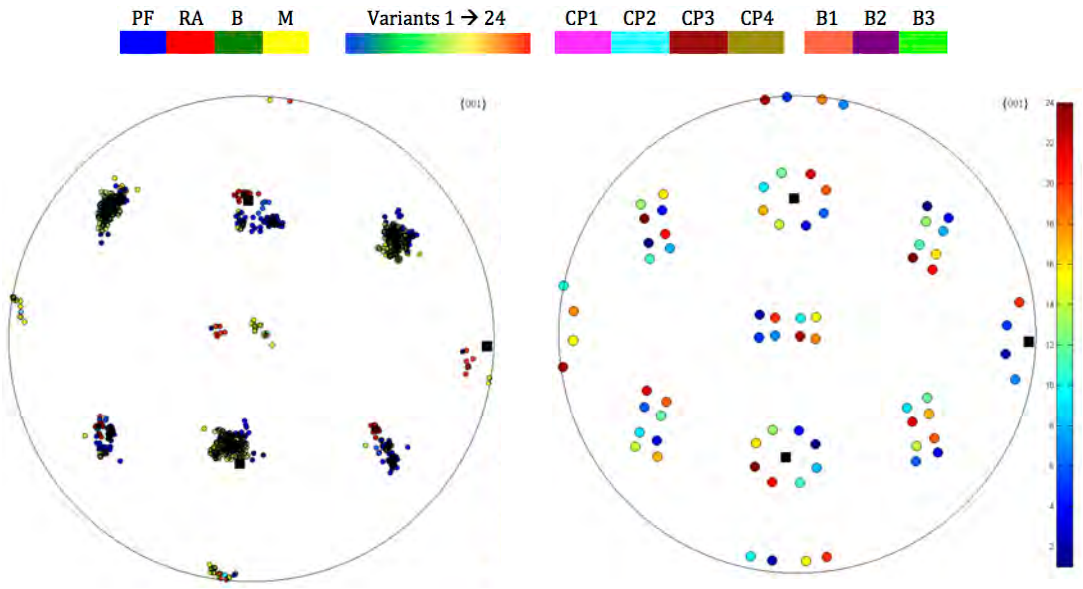
PF RA B M
Variants 1 → 24
CP1 CP2 CP3 CP4
B1 B2 B3

e) f)

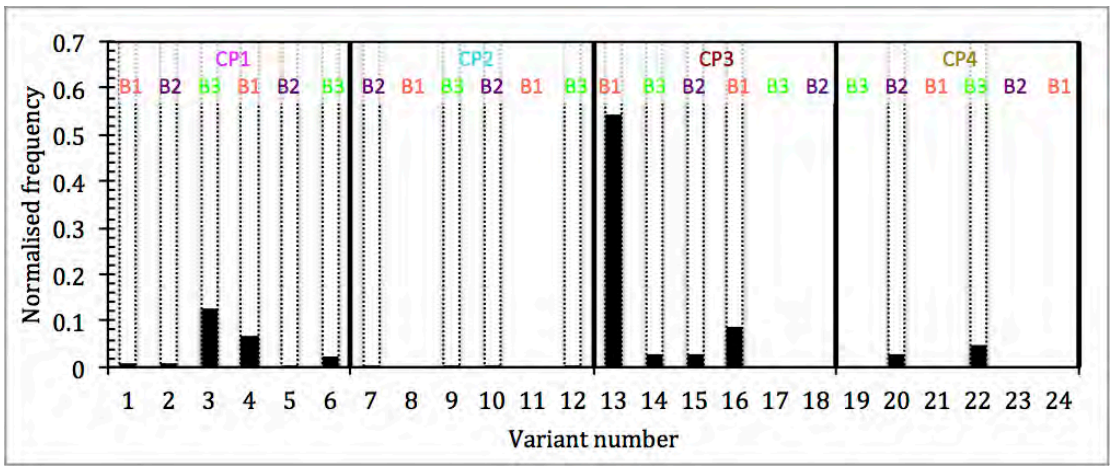
Normalised frequency
0.7
0.6
0.5
0.4
0.3
0.2
0.1
0
CP1
CP2
CP3
CP4
1 2 3 4 5 6 7 8 9 10 11 12 13 14 15 16 17 18 19 20 21 22 23 24
Variant number

g)

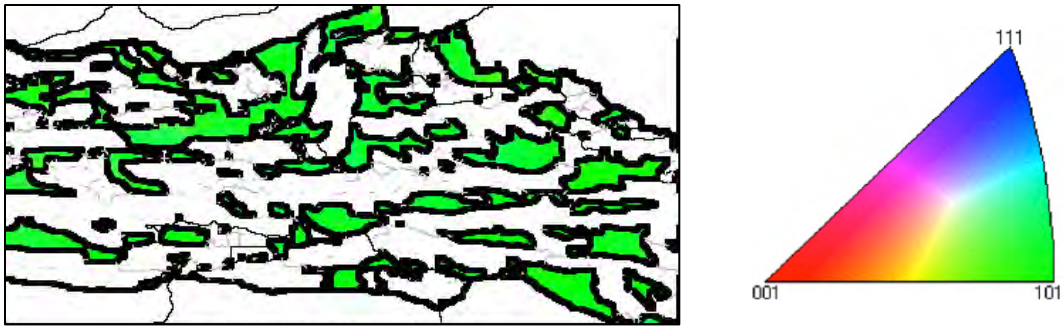
111
001
101

h)

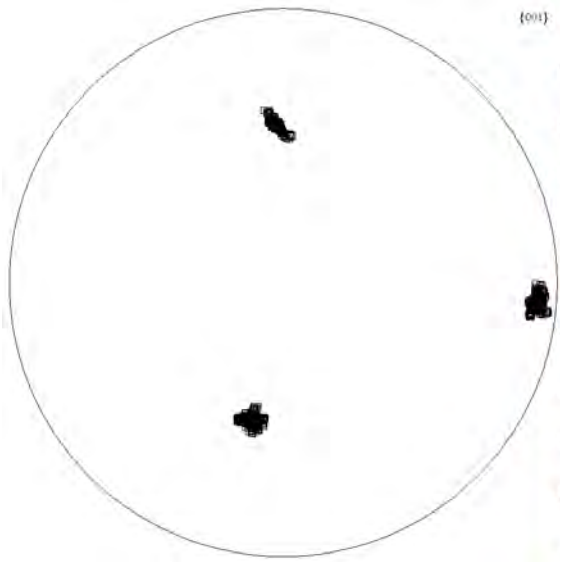

i)

Figure 6.4: EBSD maps of bainitic ferrite laths (BF) in the Nb-Ti steel; a) phases map, b) ferrite variants map, c) crystallographic packets (CPs) and d) bain groups (BGs). e) The experimental and f) theoretical {001} pole figures of the variants and the average orientation of the RA grain is represented by black squares in e) and f). g) Normalised frequency of the formed variants; dash lines represent the realisation of the variants even in a small amount. h) The inverse-pole figure map of the RA grain and i) {001} pole figure of the experimental orientation of the RA grains. LAGBs=2° to 15°; silver colour and HAGBs >15° black colour. The thick black line on all the maps represents the interphase boundary and does not denote boundary misorientation.

6.4 The Crystallography of Bainite

In the current study the large EBSD maps (105x79 μm) obtained for both steels (base and Nb-Ti steel) made it possible to analyse the formation of bainite in 18 prior austenite grains. Over the years, variant analysis has been conducted using techniques such as TEM [174], high-temperature Laser Scanning Confocal Microscopy (LSCM) [20, 176], and EBSD [14, 17, 92]. Most of these investigations were a qualitative study, with only a few being quantitative ones, and show the exact area fraction of each variant in a single austenite grain [14, 92]. This study is another one that determines the area fraction of the variants in each prior austenite grain.

The microstructure investigated in both steels had two different bainite morphologies, granular bainite (GB) and bainitic ferrite (BF); with GB being the dominant morphology in base steel and BF being dominant in Nb-Ti steel. As Fig. 6.5a shows, GB was predominantly characterised by plate-like or irregular-shaped ferrite with a small fraction of blocky RA, a morphology that also contained a high density of low angle boundaries. All the variants that were realised in this morphology are shown in the variant map (Fig. 6.5b) and variant histograms (Figs. 6.5g); the bainitic ferrite (BF) microstructures shown in Fig. 6.6a are characterised by lath-like ferrite and high fraction of coarse layers of RA between them, whereas in BF there was significantly less fraction of low angle boundaries compared to ferrite in GB. Many of variants were not realised in BF, as the variant maps in Fig. 6.6b and variant histograms in Fig. 6.6g show, whereas the microstructures in Fig. 6.7 consist of a mixture of the two types of bainite. It is clear that, the crystallography of ferrite in these two bainites differs and will be discussed in the subsequent sections.

Figure 6.8 shows a unique morphology of bainitic ferrite where each crystallographic packet has a different orientation. Moreover, the bainitic ferrite microstructure is finer in the Fig. 6.8 compared with other bainitic ferrite microstructures. The influence of the morphology on the crystallography of bainitic ferrite laths is discussed in the following sections. However, this BF morphology with multi-oriented packets was only found in one prior austenite grain, whereas all the other BF morphologies showed a typical parallel laths structure. This morphology is similar to the acicular ferrite formed in the heat affected weld zones; where the many inclusions serve as heterogeneous nucleation sites [161].

Acicular bainite can be developed at intermediate cooling rates (~20 °C·s^{-1}) in carbide-free bainite as reported in Ref. [114], but the slower cooling rate (1-10 °C·s^{-1}) led to the formation of granular bainite while a faster cooling rate (30-50 °C·s-1) led to the formation of bainitic ferrite. The size of the austenite grain available for bainite transformation could be another reason why multi-oriented BF (so-called interwoven acicular bainite [177]) formed in this microstructure. This was because the large austenite grain assisted the intragranular formation of acicular ferrite whereas smaller grain sizes favour the formation of bainitic ferrite at the boundaries [161]. By way of contrast, the large austenite grain shown in Fig. 6.4 did not lead to similar multi-oriented morphology, indeed the formation of BF with parallel ferrite laths morphology in a large austenite grain, as shown in Fig. 6.4, could be attributed to the influence of cooling rate because the fast cooling rate (30-50 °C·s-1) assisted in the formation of parallel lath morphology. The morphological difference between all these morphologies will be discussed in detail in the following sections. This discussion was divided into four sub-sections: CP arrangement, Bain arrangement, Variant pairs, and Variant selection. Each subsection discusses the crystallography of ferrite in granular bainite, bainitic ferrite laths, and a mixture of both morphologies in a single prior austenite grain.

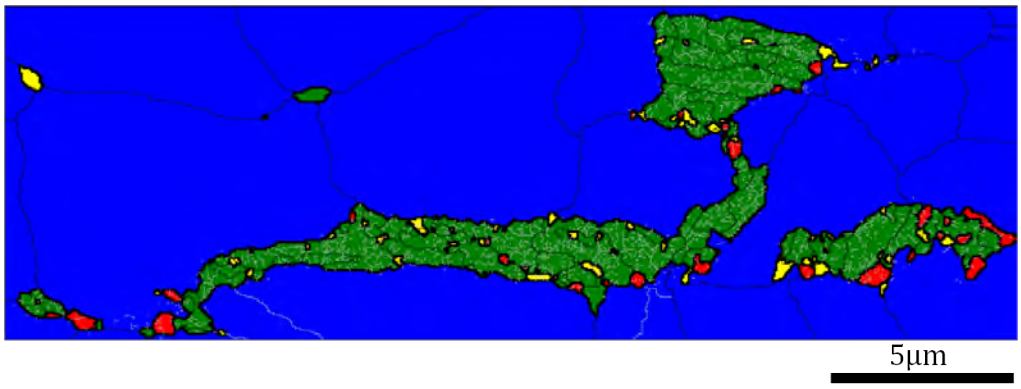

a)

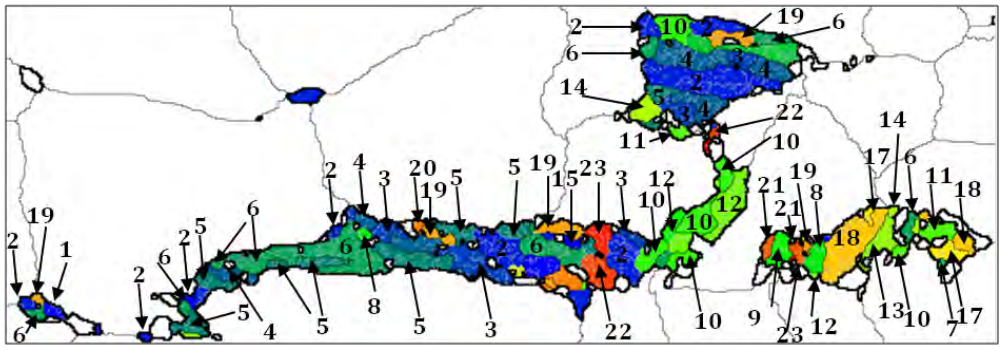

b)

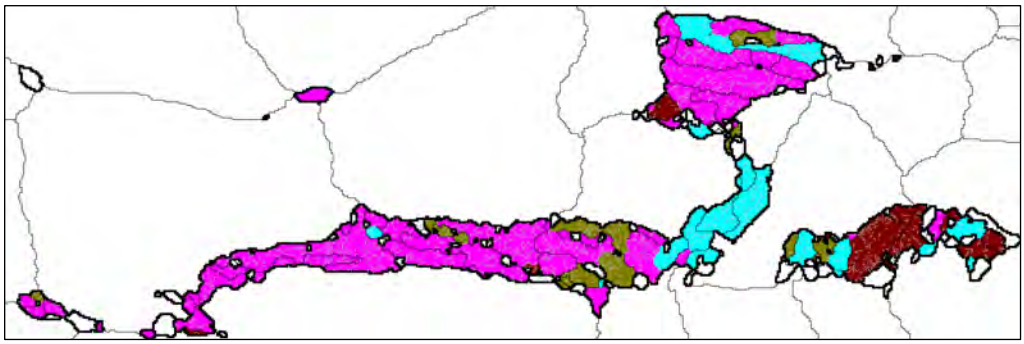

c)

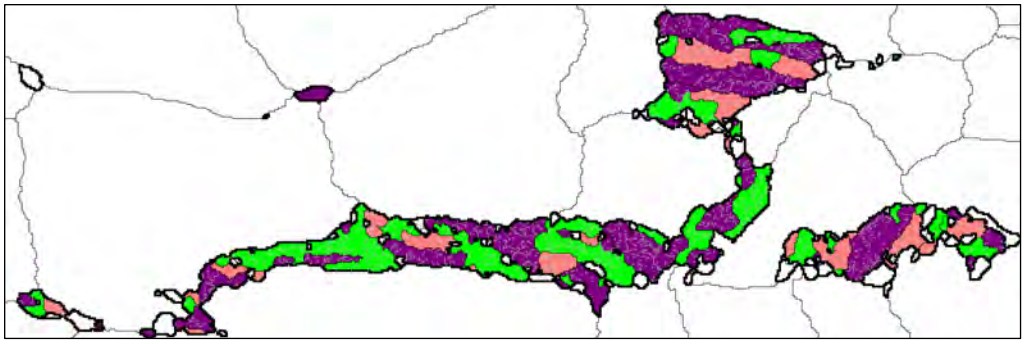

d)

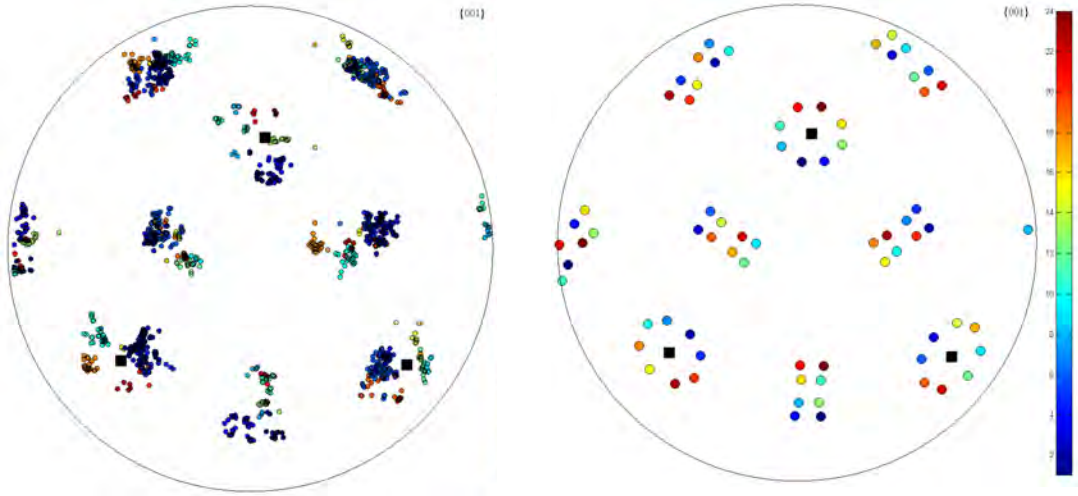

e) f)

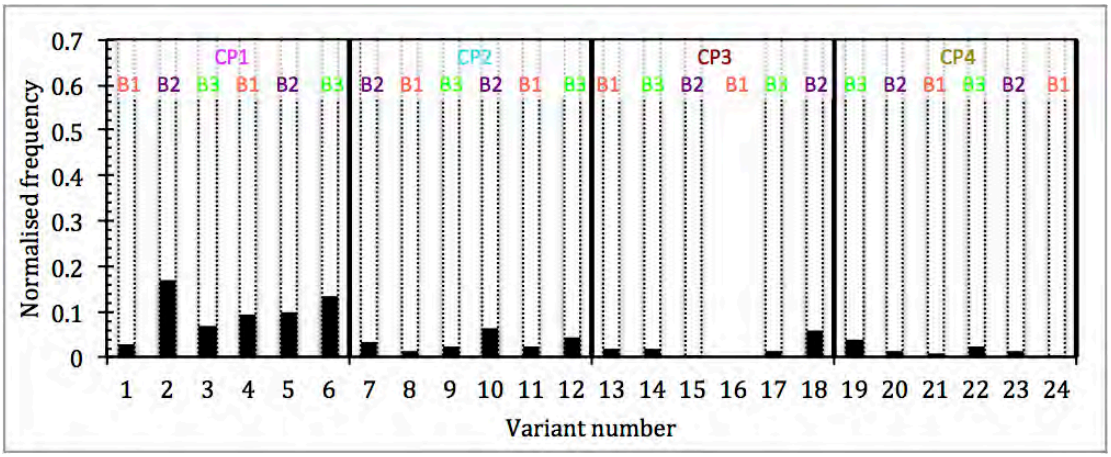
CP1
CP2
CP3
CP4
B1 B2 B3 B1 B2 B3 B2 B1 B3 B2 B1 B3 B1 B3 B2 B1 B3 B2 B3 B2 B1 B3 B2 B1
Normalised frequency
0.7
0.6
0.5
0.4
0.3
0.2
0.1
0
1 2 3 4 5 6 7 8 9 10 11 12 13 14 15 16 17 18 19 20 21 22 23 24
Variant number

g)

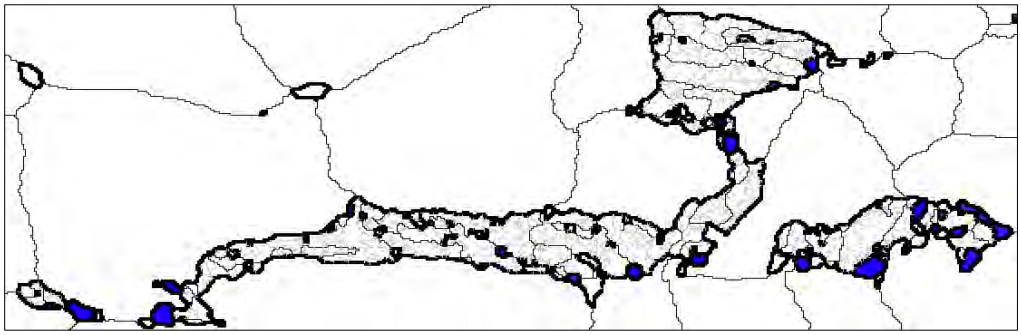

h)

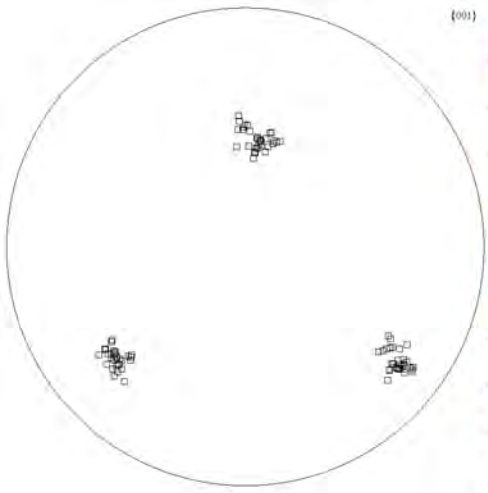

i)

Figure 6.5: EBSD maps of granular bainite (GB) in the base steel; a) phases map, b) ferrite variants map, c) crystallographic packets (CPs) and d) Bain groups (BGs). e) The experimental and f) theoretical {001} pole figures of the variants and the average orientation of the RA grain is represented by black squares in e) and f). g) Normalised frequency of the formed variants; dash lines represent the realisation of the variants even in a small amount. h) The inverse-pole figure map of the RA grain and i) {001} pole figure of the experimental orientation of the RA grains. LAGBs=2° to 15°; silver colour and HAGBs >15° black colour. The thick black line on all the maps represents the interphase boundary and does not denote boundary misorientation.

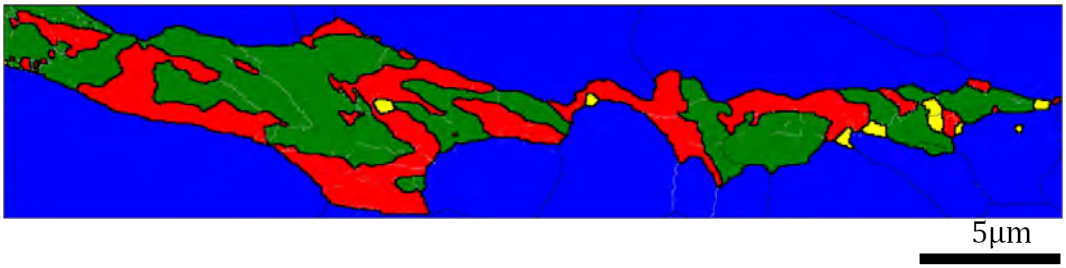
5µm

a)

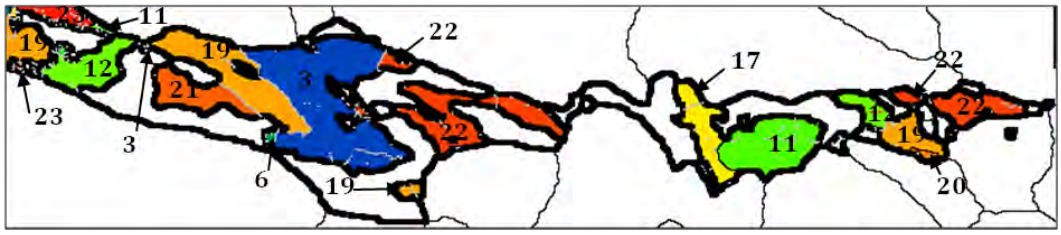
11
19
12
23
21
19
3
3
22
22
6
19
17
22
22
11
19
20

b)

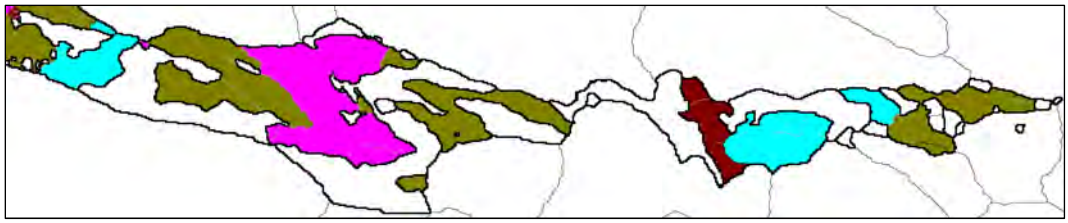

c)

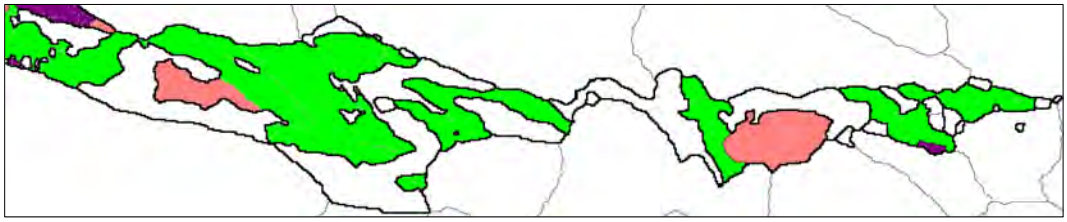

d)


PF
RA
B
M
Variants 1 → 24
CP1
CP2
CP3
CP4
B1
B2
B3

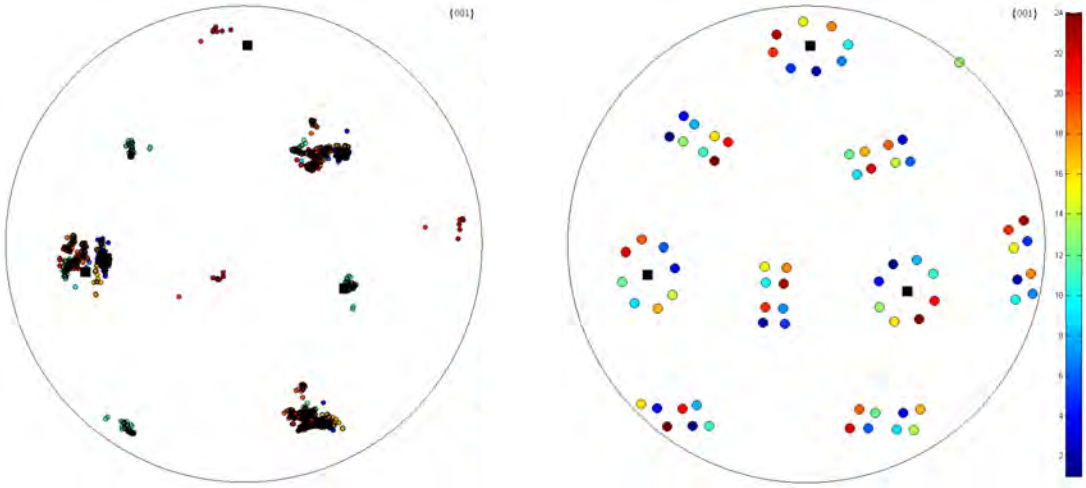

e) f)

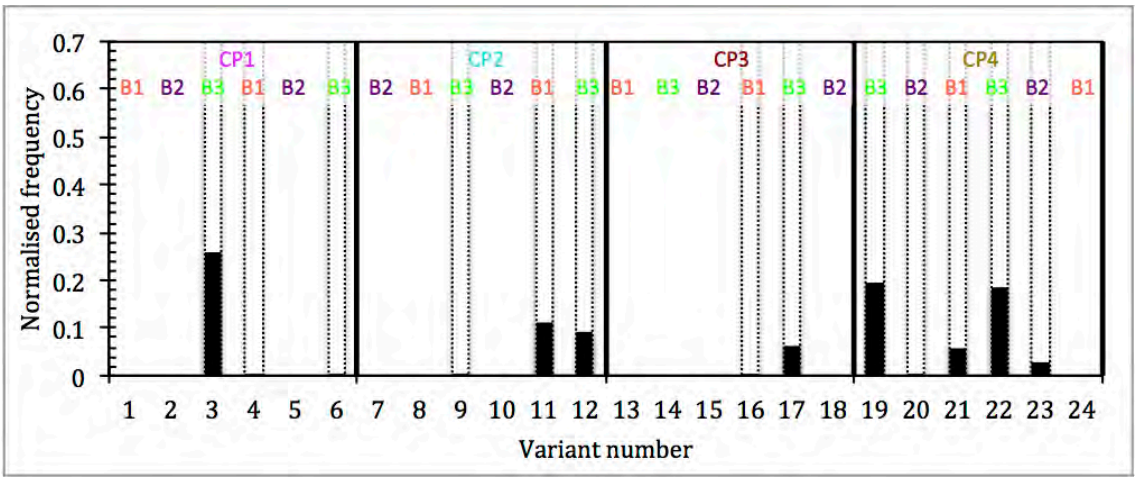
CP1
CP2
CP3
CP4
B1 B2 B3 B1 B2 B3 B2 B1 B3 B2 B1 B3 B1 B3 B2 B1 B3 B2 B3 B2 B1 B3 B2 B1
Normalised frequency
0.7
0.6
0.5
0.4
0.3
0.2
0.1
0
1 2 3 4 5 6 7 8 9 10 11 12 13 14 15 16 17 18 19 20 21 22 23 24
Variant number

g)

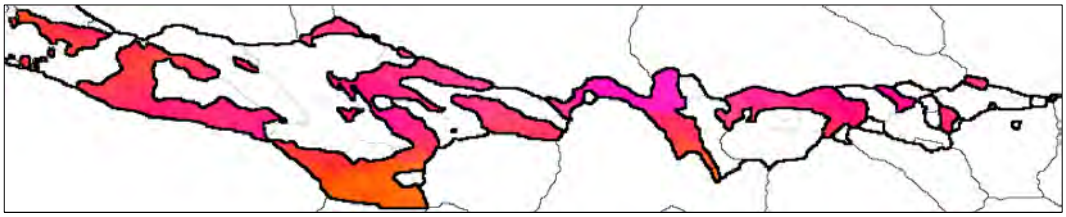

h)

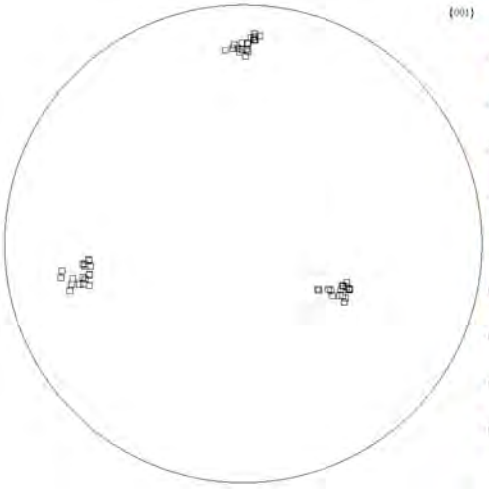

i)

Figure 6.6: EBSD maps of bainitic ferrite laths (BF) in the Nb-Ti steel; a) phases map, b) ferrite variants map, c) crystallographic packets (CPs) and d) Bain groups (BGs). e) The experimental and f) theoretical {001} pole figures of the variants and the average orientation of the RA grain is represented by black squares in e) and f). g) Normalised frequency of the formed variants; dash lines represent the realisation of the variants even in a small amount. h) The inverse-pole figure map of the RA grain and i) {001} pole figure of the experimental orientation of the RA grains. LAGBs=2° to 15°; silver colour and HAGBs >15° black colour. The thick black line on all the maps represents the interphase boundary and does not denote boundary misorientation.

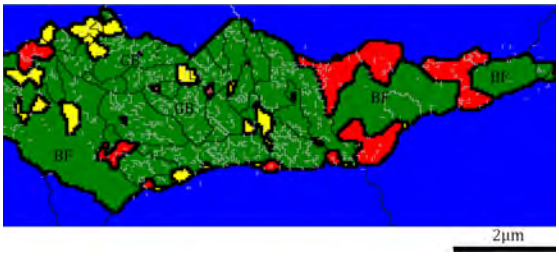

a)

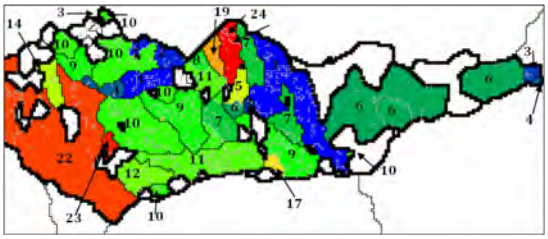

b)

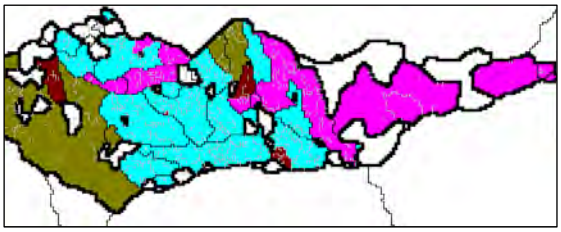

c)

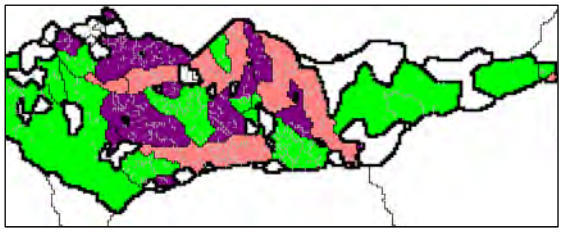

d)

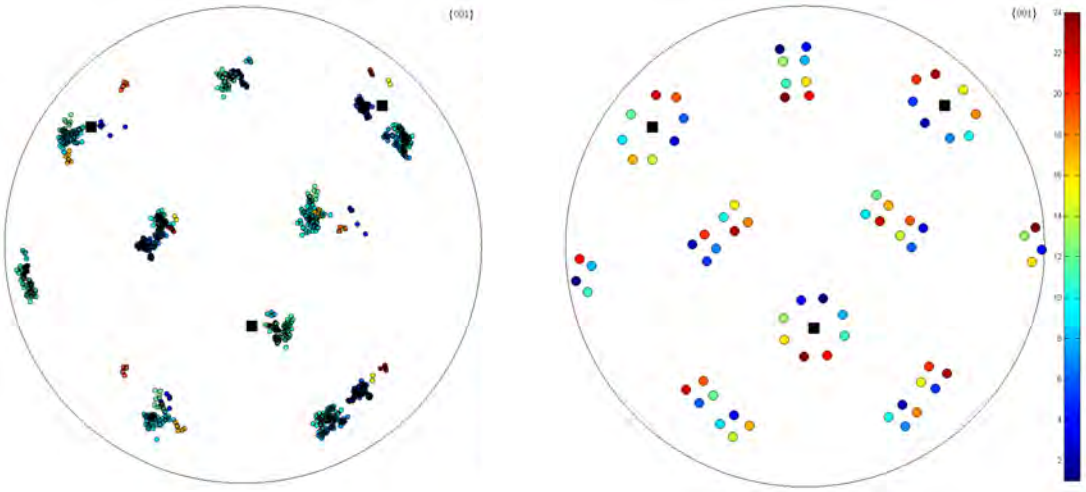

e)

f)

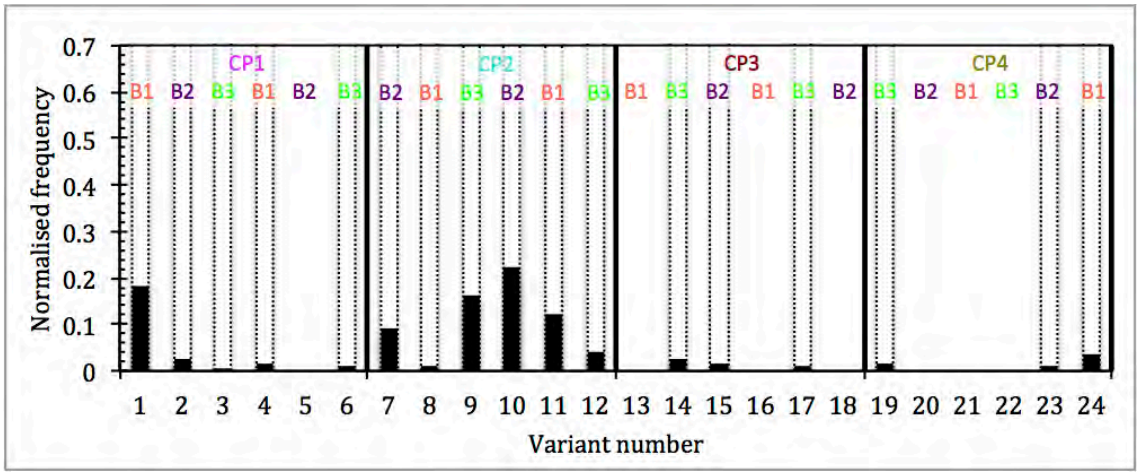
CP1
CP2
CP3
CP4
B1 B2 B3 B1 B2 B3 B2 B1 B3 B2 B1 B3 B1 B3 B2 B1 B3 B2 B3 B2 B1 B3 B2 B1
Normalised frequency
0.7
0.6
0.5
0.4
0.3
0.2
0.1
0
1 2 3 4 5 6 7 8 9 10 11 12 13 14 15 16 17 18 19 20 21 22 23 24
Variant number

g)

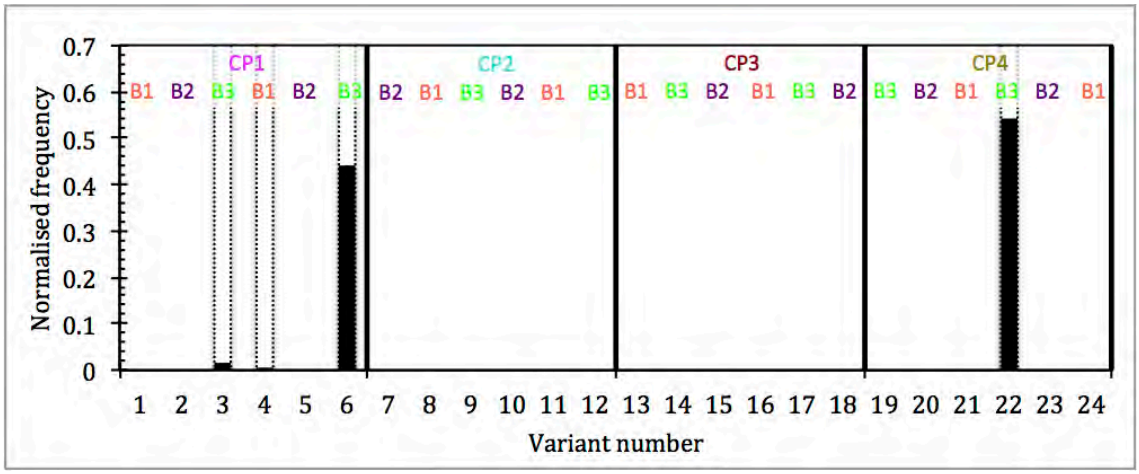
CP1
CP2
CP3
CP4
B1 B2 B3 B1 B2 B3 B2 B1 B3 B2 B1 B3 B1 B3 B2 B1 B3 B2 B3 B2 B1 B3 B2 B1
Normalised frequency
0.7
0.6
0.5
0.4
0.3
0.2
0.1
0
1 2 3 4 5 6 7 8 9 10 11 12 13 14 15 16 17 18 19 20 21 22 23 24
Variant number

h)

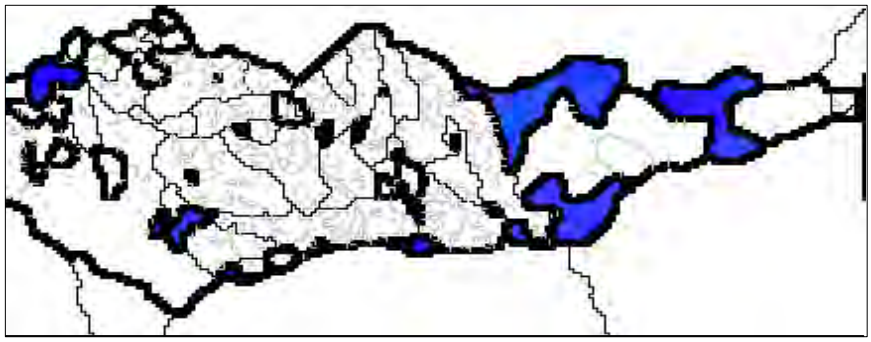

i)

j)

Figure 6.7: EBSD maps of bainitic ferrite laths (BF) and granular bainite in the base steel; a) phases map, b) ferrite variants map, c) crystallographic packets (CPs) and d) Bain groups (BGs). e) The experimental and f) theoretical {001} pole figures of the variants and the average orientation of the RA grain is represented by black squares in e) and f). Normalised frequency of the formed variants for g) GB and h) BF; dash lines represent the realisation of the variants even in a small amount. i) The inverse-pole figure map of the RA grain and j) {001} pole figure of the experimental orientation of the RA grains. LAGBs=2° to 15°; silver colour and HAGBs >15° black colour. The thick black lines on all the maps represent the interphase boundary and do not denote boundary misorientation.

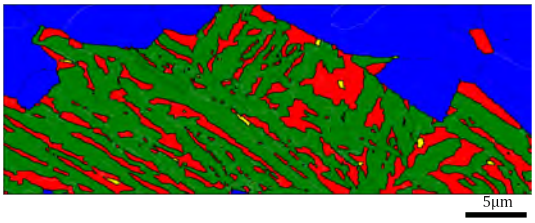

a)

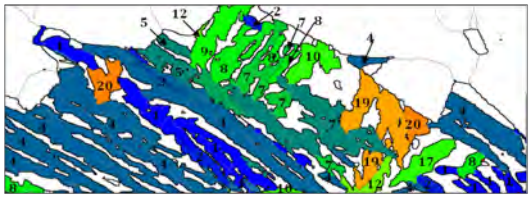

b)

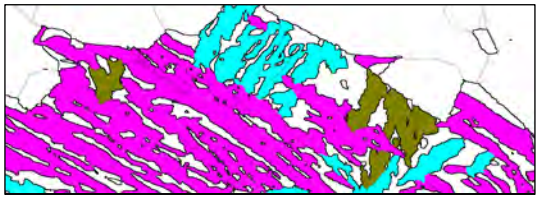

c)

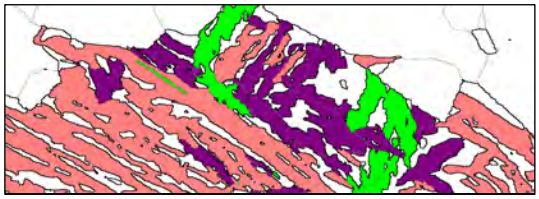

d)

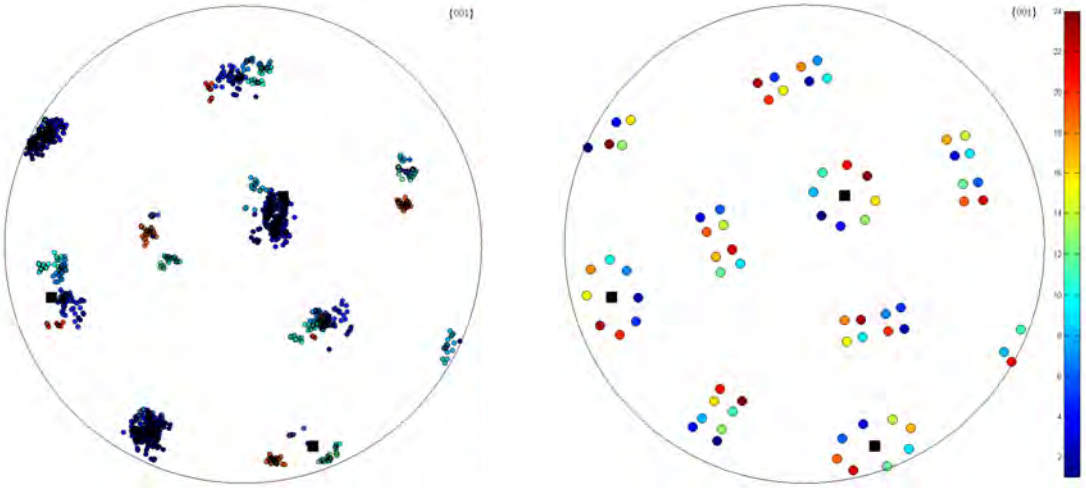

e)

f)

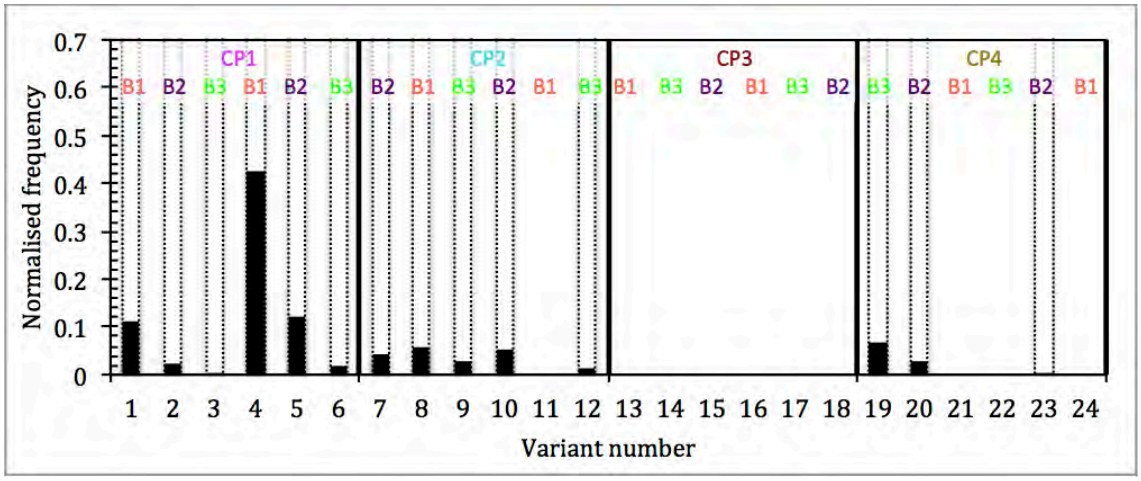

g)

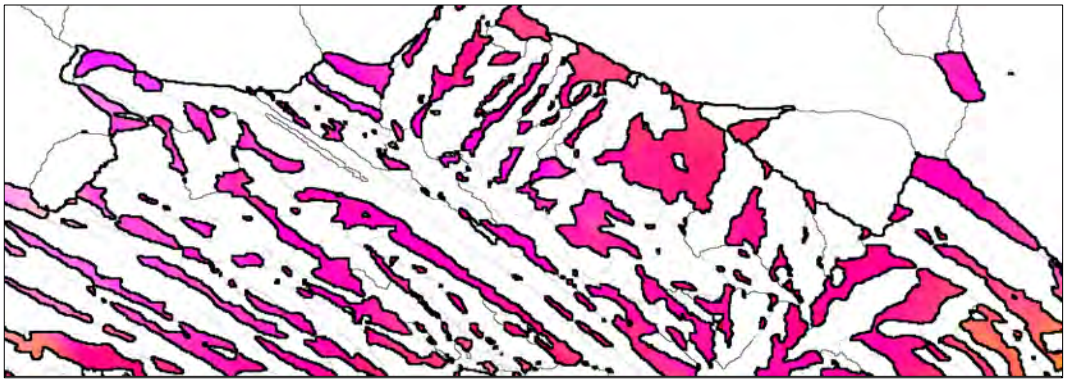

h)

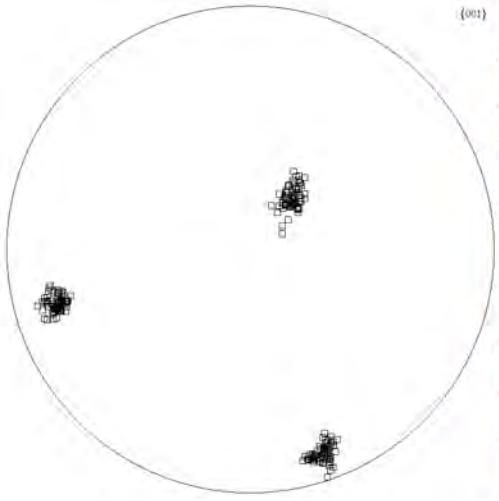

i)

Figure 6.8: EBSD maps of bainitic ferrite laths (BF) in the base steel; a) phases map, b) ferrite variants map, c) crystallographic packets (CPs) and d) Bain groups (BGs). e) The

experimental and f) theoretical {001} pole figures of the variants and the average orientation of the RA grain is represented by black squares in e) and f). g) Normalised frequency of the formed variants; dash lines represent the realisation of the variants even in a small amount. h) The inverse-pole figure map of the RA grain and i) {001} pole figure of the experimental orientation of the RA grains. LAGBs=2° to 15°; silver colour and HAGBs >15° black colour. The thick black lines on all the maps represent the interphase boundary and do not denote boundary misorientation.

6.5 Crystallographic Packets Arrangement

The CPs arrangement of ferrite in the GB was different from the BF laths in the BF. In the microstructures that were investigated, irregular-shaped ferrite in GB was characterised by the presence of all CPs, as shown in Fig. 6.5 (see appendix-A for more examples) and clearly show that the CP1 was the dominant CP in all these maps, and moreover, the variants belonging to the same CP formed adjacent to each other and almost all variants were formed in each CP.

In contrast, CP1 was only dominant in some of the BFs (Figs. 6.4, 6.6, 6.8) (see appendix-B for more examples) and not all CPs were formed in the BF. Some of the CPs disappeared in BF as a result of the variant selection (refer to Figs. B.2 and B.4c in appendix-B), which will be discussed in Section 6.8. However, in most cases only two variants were present in each CP such as V19/V21 in CP4 as seen in Figs. 6.6b,c and g (for more examples refer to Figs. B.3 and B.4 in appendix-B). It should be noted that in some cases, although two variants have realised from the same type of CP in one prior austenite grain, but only one of these variants was found in each particular CP, as these CPs were separated spatially; such as V12/V11 in CP2 as seen in Fig. 6.6 (for more examples refer to Fig. B.1 in appendix-B) shows that variants belonging to the same CP were separated by another CP.

When mixed BF and GB microstructure formed from the same prior austenite grain as seen in Fig. 6.7 (see appendix-C for more examples), the CP arrangements remained the same as if GB or BF had formed separately in different austenite grains. However, CP1 was not the dominant CP in the ferrite of GB when these two morphologies were present in one prior austenite grain. In most cases, each CP in the BF in the mixed grains contained a single variant (refer to Figs. C.2h and C.6h in appendix-C) or two variants as shown in Fig. 6.7h (for more examples refer to Figs. C.4 and C.5h in appendix-C)

According to Takayama *et al.* [17], the alignment of all the variants belonging to one CP in one area is a characteristic of martensite and upper bainite (0.15C-2Mn-0.3Si wt.%) transformed at 450°C and 500°C, whereas the CPs did not cluster in the bainite transformed at 580°C. Furuhara *et al.* [21] showed a similar observation in the upper bainite of Fe-9Ni wt.% alloy transformed at 400°C and 350°C, where the upper bainite formed at 450°C did not show the formation of variants from the same CP in one area. This clearly shows the effect of a low transformation temperature on the adjacent formation of variants from one CP, but do not explain the absence of a specific CP.

The current results are in agreement with Refs. [17, 21] with respect to the predominant clustering of the variants from the same CP, especially in relation to ferrite in GB. However, in Refs. [17, 21] this was observed for the case of low temperature carbide-containing bainite formation, whereas in our case we dealt with an incomplete transformation of bainite that resulted in the formation of carbide-free bainite at a higher temperature (470°C).

Moreover, GB was also expected for form after cooling from 680°C to an isothermal holding temperature of 470°C. However, the compositions of the steels studied in the current work differed from those studied in Refs. [17, 21], so the bainite transformation temperatures were different. It could therefore be suggested that the driving force for the transformation of bainite in current steels could be compared to the driving force at 450-500°C for 0.15C-2Mn-0.3Si wt.% steel [17] and at 350-400°C for Fe-9Ni wt.% alloy [21].

Malet *et al.* [92] investigated the growth of CPs in hot rolled TRIP steel (0.4C-1.5Mn-1.5Si wt.%) transformed at 400°C. It was stated that the growth of bainite by CP was contrary to previous conclusions about growth based on Bain groups [20]. Additionally, it was found that the amount of prior deformation of austenite affected the number of CPs realised, e.g. the number of CP was reduced when deformation increased. In the current study both steels underwent the same deformation in austenite, so the absence of some CPs in BF could not be explained by the effect of deformation.

6.6 Bain Groups Arrangement

The Bain maps in this study showed that all the BGs realised in nearly equal amount in ferrite of GB as seen in Fig. 6.5d (see appendix-A for more examples), whereas only one or two Bain groups were realised in the BF laths as seen in Figs. 6.6d and 6.8d (see appendix-B for more examples). On the other hand, two types of Bain arrangement were realised in the current microstructure, and each bainite morphology was characterised by a specific Bain arrangement.

In the first arrangement, all the variants belonging to the same Bain group did not cluster in one area, as they were separated by the blocks of variants belonging to other Bain groups. In addition, all three Bain groups were present in each CP. This arrangement is typical for ferrite in GB, as Fig. 6.5 show (see appendix-A for more examples). Similar arrangements of Bain groups were also observed by Takayama *et al.* [17] and Furuhara *et al.* [21] in upper bainite that was transformed at low temperatures of 450°C and 350°C, respectively.

It was suggested in the literature that an arrangement of Bain groups gives an insight into the sequence of variants formation, indeed Zhang *et al.* [20] suggested that the variants from the same Bain group are formed at an early stage of bainite transformation and that all variants belonging to the same Bain group have similar transformation strain accommodation mechanisms. Although several blocks of the same Bain group were transformed at an early stage of bainite transformation, they were located in different areas [20]. Similarly, Terasaki *et al.* [176] used LSCM to show a simultaneous formation of two separated variants belonging to the same Bain group during the transformation of bainite in the Fe-0.1C-1Ni-0.8Mn-0.4Mo (mass %).

The second Bain arrangement, mainly observed in BF, showed that all the variants belonging to the same Bain groups were grouped together, as Figs. 6.4, 6.6 and 6.8d show (see appendix-B for more examples). This Bain arrangement was also observed in the morphology of bainitic ferrite with multi-oriented packets (Fig. 6.8).

Similar Bain arrangements were seen by Takayama *et al.* [17] and Furuhara *et al.* [21] in upper bainite transformed at high temperatures of 540°C and 450°C, respectively. Although the Bain arrangement in BF was similar to the Bain arrangement for high transformation temperature of bainite studied by Takayama *et al.* [17], the CP arrangements differed (see previous section), so the crystallography of the BF formed in both the base and Nb-Ti steels differed from the one described by Takayama *et al.* [17].

Both Bain groups arrangements occurred in the bainite with a mixed morphology in one prior austenite grain, with that arrangement being the dominant one which corresponds to the dominant bainite morphology present in this area. For example in Fig. 6.7 (for more example refer to Fig. C.2, C.4 and C.6 in appendix-C) GB had a higher area fraction in the mixed morphology (of GB and BF) thus the Bain arrangement was mostly similar to the one for irregular-shaped ferrite in GB. In contrast, if the BF is the dominant phase, then the arrangements will be similar to the Bain arrangement observed for the BF laths (for more example refer to Figs. C.1 and C.3d in appendix-C). Thus, it could be concluded that the close proximity of two bainite morphologies did not affect either the Bain group or the CP arrangements in the ferrite of these adjacent morphologies, and each of these bainite morphologies has a specific arrangement of Bain groups and CPs.

6.7 Variant Pairing

The formation of adjacent variants can easily be tracked using their misorientation angle. For instance, when two variants are formed adjacent to each other, such as V1/V2, they form a high angle boundary or twin related variant pairing of 60° (Table 6.6). The formation of V1/V4 led to the formation of low angle boundary of 10.53°. According to the theoretical KS ORs, 10 different misorientation angles ranging from 10.53° to 60° could be formed by different variant pairings, but the formation of variant pairs within one Bain group resulted in misorientation angles from only 10.53° to 21.06°. Although, the lowest boundary angle in KS OR was ~10°, experimentally, it can be as low as 5° [17, 81]. Theoretical misorientation angle distribution shows that all the variant pairs had the same probability of forming [169]. The analysis of variant pairing based on the misorientation angle distribution could be misleading because several of the variant pairs had a similar misorientation angle, in which case the misorientation axis should also be used [17]. Moreover, some variant pairings have a very close misorientation angle and axis and cannot be distinguished via misorientation angle distribution such as V1/V3 and V1/V5, as found by Takayama *et al.* [17]. The variant histograms, which show the volume fraction of variants, can be misleading because it shows that the high frequency of some variants had a low angle boundary relationship while they were not formed adjacently. This was clear from the absence of a low angle boundary and the distribution of Bain groups in the ferrite in GB. Therefore, this method of variant analysis was not used in this study. Instead, an exact observation of variant pairs was implemented because the formation of a specific variant pair is important in analysing the transformation strain accommodation [169].

In this study, ferrite in GB was characterised by the dominancy of an inter-variant relationship with a high angle boundary or twin-related boundary. However, each GB has its different ferrite variant pairs, for instance the dominant variant pair was V2/V6 (60°) in Fig. 6.5, V1/V6 (49.5°) and V6/V16 (51.7°) in Fig. 6.9 (also Fig. A.1 in appendix-A), V1/V5 (60°) and V4/V2 (60°) were also observed in other examples (for more examples refer to Fig. A.2 and Fig. A.3 in appendix-A). Less than 5% of the pairs had low angle boundaries in the GB, as the detailed analysis of the variant pairs and misorientation histogram reveals in Figs. 6.9a and b.

Lambert-Perlade *et al.* [94] found that the formation of specific variant pairs such as V1/V2 (60°) accommodated the transformation strain more efficiently than V1/V4 (10.5°) or V1/V8 (10.5°). However, the formation of all six variants belonging to the same CP can

accommodate transformation even better than V1/V2 [178]. Takayama *et al.* [17] showed the dominancy of the twin-related V1/V2 pair in the low transformation temperature bainite, which diminished as the bainite formation temperature increased. At a high transformation temperature, the high angle boundaries disappeared and only low angle boundary pairs dominated. A similar observation was made by Furuhara *et al.* [21] where the high angle boundary pairs disappeared as the transformation temperature increased. However, there was no preference for a particular variant pair with a low angle boundary to form because some research showed the formation of V1/V4 pairs [17], whereas others showed that the variant from the same Bain group and different CP, such as V1/V8 [21, 179] was a dominant pairing. This suggested that a variant pair at high temperature could be formed with any combination satisfying a low angle boundary [20]. The difference in Gibbs free energy between austenite and ferrite in bainite was utilised to prove that the driving force influenced the variant pairing in different materials [17], and the formation of twin-related variant pairing in the ferrite in GB, can be explained by the need for the self-accommodation of strain during the transformation of austenite to bainite [17, 175]. Thus, the dominant formation of V1/V2 pair occurred because it is more efficient in accommodating the transformation strain than the other pairs [17, 178].

In BF, the formation of predominantly single variant laths separated by the RA was observed, which meant that a limited number of pairs could be analysed. A tiny amounts of V1/V11 and V1/V24 pairs with 21° misorientation were observed (refer to Fig. B.1 in appendix-B), while a small amount of 60° boundaries can be observed due to the formation of V13/V14 and V17/V18 pairs as shown in the boundary map in Fig. 6.10a (for more example refer to Fig. B.2 in appendix-B). The appearance of V5/V7 pair with 14.8° misorientation was also observed (refer to Fig. B.3 in appendix-B), while high angle boundaries were formed by V3/V4 (60°) and V14/V4 (49.5 °) pairs (refer to Fig. B.4 in appendix-B) and by V1/V2 and V3/V4 pairs in Fig. 6.8. However, all these variant pairs in the BF constituted less than 10% in each map, which was not statistically enough to draw conclusion about the variant pairs of ferrite in the BF compared to GB. However, due to the presence of RA interlayers, the pairing of BF laths differed from the ones discussed by Takayama *et al.* [17] and Furuhara *et al.* [21], whereas the pair arrangement in GB correlated well with their view on variant pairing. In the prior austenite grain with mixed bainite morphology (Figs. 6.7, see appendix-C for more examples), the dominancy of high angle boundaries in the GB area, such as V4/V6 and V5/V6 were observed (refer to Fig. C.5

in appendix-C), whereas the BF area had a small fraction of pairs such as V17/V23, as shown in boundary map in the Fig. 6.10b.

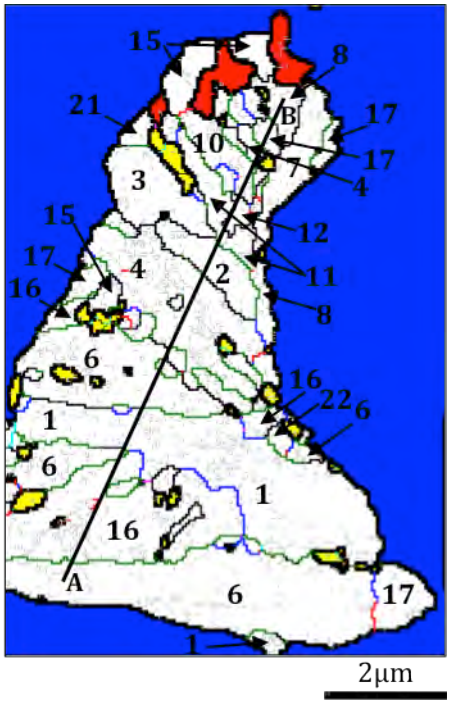

a)

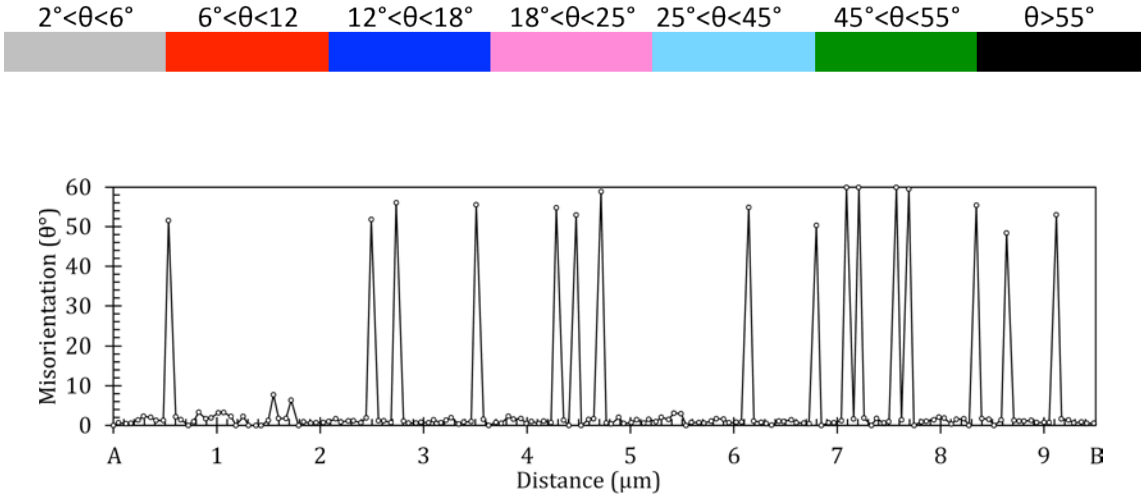

b)

Figure 6.9: Boundary map of a) GB in the base steel with the variants numbers and b) misorientation along the line (A-B) in the map a). PF is blue, martensite is yellow, RA is red and white area is bainite. Thick black lines represent phase boundary.

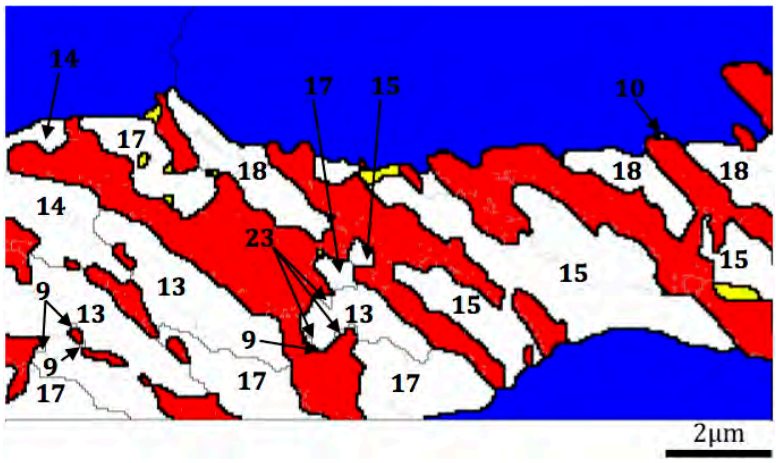

a)

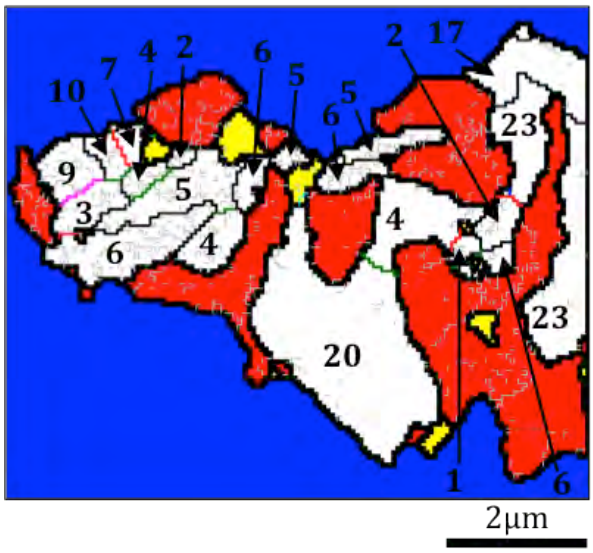

b)

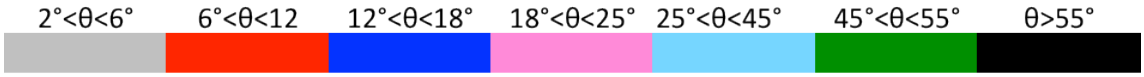

Figure 6.10: Boundary maps of a) the BF and b) mixed grain in the base steel with the variants numbers. PF is blue, martensite is yellow, RA is red and white area is bainite. Thick black lines represent phase boundary.

6.8 Variant Selection

In each prior austenite grain there was equal probability that each of the 24 variants (in KS OR) of ferrite in bainite or martensite crystals could form [86], but under certain conditions, some variants do not form. The absence of some variants is called "variant selection" [180]. However, others use the term "variant selection" when some variants do not form with the same probability/frequency [14, 79, 84, 92], whereas some consider variant selection only for a particular CP without considering all 24 variants [17].

In this study only the disappearance of some variants is described as variant selection. Typically, variant selection is pronounced when transformation takes place under applied stress/strain [15]. However, variant selection has been also reported in the bainite/martensite formed without any external load [17]. This type of variant selection was called "naturally absent variants" by S. Kundu *et al*. [14]. However, some reported that prior plastic deformation of austenite could also lead to variant selection [16, 92, 181] while others did not observe this effect on variant selection [90]. In the current study, the steels were subjected to compressive deformation in austenite, so some effect of this on bainite variant selection could be expected.

During the transformation of austenite to bainite or martensite, the transformation strain must be accommodated because the formation of all variants can easily accommodate the transformation strain. This type of accommodation is called self-accommodation (SA), and it usually happens when the driving force for transformation is high at a low transformation temperature and the remaining austenite cannot accommodate the transformation strain. At a high temperature, the low strength of austenite makes the austenite able to accommodate the transformation strain instead of SA. This accommodation of the transformation strain by the deformation of austenite is called plastic accommodation (PA) [20] .

During PA, only preferable variants are formed and variant selection appears, but this variant selection can be strong or weak depending on the number of variants that are not formed. However, some researchers refer the variant selection to space limitation [14, 91] or the small size of the prior austenite grain [91], while others believe that the refining of the bainite structure is the cause of the limitation of variants [174], or simply explain variant selection during transformation as the natural absence of variants because the nucleation of bainite is a stochastic process [14]. These contradictions in the cause of

variant selection are also associated with an unclear definition of variant selection, because some also consider the dominance of specific variants as a variant selection.

There are different ways used in literature to demonstrate variant selection, such as pole figures, orientation distribution functions (ODF) [80], and misorientation angle distributions [17]. In this study the exact number of variants realised in each prior austenite grain are reported. The realisation of the variants in each map is presented as vertical dotted lines in all variant histograms (Figs. 6.5g-6.8g), regardless of their volume fraction, while the frequency of each variant is shown by black bar. Although some variants are present, no black bar is visible for them because their frequency was very low.

In this study it was clear that mostly all variants were observed in the ferrite of GB. In Fig. 6.5, all 24 variants were observed, whereas three variants are absent in other examples (refer to Fig. A.1 in appendix -A). On the other hand, the BF laths show a very high variant selection because only some variants were formed. For example, only 5 or 8 variants are realised in the BF as seen in Fig. 6.6 (also refer to Fig. B.4 in Appendix B). In Fig. 6.6, the BF has a parallel arrangement of laths whereas the BF in Fig. 6.8 has finer laths with non-parallel orientations. This non-parallel orientations restricted the growth of laths leading to refinement, but resulted in less variant selection (only 8 variants out of 24 were absent) compared to the BF with a parallel lath arrangement. This could be explained by the need of more variants to accommodate the transformation strain when they have random orientation [14].

When both GB and BF formed (mixed bainite morphology) from the same prior austenite grain (Figures 6.7, see appendix-C for more examples), similar variant selection in the BF is observed, as in the case when only the BF formed from one austenite grain. However, the variant appearance differed in the GB located in such a mixed microstructure because there was a clear selection of CP in such GBs, as discussed previously (section 6.5), which led to a more pronounced variant selection than when GB formed separately from the BF. Thus, those variants that belonged to non-realised CPs were absent, but all the variants were realised in the present CPs.

In the literature, variant selection was related to the high transformation temperature [17, 21]. The ferrite variant selection in GB can be attributed to the transformation temperature. Since we assumed that the GB was formed during the cooling from 680^{o}C to 470^{o}C, it can be speculated that the GB which have 3 variants missing (refer to Fig. A.1 in

appendix-A), were transformed at a higher temperature compared with the GB that have only one variant missing (Fig. 6.5).

According to Takayama *et al.* [17], the lower transformation temperature of the BF compared to GB should lead to less variant selection in the BF, which contradicts the observation of a strong variant selection of the BF in this study. However, the BF transformed during isothermal holding similar to the Ref. [17] whereas the GB formed during continuous cooling which might be the reason for this contradiction. Therefore, other differences between the formation of ferrite in BF and GB, such as size, morphology, and the amount of other phases, might lead to a high variant selection in the BF.

6.8.1 The effect of the retained austenite on the variant selection

The amount of retained austenite in the BF can reach up to 40% of the whole volume fraction compared to less than 10% RA in the GB. Although the effect of RA in the variant selection was not discussed in the literature, a high amount of the RA was always found to be associated with high variant selection [20, 78, 80, 91, 169, 171-174, 176, 182, 183]. Although some papers report the total amount of RA present, the authors did not consider the exact local arrangement of RA in each prior austenite grain, which might have an influence on the variant selection [174].

This study clearly shows that GB had less amount of the RA and weak ferrite variant selection, whereas BF had a significantly higher volume fraction of the RA and strong variant selection. Therefore, the high amount of RA that remained after the BF transformation in this study was suggested as the reason for the high variant selection. Thus in the case of BF, there was no need for self-accommodation by the formation of all variants in BF due to plastic accommodation of transformation strain by RA.

When both GB and BF formed in the same grain, the formation of GB was interrupted by the formation of BF which led to a strong ferrite variant selection in the BF as well as GB. In this situation it was suggested that both mechanisms of transformation strain accommodation can occur with dominance of the plastic accommodation by the retained austenite, which led to the strong variant selection in the BF.

A similar morphology of a parallel lath-like bainite with a high amount of RA was investigated by Suikkanen *et al.* [169]. The isothermal transformation of bainite (0.2C-2.0Mn-1.5Si-0.6Cr) at 450°C led to the formation of more than 14% of RA and a strong variant selection that was indicated by the absence of one third of variants in one CP.

Nevertheless, it has been stated that the reason for variant selection is not clear. In addition, their study does not show the RA between the BF laths or all variants, it only provides a local analysis of the variants in each CP [169]. Similar to the current steels, an indication of variant selection based on an analysis of orientation distribution functions (ODF) was also found in two inter-critically annealed TRIP steels with different amounts of Si and Al [80]. Although, these steels had a high amount of the RA (>13%), the authors did not discuss the reasons for the variant selection or consider the role that RA could play in this. In another study, the development of variant selection was investigated by high-temperature laser scanning confocal microscopy (LSCM). The high amount of RA in the low-carbon 13Cr-9Ni steel [20] and Fe-0.1C-1Ni-0.8Mn-0.4Mo (mass %) steel [176] led to the high variant selection in martensite structure. This was related to the plastic accommodation (PA) which took place due to the high amount of RA. The increase in the number of variants during transformation by forming other blocks was associated with a reduction in the amount of RA.

Moreover, the variant selection was analysed locally in nanostructured bainite 0.79C–1.5Si–1.98Mn–0.98Cr–0.24Mo–1.06Al–1.58Co (wt.%) after isothermal transformation at two different temperatures of 350°C and 200°C [174]. The microstructure of the steel after both heat treatments was characterised by a high volume fraction of the RA and variant selection. However, less variant selection was observed after the transformation temperature was decreased from 350°C to 200°C, which was associated with a reduction of the temperature and refining of the microstructure. However, this reduction in the transformation temperature was also accompanied by a reduction in the RA content, which might be the main influence on variant selection.

A variant selection analysis of 0.22C-1.56Si- 1.50Mn-0.031Al-0.045Nb-0.017Ti (mass %) steel showed there was a variant selection in the undeformed prior austenite grains compared to the deformed austenite [91]. The cause of this variant selection was not understood and simply referred to space limitations. The presence of ~5% of RA in the microstructure and subsequent lack of information on its distribution precluded the use of the RA as an explanation for the observed phenomenon [91].

On another hand, Malet *et al.* [92] investigated the effect of the prior deformation of the austenite on the variant selection in TRIP steel with 20% RA, and found that an increase in reduction during austenite rolling led to a more pronounced variant selection. This variant selection has been linked to the development of dislocation substructure by ausforming,

which influences the bainite morphology and nucleation sites. It has been stated that the planar dislocations remaining in the active slip planes leads to high variant selection because this kind of dislocation helps in the transformation of bainite [16, 181].

In the current work, both steels were subjected to the same amount of deformation at 850-875°C, after which they were slowly cooled at 1 Ks^{-1} to 680-690°C. During this slow cooling the recovery of deformation substructure takes place, thus their role in variant selection is minimised [184], unlike when steel is cooled rapidly after deformation [84]. In addition, if the deformation of austenite influences variant selection in the current bainite microstructure, the same influence should be seen in both BF and GB because GB forms earlier. Consequently, it could be concluded that in the current study the prior deformation of austenite did not have a pronounced effect on variant selection in the GB or BF. However, the prior deformation of austenite has influence on its texture which might have influenced the formation of preferred variant pairs.

To understand the effect of the RA on the variant selection, the nucleation and growth of the variants of the bainitic ferrite laths has to be discussed. Since most research on variant selection was conducted at room temperature, post-mortem, and does not provide a direct insight into the sequence of variants formation. A limited number of works have reported in-situ observations of bainite formation with a focus on variant selection [20, 176]. It has been shown that during the first stage, a preferred variant (from the energy viewpoint) nucleates at the austenite grain boundary, while simultaneously, another variant belonging to the same Bain group and different CP nucleates, which also satisfies the energy conditions at different boundary locations. Typically, one Bain group is dominant and different variants from the same Bain group are formed. The growth of the second variant in the same Bain group can be retarded by the growth of the first variant or by the micro-sized particles due to high local stresses formed around them [185], which also leads to the formation of another variant from the same Bain group. Next, another variant from the third CP belonging to same Bain group nucleates. At this stage of transformation, there is only one dominant Bain group because the transformation strain is accommodated by the austenite (Plastic Accommodation, PA). At the second stage, the self-accommodation (SA) becomes dominant, which is associated with a reduction in the amount of RA available for PA.

This can suggest that when a high amount of RA is remained in the microstructure, the SA will not be initiated and variant selection will be observed regardless of the transformation temperature. However, if there is a limited amount of the RA remained in

the microstructure, the role of transformation temperature becomes more important for the variant selection. At high temperature, the ease of the RA rotation and plastic deformation reduces the need for multiple variants formation, whereas at low temperatures the rigidity of the RA increases and in combination with its low amount, this leads to the need for the self-accommodation of transformation strain by different ferrite variants in bainite.

As highlighted previously, the irregular-shaped ferrite in GB had a very limited variant selection, unlike the BF laths which formed at a lower isothermal temperature. The GB was formed predominantly during cooling [161], thus fast continuous undercooling assists nucleation at different locations but restricts the growth rate. A further reduction in temperature increased the driving force for bainite formation [46] which in turn increased the nucleation rate [186]. As a result, the microstructure of GB was characterised by finer plates in comparison to the BF and by less amount of the remaining RA. The dominant nucleation process during GB formation and the formation of only a small fraction of retained austenite, which is insufficient to provide plastic accommodation of the transformation strain, resulted in the self-accommodation of the transformation strain and the absence of variant selection in the ferrite of GB. The influence of a fast cooling rate on the realisation of all six variants in a CP was also reported by Gourgues *et al.* [179]. Their finding confirmed the influence of transformation mechanism of GB on the realisation of all variants.

Suikkanen *et al.* [169] observed that the cooling method (isothermal vs. continuous cooling) affected the variant selection, where they stated that a clear variant selection occurred on the bainite that transformed isothermally. However, the amount of RA effect was not considered in their study. Takaki *et al.* [187] suggested that a single variant transformation (similar to BF) would increase the stability of the RA compared to a multi-variant transformation (similar to GB). However, in this study, it was believed that the transformation mechanism (GB or BF) would influence the stability of RA which in turn would influence the variant formation.

The less amount of RA in the GB can be explained by the carbon diffusion to the dislocation due to fast continuous undercooling. This carbon acts as obstacles to the dislocation movement [188] during isothermal holding and leads to the formation of a high density substructure in the GB. This mechanism stopped the RA from being enriched with carbon which negatively affected its stability. On the other hand, the depletion of carbon in the parent austenite or a decrease in temperature increased the driving force for

transformation which could be why all the variants in GB were realised. In the case of BF, the higher carbon content in the interlayers of retained austenite due to the rejection of carbon: (i) from the previously formed polygonal ferrite and granular bainite, and (ii) during the growth of the bainitic ferrite laths themselves, could be also a reason for the variant selection in this morphology.

It also should be pointed out, that it could also be suggested that the phase transformation has reached a later stage in the case of the GB formation, whereas it is more incomplete in the case of the BF. Again, this could be due to the different transformation temperatures and their effect on the growth of bainite. It could be speculated that if the transformation progressed any further in BF, the amount of RA would be reduced, which would trigger the need for BF to self-accommodation resulting in the increase in the number of the realised variants.

6.9 Conclusions

A crystallography analysis was conducted on the irregular-shaped ferrite in granular bainite and bainitic ferrite laths that had formed in the carbide-free bainite after thermo-mechanical processing. The following conclusions can be drawn from this study:

1. The relationship between austenite and ferrite in bainite was close to Kurdjumov-Sachs orientation relationship with a deviation of 5° in 90% of the grains.
2. The quantitative analysis conducted in this study via calculating the volume fraction of each variant provided a statistical analysis of the variant realisation in each prior austenite grain. This approach led to a detailed analysis of the crystallographic differences between different ferrite morphologies in bainite.
3. Although the GB and BF that formed as a result of the same thermo-mechanical processing, the difference in their transformational behaviour led to a distinctive difference in their crystallography.
4. GB was formed during continuous cooling from 680°C to 470°C where the self-accommodation of the transformation strain was dominant. The small amount of retained austenite fraction remained as well as the dominant role of nucleation during cooling, which explained the absence of variant selection in this morphology and a realisation of most of the 24 possible variants of the Kurdjumov-Sachs orientation relationship.
5. The realisation of all variants in the ferrite in GB showed that in present study, hot deformation of austenite well before the bainitic transformation had no influence on variant selection. However, this behaviour can be related to the recovery of the austenite during relatively slow continuous cooling after deformation.
6. Bainitic ferrite was formed during isothermal holding at 470°C and showed a high fraction of retained austenite. This morphology was characterised by significant variant selection of BF laths, which was attributed to the plastic accommodation of the transformation strain in the remaining retained austenite, and less volume available for its formation. Consequently, variants pairing cannot be evaluated in BF due to the high amount of RA that separated between the BF laths.
7. The BF morphology with non-parallel CPs showed less variant selection of BF laths compared to many other examples of BF with parallel laths. The large area available for the bainite transformation could also explain this difference in the crystallography.

8. In most cases, the GB and BF were formed together in the same prior austenite grain, even though variant selection was still pronounced in the BF where only one or two variants formed in each CP. Although the GB displayed some reduction in the number of the CPs in the mixed microstructure, most of the variants were realised in each formed CP.

7 CONCLUSIONS AND RECOMMENDATIONS

This chapter summarises the main conclusions and the contribution of this study to the knowledge. It also addresses future work at the end of this chapter.

7.1 General Conclusions

The microstructure-property relationships in a base low Si, high Al TRIP steel with and without 0.03Nb and 0.02Ti (wt.%) additions were analysed after various thermo-mechanical processing schedules. The base steel with a short coiling time of 125 s at 470°C resulted in the highest amount of the retained austenite phase and the best combination of mechanical strength and elongation. All the thermo-mechanically processed base steel samples recorded continuous yielding behavior. However, the addition of Nb and Ti refined the final microstructure after thermo-mechanical processing and led to an increase in the time required for a high volume fraction of the stable retained austenite phase to develop. Unlike the base steel, the strength-ductility balance in the Nb-Ti steel improved slightly due to a combination of microstructure refinement, a higher volume fraction of RA, and precipitation strengthening. The Nb-Ti steel exhibited discontinuous yielding after thermo-mechanical processing when a long coiling time of 1200 s was undertaken.

The intercritically annealed samples of the base and Nb-Ti steels showed discontinuous yielding with a long Lüders elongation, as well as a steep reduction in the instantaneous n-value from its maximum at a small value of tensile strain. This was explained by the refinement of the polygonal ferrite grains and the ageing processes that occur during galvanising. The modified C-J analysis showed three stages of work hardening in both steels, where Stage 2 was associated with different rates of RA transformation.

A multi-condition phase segmentation procedure was developed and successfully applied on two thermo-mechanically processed TRIP steels using EBSD data. Based on grain orientation spread (GOS) and grain size criterion, this method was able to distinguish

between polygonal ferrite, bainite, and martensite in the low Si TRIP steels. Being able to separate these constituents makes a further detailed analysis of this steel possible.

The variations in the amount of RA at different tensile strains were measured by EBSD. The transformation rate of RA in the Nb-Ti steel was higher than that in the base steel, which indicated a higher stability of RA in the base steel. This was related to the dominancy of granular bainite in the base steel, unlike the dominancy of bainitic ferrite in the Nb-Ti steel. However, a high initial amount of RA was found in the BF morphology.

A local misorientation analysis was conducted on each phase in both steels. The changing rate of local misorienation in the bainite with tensile deformation was higher in the Nb-Ti steel than in the base steel. This behaviour was related to the dominancy of BF morphology in the Nb-Ti steel and deemed to be responsible for the lower stability of RA in BF compared to GB. The stability of large and small RA grains was investigated in this study, and it was found that the partial transformation of RA grains can lead to a misleading conclusion regarding the high stability of small RA grains, because the partial transformation of large RA grain introducesd small RA grains. The stability of RA at different locations was discussed in this study. Most of the RA was formed between the bainitic ferrite laths, but a small amount was formed at the PF/B interface. The stability of RA at the interface was much less than its stability in the bainite, but higher than its stability in the PF.

The partial transformation of RA grains at the interphase was related to the carbon enrichment of RA, and therefore the part of RA that close to the PF was less stable than the part of RA which was adjacent to the bainite. However, it was believed that the RA transformation was more complex and influenced by factors such as the segregation of Mn and the grain orientation which led to the non-anticipated transformation behaviour in some RA grains.

A crystallography analysis was conducted on carbide-free bainite and it highlighted the differences between ferrite in granular bainite and bainitic ferrite. The orientation relationship between austenite and ferrite in bainite was close to the Kurdjumov-Sachs orientation relationship with a deviation of 5° in 90% of the grains. Although the GB and BF were formed as a result of the same thermo-mechanical processing parameters, the difference in their transformation mechanism led to a distinct difference in their crystallography. GB consisting of irregular-shaped and/or plate-like ferrite with a small amount of martensite/retained austenite constituent was formed during continuous

cooling from 680°C to 470°C where the self-accommodation of transformation strain was dominant. The small amount of retained austenite fraction that remained, as well as the dominant role of nucleation during continuous cooling, can explain the absence of variant selection in this morphology and the realisation of most of the 24 variants of the Kurdjumov-Sachs orientation relationship. The realisation of all variants in the GB showed that the deformation of austenite prior to the bainitic transformation did not influence the variant selection. However, this behaviour can be related to the recovery of austenite during continuous cooling after deformation.

Bainitic ferrite consisting of relatively coarse (and sometimes parallel) ferrite laths with retained austenite between them was formed during isothermal holding at 470°C and showed a high fraction of retained austenite. This morphology was characterised by a significant variant selection, which was attributed to the plastic accommodation of the transformation strain in the remaining retained austenite. Consequently, variants pairing cannot be evaluated in BF due to the high amount of RA between the BF laths. A unique BF morphology consisting of differently oriented packets of finer parallel bainitic ferrite laths with fine interlayers of retained austenite was observed in a small area fraction, and showed less variant selection compared to BF with coarse parallel laths. The large area available for the transformation of bainite with multi-oriented laths can explain this difference in crystallography.

In most cases, the GB and BF were formed together in the same prior austenite grain, even though a variant selection was still pronounced in the BF where only one variant formed in each CP. Although the GB, formed in the same grain with BF, exhibited a reduction in the number of CPs, most of the variants were realised in each formed CP.

7.2 Contribution to the Knowledge

By utilising several techniques, particularly EBSD, this study provided a further understanding of the stability of RA and the microstructure/properties relationship in low Si TRIP steels with and without the addition of Nb and Ti. The following points summarise the contribution this study makes to the knowledge.

- This is one of the first studies to compare the mechanical properties and work hardening behaviour of low Si TRIP steel after TMP and IA. The work hardening behaviour of these steels was analysed using the modified C-J analysis and the work hardening curves were divided into three stages. The behaviour of the work hardening curves was linked to the RA transformation.
- For the first time, a multi-condition method for phase separation using EBSD only was developed and successfully applied for a thermo-mechanically processed low Si TRIP steels to separate between polygonal ferrite, ferrite in granular bainite, bainitic ferrite, and martensite. This unique procedure can be applied for a wide range of engineering alloys to separate between phases and constituents.
- This is one of the first studies to investigate the factors influencing the stability of the RA after a different strain using the EBSD technique.
- For the first time, EBSD was used to carry out a comprehensive investigation into the crystallography of the granular bainite and bainitic ferrite morphologies found in the carbide-free bainite. The variant selection was discussed for the first time from the point of view of the presence of RA and bainite morphology in each austenite grain.

7.3 Future Work

The effect of coiling time and subsequent galvanising heat treatment was investigated using a low Si TRIP steel. The work hardening rate and instantaneous n-value behaviour was discussed based on and linked to the initial fraction of RA determined by XRD and EBSD. Further discussion was possible based on the measurement of RA at UTS and fracture. However, in-situ analysis [101] using EBSD and/or neutron or synchrotron X-ray diffraction will provide further details and can analyse the same location at different strains, particularly at low strain were RA with low stability is expected to transform.

The EBSD-based segmentation method developed in this study was successfully applied to low Si TRIP steel at different strains. However, to confirm the applicability of this method on other steels, it should be applied to several steels in order to investigate its advantages and limitations. Additional criteria can be added to improve the separation method, particularly between GB and BF. One approach is to carry out the simultaneous EDS and EBSD, because a relative carbon variation is expected between these two morphologies. Moreover, three-dimensional EBSD studies [189] can confirm the current method of segmentation and verify any differences between the morphologies, as well as provide a better insight into the carbide-free morphologies of bainite.

All the discussion of the mechanical stability of RA was based on a two-dimensional analysis of the EBSD maps. A three-dimensional analysis based on EBSD can provide further understanding of the factors influencing the mechanical stability of RA in TRIP steel. Other factors should be also considered when studying the stability of RA, such as the grain orientation with respect to the deformation axis. Further investigation of the Mn variation in each austenite grain using electron probe microanalysis (EPMA)[165] is also recommended as one of the factors that can influence the stability of the RA, and which was not considered in this study.

A crystallographic analysis was conducted on the GB and BF of a local selected area of an EBSD map. A better understanding of the crystallography of these two morphologies could be achieved by applying the same analysis on more EBSD maps. This would improve our understanding of the crystallography of these two morphologies as well as the morphology observed in a small area fraction such as multi-oriented bainitic ferrite (or acicular ferrite). On the other hand, an in-situ investigation of the transformation of

carbide-free bainite by high-temperature laser scanning confocal microscopy (LSCM) [20] would also reveal further information on the variant selection in each morphology.

All the crystallographic analyses in this study were based on two-dimensional EBSD maps, so another three-dimensional EBSD analysis [189] of the variant selection could provide even better understanding.

REFERENCES

1. De Cooman, B.C., *Structure-properties relationship in TRIP steels containing carbide-free bainite.* Current Opinion in Solid State and Materials Science, 2004. **8**(3-4): p. 285-303.
2. Mintz, B., *Hot dip galvanising of transformation induced plasticity and other intercritically annealed steels.* International Materials Reviews, 2001. **46**(4): p. 169-197.
3. Bleck, W., Frehn, A., and Ohlert, J., *Niobium in Dual Phase and TRIP Steels.* Niobium–Science & Technology. Proceedings. Niobium, 2001: p. 727-752.
4. Zackay, V.F., Parker, E.R., Fahr, D., and Busch, R., *The enhancement of ductility in high-strength steels.* ASM Trans Quart, 1967. **60**(2): p. 252-259.
5. Yue, S., DiChiro, A., and ZareiHanzaki, A., *Thermomechanical processing effects on C-Mn-Si TRIP steels.* Jom-Journal of the Minerals Metals & Materials Society, 1997. **49**(9): p. 59-61.
6. Bhadeshia, H., *TRIP-assisted steels?* ISIJ International(Japan), 2002. **42**(9): p. 1059-1060.
7. Bellhouse, E.M., Mertens, A.I.M., and McDermid, J.R., *Development of the surface structure of TRIP steels prior to hot-dip galvanizing.* Materials Science and Engineering a-Structural Materials Properties Microstructure and Processing, 2007. **463**(1-2): p. 147-156.
8. Suh, D.W., Park, S.J., Oh, C.S., and Kim, S.J., *Influence of partial replacement of Si by Al on the change of phase fraction during heat treatment of TRIP steels.* Scripta Materialia, 2007. **57**(12): p. 1097-1100.
9. Maki, J., Mahieu, J., De Cooman, B.C., and Claessens, S., *Galvanisability of silicon free CMnAI TRIP steels.* Materials Science and Technology, 2003. **19**(1): p. 125-131.
10. Timokhina, I.B., Hodgson, P.D., and Pereloma, E.V., *Effect of microstructure on the stability of retained austenite in transformation-induced-plasticity steels.* Metallurgical and Materials Transactions A, 2004. **35A**(8): p. 2331-2341.
11. Jung, J., Lee, S.J., Kim, S., and De Cooman, B.C., *Effect of Ti additions on micro-alloyed Nb TRIP steel.* Steel Research International, 2011. **82**(7): p. 857-865.
12. Zaefferer, S., Romano, P., and Friedel, F., *EBSD as a tool to identify and quantify bainite and ferrite in low-alloyed Al-TRIP steels.* Journal of Microscopy, 2008. **230**(3): p. 499-508.
13. Kang, J.-Y., Kim, D.H., Baik, S.-I., Ahn, T.-H., Kim, Y.-W., Han, H.N., Oh, K.H., Lee, H.-C., and Han, S.H., *Phase analysis of steels by grain-averaged EBSD functions.* ISIJ International, 2011. **51**(1): p. 130-136.
14. Kundu, S., Verma, A.K., and Sharma, V., *Quantitative analysis of variant selection for displacive transformations under stress.* Metallurgical and Materials Transactions A, 2012. **43**(7): p. 2552-2565.
15. Mishiro, Y., Namb, S., Inoue, J., and Koseki, T., *Effect of stress on variant selection in lath martensite in low carbon steel.* Isij International, 2013. **53**(8): p. 1453.
16. Gong, W., Tomota, Y., Adachi, Y., Paradowska, A., Kelleher, J., and Zhang, S., *Effects of ausforming temperature on bainite transformation, microstructure and variant selection in nanobainite steel.* Acta Materialia, 2013. **61**: p. 4142-4154.
17. Takayama, N., Miyamoto, G., and Furuhara, T., *Effects of transformation temperature on variant pairing of bainitic ferrite in low carbon steel.* Acta Materialia, 2012. **60**(5): p. 2387-2396.
18. Morito, S., Huang, X., Furuhara, T., Maki, T., and Hansen, N., *The morphology and crystallography of lath martensite in alloy steels.* Acta Materialia, 2006. **54**(19): p. 5323-5331.

19. Morito, S., Tanaka, H., Konishi, R., Furuhara, T., and Maki, T., *The morphology and crystallography of lath martensite in Fe-C alloys.* Acta Materialia, 2003. **51**(6): p. 1789-1799.
20. Zhang, S., Morito, S., and Komizo, Y.-i., *Variant selection of low carbon high alloy steel in an austenite grain during martensite transformation.* ISIJ International, 2012. **52**(3): p. 510-515.
21. Furuhara, T., Kawata, H., Morito, S., and Maki, T., *Crystallography of upper bainite in Fe-Ni-C alloys.* Materials Science and Engineering: A, 2006. **431**(1): p. 228-236.
22. Godet, S., Georges, C., and Jacques, P.J., *On the austenite retention in low alloy steels*, in *Austenite Formation and Decomposition*. 2003. p. 523-536.
23. Bhadeshia, H. and Honeycombe, S.R., *Steels : microstructure and properties* 3rd ed. 2006. p. 209 - 233.
24. Sakuma, Y., Matsumura, O., and Akisue, O., *Influence of C content and annealing temperature on microstructure and mechanical properties of 400°C transformed steel containing retained austenite.* ISIJ International, 1991. **31**(11): p. 1348-1353.
25. Panigrahi, B.K., *Processing of low carbon steel plate and hot strip—an overview.* Bulletin of Materials Science, 2001. **24**(4): p. 361-371.
26. Llewellyn, D.T. and Hudd, R.C., *Steels: metallurgy and applications* 1998. p. 57 - 84.
27. Fonstein, N., Pottore, N., Lalam, S.H., and Bhattacharya, D., *phase transformation behavior during continuous cooling and isothermal holding of aluminum and silicon bearing TRIP steels*, in *Symposium on the Thermodynamics, Kinetics, Characterization and Modeling of: Austenite Formation and Decomposition*. 2003. p. 549 - 561.
28. Mintz, B., Tuling, A., and Delgado, A., *Influence of silicon, aluminium, phosphorus and boron on hot ductility of TRansformation Induced Plasticity assisted steels.* Materials Science and Technology, 2003. **19**(12): p. 1721.
29. Tsukatani, I., Hashimoto, S., and Inoue, T., *Effects of silicon and manganese addition on mechanical properties of high-strength hot-rolled sheet steel containing retained austenite.* ISIJ International, 1991. **31**(9): p. 992-1000.
30. Baik, S.C., Kim, S., Jin, Y.S., and Kwon, O., *Effects of alloying elements on mechanical properties and phase transformation of cold rolled TRIP steel sheets.* ISIJ International, 2001. **41**(3): p. 290-297.
31. Van Slycken, J., Verleysen, P., Degrieck, J., Bouquerel, J., and De Cooman, B., *The effect of silicon, aluminium and phosphor on the dynamic behavior and phenomenological modelling of multiphase TRIP steels.* Metals and Materials International, 2007. **13**(2): p. 93-101.
32. Kozeschnik, E. and Bhadeshia, H., *Influence of silicon on cementite precipitation in steels.* Materials Science and Technology, 2008. **24**(3): p. 343-347.
33. Gomez, M., Garcia, C.I., Haezebrouck, D.M., and Deardo, A.J., *Design of Composition in (Al/Si)-alloyed TRIP Steels.* ISIJ International, 2009. **49**(2): p. 302-311.
34. Mahieu, J., Maki, J., De Cooman, B.C., and Claessens, S., *Phase transformation and mechanical properties of Si-free CMnAl transformation-induced plasticity-aided steel.* Metallurgical and Materials Transactions A, 2002. **33**(8): p. 2573-2580.
35. Jacques, P.J., *Transformation-induced plasticity for high strength formable steels.* Current Opinion in Solid State and Materials Science, 2004. **8**(3-4): p. 259-265.
36. Li, Z. and Wu, D., *Effects of hot deformation and subsequent austempering on mechanical properties of high silicon and low silicon TRIP steel.* Materials Science and Technology, 2008. **24**(2): p. 168-176.
37. Zhang, M., Li, L., Fu, R.Y., Krizan, D., and De Cooman, B.C., *Continuous cooling transformation diagrams and properties of micro-alloyed TRIP steels.* Materials Science and Engineering: A, 2006. **438-440**: p. 296-299.

38. Kim, S.J., Lee, C.G., Choi, I., and Lee, S., *Effects of heat treatment and alloying elements on the microstructures and mechanical properties of 0.15 wt pct C transformation-induced plasticity-aided cold-rolled steel sheets.* Metallurgical and Materials Transactions A, 2001. **32**(3): p. 505-514.
39. De Meyer, M., Vanderschueren, D., and De Cooman, B.C., *The influence of the substitution of Si by Al on the properties of cold rolled C-Mn-Si TRIP steels.* ISIJ International, 1999. **39**(8): p. 813-822.
40. Suh, D.W., Park, S.J., Lee, T.H., Oh, C.S., and Kim, S.J., *Influence of Al on the microstructural evolution and mechanical behavior of low-carbon, manganese transformation-induced-plasticity steel.* Metallurgical and Materials Transactions A, 2009. **41**(2): p. 397-408.
41. Li, L., De Cooman, B.C., Wollants, P., He, Y.L., and Zhou, X.D., *Effect of aluminum and silicon on transformation induced plasticity of the TRIP steel.* Journal of Materials Science & Technology, 2004. **20**(2): p. 135-138.
42. Samek, L., Moor, E.D., Penning, J., and De Cooman, B.C., *Influence of alloying elements on the kinetics of strain-induced martensitic nucleation in low-alloy, multiphase high-strength steels.* Metallurgical and Materials Transactions A, 2006. **37A**(1): p. 109-124.
43. Traint, S., Pichler, A., Spiradek-Hahn, K., Hulka, K., and Werner, E., *The influence of Nb on the phase transformations and mechanical properties in Al- and Si- alloyed TRIP-steels.* Symposium on the Thermodynamics, Kinetics, Characterization and Modeling of Austenite Formation and Decomposition, 2003: p. 577-594.
44. Bouet, M., Root, J., Es-Sadiqi, E., and Yue, S., *The effect of Mo in Si-Mn Nb bearing TRIP steels.* Materials Science Forum (Switzerland), 1998. **284-286**: p. 319-326.
45. Jiao, S., Hassani, F., Donaberger, R.L., Essadiqi, E., and Yue, S., *The Effect of Processing History on a Cold Rolled and AnnealedMo–Nb Microalloyed TRIP Steel.* ISIJ International, 2002. **42**(3): p. 299-303.
46. Hashimoto, S., Ikeda, S., Sugimoto, K., and Miyake, S., *Effects of Nb and Mo addition to 0.2% C-1.5% Si-1.5% Mn steel on mechanical properties of hot rolled TRIP-aided steel sheets.* ISIJ International, 2004. **44**(9): p. 1590-1598.
47. Grajcar, A., *Selection of the hot-working conditions for TRIP-type microalloyed steel.* Archives of Materials Science, 2008. **76**: p. 75-78.
48. Cuddy, L. and Raley, J., *Austenite grain coarsening in microalloyed steels.* Metallurgical Transactions A, 1983. **14**(10): p. 1989-1995.
49. Tang, Z.Y., Ding, H., Du, L.X., and Li, L., *Microstructures and mechanical properties of Si-Al-Mn TRIP steel with niobium.* Journal of Materials Science & Technology, 2007. **23**(6): p. 790-794.
50. Bai, D.Q., Di Chiro, A., and Yue, S., *Stability of retained austenite in a Nb microalloyed Mn-Si TRIP steel.* Materials Science Forum (Switzerland), 1998. **284-286**: p. 253-260.
51. Mizui, N. and Kojima, N., *Effect of Si on the mechanical property of ultra-low carbon Ti-added Cold-rolled sheet steels with various content of Mn or P, coiled at 500 C in hot rolling process.* ISIJ International, 1994. **34**(1): p. 123-131.
52. Barbe, L., Verbeken, K., and Wettinck, E., *Effect of the addition of P on the mechanical properties of low alloyed TRIP steels.* ISIJ International, 2006. **46**(8): p. 1251-1257.
53. Pichler, A., Stiaszny, P., Potzinger, R., Tikal, R., and Werner, E., TRIP steels with reduced Si content. in *Proc. 40th MWSP Conf.,* 1998. p. 259.
54. Chen, H.C., Era, H., and Shimizu, M., *Effect of phosphorus on the formation of retained austenite and mechanical properties in Si-containing low-carbon steel sheet.* Metallurgical and Materials Transactions A, 1989. **20**(3): p. 437-445.

55. Hertveldt, I., De Cooman, B.C., and Claessens, S., *Influence of annealing conditions on the galvanizability and galvannealing properties of TiNb interstitial-free steels, strengthened with phosphorous and manganese.* Metallurgical and Materials Transactions A, 2000. **31**(4): p. 1225-1232.
56. De Cooman, B.C., Samek, L., Mahicu, J., Van Slycken, J., Verleysen, P., Degrieck, J., Lin, L., Wang, L., Wei, X.C., and Peng, S., *Quasi-adiabatic effects during the high strain rate deformation of dispersed-phase systems with strain-induced martensitic transformation*, in *Symposium on the Thermodynamics, Kinetics, Characterization and Modeling of Austenite Formation and Decomposition*. 2004. p. 537-548.
57. Timokhina, I.B., Hodgson, P.D., and Pereloma, E.V., *Effect of deformation schedule on the microstructure and mechanical properties of a thermomechanically processed C-Mn-Si transformation-induced plasticity steel.* Metallurgical and Materials Transactions A, 2003. **34A**(8): p. 1599-1609.
58. Hanzaki, A.Z. and Yue, S., *Ferrite formation characteristics in Si-Mn TRIP steels.* Isij International, 1997. **37**(6): p. 583-589.
59. Sugimoto, K., Muramatsu, T., Hashimoto, S., and Mukai, Y., *Formability of Nb bearing ultra high-strength TRIP-aided sheet steels.* Journal of Materials Processing Technology, 2006. **177**(1-3): p. 390-395.
60. Gallagher, M.F., Speer, J.G., and Matlock, D.K., *Effect of annealing temperature on austenite decomposition in a Si-alloyed trip steel*. 2003. p. 563-576.
61. Bablik, H., *Galvanizing (hot-dip)*. 1950: E. & FN Spon.
62. Chattopadhyay, A., Subramanya Sarma, V., Murty, B.S., Haldar, A., and Bhattacharjee, D., *Studies on hot rolled galvanized steel sheets: Effect of reheating on galvanizing.* Surface and Coatings Technology, 2009. **203**(22): p. 3465-3471.
63. Marder, A.R., *The metallurgy of zinc-coated steel.* Progress in Materials Science, 2000. **45**(3): p. 191-271.
64. Pereloma, E.V., Gazder, A.A., and Timokhina, I., *The transformation-induced plasticity effect and the stability of retained austenite in steels*, in *The Encyclopaedia of Iron, Steel and Their Alloys*, R. Colás and G.E. Totten, Editors. 2014, Taylor and Francis: New York, Accepted.
65. Petrov, R., Kestens, L., Wasilkowska, A., and Houbaert, Y., *Microstructure and texture of a lightly deformed TRIP-assisted steel characterized by means of the EBSD technique.* Materials Science and Engineering: A, 2007. **447**(1-2): p. 285-297.
66. Tanaka, T., *Controlled rolling of steel plate and strip.* International Materials Reviews, 1981. **26**(1): p. 185-212.
67. Bengochea, R., Lopez, B., and Gutierrez, I., *Microstructural evolution during the austenite-to-ferrite transformation from deformed austenite.* Metallurgical and Materials Transactions a-Physical Metallurgy and Materials Science, 1998. **29**(2): p. 417-426.
68. Hanzaki, A.Z., Hodgson, P.D., and Yue, S., *The influence of bainite on retained austenite characteristics in Si-Mn TRIP steels.* ISIJ International, 1995. **35**(1): p. 79-85.
69. Zajac, S., Komenda, J., Morris, P., Dierickx, P., Matera, S., and Penalba, D.F., *Quantitative structure-property relationships for complex bainitic microstructures.* Technical Steel Research report no. EUR 21245EN, European Commission, Luxembourg., 2005: p. 1-157.
70. Thompson, S., Col, D.V., and Krauss, G., *Continuous cooling transformations and microstructures in a low-carbon, high-strength low-alloy plate steel.* Metallurgical Transactions A, 1990. **21**(6): p. 1493-1507.
71. Bramfitt, B. and Speer, J., *A perspective on the morphology of bainite.* Metallurgical Transactions A, 1990. **21**(3): p. 817-829.

72. Caballero, F.G., Roelofs, H., Hasler, S., Capdevila, C., Chao, J., Cornide, J., and Garcia-Mateo, C., *Influence of bainite morphology on impact toughness of continuously cooled cementite free bainitic steels.* Materials Science and Technology, 2012. **28**(1): p. 95-102.
73. Bain, E.C., *The nature of martensite.* Trans. AIME, 1924. **70** p. 25-47.
74. Kurdjumov, G. and Sachs, G., *Over the mechanisms of steel hardening.* Z. Phys, 1930. **64**: p. 325-343.
75. Nishiyama, Z., *Kinzoku-no-Kenkyu, 13 (1936), 300.* Sei. Rep., Tohoku Imp. Univ, 1936. **25**: p. 79.
76. Wassermann, G., *Einfluss der alpha-gamma-Umwandlung eines irreversiblen Nickelstahls auf Kristallorientierung und Zugfestigkeit [Influence of the alpha-gamma transformation of an irreversible nickel steel on crystal orientation and tensile strength].* Archiv fur das Eisenhuttenwesen, 1933. **6**(8): p. 347-351.
77. Greninger, A.B. and Troiano, A.R., *Crystallography of austenite decomposition.* Trans. AIME, 1940. **140**: p. 307 - 336.
78. Verbeken, K., Barbe, L., and Raabe, D., *Evaluation of the crystallographic orientation relationships between FCC and BCC phases in TRIP steels.* ISIJ International, 2009. **49**(10): p. 1601-1609.
79. Ray, R. and Jonas, J., *Transformation textures in steels.* International Materials Reviews, 1990. **35**(1): p. 1-36.
80. De Meyer, M., Kestens, L., and De Cooman, B., *Texture development in cold rolled and annealed C-Mn-Si and C-Mn-Al-Si TRIP steels.* Materials Science and Technology, 2001. **17**(11): p. 1353-1359.
81. Kitahara, H., Ueji, R., Tsuji, N., and Minamino, Y., *Crystallographic features of lath martensite in low-carbon steel.* Acta Materialia, 2006. **54**(5): p. 1279-1288.
82. Kitahara, H., Ueji, R., Ueda, M., Tsuji, N., and Minamino, Y., *Crystallographic analysis of plate martensite in Fe-28.5 at.% Ni by FE-SEM/EBSD.* Materials Characterization, 2005. **54**(4): p. 378-386.
83. Abbasi, M., Nelson, T.W., Sorensen, C.D., and Wei, L., *An approach to prior austenite reconstruction.* Materials Characterization, 2012. **66**(0): p. 1-8.
84. Miyamoto, G., Iwata, N., Takayama, N., and Furuhara, T., *Quantitative analysis of variant selection in ausformed lath martensite.* Acta Materialia, 2012. **60**(3): p. 1139-1148.
85. Godet, S., Glez, J.C., He, Y., Jonas, J.J., and Jacques, P.J., *Grain-scale characterization of transformation textures.* Journal of Applied Crystallography, 2004. **37**(3): p. 417-425.
86. Abbasi, M., Nelson, T.W., and Sorensen, C.D., *Analysis of variant selection in friction-stir-processed high-strength low-alloy steels.* Journal of Applied Crystallography, 2013. **46**(3): p. 716-725.
87. Bhadeshia, H., *Nanostructured bainite.* Proceedings of the Royal Society A: Mathematical, Physical and Engineering Science, 2010. **466**(2113): p. 3-18.
88. EN 10002-1, *Metallic materials-Tensile testing.* 2001.
89. Jonas, J. and Wittridge, N., *The γ-to-α transformation of hot rolled austenite.* Metals and Materials, 2000. **6**(3): p. 211-220.
90. Shirzadi, A., Abreu, H., Pocock, L., Klobcar, D., Withers, P., and Bhadeshia, H., *Bainite orientation in plastically deformed austenite.* Int. J. Mater. Res, 2009. **100**: p. 40-45.
91. He, Y., Jonas, J., Godet, S., and Jacques, P., *Crystallographic features of the γ-to-α transformation in a Nb-added transformation-induced plasticity steel.* Metallurgical and Materials Transactions A, 2006. **37**(9): p. 2641-2653.
92. Malet, L., Barnett, M.R., Jacques, P.J., and Godet, S., *Variant selection during the γ-to-α_b phase transformation in hot-rolled bainitic TRIP-aided steels.* Scripta Materialia, 2009. **61**(5): p. 520-523.

93. Bate, P. and Hutchinson, B., *The effect of elastic interactions between displacive transformations on textures in steels.* Acta Materialia, 2000. **48**(12): p. 3183-3192.
94. Lambert-Perlade, A., Gourgues, A.-F.ß., and Pineau, A., *Austenite to bainite phase transformation in the heat-affected zone of a high strength low alloy steel.* Acta Materialia, 2004. **52**(8): p. 2337-2348.
95. Zhang, M.X. and Kelly, P.M., *Determination of carbon content in bainitic ferrite and carbon distribution in austenite by using CBKLDP.* Materials Characterization, 1998. **40**(3): p. 159-168.
96. De Meyer, M., Vanderschueren, D., De Blauwe, K., De Cooman, B.C., and Iron Steel Soc, I.S.S., *The characterization of retained austenite in TRIP steels by X ray diffraction*, in *41st Mechanical Working and Steel Processing Conference Proceedings, Vol 37*. 1999, Iron & Steel Society: Warrendale. p. 483-491.
97. Scott, C.P. and Drillet, J., *A study of the carbon distribution in retained austenite.* Scripta Materialia, 2007. **56**(6): p. 489-492.
98. Jimenez-Melero, E., van Dijk, N.H., Zhao, L., Sietsma, J., Offerman, S.E., Wright, J.P., and van der Zwaag, S., *Martensitic transformation of individual grains in low-alloyed TRIP steels.* Scripta Materialia, 2007. **56**(5): p. 421-424.
99. Lee, S., Lee, S.-J., and De Cooman, B.C., *Reply to comments on Austenite stability of ultrafine-grained transformation-induced plasticity steel with Mn partitioning.* Scripta Materialia, 2012. **66**(10): p. 832-833.
100. Kammouni, A., Saikaly, W., Dumont, M., Marteau, C., Bano, X., and Chara√Ø, A., *Effect of the bainitic transformation temperature on retained austenite fraction and stability in Ti microalloyed TRIP steels.* Materials Science and Engineering: A, 2009. **518**(1): p. 89-96.
101. Lomholt, T.N., Adachi, Y., Bastos, A., Pantleon, K., and Somers, M.A., *Partial transformation of austenite in Al-Mn-Si TRIP steel upon tensile straining: an in situ EBSD study.* Materials Science and Technology, 2013. **29**(11): p. 1383-1388.
102. Sugimoto, K., Misu, M., Kobayashi, M., and Shirasawa, H., *Effects of second phase morphology on retained austenite morphology and tensile properties in a TRIP-aided dual-phase steel sheet.* ISIJ International, 1993. **33**(7): p. 775-782.
103. Zhang, S. and Findley, K., *Quantitative assessment of the effects of microstructure on the stability of retained austenite in TRIP steels.* Acta Materialia, 2013. **61**(6): p. 1895-1903.
104. Zrník, J., Stejskal, O., Nový, Z., Hornak, P., and Fujda, M., *Structure dependence of the TRIP phenomenon in Si-Mn bulk steel.* Materials Science and Engineering: A, 2007. **462**(1-2): p. 253-258.
105. Li, Z. and Wu, D., *Effects of hot deformation and subsequent austempering on the mechanical properties of Si–Mn TRIP steels.* ISIJ International, 2006. **46**(1): p. 121-128.
106. Moor, E.D., Lacroix, S., Clarke, A.J., Penning, J., and Speer, J.G., *Effect of retained austenite stabilized via quench and partitioning on the strain hardening of martensitic steels.* Metallurgical and Materials Transactions A, 2008. **39**(11): p. 2586-2595.
107. Srivastava, A.K., Jha, G., Gope, N., and Singh, S.B., *Effect of heat treatment on microstructure and mechanical properties of cold rolled C-Mn-Si TRIP-aided steel.* Materials Characterization, 2006. **57**(2): p. 127-135.
108. Han, S., Seong, H., Ahn, Y., Garcia, C.I., DeArdo, A.J., and Kim, I., *Effect of alloying elements and coiling temperature on the recrystallization behavior and the bainitic transformation in TRIP steels.* Metals and Materials International, 2009. **15**(4): p. 521-529.
109. Schwartz, A.J., *Electron backscatter diffraction in materials science*. 2009: Springer.

110. Humphreys, F., *Review grain and subgrain characterisation by electron backscatter diffraction.* Journal of Materials Science, 2001. **36**(16): p. 3833-3854.
111. Wu, J., Wray, P.J., Garcia, C.I., Hua, M., and DeArdo, A.J., *Image quality analysis: A new method of characterizing microstructures.* ISIJ International, 2005. **45**(2): p. 254-262.
112. Ryde, L., *Application of EBSD to analysis of microstructures in commercial steels.* Materials Science and Technology, 2006. **22**(11): p. 1297-1306.
113. Wright, S.I., Nowell, M.M., and Field, D.P., *A review of strain analysis using electron backscatter diffraction.* Microscopy and microanalysis, 2011. **17**(03): p. 316-329.
114. Kang, J.-Y., Park, S.-J., Suh, D.-W., and Han, H.N., *Estimation of phase fraction in dual phase steel using microscopic characterizations and dilatometric analysis.* Materials Characterization, 2013 p. 205-215.
115. Wilson, A., Madison, J., and Spanos, G., *Determining phase volume fraction in steels by electron backscattered diffraction.* Scripta Materialia, 2001. **45**(12): p. 1335-1340.
116. Wilson, A.W. and Spanos, G., *Application of orientation imaging microscopy to study phase transformations in steels.* Materials Characterization, 2001. **46**(5): p. 407-418.
117. Cruz, J.A., Rodrigues, T.F.M., Viana, V.D.C., Abreu, H., and Santos, D.B., *Influence of temperature and time of austempering treatment on mechanical properties of SAE 9254 commercial steel.* Steel Research International, 2012. **83**(1): p. 22-31.
118. Kwon, E.P., Fujieda, S., Shinoda, K., and Suzuki, S., *Characterization of transformed and deformed microstructures in transformation induced plasticity steels using electron backscattering diffraction.* Materials Science and Engineering: A, 2011. **528**(15): p. 5007-5017.
119. Calcagnotto, M., Ponge, D., Demir, E., and Raabe, D., *Orientation gradients and geometrically necessary dislocations in ultrafine grained dual-phase steels studied by 2D and 3D EBSD.* Materials Science and Engineering: A, 2010. **527**(10): p. 2738-2746.
120. Man, O., Pantelejev, L., and Pesina, Z., *EBSD analysis of phase compositions of TRIP steel on various strain levels.* Materials Engineering, 2009. **16**(2): p. 15-21.
121. Zhu, K., Barbier, D., and Iung, T., *Characterization and quantification methods of complex BCC matrix microstructures in advanced high strength steels.* Journal of Materials Science, 2013. **48**(1): p. 413-423.
122. Bordignon, L., *Galvanising of hot rolled strip*, in *Galvatech'2001: 5 th International Conference on Zinc and Zinc Alloy Coated Steel Sheet*. Bruxelles. p. 19-26.
123. De, A.K., Speer, J.G., and Matlock , D.K., *Color tint-etching for multiphase steels.* Advanced Materials & Processes, 2003. **161**(2): p. 27-30.
124. Parish, C.M., *Fundamental study of phase transformation in Si-Al TRIP steels.* PhD diss., University of Pittsburgh., 2003.
125. Cullity, B.D. and Stock, S.R., *Elements of X-ray diffraction*. 3 ed. 2001: Prentice Hall, Upper Saddle River.
126. Magner, S., De Angelis, R., Weins, W., and Makinson, J., *A historical review of retained austenite and its measurement by x-ray diffraction.* JCPDS, 2002. **45**: p. 92-97.
127. Onink, M., Brakman, C.M., Tichelaar, F.D., Mittemeijer, E.J., Van der Zwaag, S., Root, J.H., and Konyer, N.B., *The lattice parameters of austenite and ferrite in Fe-C alloys as functions of carbon concentration and temperature.* Scripta Metallurgica et materialia 1993. **29**(8): p. 1011-1016.
128. Jacques, P., Allain, S., Bouaziz, O., De, A., Gourgues, A.-F., Hance, B., Houbaert, Y., Huang, J., Iza-Mendia, A., and Kruger, S., *On measurement of retained austenite in*

multiphase TRIP steels - results of blind round robin test involving six different techniques. Materials Science and Technology, 2009. **25**(5): p. 567-574.
129. ASTM E8-M, *Standard test methods for tension testing of metallic materials.* ASTM International, 1995.
130. Dieter, G.E. and Bacon, D., *Mechanical metallurgy*. Vol. 2. 1986: McGraw-Hill New York.
131. Brammar, I. and Harris, D., *Production and properties of sheet steel and aluminum alloys for forming applications.* J. Aust. Inst. Met., 1975. **20**(2): p. 85-100.
132. Hollomon, J.H., *Tensile deformation.* Trans. AIME, 1945. **162**: p. 268 -290.
133. Ludwik, P., Elemente der Technonogischen Mechanic., Springer-Verlag, 1909.
134. Voce, E., *The relationship between stress and strain for homogeneous deformation.* J. Inst. Met., 1948. **74**: p. 537 - 562.
135. Swift, H.W., *Plastic instability under plane stress.* J. Mech. Phys. Solids, 1952. **1**(1): p. 1–18.
136. Ludwigson, D.C., *Modified stress-strain relation for FCC metals and alloys.* Metallurgical Transactions, 1971. **2**(10): p. 2825-2828.
137. Jacques, P.J., Delannay, F., and Ladriere, J., *On the influence of interactions between phases on the mechanical stability of retained austenite in transformation-induced plasticity multiphase steels.* Metallurgical and Materials Transactions A, 2001. **32**(11): p. 2759-2768.
138. Embury, D. and Bouaziz, O., *Steel-based composites: driving forces and classifications.* Annual Review of Materials Research, 2010. **40**: p. 213-241.
139. Davut, K. and Zaefferer, S., *The effect of size and shape of austenite grains on the mechanical properties of a low-alloyed TRIP steel.* Steel Research International, 2012. **83**(6): p. 584-589.
140. Pereloma, E., Russell, K., Miller, M., and Timokhina, I., *Effect of pre-straining and bake hardening on the microstructure of thermomechanically processed CMnSi TRIP steels with and without Nb and Mo additions.* Scripta Materialia, 2008. **58**(12): p. 1078-1081.
141. Timokhina, I.B., Hodgson, P.D., and Pereloma, E.V., *Transmission electron microscopy characterization of the bake-hardening behavior of transformation-induced plasticity and dual-phase steels.* Metallurgical and Materials Transactions A, 2007. **38**(10): p. 2442-2454.
142. Bleck, W., Hulka, K., and Papamentellos, K., *Effect of niobium on the mechanical properties of TRIP steels.* Materials Science Forum 1998. **284 - 286**: p. 327-334.
143. Krauss, G., *Steels: processing, structure, and performance*. 2005: ASM International, Materials Park, Ohio. p. 327.
144. Pereloma, E., Miller, M.K., and Timokhina, I., *On the decomposition of martensite during bake hardening of thermomechanically processed transformation-induced plasticity steels.* Metallurgical and Materials Transactions A, 2008. **39**(13): p. 3210-3216.
145. Pereloma, E., Beladi, H., Zhang, L., and Timokhina, I., *Understanding the behavior of advanced high-strength steels using atom probe tomography.* Metallurgical and Materials Transactions A, 2012. **43**(11): p. 3958-3971.
146. Cochardt, A., Schoek, G., and Wiedersich, H., *Interaction between dislocations and interstitial atoms in body-centered cubic metals.* Acta Metallurgica, 1955. **3**(6): p. 533-537.
147. Jung, J., Kim, H., and De Cooman, B., *Yielding behavior of Nb micro-alloyed C-Mn-Si TRIP steel studied by in-situ synchrotron X-ray diffraction.* ISIJ International, 2010. **50**(4): p. 620-629.

148. Tsuchida, N., Tomota, Y., Nagai, K., and Fukaura, K., *A simple relationship between Luders elongation and work-hardening rate at lower yield stress.* Scripta Materialia, 2006. **54**(1): p. 57-60.
149. Tomita, Y. and Okabayashi, K., *Tensile stress-strain analysis of cold worked metals and steels and dual-phase steels.* Metallurgical and Materials Transactions A, 1985. **16**(5): p. 865-872.
150. Kumar, A., Singh, S.B., and Ray, K.K., *Influence of bainite/martensite-content on the tensile properties of low carbon dual-phase steels.* Materials Science and Engineering: A, 2008. **474**(1-2): p. 270-282.
151. Moor, E.D., Speer, J.G., Matlock, D.K., Kwak, J.H., and Lee, S.B., *Effect of carbon and manganese on the quenching and partitioning response of CMnSi steels.* Isij International, 2011. **51**(1): p. 137-144.
152. Tomota, Y., Tokuda, H., Adachi, Y., Wakita, M., Minakawa, N., Moriai, A., and Morii, Y., *Tensile behavior of TRIP-aided multi-phase steels studied by in situ neutron diffraction.* Acta Materialia, 2004. **52**(20): p. 5737-5745.
153. Gazder, A.A., Sanchez-Araiza, M., Jonas, J.J., and Pereloma, E.V., *Evolution of recrystallization texture in a 0.78 wt.% Cr extra-low-carbon steel after warm and cold rolling.* Acta Materialia, 2011. **59**(12): p. 4847-4865.
154. Furnemont, Q., Lacroix, G., Godet, S., Conlon, K.T., and Jacques, P.J., *Critical assessment of the micromechanical behaviour of dual phase and TRIP-assisted multiphase steels.* Canadian Metallurgical Quarterly, 2004. **43**(1): p. 35-42.
155. Ryu, J.H., Kim, D.-I., Kim, H.S., Bhadeshia, H.K.D.H., and Suh, D.-W., *Strain partitioning and mechanical stability of retained austenite.* Scripta Materialia, 2010. **63**(3): p. 297-299.
156. Wronski, S., Tarasiuk, J., Bacroix, B., Baczmanski, A., and Braham, C., *Investigation of plastic deformation heterogeneities in duplex steel by EBSD.* Materials Characterization, 2012. **73**(0): p. 52-60.
157. Kamaya, M., *Measurement of local plastic strain distribution of stainless steel by electron backscatter diffraction.* Materials Characterization, 2009. **60**(2): p. 125-132.
158. Takahashi, M. and Bhadeshia, H., *A model for the microstructure of some advanced bainitic steels.* Materials Transactions, JIM, 1991. **32**(8): p. 689-696.
159. Tirumalasetty, G.K., van Huis, M.A., Kwakernaak, C., Sietsma, J., Sloof, W.G., and Zandbergen, H.W., *Deformation-induced austenite grain rotation and transformation in TRIP-assisted steel.* Acta Materialia, 2012. **60**(3): p. 1311-1321.
160. Goel, N., Sangal, S., and Tangri, K., *A theoretical model for the flow behavior of commercial dual-phase steels containing metastable retained austenite: Part I. derivation of flow curve equations.* Metallurgical Transactions A, 1985. **16**(11): p. 2013-2021.
161. Bhadeshia, H., *Bainite in Steels*. 2 ed. 2001.
162. Itami, A., Takahashi, M., and Ushioda, K., *Plastic stability of retained austenite in the cold-rolled 0. 14% C-1. 9% Si-1. 7% Mn sheet steel.* ISIJ International, 1995. **35**(9): p. 1121-1127.
163. Ernst, F., Avishai, A., Kahn, H., Gu, X., Michal, G.M., and Heuer, A.H., *Enhanced Carbon Diffusion in Austenitic Stainless Steel Carburized at Low Temperature.* Metallurgical and Materials Transactions A, 2009. **40**(8): p. 1768-1780.
164. Ernst, F., Cao, Y., Michal, G.M., and Heuer, A.H., *Carbide precipitation in austenitic stainless steel carburized at low temperature.* Acta Materialia, 2007. **55**(6): p. 1895-1906.
165. Tirumalasetty, G., Van Huis, M., Kwakernaak, C., Sietsma, J., Sloof, W., and Zandbergen, H., *Unravelling the structural and chemical features influencing*

deformation-induced martensitic transformations in steels. Scripta Materialia, 2014. **71**: p. 29-32.
166. Cayron, C., *ARPGE: a computer program to automatically reconstruct the parent grains from electron backscatter diffraction data.* Journal of Applied Crystallography, 2007. **40**(6): p. 1183-1188.
167. Cayron, C., Artaud, B., and Briottet, L., *Reconstruction of parent grains from EBSD data.* Materials Characterization, 2006. **57**(4): p. 386-401.
168. Chintha, A., Sharma, V., and Kundu, S., *analysis of martensite pole figure from crystallographic view point.* Metallurgical and Materials Transactions A, 2013. **44**(11): p. 4861-4865.
169. Suikkanen, P.P., Cayron, C., DeArdo, A.J., and Karjalainen, L.P., *Crystallographic analysis of isothermally transformed bainite in 0.2C-2.0Mn-1.5 Si-0.6Cr steel using EBSD.* Journal of Materials Science & Technology, 2013: p. 359 - 366.
170. Viana, C.D.C., Butron-Guillen, M., and Jonas, J., *A variant selection model for the prediction of fcc-to-bcc transformation textures.* Textures and Microstructures, 1996. **27**(1): p. 599-610.
171. Song, T. and De Cooman, B.C., *Effect of boron on the isothermal bainite transformation.* Metallurgical and Materials Transactions A, 2013. **44**(4): p. 1686-1705.
172. Zaefferer, S., Ohlert, J., and Bleck, W., *A study of microstructure, transformation mechanisms and correlation between microstructure and mechanical properties of a low alloyed TRIP steel.* Acta Materialia, 2004. **52**(9): p. 2765-2778.
173. Guo, H., Gao, X., Bai, Y., Enomoto, M., Yang, S., and He, X., *Variant selection of bainite on the surface of allotriomorphic ferrite in a low carbon steel.* Materials Characterization, 2012. **67**: p. 34-40.
174. Beladi, H., Adachi, Y., Timokhina, I., and Hodgson, P., *Crystallographic analysis of nanobainitic steels.* Scripta Materialia, 2009. **60**(6): p. 455-458.
175. Suikkanen, P.P., Cayron, C., DeArdo, A.J., and Karjalainen, L.P., *Crystallographic analysis of martensite in 0.2 C-2.0 Mn-1.5 Si-0.6 Cr steel using EBSD.* Journal of Materials Science & Technology, 2011. **27**(10): p. 920-930.
176. Terasaki, H. and Komizo, Y.-i., *Morphology and crystallography of bainite transformation in a single prior-austenite grain of low-carbon steel.* Metallurgical and Materials Transactions A, 2013: p. 1-7.
177. Kang, J., Seol, J.-B., and Park, C., *Three-dimensional characterization of bainitic microstructures in low-carbon high-strength low-alloy steel studied by electron backscatter diffraction.* Materials Characterization, 2013. **79**: p. 110-121.
178. Pancholi, V., Krishnan, M., Samajdar, I., Yadav, V., and Ballal, N., *Self-accommodation in the bainitic microstructure of ultra-high-strength steel.* Acta Materialia, 2008. **56**(9): p. 2037-2050.
179. Gourgues, A.F., Flower, H.M., and Lindley, T.C., *Electron backscattering diffraction study of acicular ferrite, bainite, and martensite steel microstructures.* Materials Science and Technology, 2000. **16**(1): p. 26-40.
180. Jonas, J.J., *Microstructure and Texture in Steels and Other Materials*. 3rd ed, ed. A. Haldar, S. Suwas, and D. Bhattacharjee. 2009, Jamshedpur, India: Springer. p. 19 - 30.
181. Gong, W., Tomota, Y., Koo, M., and Adachi, Y., *Effect of ausforming on nanobainite steel.* Scripta Materialia, 2010. **63**(8): p. 819-822.
182. Kim, D., Lee, S.-J., and De Cooman, B.C., *Microstructure of low c steel isothermally transformed in the MS to Mf temperature range.* Metallurgical and Materials Transactions A, 2012. **43**(13): p. 4967-4983.
183. You, Y., Shang, C., Wenjin, N., and Subramanian, S., *Investigation on the microstructure and toughness of coarse grained heat affected zone in X-100 multi-*

phase pipeline steel with high Nb content. Materials Science and Engineering: A, 2012: p. 692 - 701.
184. Wang, H.-Z., Yang, P., Mao, W.-M., and Lu, F.-Y., *Effect of hot deformation of austenite on martensitic transformation in high manganese steel.* Journal of Alloys and Compounds, 2013. **558**(0): p. 26-33.
185. Pham, H.A., Ohba, T., Morito, S., Hayashi, T., Furuhara, T., and Miyamoto, G., *Effect of titanium carbide inclusions on morphology of low-carbon steel martensite.* Materials Science Forum, 2013. **738**: p. 25-30.
186. Caballero, F.G., Miller, M.K., and Garcia-Mateo, C., *Carbon supersaturation of ferrite in a nanocrystalline bainitic steel.* Acta Materialia, 2010. **58**(7): p. 2338-2343.
187. Takaki, S., Fukunaga, K., Syarif, J., and Tsuchiyama, T., *Effect of grain refinement on thermal stability of metastable austenitic steel.* Materials Transactions, 2004. **45**(7): p. 2245-2251.
188. Caballero, F.G., Miller, M.K., Babu, S.S., and Garcia-Mateo, C., *Atomic scale observations of bainite transformation in a high carbon high silicon steel.* Acta Materialia, 2007. **55**(1): p. 381-390.
189. Morito, S., Edamatsu, Y., Ichinotani, K., Ohba, T., Hayashi, T., Adachi, Y., Furuhara, T., Miyamoto, G., and Takayama, N., *Quantitative analysis of three-dimensional morphology of martensite packets and blocks in iron-carbon-manganese steels.* Journal of Alloys and Compounds, 2012. **577**: p. S587-S592.

APPENDIX .A

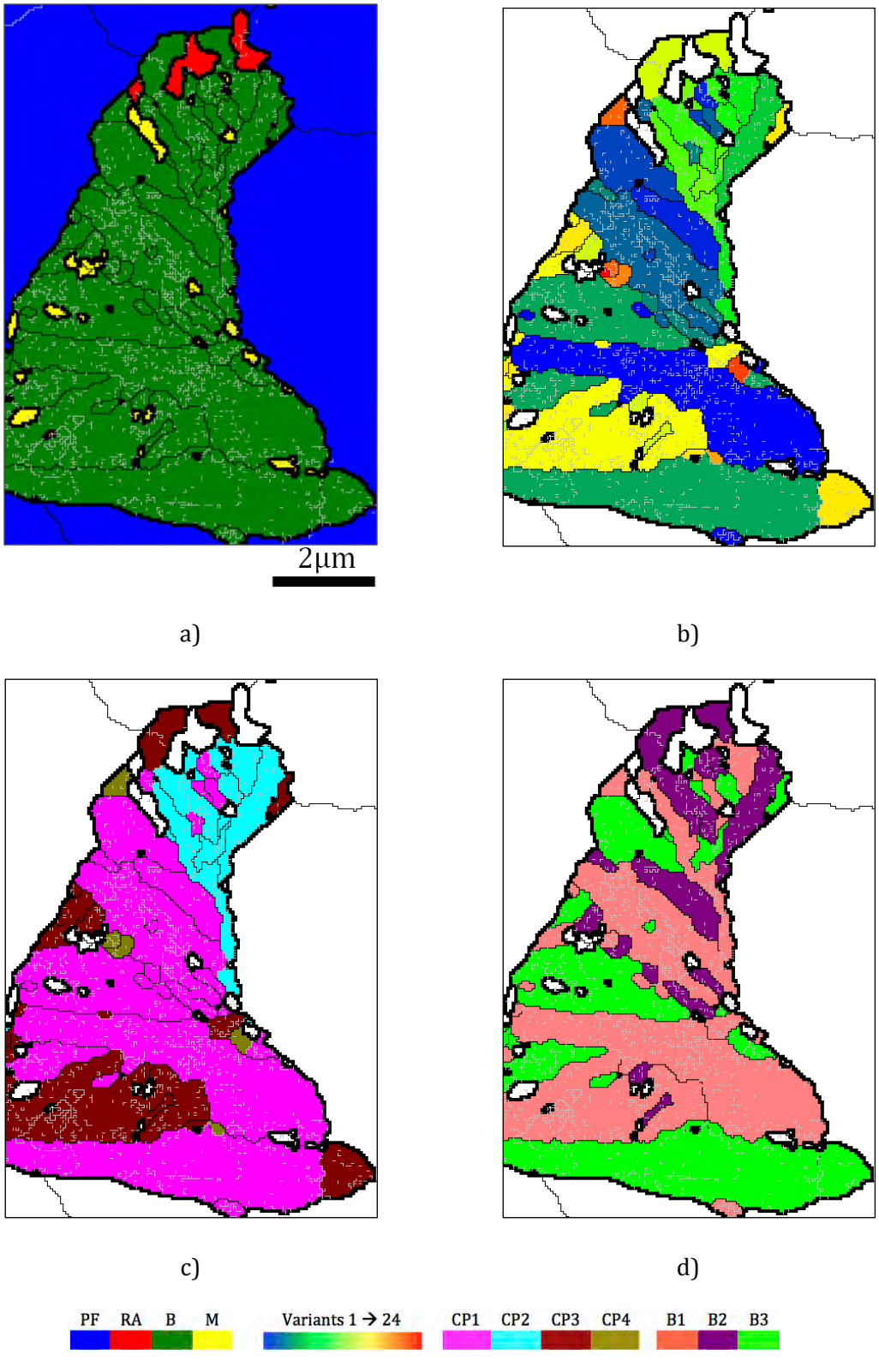
2µm
a)
b)
c)
d)
PF RA B M
Variants 1 → 24
CP1 CP2 CP3 CP4
B1 B2 B3

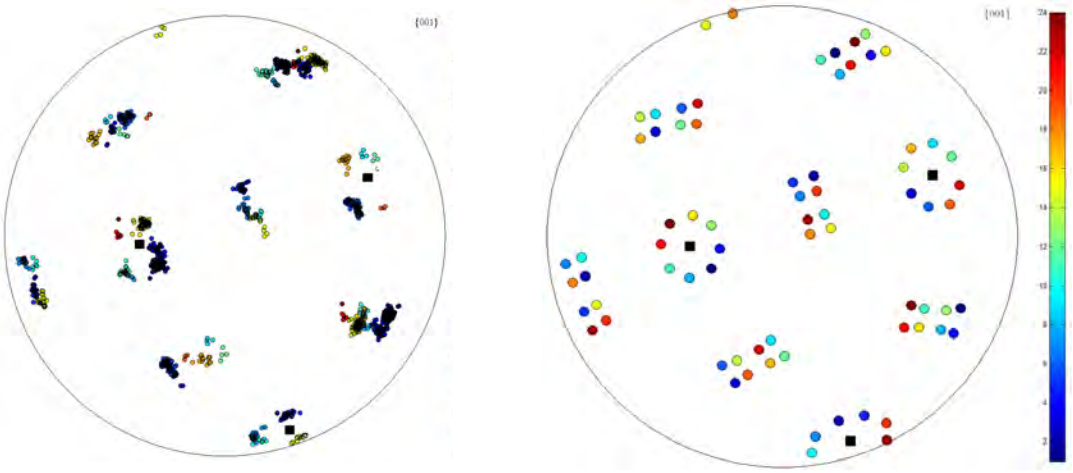

e) f)

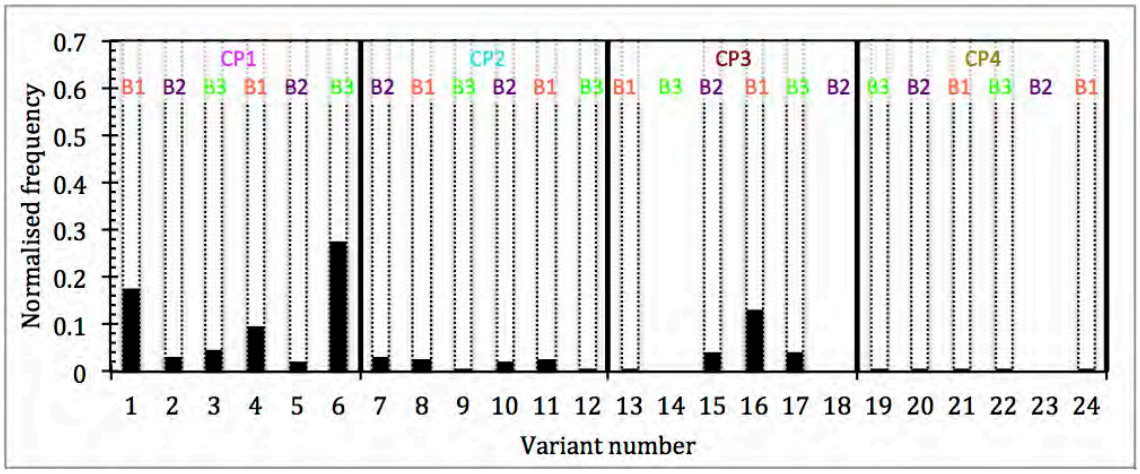
CP1
CP2
CP3
CP4
B1 B2 B3 B1 B2 B3 B2 B1 B3 B2 B1 B3 B1 B3 B2 B1 B3 B2 B3 B2 B1 B3 B2 B1
Normalised frequency
0.7
0.6
0.5
0.4
0.3
0.2
0.1
0
1 2 3 4 5 6 7 8 9 10 11 12 13 14 15 16 17 18 19 20 21 22 23 24
Variant number

g)

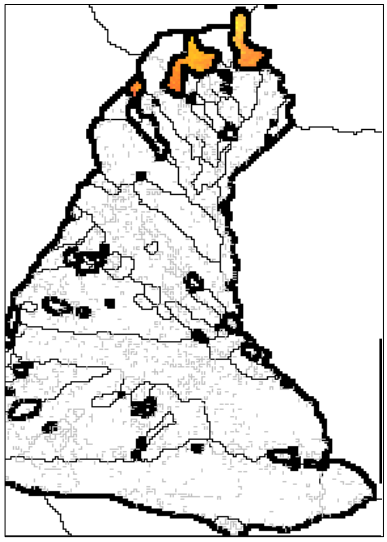

h)

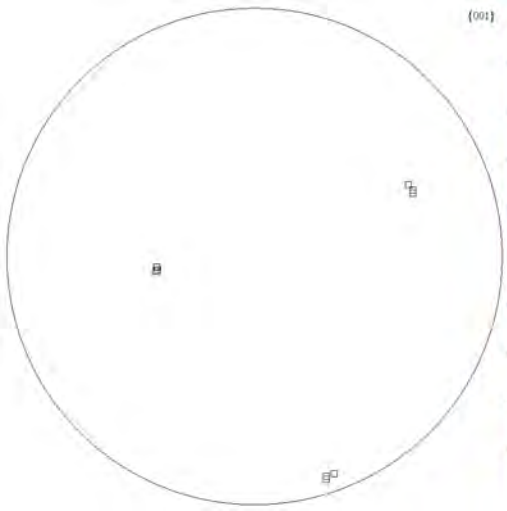

i)

Figure A.1: EBSD maps of Granular Bainite (GB) in base steel; a) phases map, b) ferrite variants map, c) crystallographic packets (CPs) and d) Bain groups (BGs). e) The experimental and f) theoretical {001} pole figures of the variants and the average orientation of the RA grain is represented by black squares in e) and f). g) Normalised frequency of the formed variants; dash lines represent the realisation of the variants even in a small amount. h) The inverse-pole figure map of the RA grain and i) {001} pole figure of the experimental orientation of the RA grains. LAGBs=2° to 15°; silver colour and HAGBs >15° black colour. The thick black lines on all the maps represent the interphase boundary and do not denote boundary misorientation.

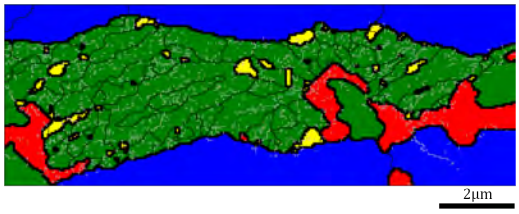

a)

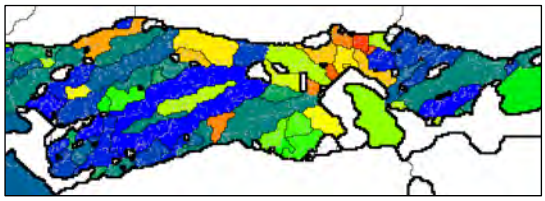

b)

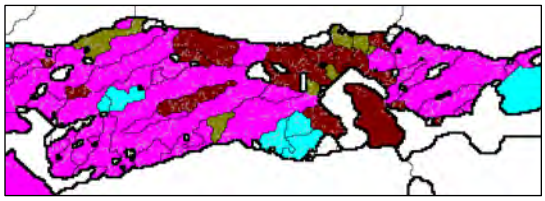

c)

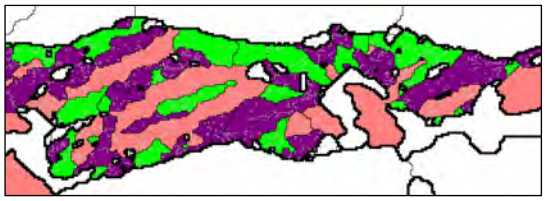

d)

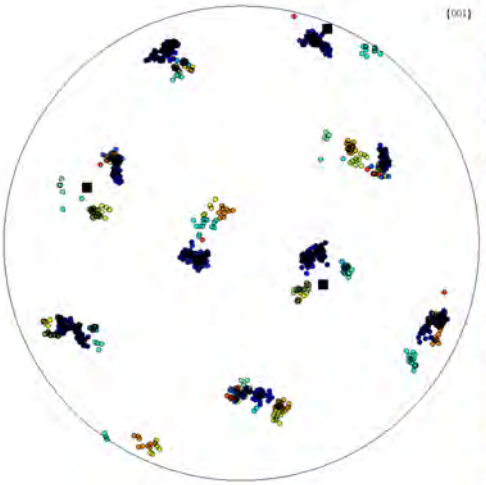

e)

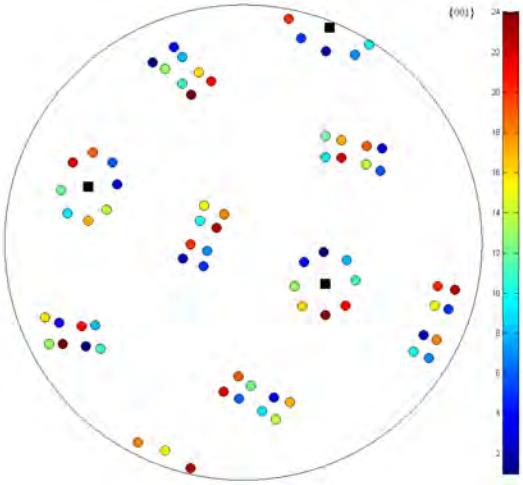

f)

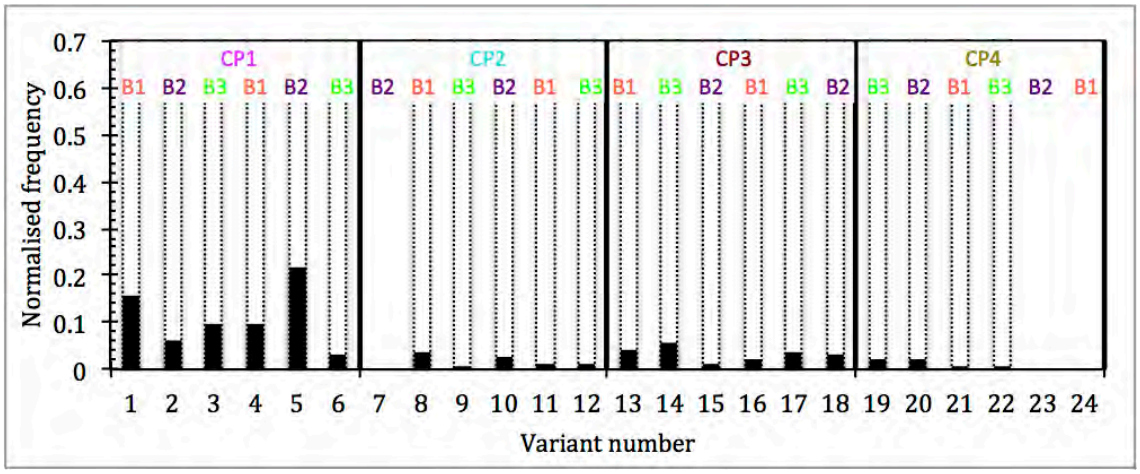

g)

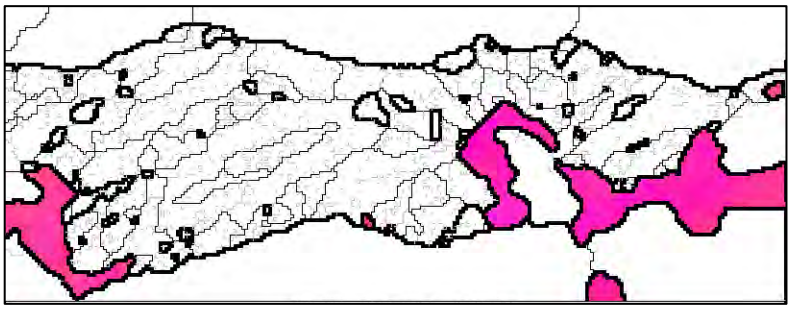

h)

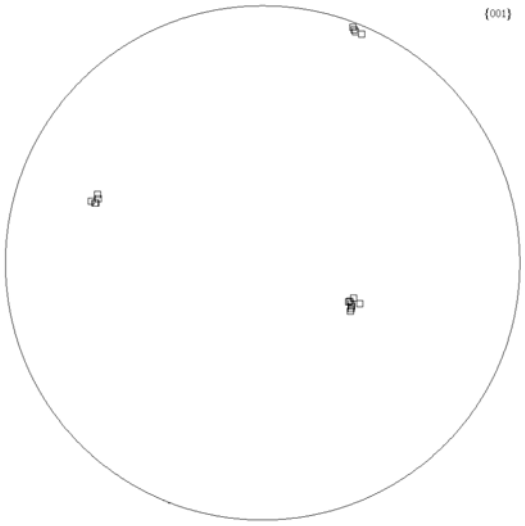

i)

Figure A.2: EBSD maps of predominantly Granular Bainite (GB) in base steel; a) phases map, b) ferrite variants map, c) crystallographic packets (CPs) and d) Bain groups (BGs). e) The experimental and f) theoretical {001} pole figures of the variants with the average

orientation of the RA grain represented by black squares in e) and f). g) Normalised frequency of the formed variants; dash lines represent the realisation of the variants even in a small amount. h) The inverse-pole figure map of the RA grain and i) {001} pole figure of the experimental orientation of the RA grains. LAGBs=2° to 15°; silver colour and HAGBs >15° black colour. The thick black line on all the maps represents the interphase boundary and does not denote boundary misorientation.

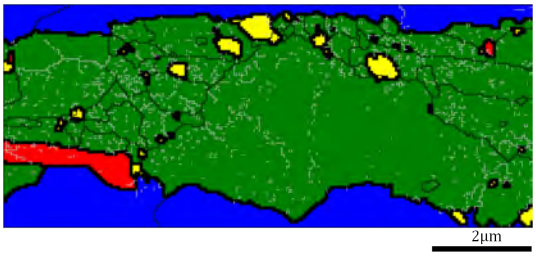

a)

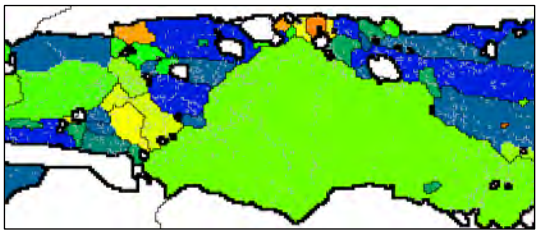

b)

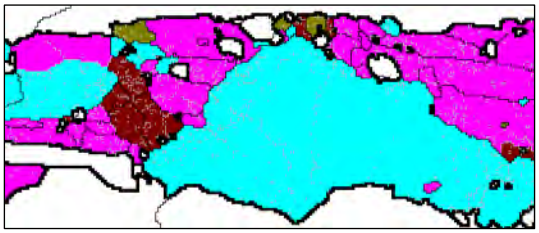

c)

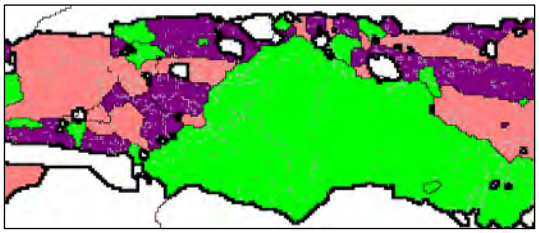

d)

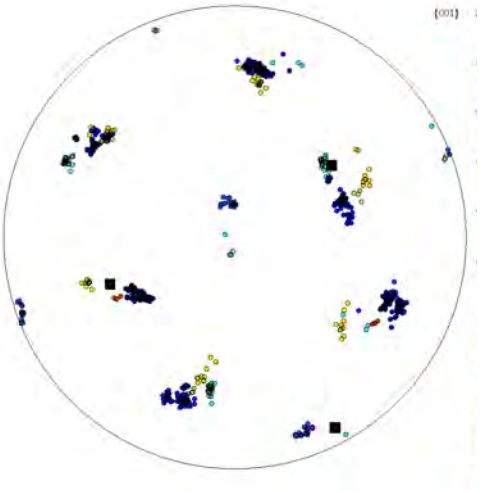

e)

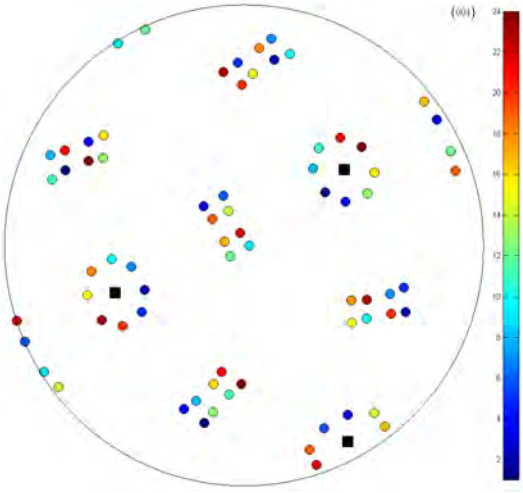

f)

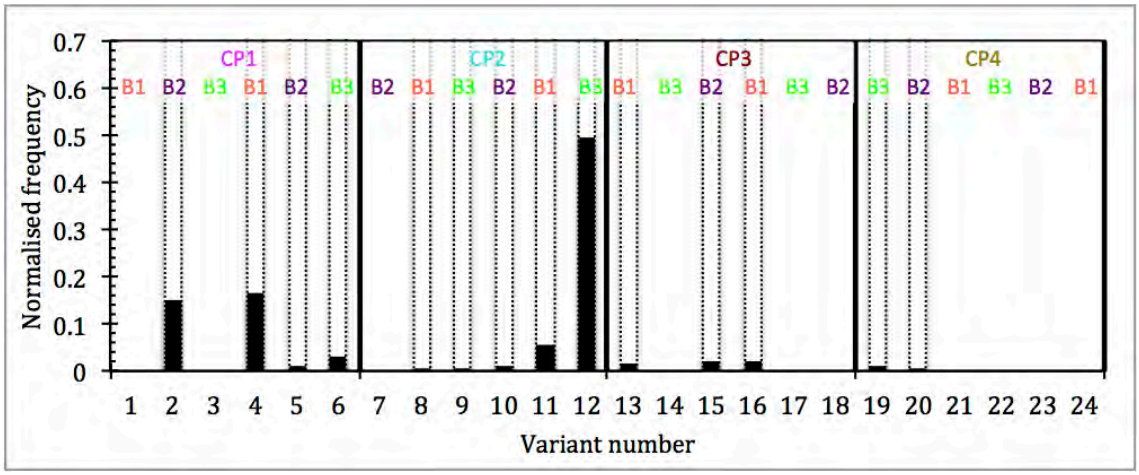

g)

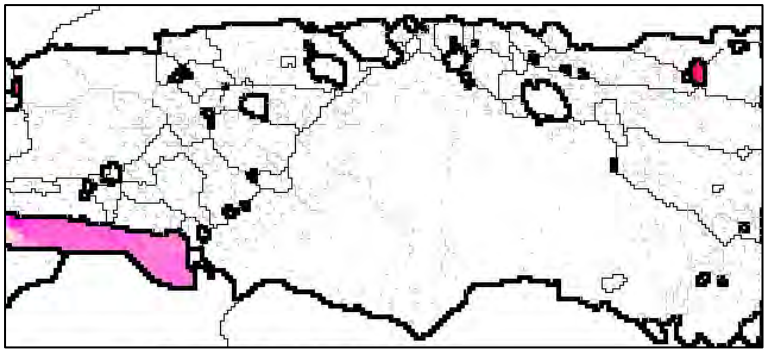

h)

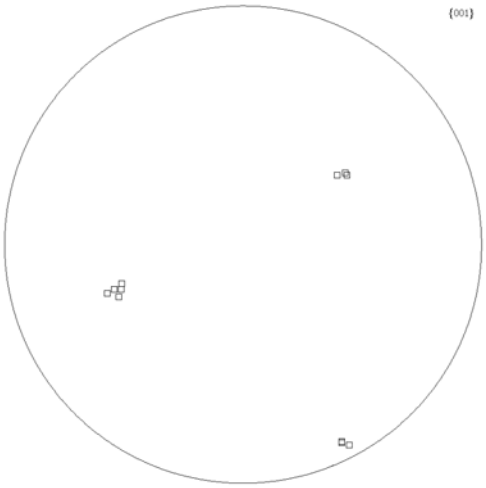

i)

Figure A.3: EBSD maps of granular bainite (GB) in the base steel; a) phases map, b) ferrite variants map, c) crystallographic packets (CPs) and d) Bain groups (BGs). e) The

experimental and f) theoretical {001} pole figures of the variants in which the average orientation of the RA grain is represented by black squares. g) Normalised frequency of the formed variants; dash lines represent the realisation of the variants even in a small amount. h) The inverse-pole figure map of the RA grain and i) {001} pole figure of the experimental orientation of the RA grains. LAGBs=2° to 15°; silver colour and HAGBs >15° black colour. The thick black line on all the maps represents the interphase boundary and does not denote boundary misorientation.

APPENDIX .B

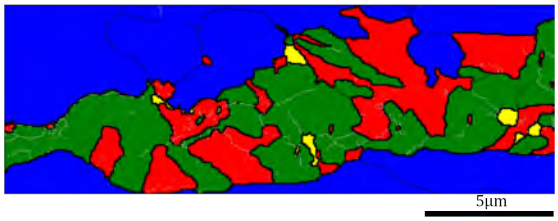

a)

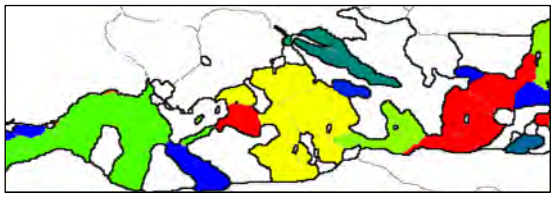

b)

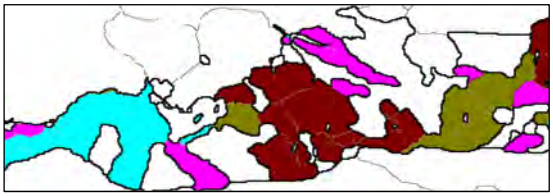

c)

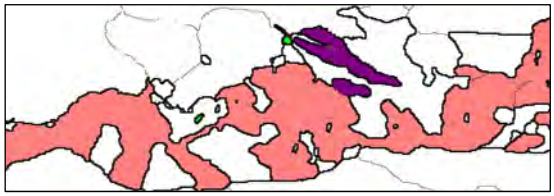

d)

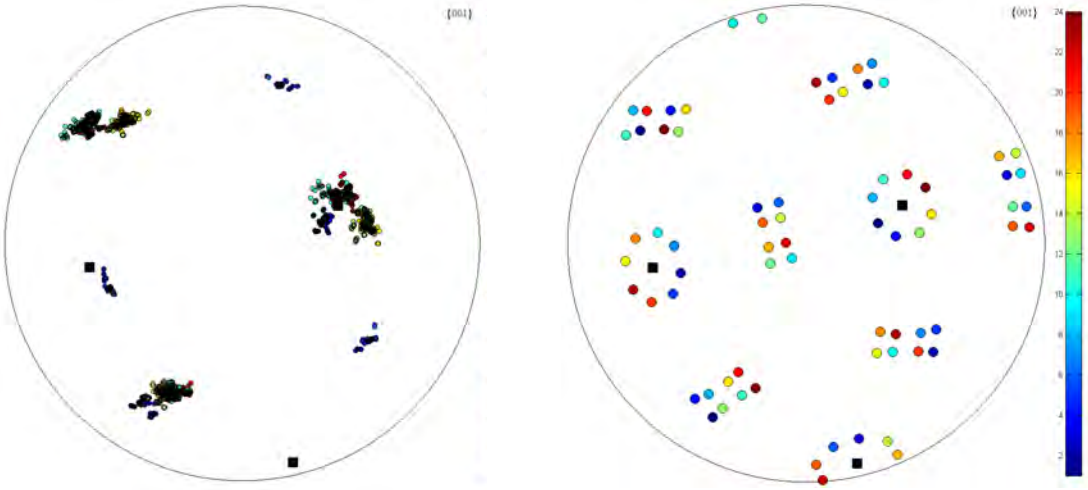

e)

f)

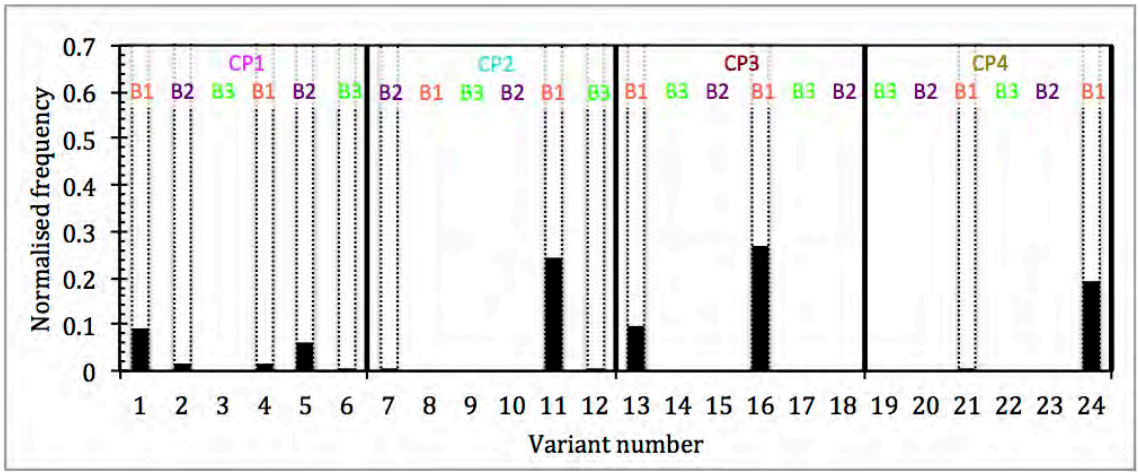
CP1
CP2
CP3
CP4
B1 B2 B3 B1 B2 B3
B2 B1 B3 B2 B1 B3
B1 B3 B2 B1 B3 B2
B3 B2 B1 B3 B2 B1
Normalised frequency
0.7
0.6
0.5
0.4
0.3
0.2
0.1
0
1 2 3 4 5 6 7 8 9 10 11 12 13 14 15 16 17 18 19 20 21 22 23 24
Variant number

g)

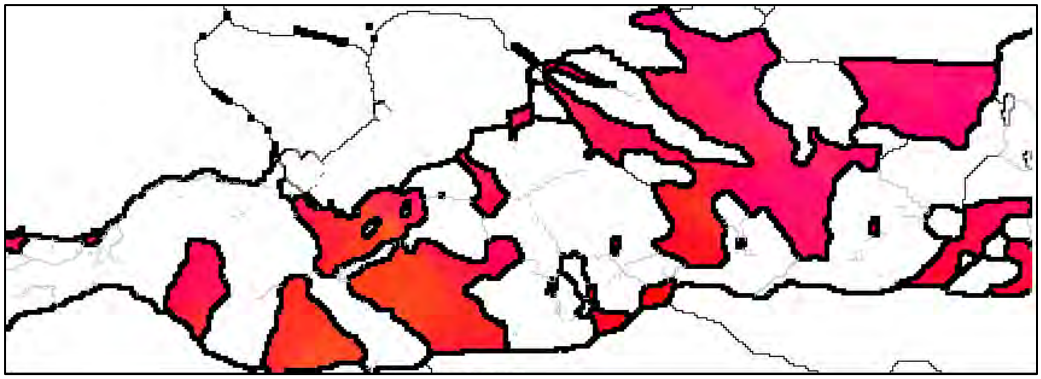

h)

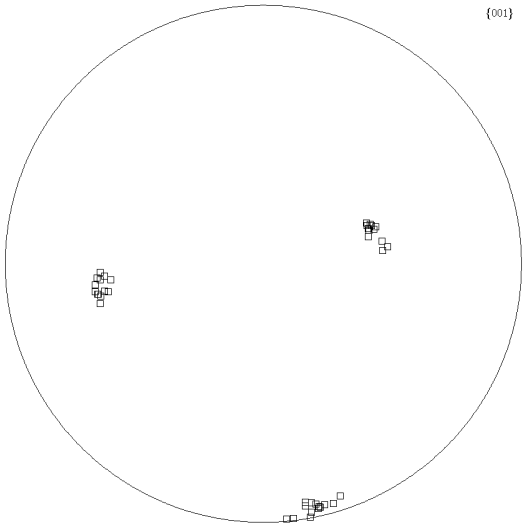
{001}

i)

Figure B.1: EBSD maps of bainitic ferrite laths (BF) in the Nb-Ti steel; a) phases map, b) ferrite variants map, c) crystallographic packets (CPs) and d) Bain groups (BGs). e) The experimental and f) theoretical {001} pole figures of the variants, and the average orientation of the RA grain which is represented by black squares in e) and f). g) Normalised frequency of the formed variants; dash lines represent the realisation of the variants even in a small amount. h) The inverse-pole figure map of the RA grain and i) {001} pole figure of the experimental orientation of the RA grains. LAGBs=2° to 15°; silver colour and HAGBs >15° black colour. The thick black line on all the maps represents the interphase boundary and does not denote boundary misorientation.

a)

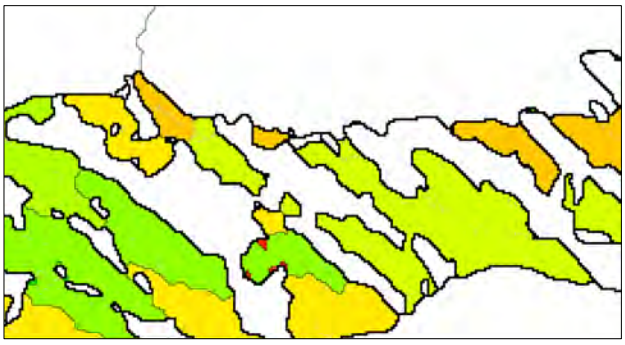

b)

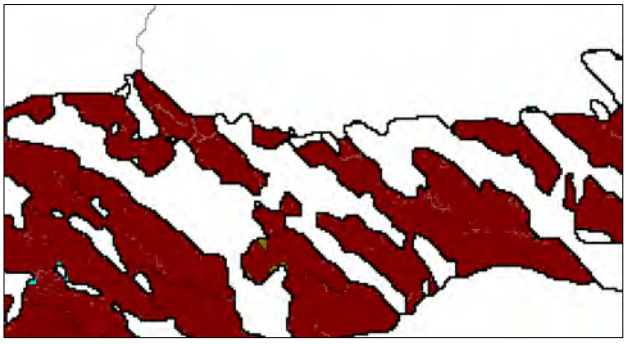

c)

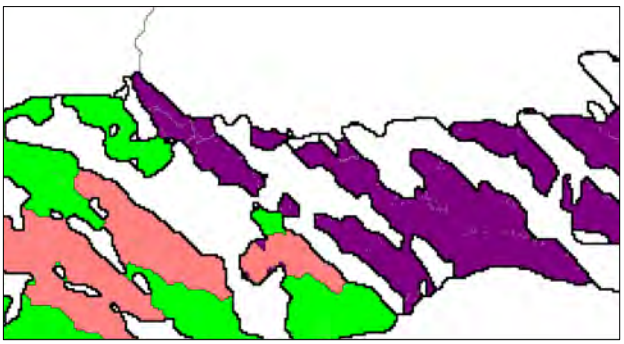

d)

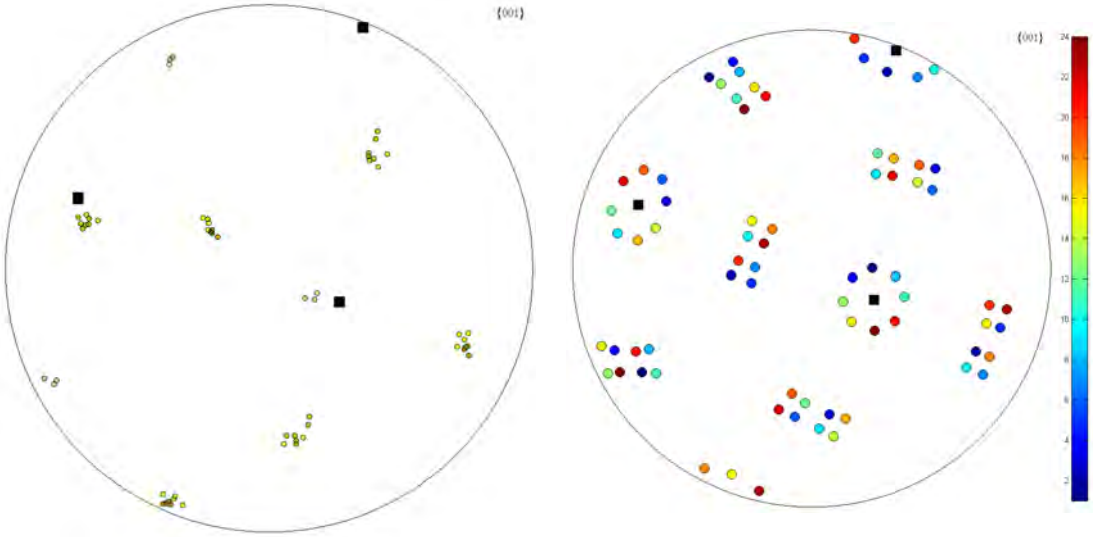

e) f)

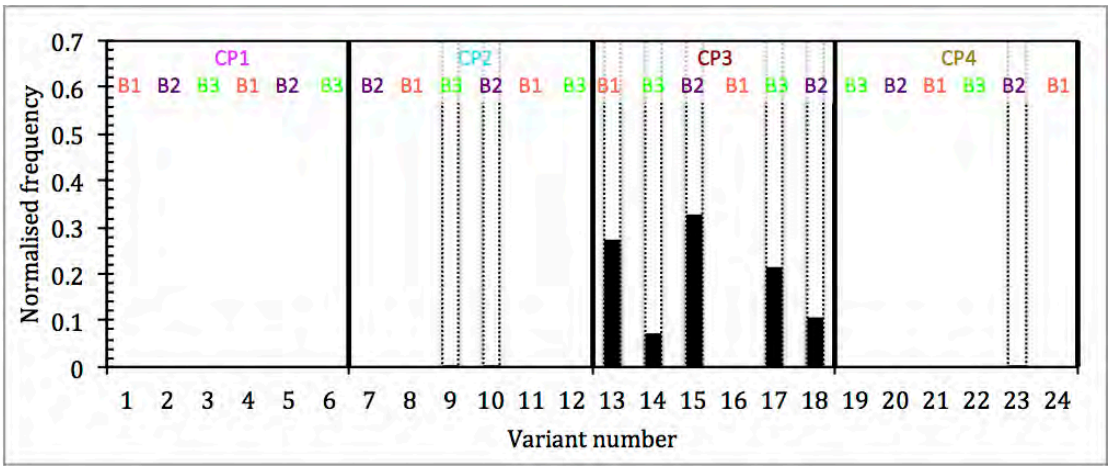
CP1
CP2
CP3
CP4
B1 B2 B3 B1 B2 B3 B2 B1 B3 B2 B1 B3 B1 B3 B2 B1 B3 B2 B3 B2 B1 B3 B2 B1
Normalised frequency
0.7
0.6
0.5
0.4
0.3
0.2
0.1
0
1 2 3 4 5 6 7 8 9 10 11 12 13 14 15 16 17 18 19 20 21 22 23 24
Variant number

g)

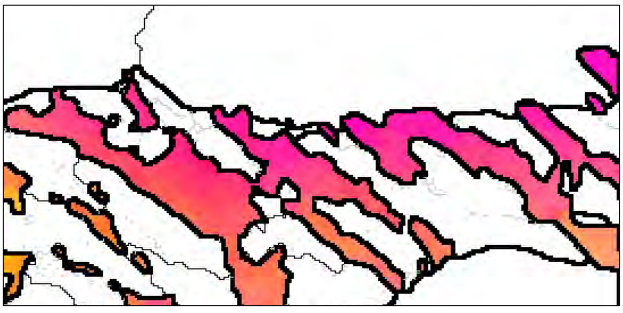

h)

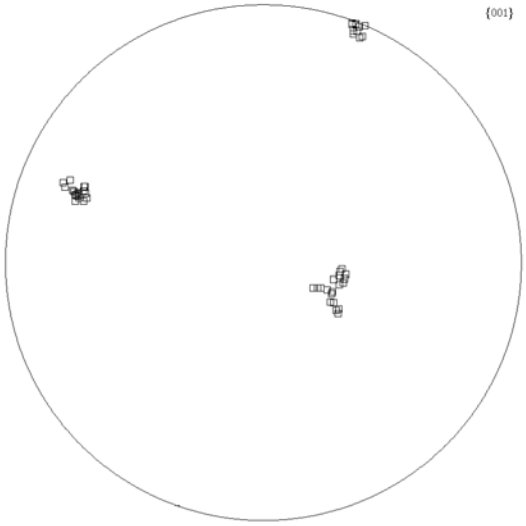

i)

Figure B.2: EBSD maps of bainitic ferrite laths (BF) in the base steel; a) phases map, b) ferrite variants map, c) crystallographic packets (CPs) and d) Bain groups (BGs). e) The experimental and f) theoretical {001} pole figures of the variants with the average orientation of the RA grain represented by black squares. g) Normalised frequency of the formed variants; dash lines represent the realisation of the variants even in a small amount. h) The inverse-pole figure map of the RA grain and i) {001} pole figure of the experimental orientation of the RA grains. LAGBs=2° to 15°; silver colour and HAGBs >15° black colour. The thick black line on all the maps represents the interphase boundary and does not denote boundary misorientation.

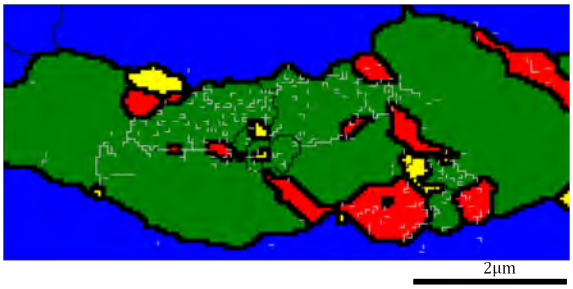

a)

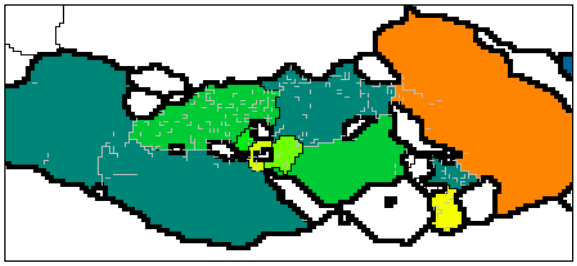

b)

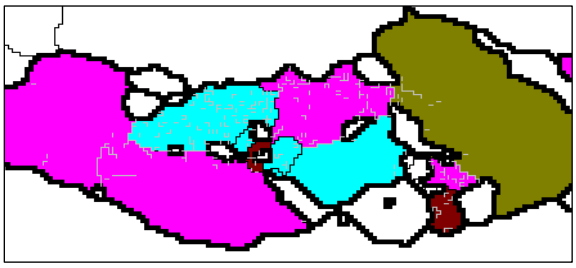

c)

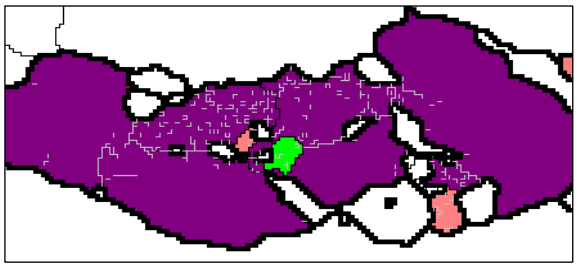

d)

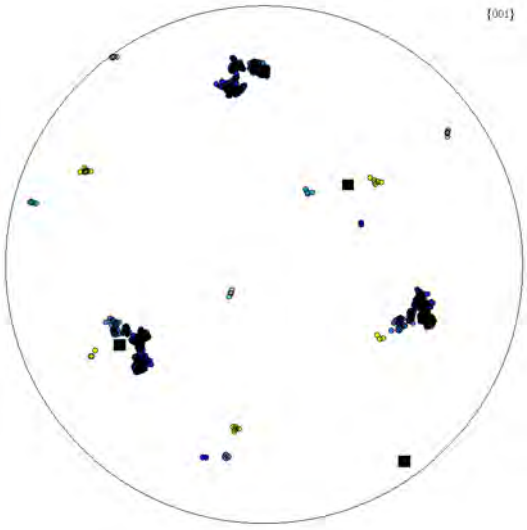

e)

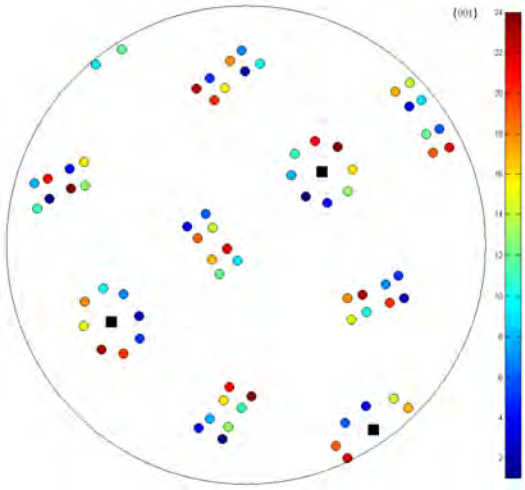

f)

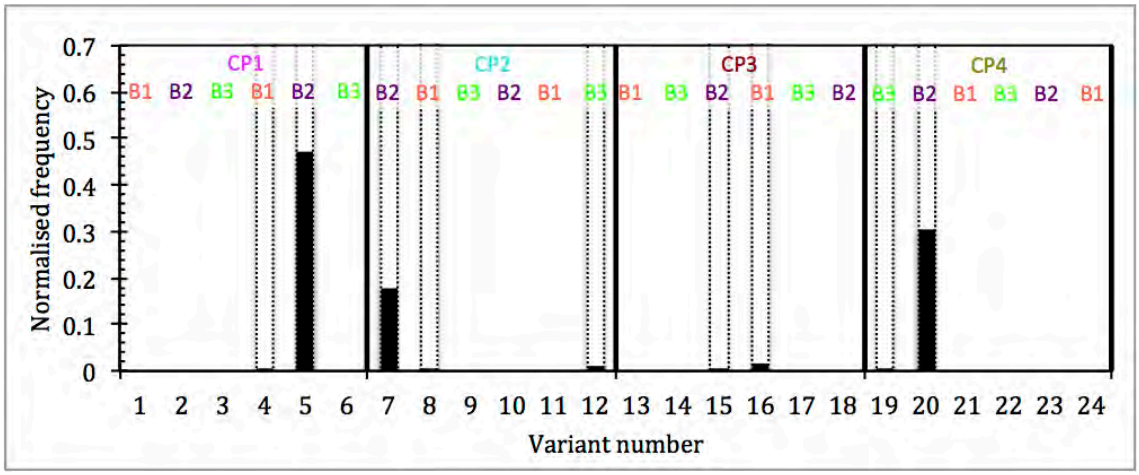
CP1
CP2
CP3
CP4
B1 B2 B3 B1 B2 B3
B2 B1 B3 B2 B1 B3
B1 B3 B2 B1 B3 B2
B3 B2 B1 B3 B2 B1
Normalised frequency
0.7
0.6
0.5
0.4
0.3
0.2
0.1
0
1 2 3 4 5 6 7 8 9 10 11 12 13 14 15 16 17 18 19 20 21 22 23 24
Variant number

g)

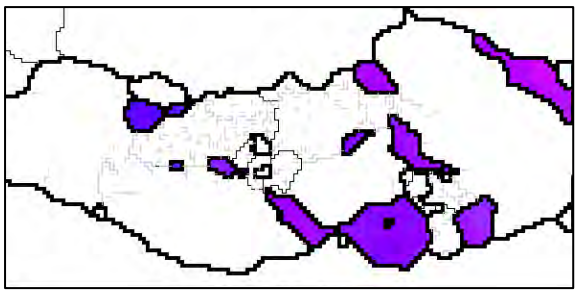

h)

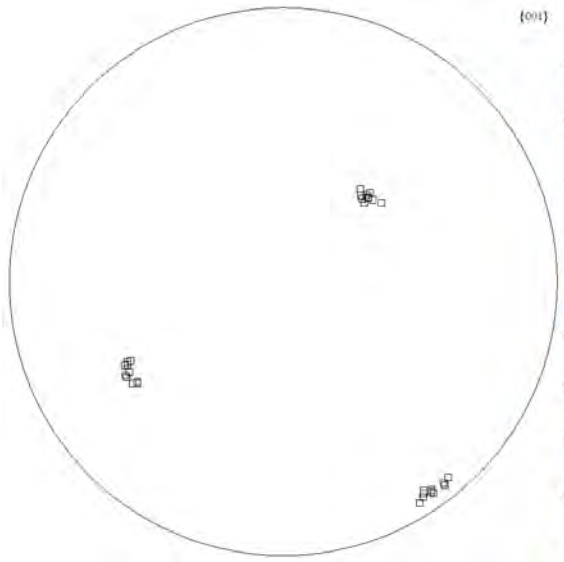

i)

Figure B.3: EBSD maps of bainitic ferrite laths (BF) in the Nb-Ti steel; a) phases map, b) ferrite variants map, c) crystallographic packets (CPs) and d) Bain groups (BGs). e) The experimental and f) theoretical {001} pole figures of the variants with the average orientation of the RA grain represented by black squares. g) Normalised frequency of the formed variants; dash lines represent the realisation of the variants even in a small amount. h) The inverse-pole figure map of the RA grain and i) {001} pole figure of the experimental orientation of the RA grains. LAGBs=2° to 15°; silver colour and HAGBs >15° black colour. The thick black line on all the maps represents the interphase boundary and does not denote boundary misorientation.

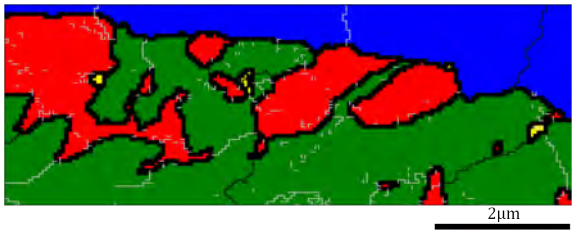

a)

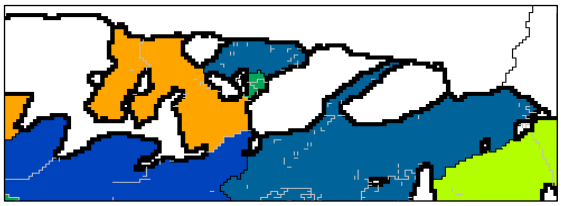

b)

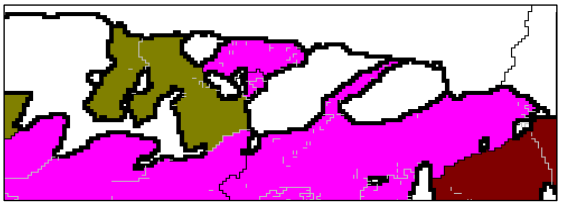

c)

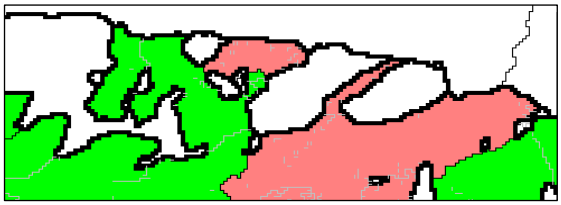

d)

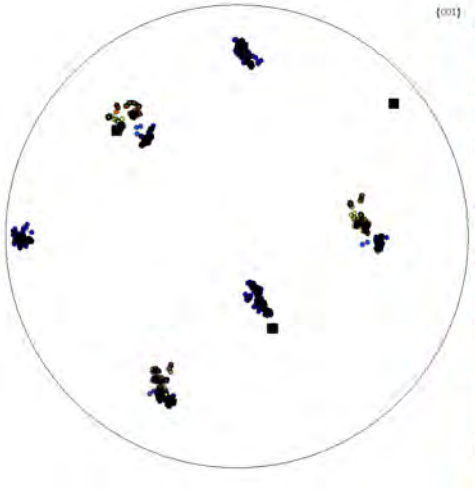

e)

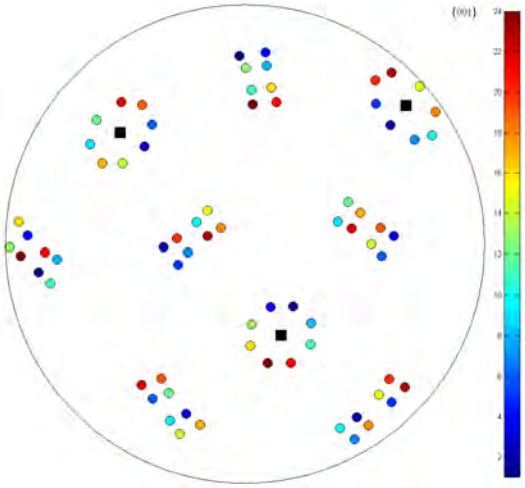

f)

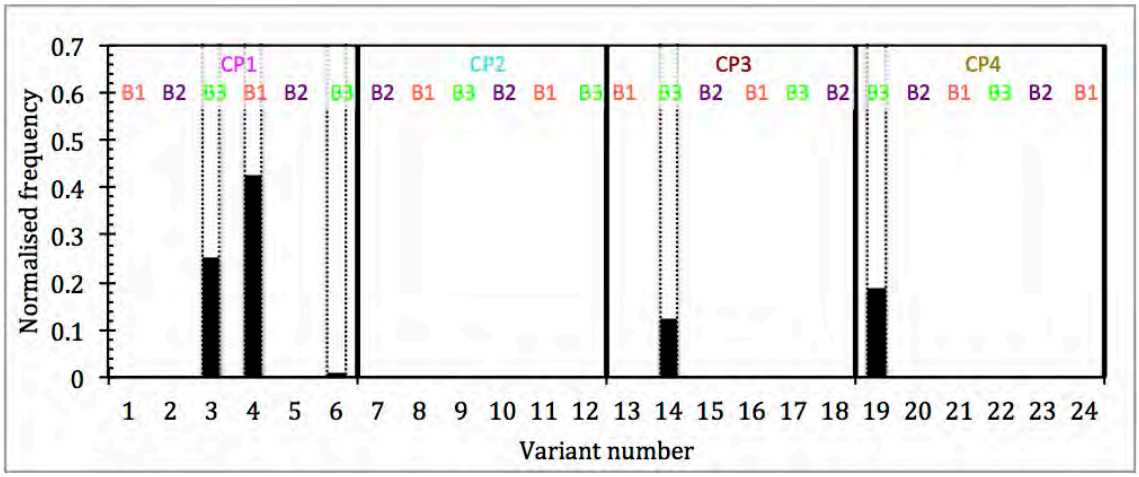
CP1
CP2
CP3
CP4
B1 B2 B3 B1 B2 B3 B2 B1 B3 B2 B1 B3 B1 B3 B2 B1 B3 B2 B3 B2 B1 B3 B2 B1
Normalised frequency
0.7
0.6
0.5
0.4
0.3
0.2
0.1
0
1 2 3 4 5 6 7 8 9 10 11 12 13 14 15 16 17 18 19 20 21 22 23 24
Variant number

g)

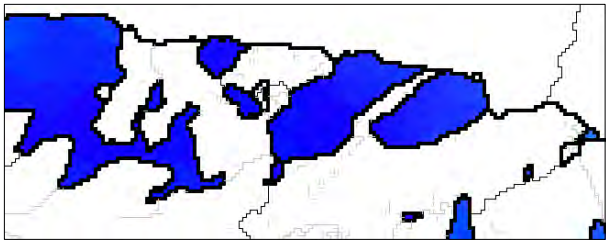

h)

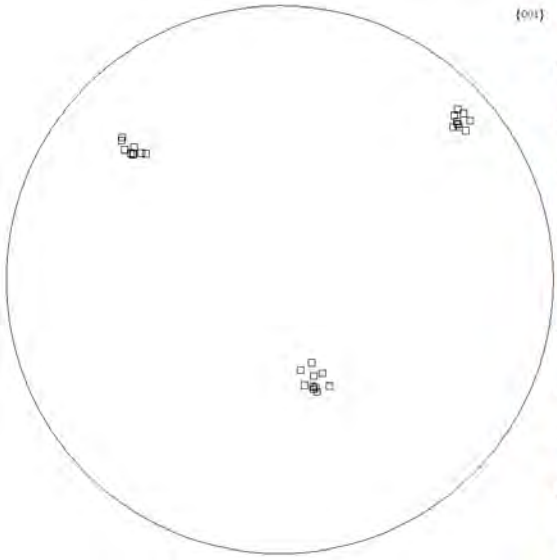

i)

Figure B.4: EBSD maps of bainitic ferrite laths (BF) in the base steel; a) phases map, b) ferrite variants map, c) crystallographic packets (CPs) and d) Bain groups (BGs). e) The experimental and f) theoretical {001} pole figures of the variants with the average orientation of the RA grain represented by black squares. g) Normalised frequency of the formed variants; dash lines represent the realisation of the variants even in a small amount. h) The inverse-pole figure map of the RA grain and i) {001} pole figure of the experimental orientation of the RA grains. LAGBs=2° to 15°; silver colour and HAGBs >15° black colour. The thick black line on all the maps represents the interphase boundary and does not denote boundary misorientation.

APPENDIX .C

a)

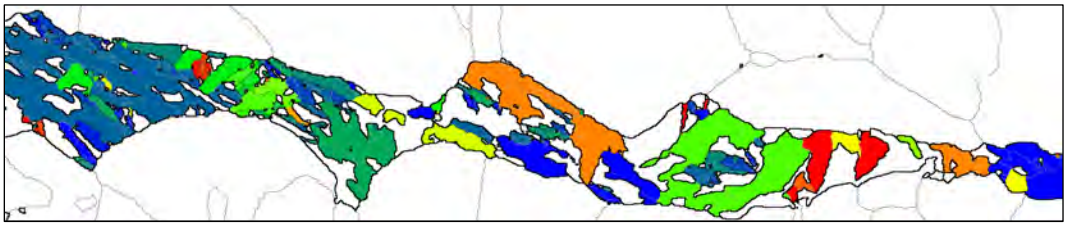

b)

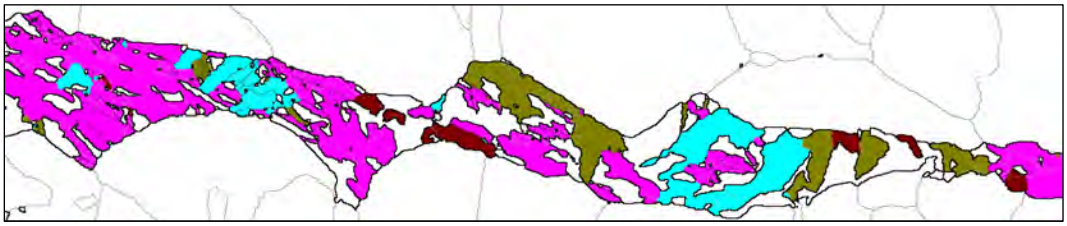

c)

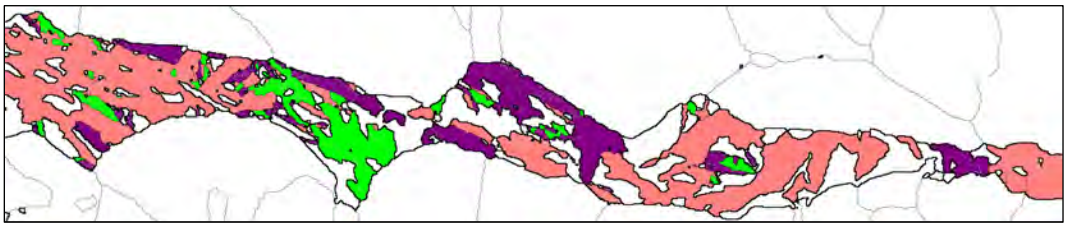

d)

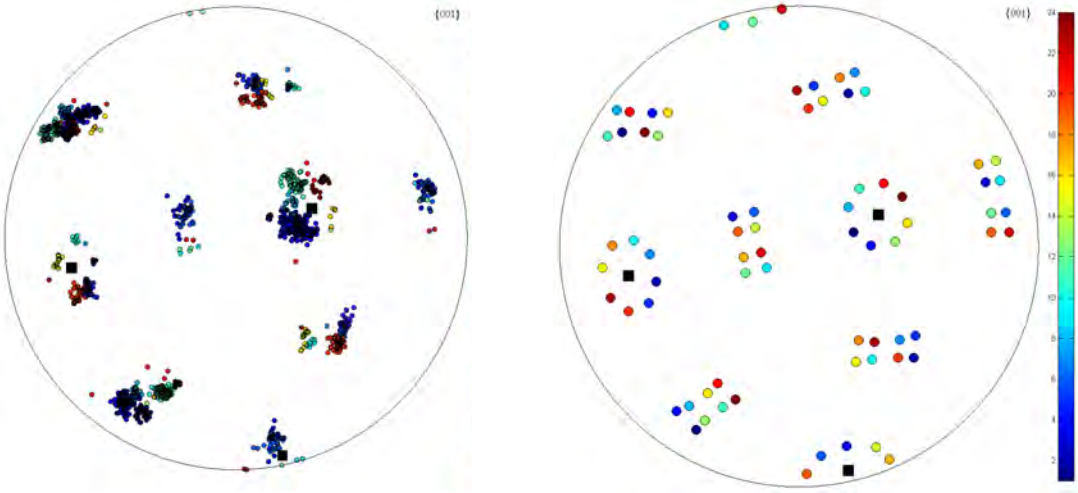

e) f)

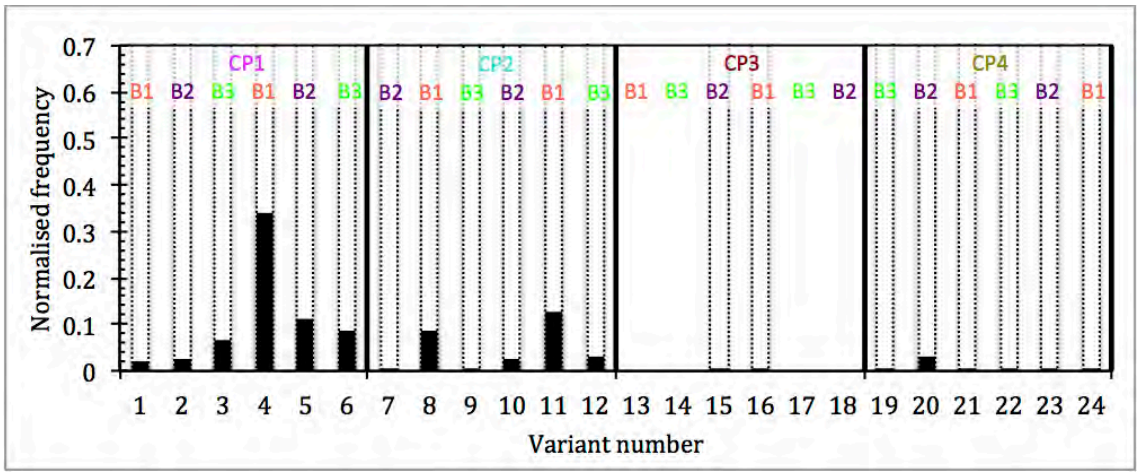
CP1
CP2
CP3
CP4
B1 B2 B3 B1 B2 B3 B2 B1 B3 B2 B1 B3 B1 B3 B2 B1 B3 B2 B3 B2 B1 B3 B2 B1
Normalised frequency
0.7
0.6
0.5
0.4
0.3
0.2
0.1
0
1 2 3 4 5 6 7 8 9 10 11 12 13 14 15 16 17 18 19 20 21 22 23 24
Variant number

g)

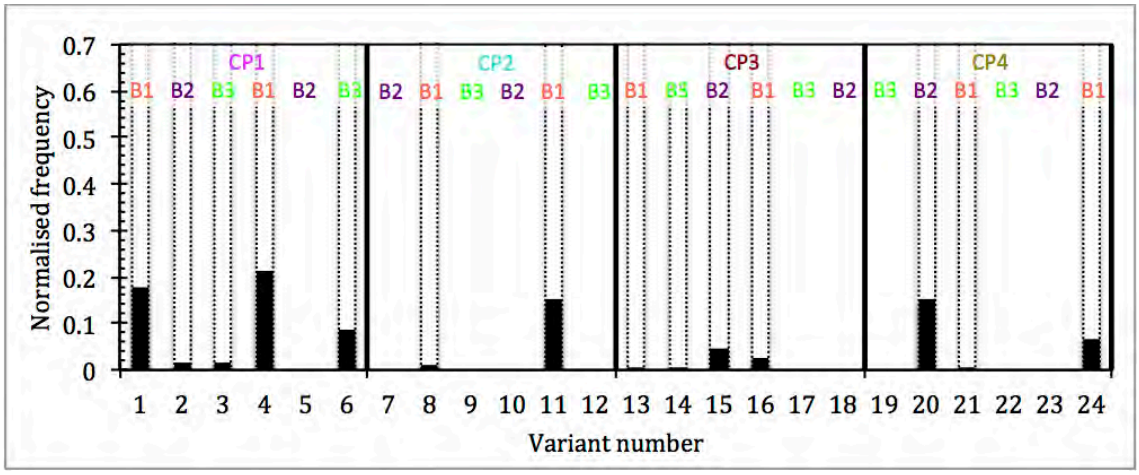
CP1
CP2
CP3
CP4
B1 B2 B3 B1 B2 B3 B2 B1 B3 B2 B1 B3 B1 B3 B2 B1 B3 B2 B3 B2 B1 B3 B2 B1
Normalised frequency
0.7
0.6
0.5
0.4
0.3
0.2
0.1
0
1 2 3 4 5 6 7 8 9 10 11 12 13 14 15 16 17 18 19 20 21 22 23 24
Variant number

h)

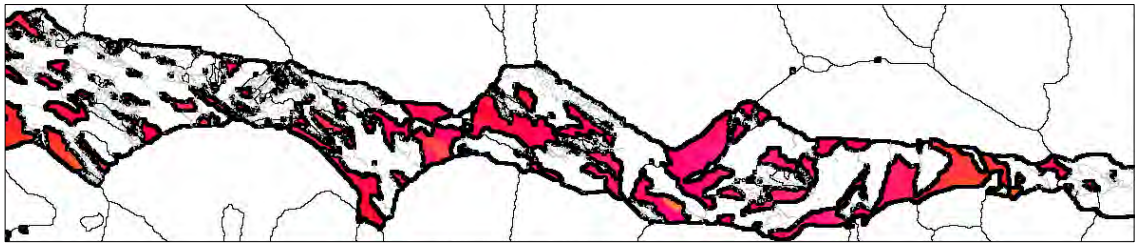

i)

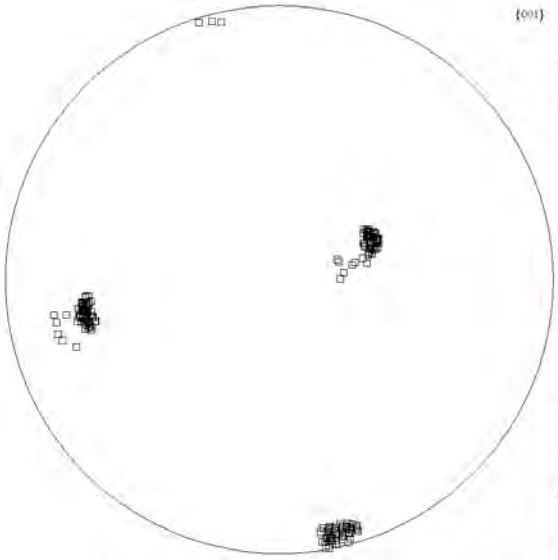

j)

Figure C.1: EBSD maps of bainitic ferrite laths (BF) and GB in the Nb-Ti steel; a) phases map, b) ferrite variants map, c) crystallographic packets (CPs) and d) Bain groups (BGs). e) The experimental and f) theoretical {001} pole figures of the variants with the average orientation of the RA grain represented by black squares. Normalised frequency of the formed variants for g) GB and h) BF; dash lines represent the realisation of the variants even in a small amount. i) The inverse-pole figure map of the RA grain and j) {001} pole figure of the experimental orientation of the RA grains. LAGBs=2° to 15°; silver colour and HAGBs >15° black colour. The thick black line on all the maps represents the interphase boundary and does not denote boundary misorientation.

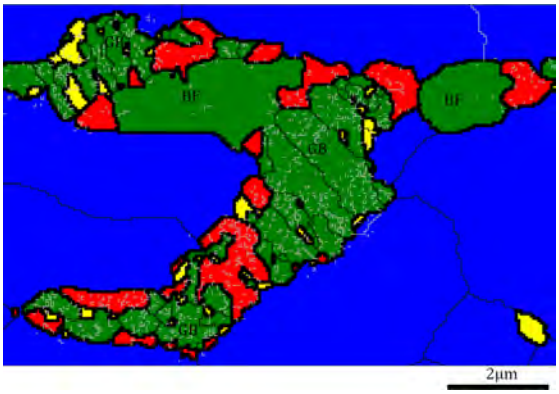

a)

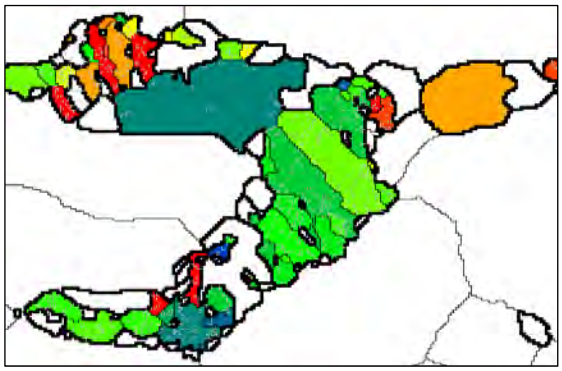

b)

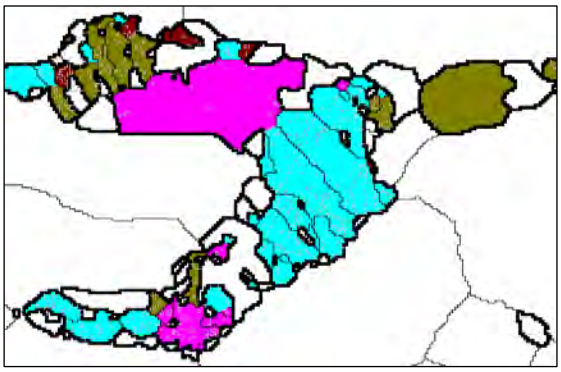

c)

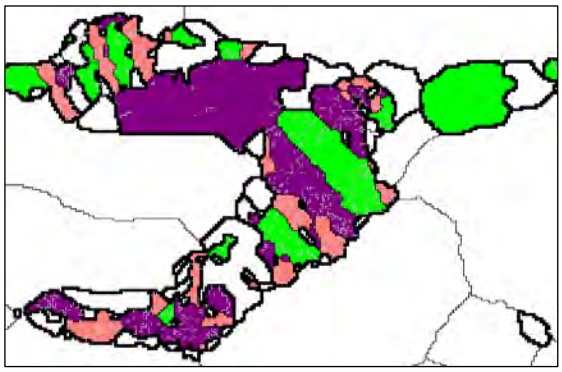

d)

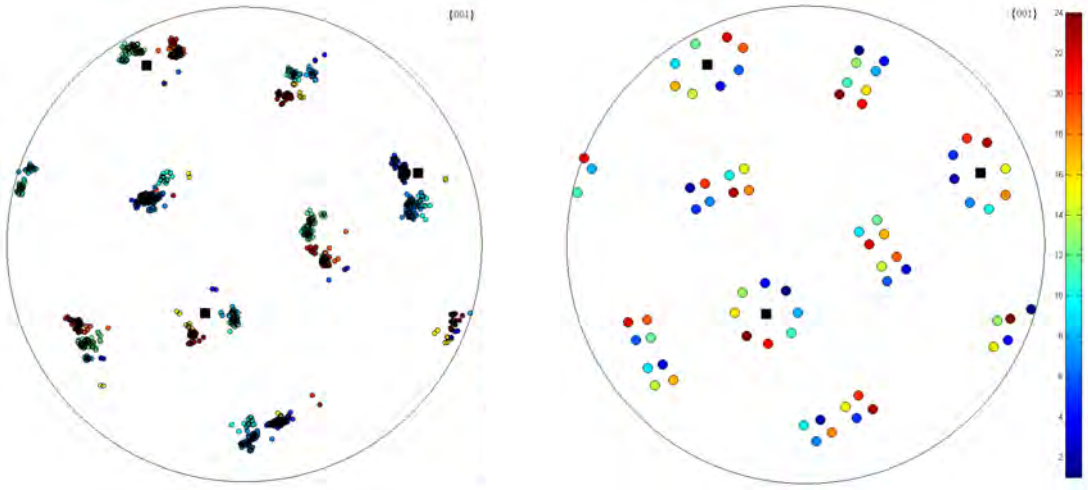

e)

f)

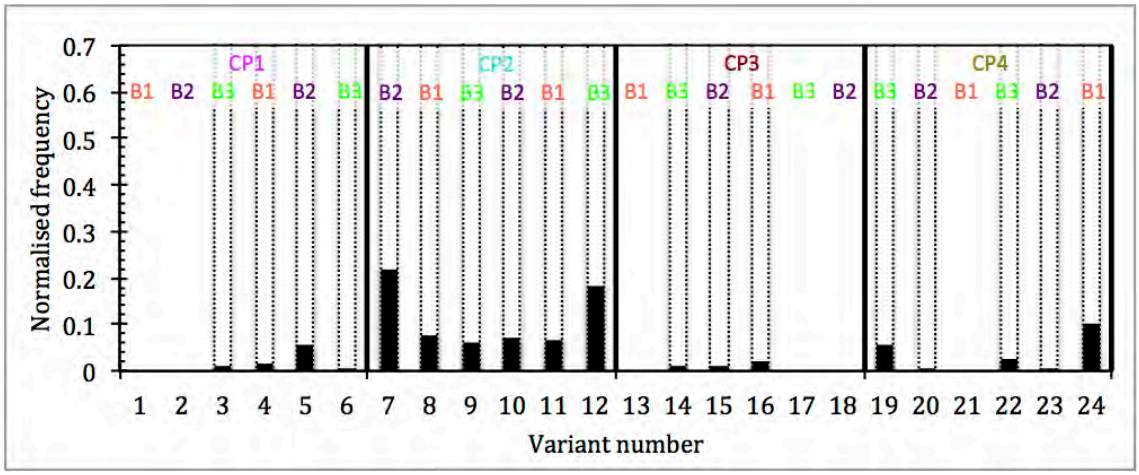
CP1
CP2
CP3
CP4
B1 B2 B3 B1 B2 B3 B2 B1 B3 B2 B1 B3 B1 B3 B2 B1 B3 B2 B3 B2 B1 B3 B2 B1
Normalised frequency
0.7
0.6
0.5
0.4
0.3
0.2
0.1
0
1 2 3 4 5 6 7 8 9 10 11 12 13 14 15 16 17 18 19 20 21 22 23 24
Variant number

g)

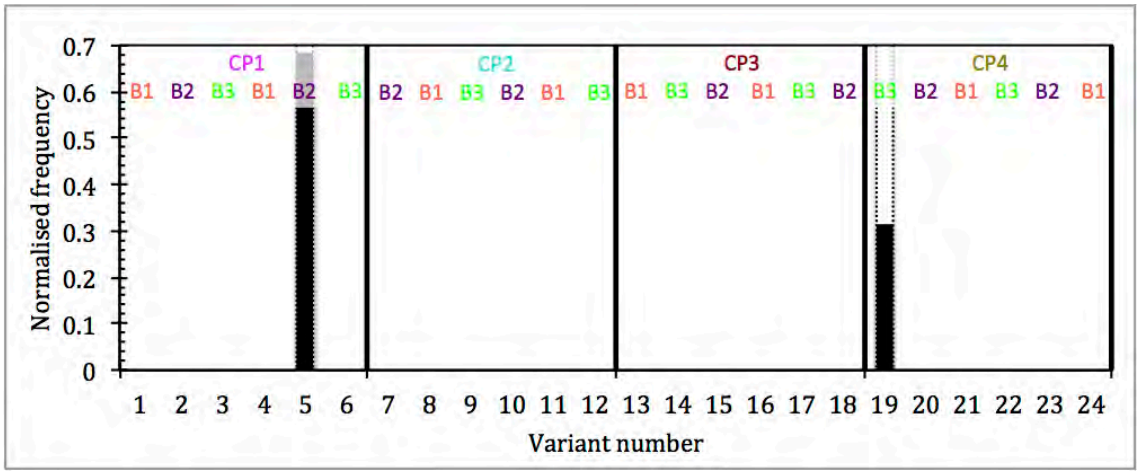
CP1
CP2
CP3
CP4
B1 B2 B3 B1 B2 B3 B2 B1 B3 B2 B1 B3 B1 B3 B2 B1 B3 B2 B3 B2 B1 B3 B2 B1
Normalised frequency
0.7
0.6
0.5
0.4
0.3
0.2
0.1
0
1 2 3 4 5 6 7 8 9 10 11 12 13 14 15 16 17 18 19 20 21 22 23 24
Variant number

h)

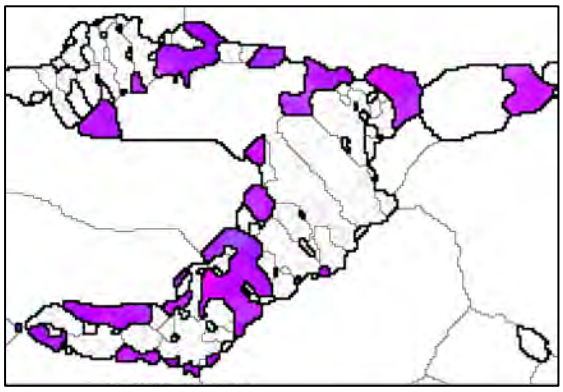

i)

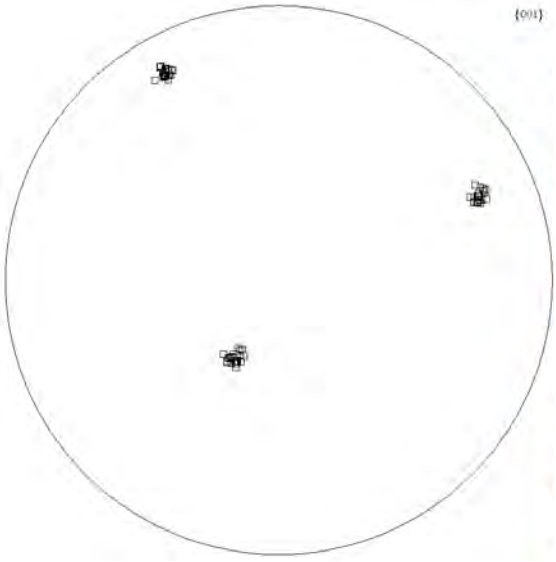

j)

Figure C.2: EBSD maps of bainitic ferrite laths (BF) and GB in the base steel; a) phases map, b) ferrite variants map, c) crystallographic packets (CPs) and d) Bain groups (BGs). e) The experimental and f) theoretical {001} pole figures of the variants with the average orientation of the RA grain represented by black squares. Normalised frequency of the formed variants for g) GB and h) BF; dash lines represent the realisation of the variants even in a small amount. i) The inverse-pole figure map of the RA grain and j) {001} pole figure of the experimental orientation of the RA grains. LAGBs=2° to 15°; silver colour and HAGBs >15° black colour. The thick black lines on all the maps represent the interphase boundaries and do not denote boundary misorientation.

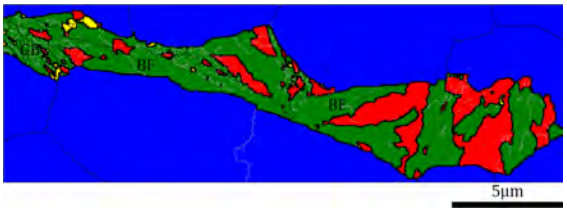

a)

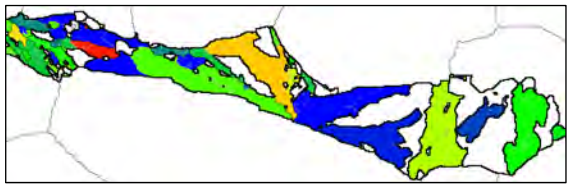

b)

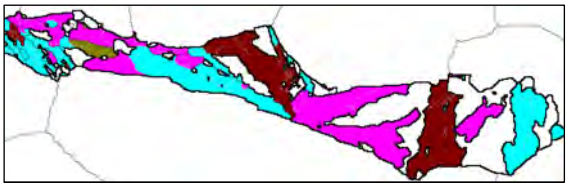

c)

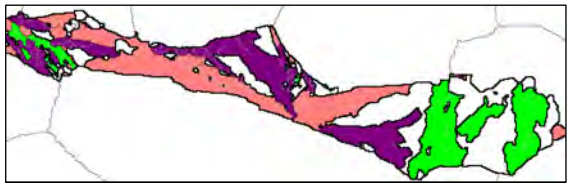

d)

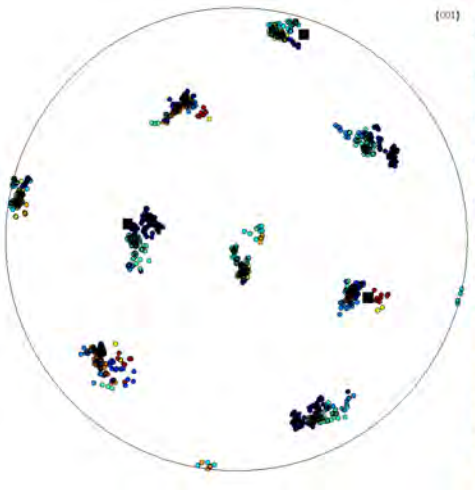

e)

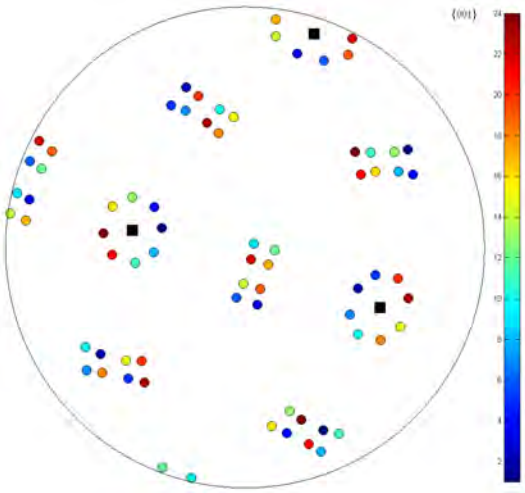

f)

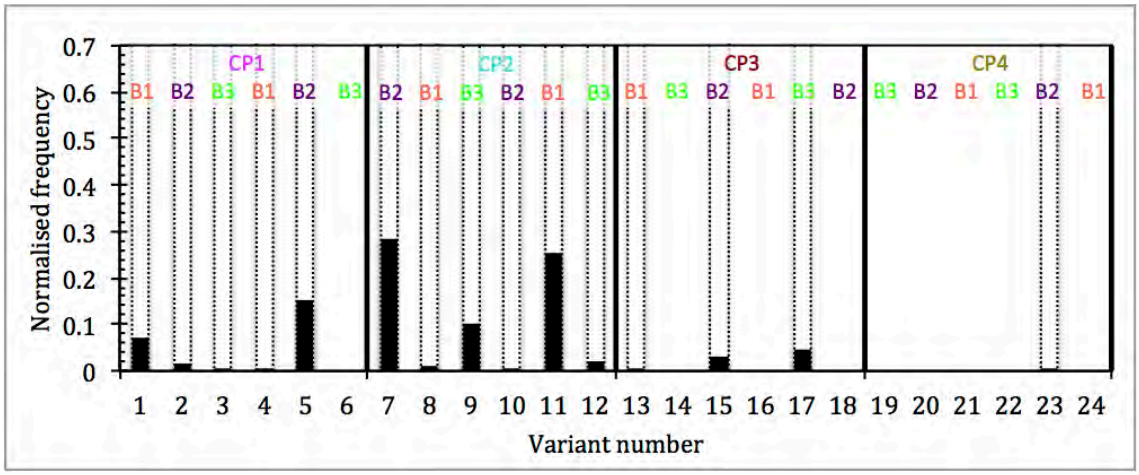
CP1
CP2
CP3
CP4
B1 B2 B3 B1 B2 B3 B2 B1 B3 B2 B1 B3 B1 B3 B2 B1 B3 B2 B3 B2 B1 B3 B2 B1
Normalised frequency
0 0.1 0.2 0.3 0.4 0.5 0.6 0.7
1 2 3 4 5 6 7 8 9 10 11 12 13 14 15 16 17 18 19 20 21 22 23 24
Variant number

g)

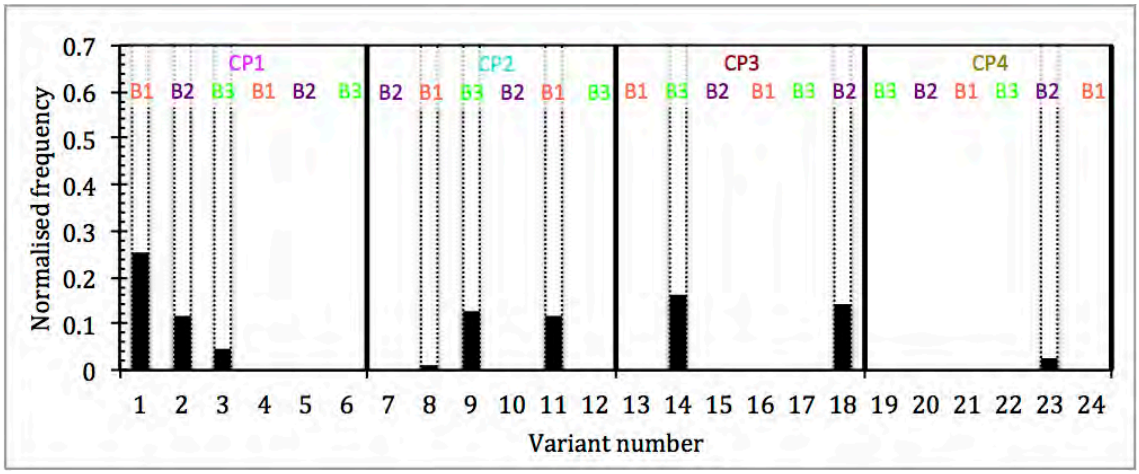
CP1
CP2
CP3
CP4
B1 B2 B3 B1 B2 B3 B2 B1 B3 B2 B1 B3 B1 B3 B2 B1 B3 B2 B3 B2 B1 B3 B2 B1
Normalised frequency
0 0.1 0.2 0.3 0.4 0.5 0.6 0.7
1 2 3 4 5 6 7 8 9 10 11 12 13 14 15 16 17 18 19 20 21 22 23 24
Variant number

h)

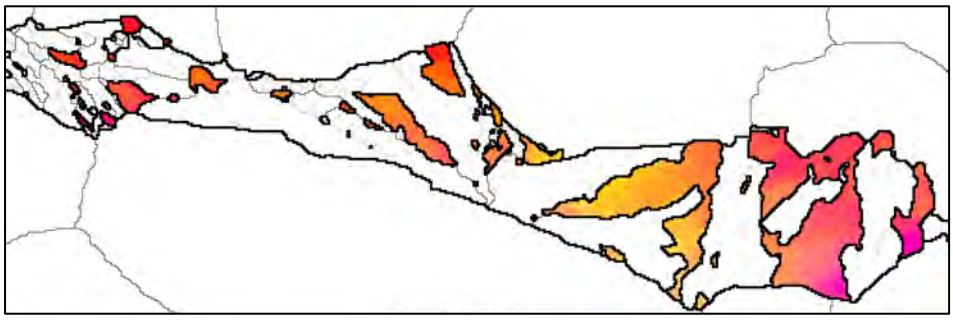

i)

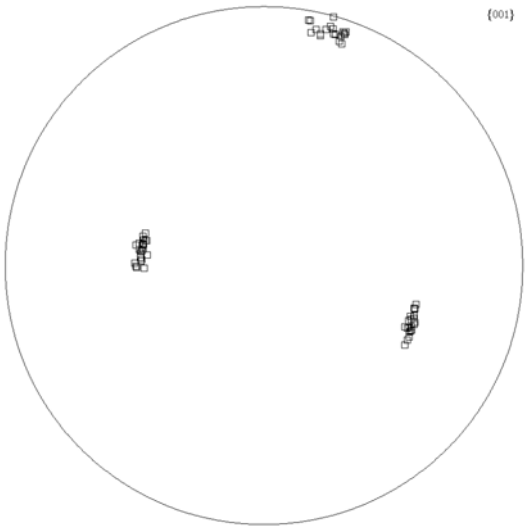

j)

Figure C.3: EBSD maps of bainitic ferrite laths (BF) and GB in the Nb-Ti steel; a) phases map, b) ferrite variants map, c) crystallographic packets (CPs) and d) Bain groups (BGs). e) The experimental and f) theoretical {001} pole figures of the variants with the average orientation of the RA grain indicated by black squares . Normalised frequency of the formed variants for g) GB and h) BF; dash lines represent the realisation of the variants even in a small amount. i) The inverse-pole figure map of the RA grain and j) {001} pole figure of the experimental orientation of the RA grains. LAGBs=2° to 15°; silver colour and HAGBs >15° black colour. The thick black lines on all the maps represents the interphase boundaries and do not denote boundary misorientation.

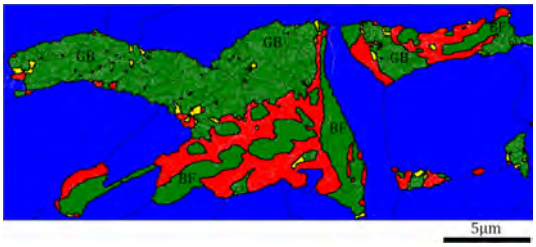

a)

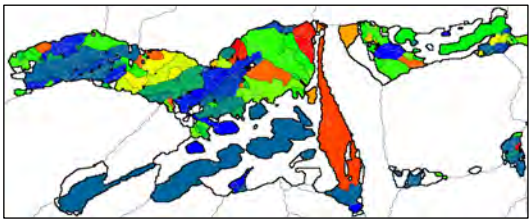

b)

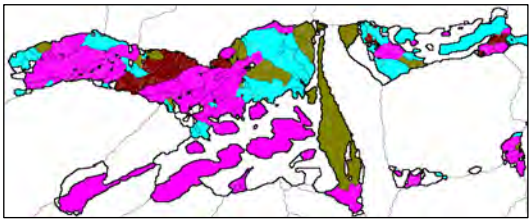

c)

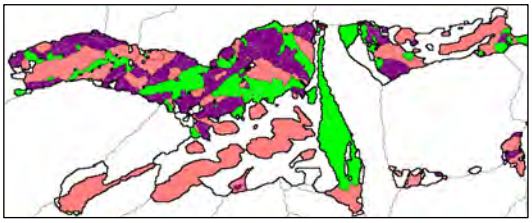

d)

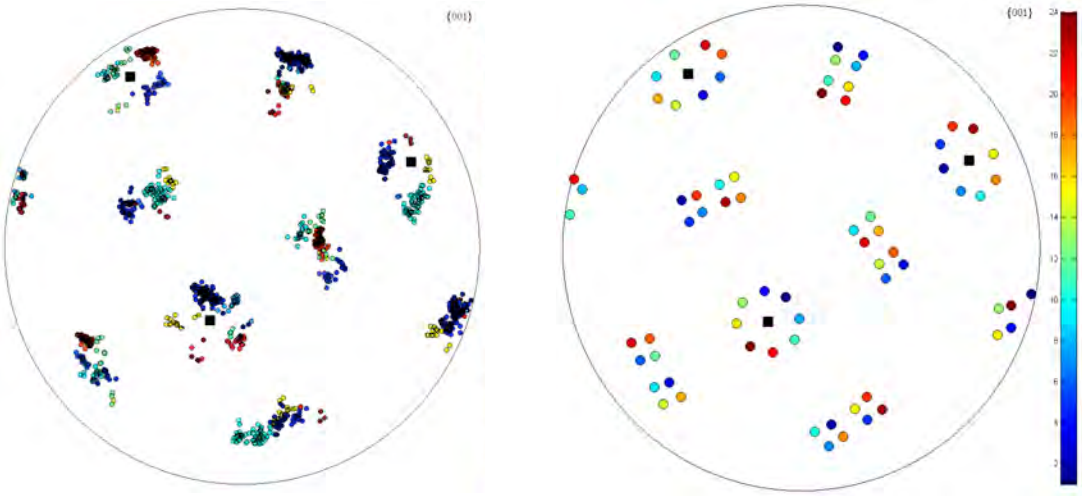

e)

f)

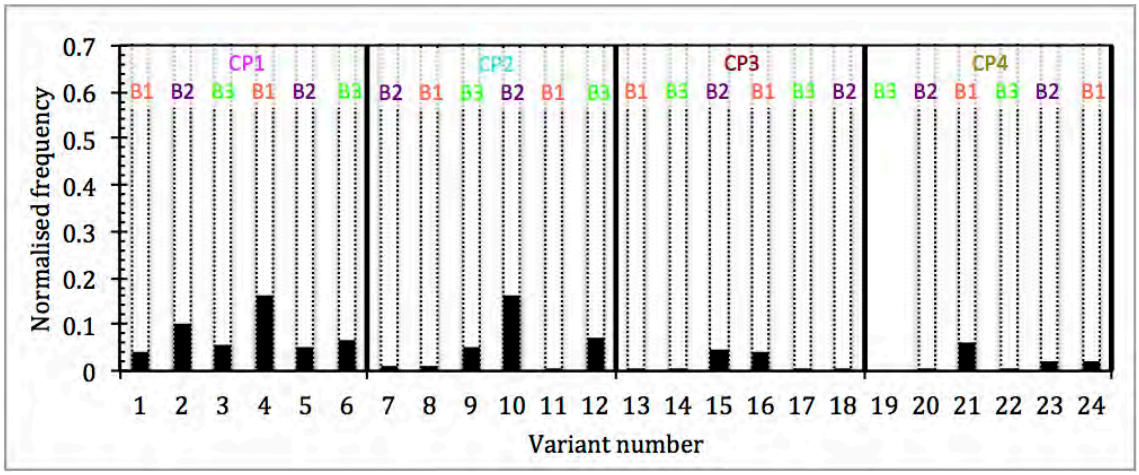
CP1
CP2
CP3
CP4
B1 B2 B3 B1 B2 B3 B2 B1 B3 B2 B1 B3 B1 B3 B2 B1 B3 B2 B3 B2 B1 B3 B2 B1
Normalised frequency
0.7
0.6
0.5
0.4
0.3
0.2
0.1
0
1 2 3 4 5 6 7 8 9 10 11 12 13 14 15 16 17 18 19 20 21 22 23 24
Variant number

g)

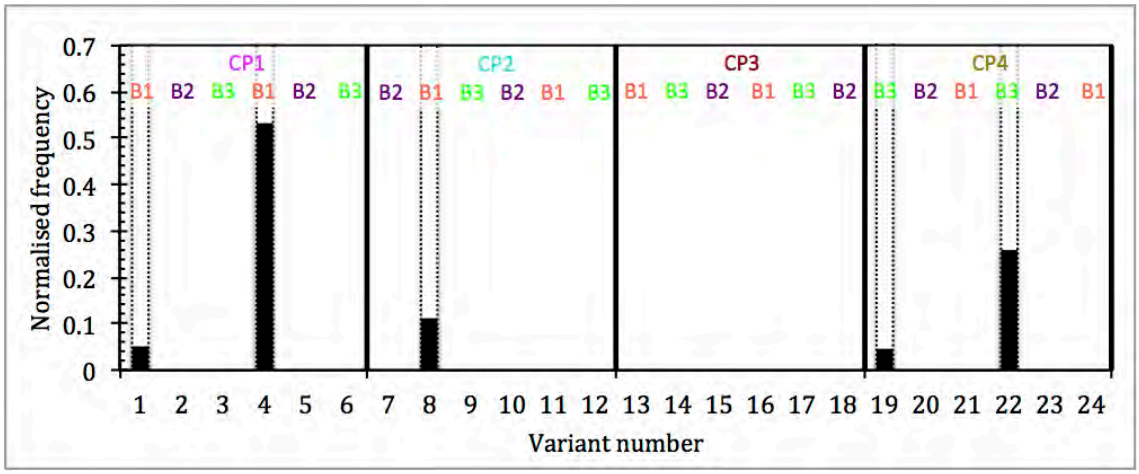
CP1
CP2
CP3
CP4
B1 B2 B3 B1 B2 B3 B2 B1 B3 B2 B1 B3 B1 B3 B2 B1 B3 B2 B3 B2 B1 B3 B2 B1
Normalised frequency
0.7
0.6
0.5
0.4
0.3
0.2
0.1
0
1 2 3 4 5 6 7 8 9 10 11 12 13 14 15 16 17 18 19 20 21 22 23 24
Variant number

h)

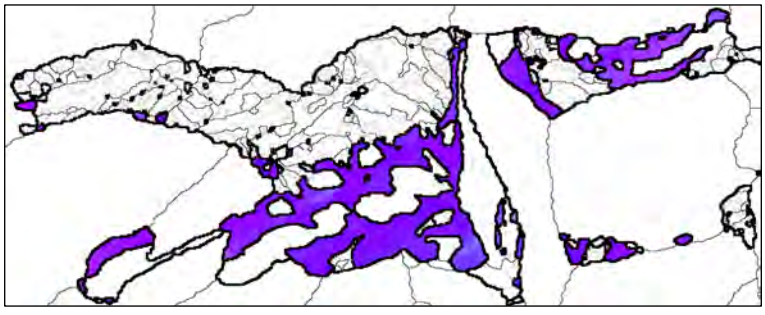

i)

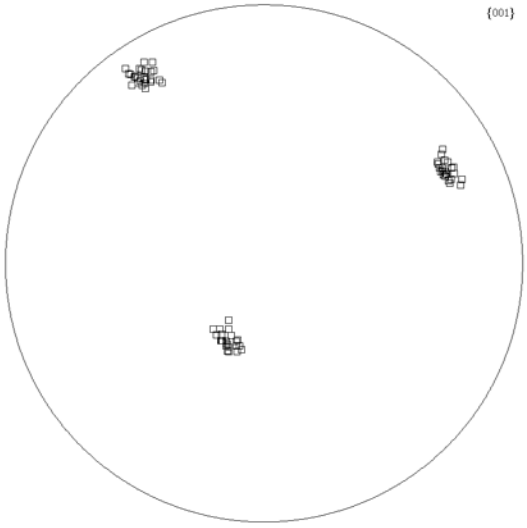

j)

Figure C.4: EBSD maps of bainitic ferrite laths (BF) and GB in the base steel; a) phases map, b) ferrite variants map, c) crystallographic packets (CPs) and d) Bain groups (BGs). e) The experimental and f) theoretical {001} pole figures of the variants with the average orientation of the RA grain shown by black squares. Normalised frequency of the formed variants for g) GB and h) BF; dash lines represent the realisation of the variants even in a small amount. i) The inverse-pole figure map of the RA grain and j) {001} pole figure of the experimental orientation of the RA grains. LAGBs=2° to 15°; silver colour and HAGBs >15° black colour. The thick black lines on all the maps represent the interphase boundaries and do not denote boundary misorientation.

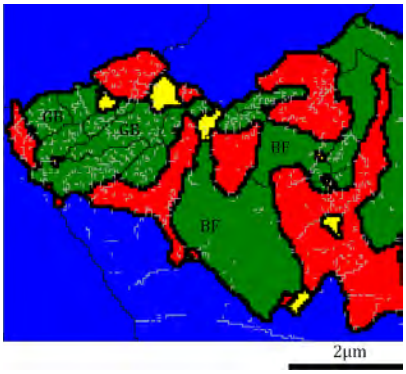

a)

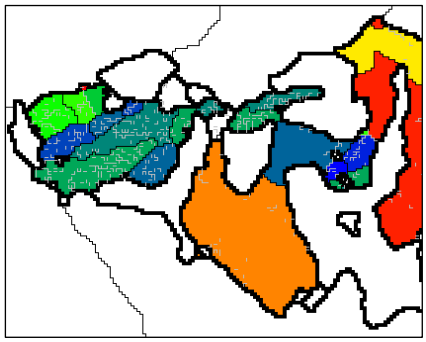

b)

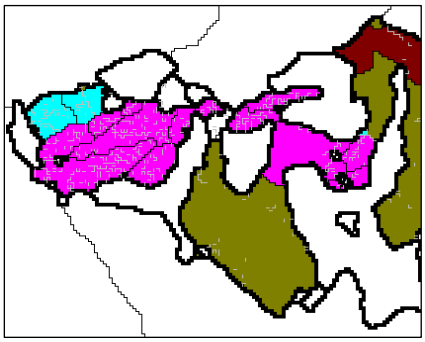

c)

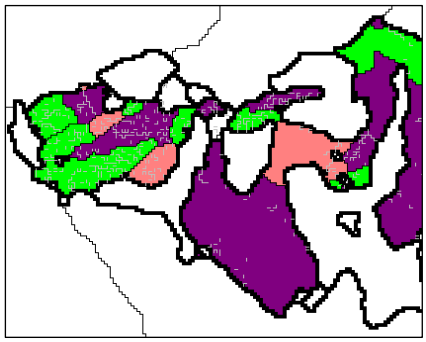

d)

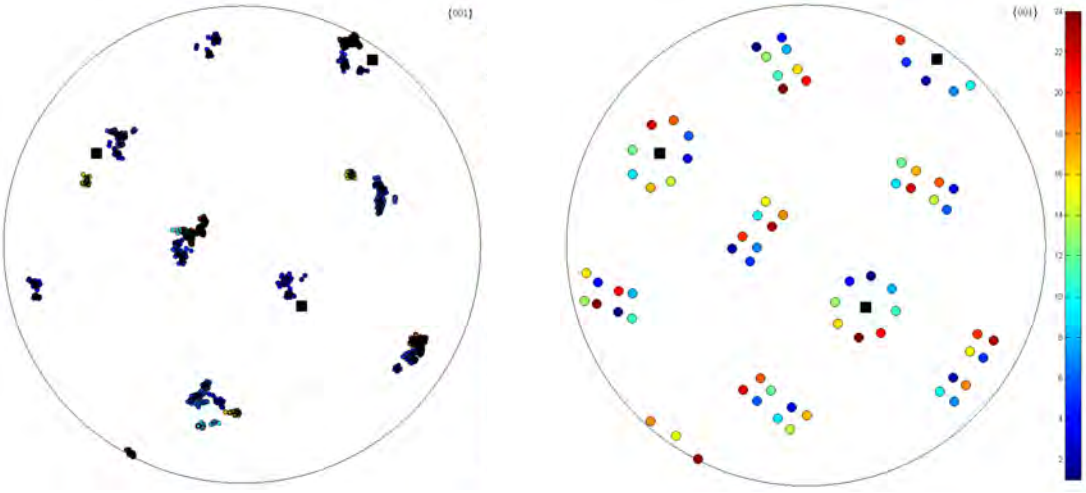

e)

f)

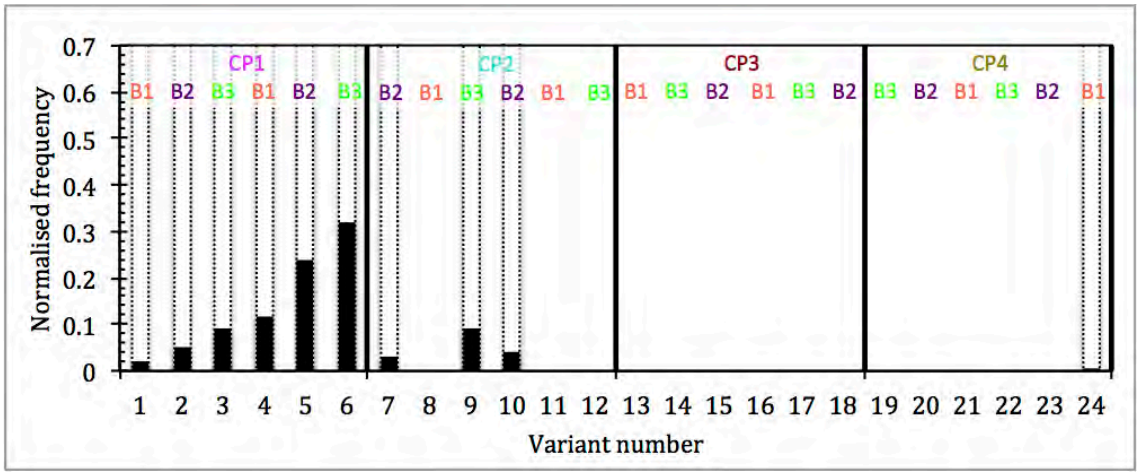
Normalised frequency
0.7
0.6
0.5
0.4
0.3
0.2
0.1
0
CP1
CP2
CP3
CP4
B1 B2 B3 B1 B2 B3 B2 B1 B3 B2 B1 B3 B1 B3 B2 B1 B3 B2 B3 B2 B1 B3 B2 B1
1 2 3 4 5 6 7 8 9 10 11 12 13 14 15 16 17 18 19 20 21 22 23 24
Variant number

g)

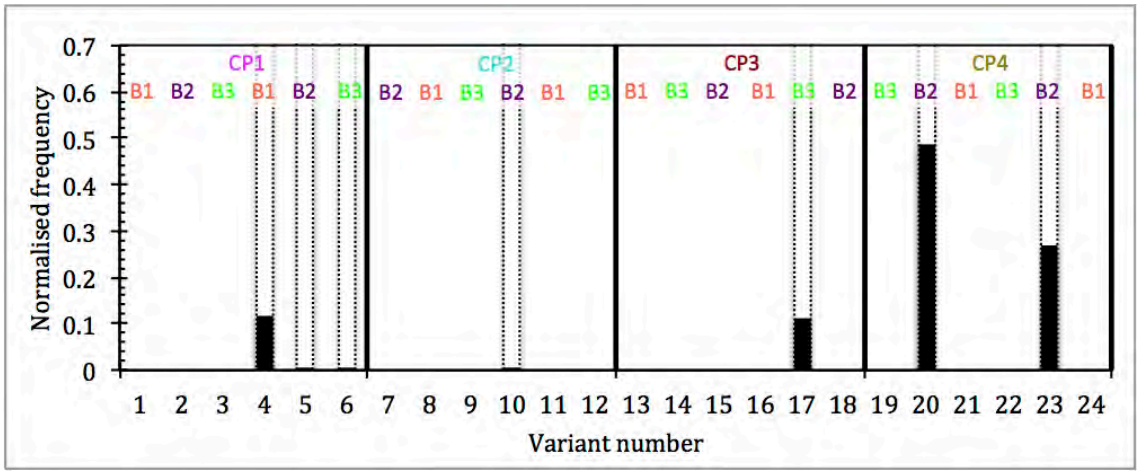
Normalised frequency
0.7
0.6
0.5
0.4
0.3
0.2
0.1
0
CP1
CP2
CP3
CP4
B1 B2 B3 B1 B2 B3 B2 B1 B3 B2 B1 B3 B1 B3 B2 B1 B3 B2 B3 B2 B1 B3 B2 B1
1 2 3 4 5 6 7 8 9 10 11 12 13 14 15 16 17 18 19 20 21 22 23 24
Variant number

h)

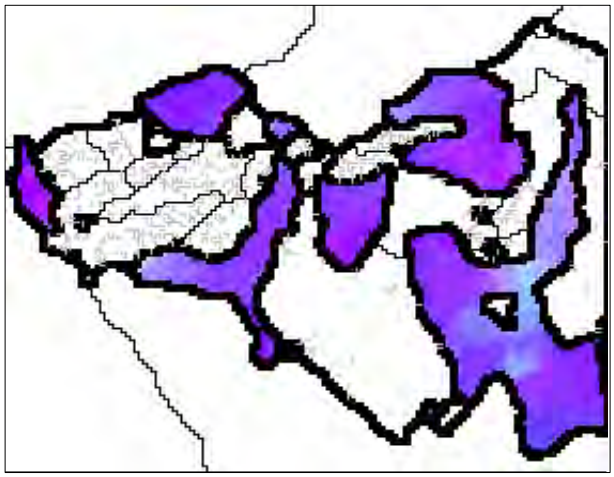

i)

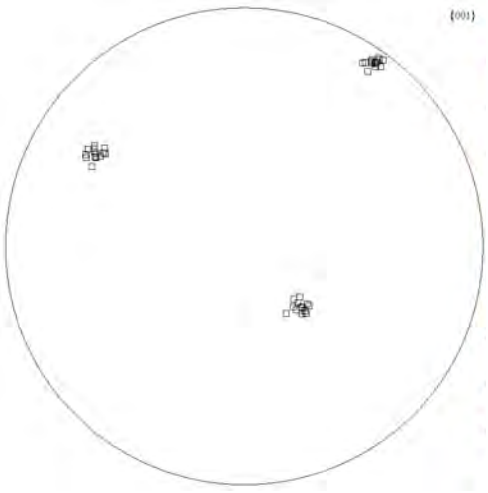

j)

Figure C.5: EBSD maps of bainitic ferrite laths (BF) and GB in the base steel; a) phases map, b) ferrite variants map, c) crystallographic packets (CPs) and d) Bain groups (BGs). e) The experimental and f) theoretical {001} pole figures of the variants, and the average orientation of the RA grain indicated by black squares in e) and f). Normalised frequency of the formed variants for g) GB and h) BF; dash lines represent the realisation of the variants even in a small amount. i) The inverse-pole figure map of the RA grain and j) {001} pole figure of the experimental orientation of the RA grains. LAGBs=2° to 15°; silver colour and HAGBs >15° black colour. The thick black line on all the maps represents the interphase boundary and does not denote boundary misorientation.

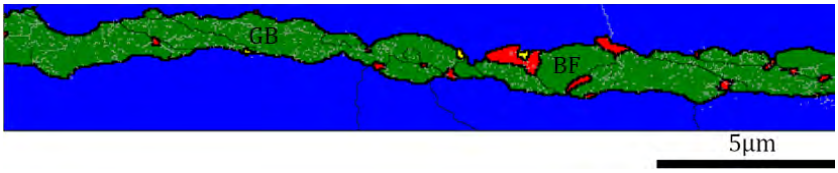

a)

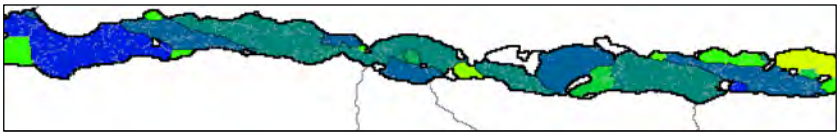

b)

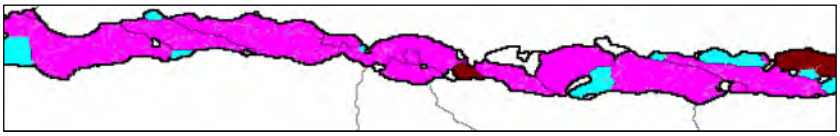

c)

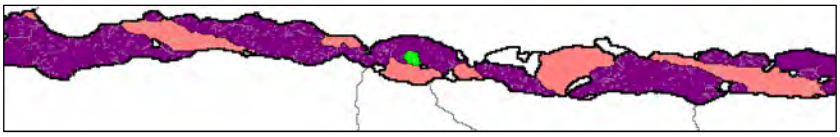

d)

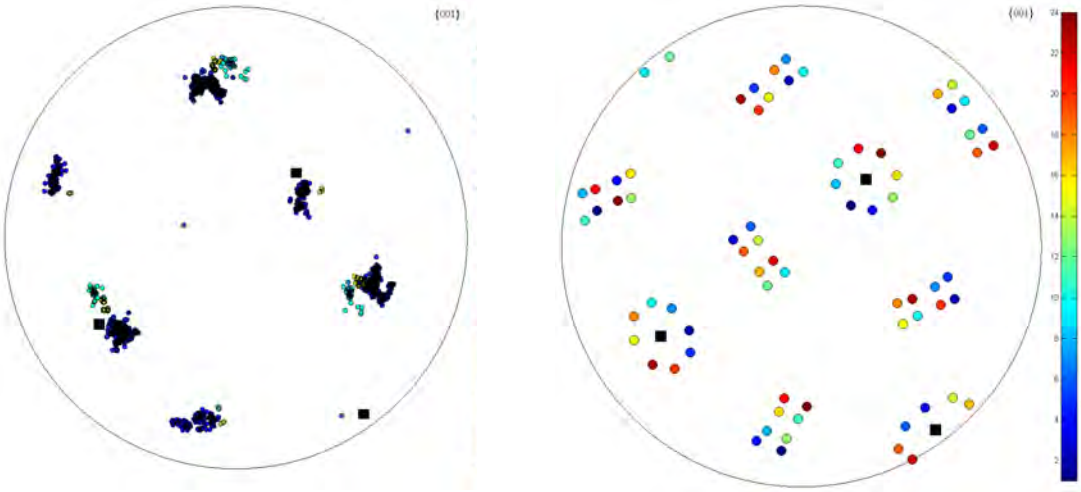

e) f)

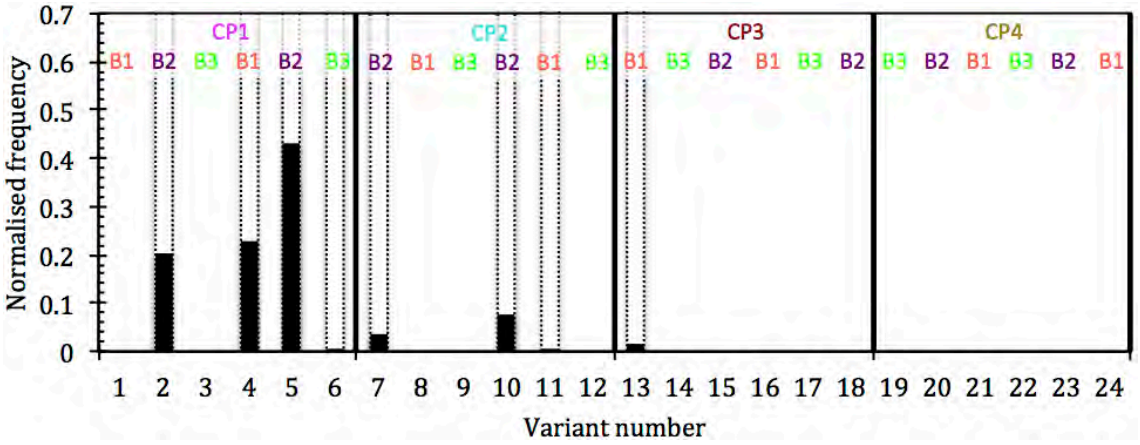
CP1
CP2
CP3
CP4
B1 B2 B3 B1 B2 B3
B2 B1 B3 B2 B1 B3
B1 B3 B2 B1 B3 B2
B3 B2 B1 B3 B2 B1
Normalised frequency
0.7
0.6
0.5
0.4
0.3
0.2
0.1
0
1 2 3 4 5 6 7 8 9 10 11 12 13 14 15 16 17 18 19 20 21 22 23 24
Variant number

g)

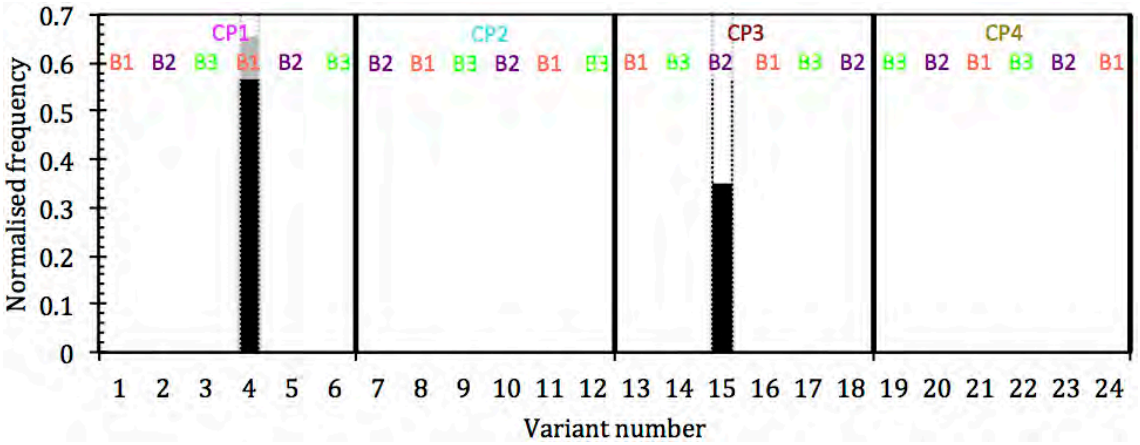
CP1
CP2
CP3
CP4
B1 B2 B3 B1 B2 B3
B2 B1 B3 B2 B1 B3
B1 B3 B2 B1 B3 B2
B3 B2 B1 B3 B2 B1
Normalised frequency
0.7
0.6
0.5
0.4
0.3
0.2
0.1
0
1 2 3 4 5 6 7 8 9 10 11 12 13 14 15 16 17 18 19 20 21 22 23 24
Variant number

h)

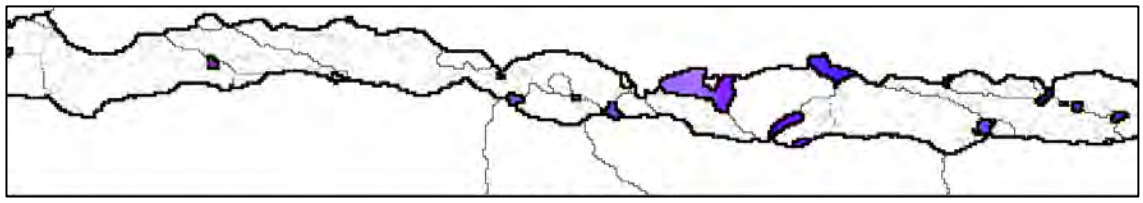

i)

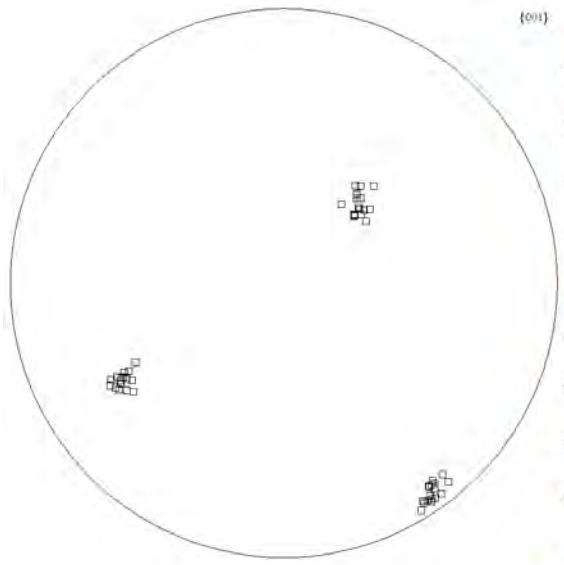

j)

Figure C.6: EBSD maps of bainitic ferrite laths (BF) and GB in the Nb-Ti steel; a) phases map, b) ferrite variants map, c) crystallographic packets (CPs) and d) Bain groups (BGs). e) The experimental and f) theoretical {001} pole figures of the variants with the average orientation of the RA grain represented by black squares. Normalised frequency of the formed variants for g) GB and h) BF; dash lines represent the realisation of the variants even in a small amount. i) The inverse-pole figure map of the RA grain and j) {001} pole figure of the experimental orientation of the RA grains. LAGBs=2° to 15°; silver colour and HAGBs >15° black colour. The thick black line on all the maps represents the interphase boundary and does not denote boundary misorientation.